Modeling Pulsed Power Plasmas and Applications to In-situ Nanoparticle Growth

by

Steven J. Lanham

A dissertation submitted in partial fulfillment
of the requirements for the degree of
Doctor of Philosophy
(Chemical Engineering)
in the University of Michigan
2022

Doctoral Committee:

Professor Mark J. Kushner, Chair
Professor Karthik Duraisamy
Professor Bryan R. Goldsmith
Professor Max Shtein

Steven J. Lanham

sjlanham@umich.edu

ORCID iD: 0000-0001-9715-4134

Dedication

To my family, friends, and anyone else who has helped me out along the way.

Acknowledgements

Finishing my degree has been a long road, filled with many challenges that I never anticipated. This work would not have been possible without the love and support from my friends, coworkers, collaborators, and family. First, I would like to thank Prof. Mark Kushner who treated me with near unlimited patience and support throughout my journey. His positive influence extends far past the role of an academic advisor, always encouraging students to be better people. I would also like to thank my other committee members – Professors Bryan Goldsmith, Karthik Duraisamy, and Max Shtein. I am lucky to have had the opportunity to learn from these people and for their valuable input.

Second, I would like to thank my many friends and colleagues: Peng Tian, Chad Huard, Amanda Lietz, Shuo Huang, Juliusz Kruszelnicki, Chenhui Qu, Jordyn Polito, Florian Krueger, Kseniia Konina, Mackenzie Meyer, Evan Litch, Aram Markosyan, Guy Parsey, Xifeng Wang, Soheila Mohades, Astrid Raisanen, Tugba Piskin, and Sanjana Kerketta. Special thanks to Julia Falkovitch-Khan who has worked tirelessly to help keep the research group running smoothly. I would also like to thank my collaborators – Jia Han, Patrick Pribyl, Walter Geckelman, Paolo Elvati, Angela Violi, Neeraj Chaubey, John Goree, Zichang Xiong, Gunnar Nelson, Uwe Kortshagen, Necip Uner, Eric Husmann, and Elijah Thimsen. Many more people besides those listed have helped me – and if you fall in that category thank you.

Third, I would like to thank the US Department of Energy Office of Fusion Energy Science, the National Science Foundation, the Army Research Office, and The Michigan Institute of Plasma Science and Engineering for providing financial support, making this work possible.

Finally, I would like to thank my family – my parents Gregory and Brenda Lanham, my siblings Julie Mower, Amy Findlay, and Tyler Lanham, and their growing families. Their love and support have gotten me through many difficult times, and they bring a lot of happiness to my life.

Table of Contents

List of Tables

List of Figures

Abstract

Low temperature plasmas (LTPs) have been an essential tool for semiconductor device fabrication. LTPs have been increasingly used in other fields, such as for the synthesis of nanometer sized particles. The prevalence of LTPs is largely due to the unique plasma environment – energy is coupled into the plasma electrons, resulting in unique chemistry far from thermal equilibrium. As such, the specifics of how power is coupled into the plasma system plays a primary role in how chemical reactivity can be utilized. This has led to techniques such as using pulsed power to increase control of the plasma, however, this technique has not been fully characterized particularly from a computational modeling perspective. Modeling of pulsed inductively coupled plasmas was done using the Hybrid Plasma Equipment Model (HPEM), a 2-dimensional reactor scale plasma multi-fluid simulator, and found that pulsing in electronegative plasmas requires resolving both the electromagnetic and electrostatic effects from the antenna. These systems are a sensitive function of the matching network used for power delivery, with good agreement from experiments.

LTPs have been used to synthesize high quality nanoparticles (NPs) that would be difficult to create using traditional methods, which may sinter or fail to anneal. Particles in plasmas generally charge negative, leading to mutual coulomb repulsion that results in monodisperse particle size distributions. However, a comprehensive growth mechanism of NPs in plasma is not well understood. Measuring even the most basic plasma parameters in these reactors proves challenging, leaving large gaps in knowledge about their fundamental operation.

In this thesis, a 3-dimensional kinetic simulation for particle growth and trajectories in LTPs, the Dust Transport Simulator (DTS), was developed to interface with the HPEM for self-consistent reactor scale modeling of plasma-based nanoparticle synthesis. Electrostatic trapping of particles in the plasmas was found to be a major component of the nanoparticle growth mechanism – a result contrary to what was previously believed in the field, and further confirmed by multiple experiments and models from several research groups. The updated DTS was used to develop scaling laws for nanoparticle growth rates as functions of plasma operating conditions, a necessary tool for the future design of NPs. Finally, the idea of using pulsed power was theorized as a viable tool to customize particle size distributions by manipulating the nanoparticles trapped in the plasma.

The main contributions to the field of low temperature plasmas and nanoparticle forming plasmas are as follows. First, pulsing the power in inductively coupled plasma (in many cases) requires transitioning from primarily electrostatic to electromagnetic power deposition, which is a sensitive function of the matching network. Second, electrostatic trapping of nanometer sized particles growing in the plasma occurs under typical operating conditions and may be the predominant factor for predicting particle growth. Third, trapped particles can be manipulated, for example by pulsing the power, to customize the nanoparticles grown in the plasma. Finally, the updated capabilities of the DTS may be used by others to investigate particle growth in low temperature plasmas.

Chapter 1 Introduction

1.1 Low Temperature Plasmas (LTPs)

Plasma is considered the most abundant state of matter in the observable universe – a major component of stars and intergalactic space [1]. Plasma consists of charged particles, generally electrons and ions, making them electrically conductive and exhibit cohesive behavior. Most man-made plasmas are partially ionized gases where an external source of power is used to couple energy into the system. Low temperature plasmas (LTPs) are named as such because energy is coupled into the system selectively, resulting in hierarchies of temperature among species. This process is shown in Fig. 1-1, electrons will quickly gain energy from electric fields due to their low mass. The time scales which electrons in a plasma can respond to an external disturbance, such as electromagnetic waves, is called the plasma frequency and is typically ~GHz for processing plasmas:

$$\omega_p = \sqrt{\frac{q^2 n_e}{\varepsilon_0 m_e}} \tag{1.1}$$

These hot electrons can collide with background gas molecules and impart energy in a variety of ways – elastic collisions where kinetic energy is conserved or inelastic collisions where some energy goes into internal excitation, e.g. electronic excitation, ionization, and breaking of chemical bonds. This results in electron temperatures greater than ion and gas temperatures ($T_e \gg T_{ion} > T_{gas}$).

Low temperature plasmas have long been a staple tool used in the semiconductor industry, operated under vacuum conditions (typically 10-100s mTorr). Quiescent plasmas under these conditions will form plasma sheaths when in contact with surfaces, shown in Fig. 1-2, which can directionally accelerate ions into the surface [2]. Due to the high thermal temperature, electrons will naturally diffuse to surfaces faster than ions. The surface flux of positive and negative charges will naturally equilibrate to a floating potential lower than the bulk electric potential in the plasma, forming an electric field to repel electrons but accelerate positive charged species directionally into surfaces. The distance over which a plasma can violate charge neutrality is generally characterized as the Debye length:

$$\lambda_D = \sqrt{\frac{\varepsilon_0 T_e}{q^2 n_e}} \tag{1.2}$$

where T_e is the electron temperature and n_e is the electron density. The thickness of a plasma sheath is often several λ_D. Manipulation of the sheath voltage with external power sources has enabled engineering on the atomic scale, etching complex structures such as the transistor shown in Fig. 1-3 [3].

Chemical reactivity transfer in low temperature plasmas is also fundamentally important for the microelectronics industry. Reaction rate coefficients for different processes can be determined by using a cross section and $f(\varepsilon)$, the electron energy distribution function:

$$k = \int_0^\infty \sigma(\varepsilon)\left(\frac{2\varepsilon}{m}\right)^{1/2} f(\varepsilon)\, d\varepsilon \tag{1.3}$$

The seminal work of Coburn and Winters exhibits the synergistic effects of Si etching by simultaneous exposure to both an ion beam (Ar^+) and a fluorinating gas (XeF_2), shown in Fig. 1-4 [4]. Modern semiconductor processes use complex gas mixtures, and current research into etching with near atomic layer precision involves control over the chemistry just as much as ion energies.

More recently, the chemical reactivity transfer from low temperature plasmas have enabled advances in many different fields, the main example discussed in this work being plasma-based nanoparticle synthesis.

The rest of this chapter is outlined as follows: the main types of plasma sources, and pulsing the power are discussed in Sec. 1.2. A brief discussion of the field of dusty plasmas, with an emphasis on nanoparticle containing plasmas are discussed in Sec. 1.3. Modeling of plasmas and plasma-based nanoparticle synthesis are discussed in Sec. 1.4. Motivation for the work presented in this thesis is discussed in Sec. 1.5. The scope of the work is discussed in Sec. 1.6.

1.2 Plasma Sources

Radio frequency (RF) power is the primary source for generating plasmas for materials processing. The two dominant configurations for delivering this power are capacitively coupled plasmas (CCPs) and inductively coupled plasmas (ICPs) [5]. Examples of both reactor setups are shown in Fig. 1-5, and are discussed in more detail below.

1.2.1 Capacitively Coupled Plasmas

Capacitively coupled plasmas are sometimes called parallel plate reactors because they typically deliver RF power to the plasma using a plate electrode with a separate ground electrode on the opposite side. Typical processing reactors add an additional capacitor in between the power source and the powered electrode called a blocking capacitor where charge builds up to balance the current in the plasma. The plasma sheath oscillates at the applied RF frequency, delivering power to the system. The plasma is sustained by secondary electron emission of hot electrons that originate from accelerating ions into surfaces, but stochastic heating of electrons from sheath

expansion can also contribute. The discharge is characterized by the applied voltage on the electrode rather.

Additionally, capacitively coupled systems are typically used to study the fundamental properties of dusty plasmas [6–9], and are commonly used for plasma based nanoparticle synthesis.

1.2.2 Inductively Coupled Plasmas

In the ICP configuration, power is electromagnetically delivered by antennas taking the form of external coils. In the stovetop geometry, the coils are flat spirals mounted on an insulating ceramic window which is usually the top of the vacuum system. The coils are driven at frequencies ranging from hundreds of kilohertz to tens of megahertz depending upon the application, pressure, and power. The incident electromagnetic wave from the antenna typically has a dominant component in the azimuthal direction and propagates in the axial direction. The wavelength is usually much longer than either the skin depth or the chamber, and so propagation is in near field. Electrons in plasma, accelerated by the incident RF field, produce a harmonic current, which in turn generates a small magnetic field within the plasma.

Industrial applications typically use RF power at 13.56 MHz with pressure at 10s of mTorr. The momentum transfer collision frequency (ν_m) is less than or close to the driving frequency of the coil. The skin depth (δ), the e-folding distance of current density from the electromagnetic field into the plasma can be approximated by

$$\delta = \left(\frac{m_e}{q^2 \mu_0 n_e} \right)^{1/2} \tag{1.1}$$

and is typically 1-2 cm for a typical ICP. Power is primarily transferred to the plasma within this range through collisionless heating due to the low pressure.

Although power in inductively coupled plasmas is typically deposited through electromagnetic means, under certain circumstances power can couple capacitively from the high voltage on the antenna causing sheath oscillations reminiscent of capacitively coupled plasmas discussed above. When pulsing the power, these conditions naturally arise, so will be discussed below.

1.2.3 Pulsing Inductively Coupled Plasmas

Pulsed ICPs as used in microelectronics fabrication operate at pressures of tens of mTorr in attaching gas mixtures such as Ar/Cl_2 powered with radio frequency (RF) supplies of a few to tens of MHz. The pulsed repetition frequency (PRF), pulses per second, can be hundreds of Hz to tens of kHz. Duty cycle (DC), the fraction of time the power is applied per cycle, can be 10-50%. The end result is that the electron density at the time the power is applied at the leading edge of the pulse can be as low as 10^8 cm^{-3} whereas later during the pulse, the electron density can exceed 10^{11} cm^{-3} [10,11]. These densities can increase across these three decades during a few to 10s or 100s of μs depending on the power delivery system and reactor design.

If the electron density at the beginning of a power pulse is too low, the electromagnetic skin depth, δ_P, may exceed the dimensions of the reactor which then makes inductive coupling of power from the antenna problematic [5,12–15]. For these conditions, the antenna simply acts as an electrode which electrostatically and capacitively couples power into the plasma through the dielectric window between the antenna and the plasma [12]. This is the E-mode during which power can be dominantly coupled into the plasma by sheath oscillation (much like a capacitively coupled plasma) with power mainly deposited by ion acceleration from the plasma into the dielectric window under the antenna [15]. During the capacitive E-mode, the reactance of the plasma is negative. As the electron density increases, δ decreases which increases the fraction of

power that is inductively coupled until the power is dominantly delivered by electron acceleration in the electromagnetic field within δ of the antenna. This is the H-mode during which the reactance of the plasma is positive. In practice there may be mixed-mode coupling, both E-mode and H-mode during quasi-steady state operation of the ICP [12,13]. The degree of E- and H-mode coupling depends on factors such as the voltage across the antenna, the proximity of antenna to the plasma, the shape of the antenna, gas pressure and composition, and the use of a Faraday shield between the antenna and plasma [16].

The E-H transition in ICPs has been addressed both experimentally and theoretically [17–25], and will be further discussed in subsequent chapters. However, little work has been done specifically addressing the E-H transition for pulsed systems, particularly when also considering the matching network. The change in Z_L due to the E-to-H transition in addition to the reduction in the resistance of the plasma is typically over shorter times than the components in the match box can change, so power delivery cannot be efficiently matched to the plasma for an entire pulsed cycle.

1.3 Dusty Plasmas

The term dusty plasma refers to a weakly ionized gas containing solid particulates [26,27]. Over the past two decades, nonthermal dusty plasmas in low pressure flowing systems have become critically important sources for the synthesis of nanoparticles and quantum dots [6,7,28–31]. In these plasmas, energetic plasma electrons decompose molecular gaseous precursors, producing radicals, which lead to the nucleation and growth of nanoparticles. Based on the extreme nonequilibrium in these plasmas, with the temperature of electrons (several eV) exceeding the temperature of the gas atoms and plasma ions (near ambient) by about two orders of magnitude,

dusty plasmas offer the ability to synthesize crystalline nanoparticles even of high melting point, including covalently bonded materials. This capability is due to the selective heating of nanoparticles to temperatures far above the gas temperature [31] which enables the synthesis of nanocrystals that are commonly inaccessible to liquid phase synthesis [32–34]. Once the nanoparticles growing in the plasma reach a certain minimum size, they acquire a negative charge based on the higher mobility of free plasma electrons compared to that of plasma ions which suppresses agglomeration of larger nanoparticles as a result of the resulting Coulombic repulsion [35,36]. This mechanism is widely credited with the ability of plasmas to produce nanoparticles with much more monodisperse size distributions than other gas-phase approaches [31].

Dust particles immersed in plasmas are subject to a variety of forces, including electrostatic, gas and ion drag, thermophoresis, Brownian motion, and gravity [37–45]. The relative magnitude of each force depends on the size of the particle and the plasma conditions. The plasmas of interest here are produced by application of radio frequency (RF) voltages, typically sustained in cylindrical reactors of up to a few cm in diameter and 10-15 cm length, operating at pressures of a few Torr with nominal power deposition of up to about 50 W. The electrostatic force originates from the negative charge acquired by dust grains and the electric fields in the plasma. These electric fields are either ambipolar in nature, self-generated to confine the highly mobile electrons in a way that the plasma bulk is charged slightly positively compared to the surrounding reactor walls, or due to applied voltages, which for the plasmas of interest produce moderate electric fields of only a few V-cm^{-1} in the bulk plasma and hundreds of V-cm^{-1} in the bounding sheaths. In dusty plasmas containing micron-sized particles, particles can carry many thousands of elementary charges and electrostatic forces produced by the RF sheaths at the plasma boundary can be strong enough to balance the gravitational and ion drag forces, leading to

particle levitation and trapping close to the plasma boundary sheath [27,46]. In semiconductor processing, this trapping of particles was recognized as a problem as early as the 1990s [47], as dust particles that form during plasma processing can accumulate in these electrostatic particle traps and then drop onto the wafer being processed after the plasma is turned off.

Plasma reactors used for nanoparticle synthesis are fundamentally different from reactors used in semiconductor processing and those typically used to study the fundamental properties of dusty plasmas which are parallel plate, capacitively coupled systems [6–9]. A typical reactor geometry is shown in Fig. 1-6, the plasmas typically used for nanoparticle synthesis are based on tubular laminar flow reactors, in which a plasma is excited either by capacitive or inductive coupling of RF power. Gas flow rates are commonly large so that the gas residence time in the reactor is on the order of milliseconds in order to limit particle growth to the nanometer size range. For nanometer-sized particles, gravity does not play a significant role.

1.4 Modeling of Low Temperature Plasmas

1.4.1 Reactor Scale Modeling of LTPs

There are two main methods for modeling low temperature plasmas – using a fluid-based approach or a kinetic based. Fluid models are based on macroscopic quantities (species densities, average velocity, average energy) governed by the fluid equations which are obtained from taking moments of the Boltzmann (or similar) equation. Assumptions need to be made about the velocity distribution (often assumed Maxwellian) to determine transport coefficients. Kinetic methods naturally produce distribution functions that can better characterize the system. Procedurally, this method tracks trajectories of pseudoparticles, but can be computationally expensive, so is typically only done for electrons and ion species. The work in this thesis uses a hybrid approach in

modeling, where quantities that are not well described by a fluid-based approach are derived kinetically. This allows for a full reactor scale simulation of low temperature plasmas including tracking dozens of chemical species with reactions. Further details about the modeling platform are contained in Chapter 2.

1.4.2 Nanoparticle Synthesis in LTPs

Low temperature plasmas are keen alternatives to traditional liquid phase methods for synthesis of nanoparticles due to the unique nonthermal plasma environment [48]. Plasmas are particularly useful for synthesis of nanoparticles (diameters of a few to 10s of nm) composed of high melting point materials that require crystallization temperatures above which can be sustained in liquid solvents [49]. Liquid based techniques have a hard limit on the temperature which nanoparticles can be synthesized because the organic solvents typically used vaporize at low temperatures. Gas phase synthesis techniques typically operate at thermal equilibrium, which can cause nanoparticles to sinter and agglomerate together rather than form separately.

Plasmas also enable synthesis of compound nanoparticles (NPs) such as group III-V semiconducting materials and metal oxides that require covalent bonding rather than the ionic bonding promoted by liquid phase synthesis [50]. NPs synthesized in plasmas include: silicon nanoparticles with high photoluminescent yields, gold nanoparticles and nanostructures used for solar water splitting and enhancement of solar cells, doped copper sulfide and titanium nitride nanoparticles with extended plasmonic range for use in photocatalysis, gallium nitride nanoparticles for electroluminescent and power electronics, and zinc oxide nanoparticles for use in cancer treatment, among others [7,32,51–53]. Plasma produced NPs have properties (size, luminescence, hardness, and composition) that are tunable by changing plasma operating

parameters such as power, pressure, gas flow rate, excitation method and gas composition [8,31,54].

Nanoparticles have been synthesized in a variety of radio frequency (RF) or DC driven reactor configurations by flowing small fractions of a metal-containing precursor gas, such as silane (SiH_4) for Si nanoparticle production, in a carrier gas such as argon or helium. The precursor gas is then dissociated by electron impact processes creating radicals in the plasma, leading to nanoparticle growth by nucleation, agglomeration and eventually surface deposition. A three-step growth mechanism has been widely accepted for plasma produced nanoparticles, though not all aspects are fully understood. Boufendi and Bouchoule showed that plasma-assisted nanoparticle synthesis occurs by nucleation, coagulation, and growth by surface deposition [55]. The nucleation phase is characterized by a rapid increase in particle size and decrease in particle concentration, resulting in crystalline particles a few nm in size. The small particles coagulate, resulting in larger nanoparticles (~50 nm) that gain increasingly negative charge and become trapped in the center of the plasma where the electrical potential is highest. The growth of the trapped particles is dominated by surface deposition by radicals, and particles with diameters from a few hundred nm to a few microns can be produced. Since particles of the same polarity repel each other, mechanisms for coagulation are among the most debated of the nanoparticle growth processes.

Particle charging is thought to be one of the most important factors contributing to the unique properties and morphologies of low temperature plasma (LTP) produced nanoparticles. Particles of sizes greater than a few nm in LTPs typically charge negatively, which prevents sometimes undesired agglomeration due to the NP mutual electrostatic repulsion, leading to a narrower size distribution compared with other synthesis methods. With most LTPs having a

positive electrical potential, charging also results in particle trapping at the center of the plasma, which can facilitate more growth and heat nanoparticles to temperatures sufficient for crystallization [36]. Particle charge distributions are sensitive functions of plasma properties and may be one of the most useful NP properties for correlating nanoparticle growth to plasma operating conditions. The number of elementary charges on NPs span several orders of magnitude with small NPs (< 1 nm) having zero to a few negative elementary charges (and in some cases positive), while larger nano- and micron-sized particles having several thousands of negative elementary charges [56]. Monte Carlo simulations performed of particle charging showed that small particles in LTPs may also carry small positive charge with the rate of charge fluctuation decreasing with increasing particle size [57]. The charge on small NPs (< a few nm) have stochastic fluctuations that occur on time scales that are much shorter (10^5 - 10^6 s^{-1}) than the time for particle charge to reach equilibrium (a few ms).

Several computational investigations of LTP facilitated nanoparticle synthesis have been conducted while also facing several challenges. NPs are chemically reactive, nucleating, coagulating, and grow at different rates dependent on plasma parameters, such as gas mixture power and residence time, while local reactant densities can vary over the length of a reactor. The polydispersity of particle size distributions adds a level of complexity and computational burden. To address the large range of sizes of plasma produced NPs, many models employ a sectional growth approach, adapted from the aerosol physics community, in which the particle size range is divided into bins and a population balance is solved for each bin [56,58–60]. Each size bin may be further divided into different charge states. Due to the large number of equations needed to resolve the systems of interest, these models are computationally expensive and are often 0- or 1-dimensional. When including particle charge distributions in sectional models, the computational

burden increases. Monte Carlo (MC) methods have been used to address these computational scaling challenges, and have produced nano-particle size and charge distributions which agree very well with experiments [61]. With the emphasis on particle properties, these MC methods often specify the plasma conditions as opposed to computing the plasma conditions from first principles.

1.5 Motivation

The main motivation for the work presented in this thesis is to improve the materials that can be made using low temperature plasma processes. Manufacturing processes generally use gas mixtures that can be difficult to take measurements in (e.g. depositing material on probes), so experimental information may be sparse or non-existent. The general approach in this work is to create and use computational models to improve understanding of these plasma systems. The fundamental physics that are important in these processes are captured while varying the processing conditions to develop scaling laws that can inform experiments and theorists.

One of the main points addressed in this thesis is pulsed low temperature inductively coupled plasmas. Although pulsing in plasma processing chambers has been researched previously, and even used in industry, these systems have not been fully characterized numerically. In the late afterglow, the plasma density can significantly decrease and necessitate re-ignition through capacitive coupling. The specifics of the impedance matching network also heavily impact pulsing, and have not been thoroughly addressed. The work done in this thesis seeks to address both of these points by resolving the mode transitions of power deposition in pulsed inductively coupled electronegative plasmas and characterizing the effects of the matching network on how power is deposited in the plasma when pulsing.

The other main topic presented in this work is understanding the mechanism for plasma-based nanoparticle growth. The types of plasmas used for this work are difficult to measure due to deposition by particles and precursor radicals, so much of the current understanding of these types of plasmas come from experience and assumptions about the plasma conditions. The modeling work in this thesis aims to give insight into the conditions in these plasmas by coupling full reactor scale simulations of the plasma to a kinetic nanoparticle growth model. Understanding the relationship between plasma operating parameters and particle growth, morphology, and composition will lead to optimization of plasma nanoparticle production techniques and enable rapid development of new and novel nanomaterials.

The main contributions to the field of low temperature plasmas and nanoparticle forming plasmas of this work are as follows. First, pulsing the power in inductively coupled plasma (in many cases) requires transitioning from primarily electrostatic to electromagnetic power deposition, which is a sensitive function of the matching network. Second, electrostatic trapping of nanometer sized particles growing in the plasma occurs under typical operating conditions and may be the predominant factor for predicting particle growth. Third, trapped particles can be manipulated, for example by pulsing the power, to customize the nanoparticles grown in the plasma. Finally, the updated capabilities of the DTS may be used by others to investigate particle growth in low temperature plasmas.

1.6 Scope of Dissertation

The motivation for the work in this thesis is addressed in the subsequent chapters, briefly detailed below. In Chapter 2, the computational models used for this thesis were discussed. Plasma simulation was done using the Hybrid Plasma Equipment Model (HPEM), a 2-dimensional

multi-fluid simulator for low temperature plasmas. The HPEM was updated to better interface with the Dust Transport Simulator (DTS), a 3-dimensional kinetic particle model to track trajectories, charge, and growth of nanoparticles in the plasma. Significant modifications of the DTS were needed to capture particle growth. The updated code enables numerical exploration into the mechanism of nanoparticle growth in low temperature plasmas, something that is difficult to measure via experiments.

Chapter 3 details collaborative research into pulsed inductively coupled plasmas. The 2-dimensional plasma model (HPEM) was benchmarked against 3-dimensional plasma measurements for pulsed Ar plasmas and were found to be in good agreement. This modeling was extended to pulsed electronegative plasmas (Ar/Cl_2) where the E- to H-mode transition of power deposition naturally occurs from pulse to pulse. Modeling of these types of plasmas was found to heavily depend on the power matching network connected to the antenna.

In Chapter 4, the effects of a chirped bias electrode in an inductively coupled plasma processing chamber were discussed. Sweeping the frequency of the voltage applied to the bias lead to ions hitting a wafer for processing at energies that differ from using the component frequencies independently. This difference was a consequence of the dynamic charging and discharging of the self-generated dc bias which balances the current. Plasma systems should be treated holistically when modeling, a major benefit of using a full system simulator. The idea of frequency tuning as a tool for matching power was also briefly discussed.

In Chapter 5, the idea of particle trapping in plasma nanoparticle synthesis reactors was introduced. Experimental results from three separate plasma reactors, and two separate computational models for nanoparticle trajectories (one being the Dust Transport Simulator) were used to give credence to this theory. This work may constitute a shift in perspective of the plasma-

based nanoparticle synthesis community – previous works assumed nanometer sized particles were not confined in the plasma and simply were entrained by the local gas flow. Engineering of systems to trap particles in specific locations may be possible to create custom-designed nanoparticles.

In Chapter 6, the scaling of Si nanoparticle growth rates in Ar/SiH_4 plasmas was explored using the coupled HPEM/DTS. Small, sub-nm sized particles were initialized in the plasma and particle trajectories, charge, and growth were tracked. The mechanism for particle growth under a wide range of conditions showed that particles were trapped in the plasma over multiple gas residence times. During this time, particles grew via flux of radical growth species until a critical particle size was reached – where the force due to fluid drag overcame the electrostatic trapping force, and particles naturally flowed out of the reactor. Particle growth rates while varying operating conditions (power, flow rate, pressure, reactor diameter) were discussed.

Chapter 7 details how pulsed power may be beneficial for plasma-based nanoparticle synthesis. The HPEM/DTS combined computational model was used to model nanoparticle synthesis using Ar/SiH_4 plasmas. It was found that for the same average power, more narrow particle size distributions may be achieved using pulsing. This is due to increased particle trapping when the power is on – both the increased T_e and n_e lead to more negative charged particles. The effects of varying the pulse repetition frequency and duty cycle on particle sizes were characterized.

Chapter 8 gives a summary of the work presented in this thesis, the main contributions to the low temperature plasma field, and details future work.

1.7 Figures

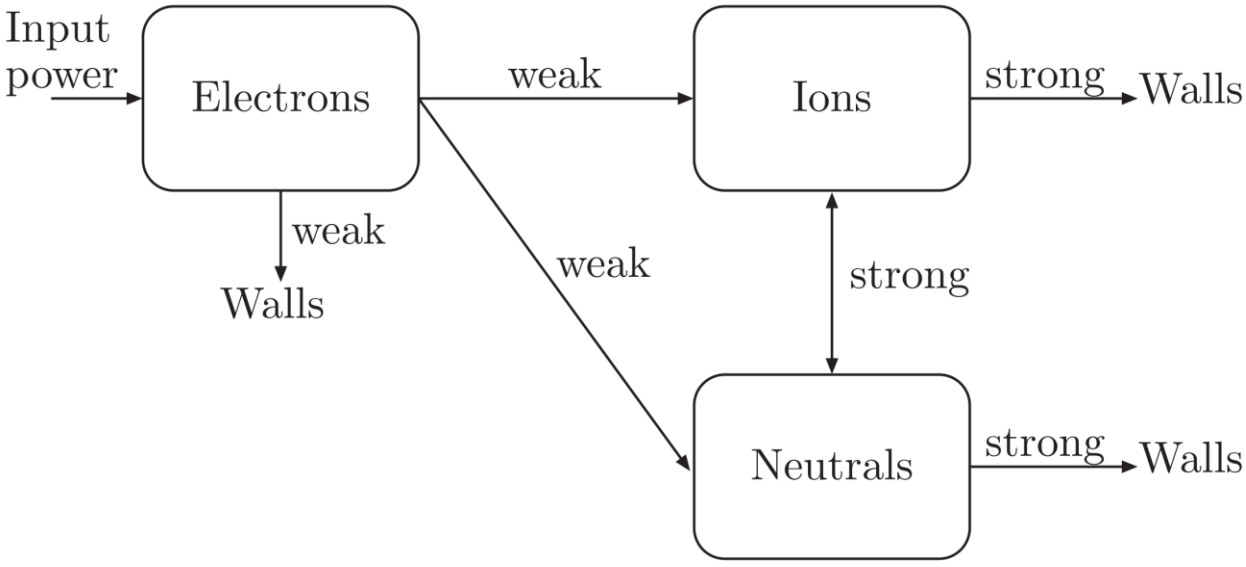

Figure 1-1. Schematic of energy coupling into a plasma system, where natural gradients in temperature between species arises ($T_e >> T_{ion} > T_{gas}$). Reproduced from notes from a plasma short course [5].

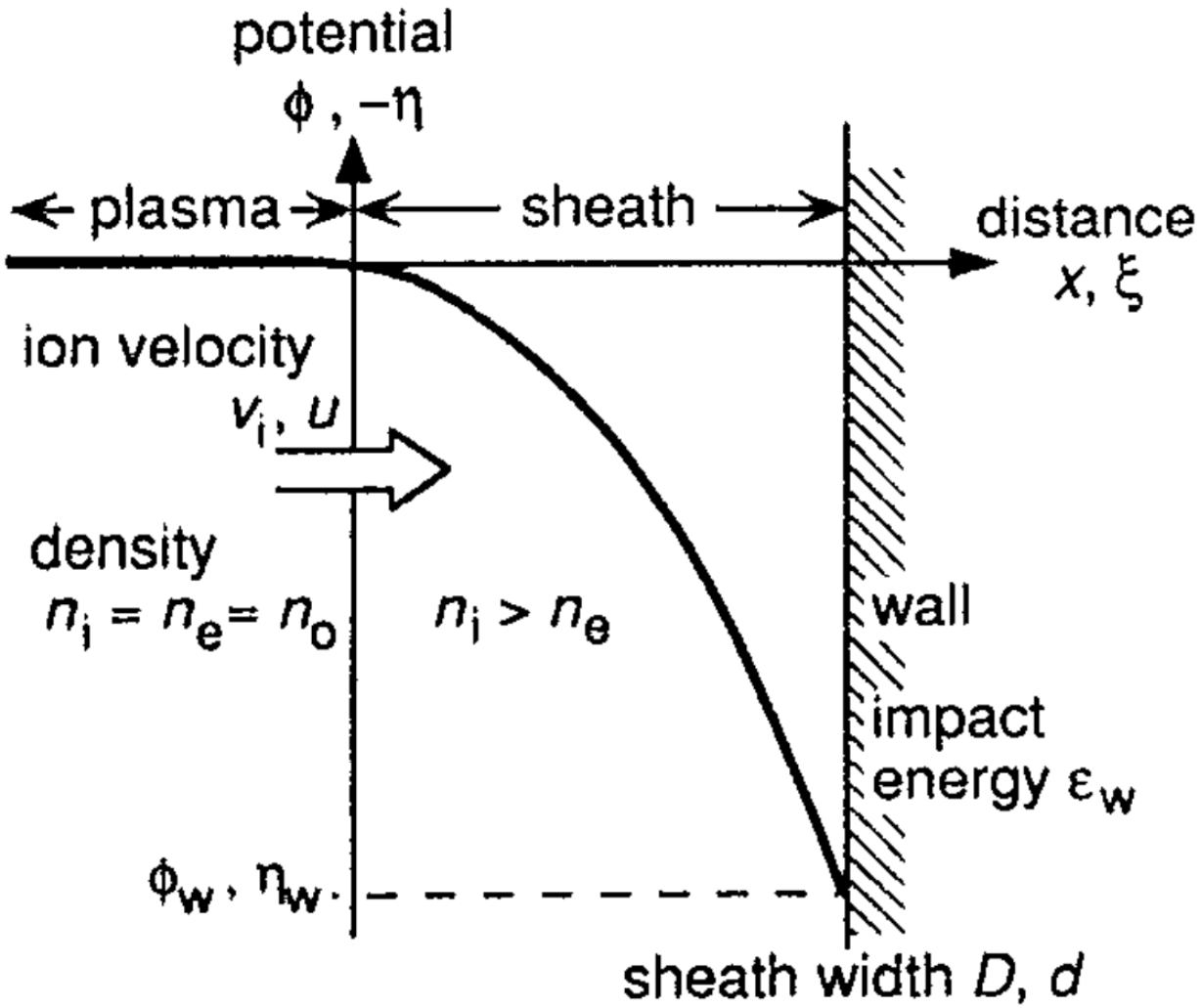

Figure 1-2. Model of a plasma sheath that forms in contact with a wall in a low temperature plasma. Reproduced from Ref. [2].

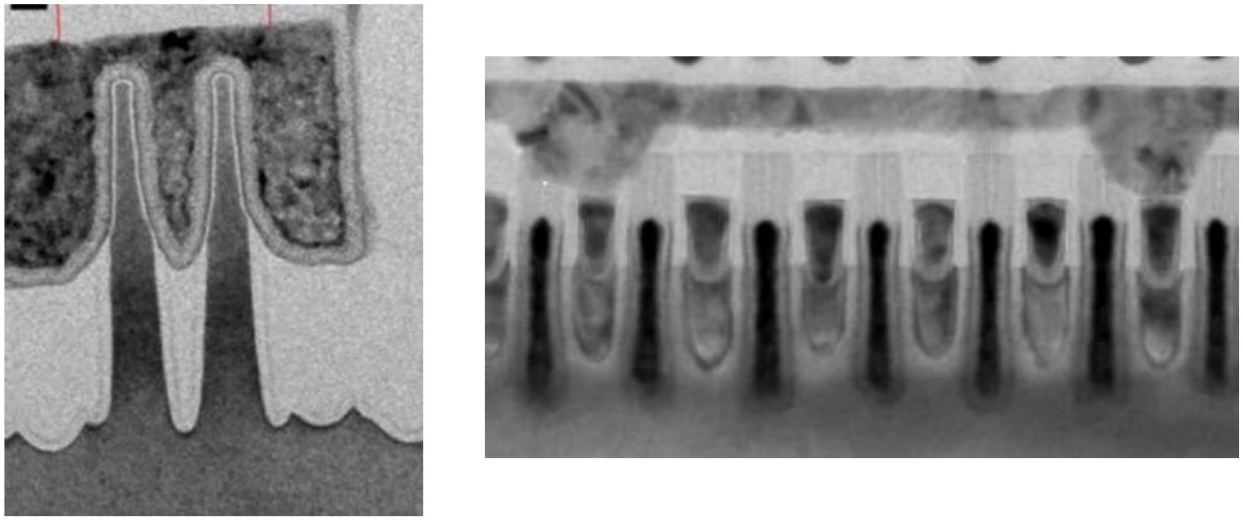

Figure 1-3. Microscopic image of a transistor fin (7 nm fin width, 47 nm fin height) and gate structure using Intel's 10 nm process. Reproduced from Ref. [3].

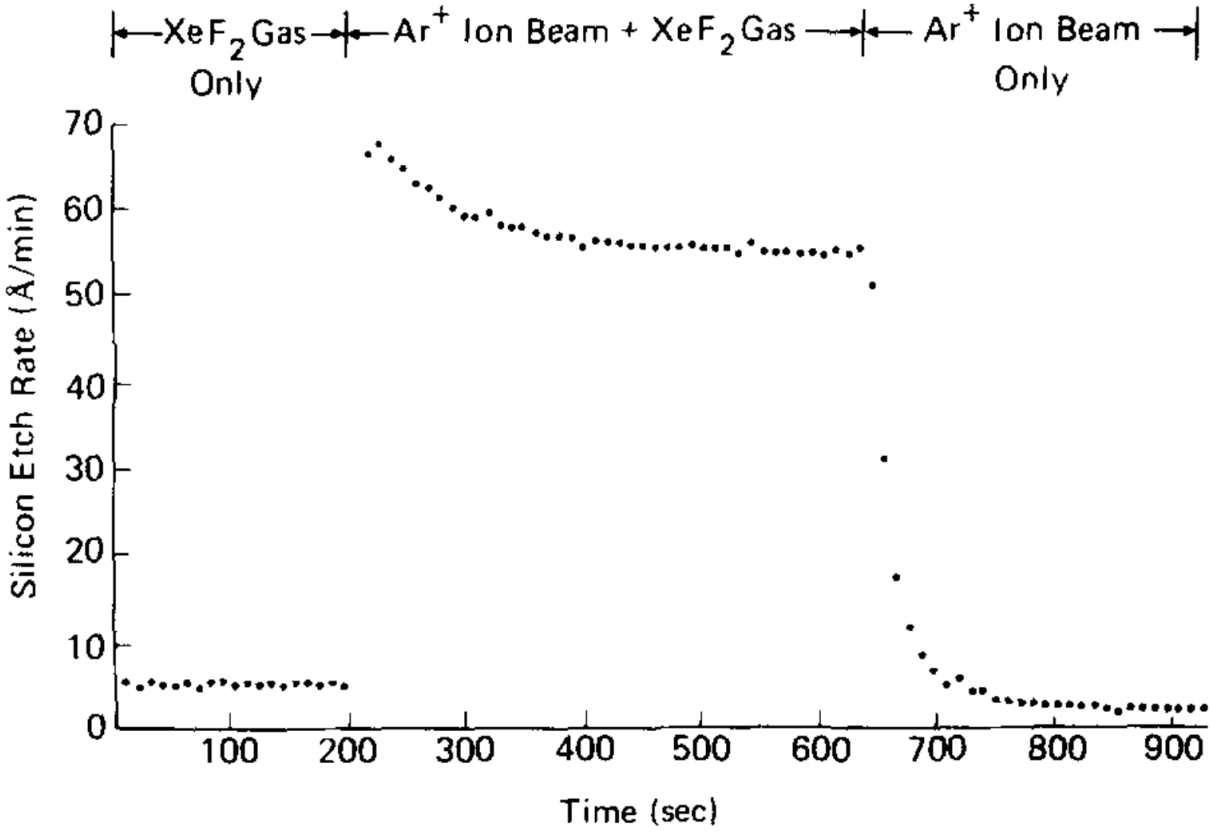

Figure 1-4. Experimental results for ion-assisted etching of a silicon surface, showing synergistic effects from exposure to both a fluorinating gas (XeF_2) and an Ar^+ ion beam. Reproduced from Ref. [4].

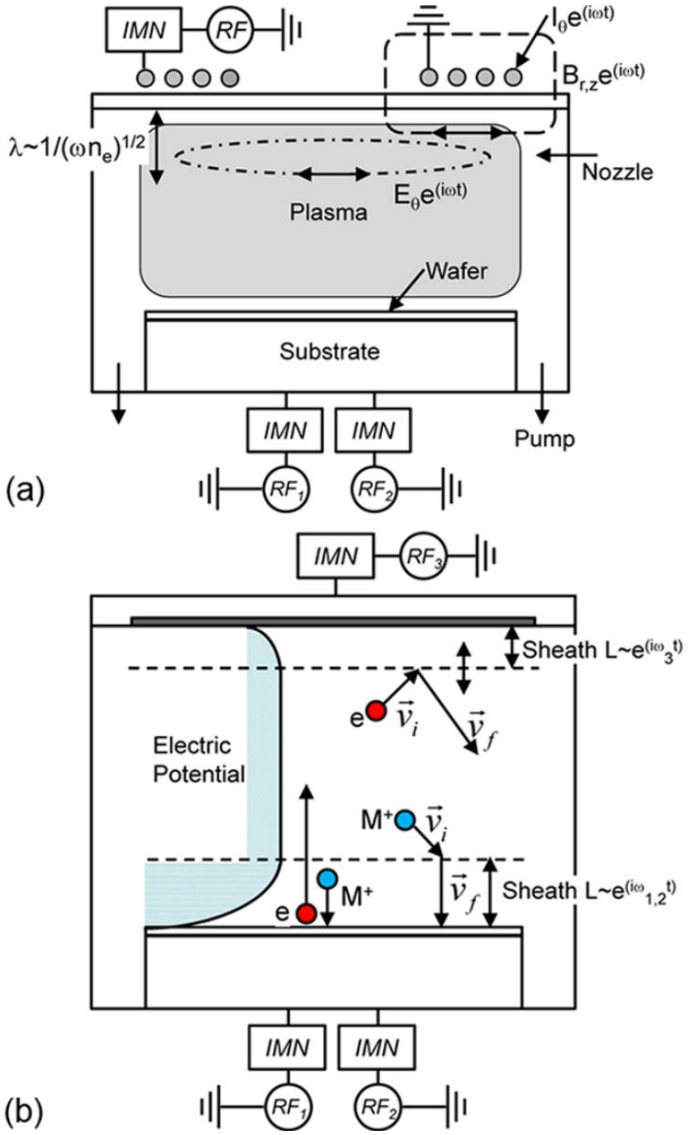

Figure 1-5. Schematics of typical plasma sources used in industrial applications. a) Inductively coupled plasma where power is primarily deposited through the oscillating field in the azimuthal direction and b) a capacitive coupled plasma where power primarily comes from ion acceleration by sheaths. The reactors can be powered by multiple RF power sources, each requiring an impedance matching network.

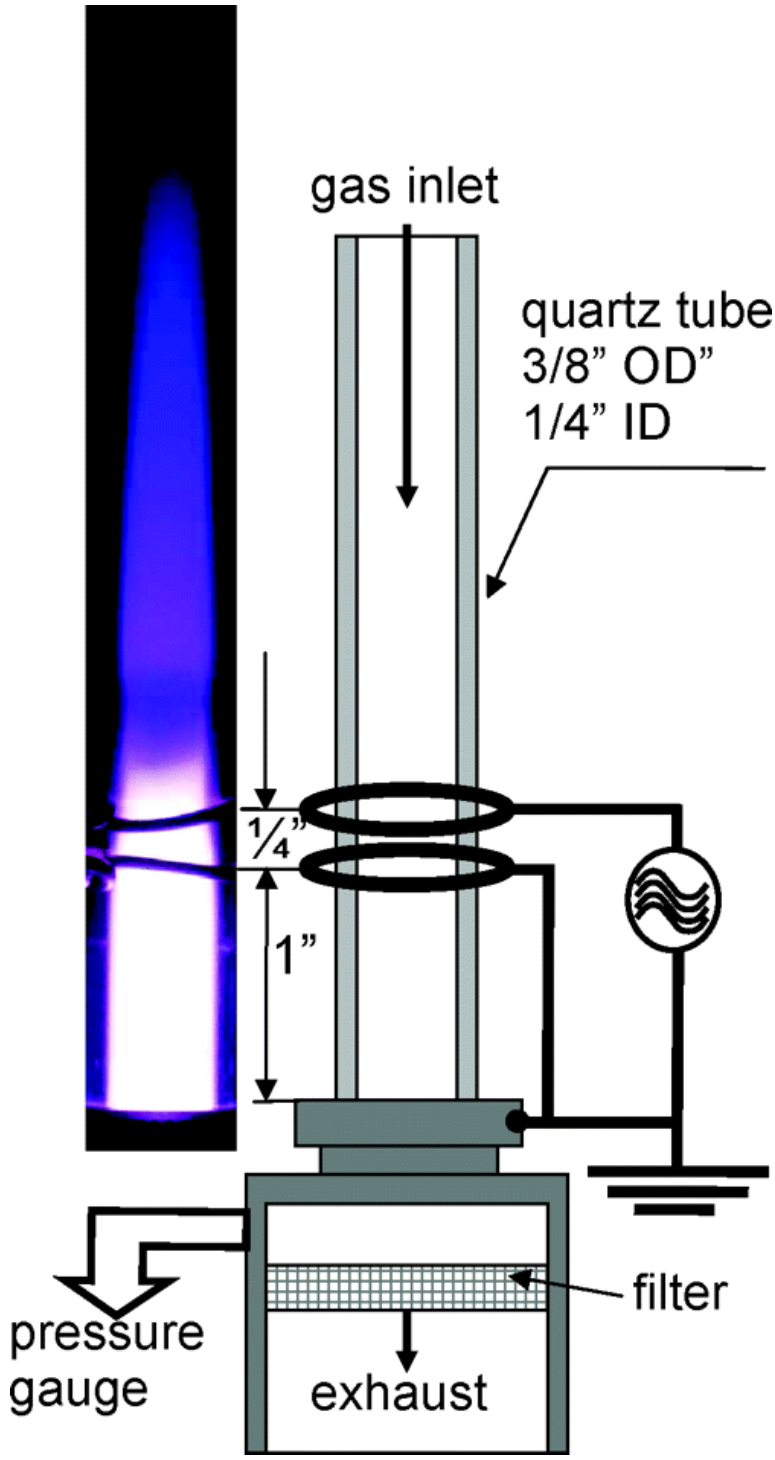

Figure 1-6. Typical plasma reactor used for nanoparticle synthesis. Reproduced from Ref. [7].

1.8 References

[1] F. F. Chen, *Introduction to Plasma Physics and Controlled Fusion*, Springer International Publishing (2016).

[2] T. E. Sheridan and J. Goree, Phys. Fluids B Plasma Phys. **3,** 2796 (1991).

[3] C. Auth, A. Aliyarukunju, M. Asoro, D. Bergstrom, V. Bhagwat, J. Birdsall, N. Bisnik, A. Yeoh, et al., in 2017 IEEE International Electron Devices Meeting (IEDM) 29.1.1 (IEEE, 2017).

[4] J. W. Coburn and H. F. Winters, J. Appl. Phys. **50,** 3189 (1979).

[5] M. A. Lieberman and A. J. Lichtenberg, *Principles of Plasma Discharges and Materials Processing*, John Wiley & Sons, Inc. (2005).

[6] J. Knipping, H. Wiggers, B. Rellinghaus, P. Roth, D. Konjhodzic and C. Meier, J. Nanosci. Nanotechnol. **4,** 1039 (2004).

[7] L. Mangolini, E. Thimsen and U. Kortshagen, Nano Lett. **5,** 655 (2005).

[8] C. R. Gorla, S. Liang, G. S. Tompa, W. E. Mayo and Y. Lu, J. Vac. Sci. Technol. A Vacuum, Surfaces, Film. **15,** 860 (1997).

[9] R. M. Sankaran, D. Holunga, R. C. Flagan and K. P. Giapis, Nano Lett. **5,** 537 (2005).

[10] L. Liu, S. Sridhar, V. M. Donnelly and D. J. Economou, J. Phys. D. Appl. Phys. **48,** 485201 (2015).

[11] C. Xue, D.-Q. Wen, W. Liu, Y.-R. Zhang, F. Gao and Y.-N. Wang, J. Vac. Sci. Technol. A Vacuum, Surfaces, Film. **35,** 021301 (2017).

[12] T. Wegner, C. Küllig and J. Meichsner, Plasma Sources Sci. Technol. **26,** 025006 (2017).

[13] T. Wegner, C. Küllig and J. Meichsner, Plasma Sources Sci. Technol. **26,** 025007 (2017).

[14] J. Wang, Y. Du, X. Zhang, Z. Zheng, Y. Liu, L. Xu, P. Wang and J. Cao, Phys. Plasmas **21,**

073502 (2014).

[15] P. Chabert and N. Braithwaite, *Physics of Radio-Frequency Plasmas*, Cambridge University Press (2011).

[16] S. V. Singh and C. Pargmann, J. Appl. Phys. **104,** 083303 (2008).

[17] T. Gans, M. Osiac, D. O'Connell, V. A. Kadetov, U. Czarnetzki, T. Schwarz-Selinger, H. Halfmann and P. Awakowicz, Plasma Phys. Control. Fusion **47,** A353 (2005).

[18] G. Cunge, B. Crowley, D. Vender and M. M. Turner, Plasma Sources Sci. Technol. **8,** 576 (1999).

[19] M.-H. Lee and C.-W. Chung, Plasma Sources Sci. Technol. **19,** 015011 (2010).

[20] M. M. Turner and M. A. Lieberman, Plasma Sources Sci. Technol. **8,** 313 (1999).

[21] T. Czerwiec and D. B. Graves, J. Phys. D. Appl. Phys. **37,** 2827 (2004).

[22] T. Wegner, C. Küllig and J. Meichsner, Plasma Sources Sci. Technol. **24,** 044001 (2015).

[23] P. Chabert, A. J. Lichtenberg, M. A. Lieberman and A. M. Marakhtanov, Plasma Sources Sci. Technol. **10,** 478 (2001).

[24] U. Kortshagen, N. D. Gibson and J. E. Lawler, J. Phys. D. Appl. Phys. **29,** 1224 (1996).

[25] E. Despiau-Pujo and P. Chabert, Plasma Sources Sci. Technol. **18,** 045028 (2009).

[26] A. Piel, *Plasma Physics*, Springer Berlin Heidelberg (2010).

[27] A. Melzer, **962,** *Physics of Dusty Plasmas*, 962: Springer International Publishing (2019).

[28] T. Chen, K. V. Reich, N. J. Kramer, H. Fu, U. R. Kortshagen and B. I. Shklovskii, Nat. Mater. **15,** 299 (2016).

[29] F. Meinardi, S. Ehrenberg, L. Dhamo, F. Carulli, M. Mauri, F. Bruni, R. Simonutti, U. Kortshagen and S. Brovelli, Nat. Photonics **11,** 177 (2017).

[30] P. Xia, E. K. Raulerson, D. Coleman, C. S. Gerke, L. Mangolini, M. L. Tang and S. T.

Roberts, Nat. Chem. **12,** 137 (2020).

[31] U. R. Kortshagen, R. M. Sankaran, R. N. Pereira, S. L. Girshick, J. J. Wu and E. S. Aydil, Chem. Rev. **116,** 11061 (2016).

[32] A. Alvarez Barragan, N. V. Ilawe, L. Zhong, B. M. Wong and L. Mangolini, J. Phys. Chem. C **121,** 2316 (2017).

[33] S. Exarhos, A. Alvarez-Barragan, E. Aytan, A. A. Balandin and L. Mangolini, ACS Energy Lett. **3,** 2349 (2018).

[34] N. B. Uner and E. Thimsen, J. Phys. D. Appl. Phys. **53,** (2020).

[35] T. Matsoukas, M. Russell and M. Smith, J. Vac. Sci. Technol. A Vacuum, Surfaces, Film. **14,** 624 (1996).

[36] V. A. Schweigert and I. V. Schweigert, J. Phys. D. Appl. Phys. **29,** 655 (1996).

[37] M. S. Barnes, J. H. Keller, J. C. Forster, J. A. O'Neill and D. K. Coultas, Phys. Rev. Lett. **68,** 313 (1992).

[38] V. E. Fortov, A. G. Khrapak, S. A. Khrapak, V. I. Molotkov and O. F. Petrov, Physics-Uspekhi **47,** 447 (2004).

[39] V. Fortov, A. Ivlev, S. Khrapak, A. Khrapak and G. Morfill, Phys. Rep. **421,** 1 (2005).

[40] S. Khrapak and G. Morfill, Contrib. to Plasma Phys. **49,** 148 (2009).

[41] H. M. Thomas, M. Schwabe, M. Y. Pustylnik, C. A. Knapek, V. I. Molotkov, A. M. Lipaev, O. F. Petrov, V. E. Fortov and S. A. Khrapak, Plasma Phys. Control. Fusion **61,** (2019).

[42] T. J. A. Staps, M. I. van de Ketterij, B. Platier and J. Beckers, Commun. Phys. **4,** (2021).

[43] R. Gopalakrishnan and C. J. Hogan, Phys. Rev. E - Stat. Nonlinear, Soft Matter Phys. **85,** 1 (2012).

[44] T. Ono, U. R. Kortshagen and C. J. Hogan, Phys. Rev. E **102,** 1 (2020).

[45] K. S. Ashrafi, R. Yousefi, M. Chen, L. S. Matthews and T. W. Hyde, Phys. Rev. E **102,** 1 (2020).

[46] G. Praburam and J. Goree, J. Vac. Sci. Technol. A Vacuum, Surfaces, Film. **12,** 3137 (1994).

[47] G. S. Selwyn, J. E. Heidenreich and K. L. Haller, Appl. Phys. Lett. **57,** 1876 (1990).

[48] U. Kortshagen, J. Phys. D. Appl. Phys. **42,** (2009).

[49] A. Bapat, C. Anderson, C. R. Perrey, C. B. Carter, S. A. Campbell and U. Kortshagen, Plasma Phys. Control. Fusion **46,** (2004).

[50] U. Kortshagen, Plasma Chem. Plasma Process. **36,** 73 (2016).

[51] E. Thimsen, U. R. Kortshagen and E. S. Aydil, J. Phys. D. Appl. Phys. **48,** (2015).

[52] B. L. Greenberg, S. Ganguly, J. T. Held, N. J. Kramer, K. A. Mkhoyan, E. S. Aydil and U. R. Kortshagen, Nano Lett. **15,** 8162 (2015).

[53] A. Ho, R. Mandal, R. R. Lunt and R. J. Anthony, ACS Appl. Nano Mater. **4,** 5624 (2021).

[54] A. Izadi and R. J. Anthony, Plasma Process. Polym. **16,** 1 (2019).

[55] L. Boufendi and A. Bouchoule, Plasma Sources Sci. Technol. **3,** 262 (1994).

[56] P. Agarwal and S. L. Girshick, Plasma Sources Sci. Technol. **21,** 055023 (2012).

[57] Chunshi Cui and J. Goree, IEEE Trans. Plasma Sci. **22,** 151 (1994).

[58] P. Agarwal and S. L. Girshick, Plasma Chem. Plasma Process. **34,** 489 (2014).

[59] U. Kortshagen and U. Bhandarkar, Phys. Rev. E **60,** 887 (1999).

[60] R. Le Picard, A. H. Markosyan, D. H. Porter, S. L. Girshick and M. J. Kushner, Plasma Chem. Plasma Process. **36,** 941 (2016).

[61] X. Chen and C. J. Hogan, Chem. Eng. J. **411,** 128383 (2021).

Chapter 2 Description of the Models

The simulations presented in this thesis were done using two different models. The Hybrid Plasma Equipment Model (HPEM) was used to model the low temperature plasma systems and is described in Section 2.1. Modeling nanoparticle growth and trajectories was done using the Dust Transport Simulator, and is described in Section 2.2. Contributions to these models by the author are described in Section 2.3.

2.1 Description of the HPEM[*]

Low temperature plasmas were modeled using the Hybrid Plasma Equipment Model (HPEM) [1]. The HPEM is a simulator that combines modules addressing different physical phenomena in a time slicing manner. The main modules used for a typical simulation are the Electromagnetics Module (EMM), Electron Energy Transport Module (with the option of kinetically derived values from the Electron Monte Carlo Simulation (eMCS)), and the Fluid Kinetics Module (FKM). Harmonic electromagnetic fields launched from the coil are produced in the EMM by solving the frequency domain wave equation. Continuity, momentum, and energy equations for ions and neutral particles, continuity and momentum equations for electrons, and Poisson's equation for the electric potential are integrated in time in the FKM. RF electric and

[*] Portions of the text that appear in this section were previously published in the papers by C. Qu *et al.*, "Power matching to pulsed indutively coupled plasmas" J. Appl. Phys. **127,** 133302 (2020) [21] and J. Han *et. al.*, "Three-dimensional mesaurements of plasma parameters in an inductively coupled plasma processing chamber" Phys. Plamas **26**, 103503 (2019) [22].

magnetic fields from the EMM and electrostatic fields from the FKM are then used in the eMCS to advance pseudoparticle trajectories produce electron energy distributions as a function of position including electron-electron collisions. These distributions are then used to produce electron transport coefficients and electron impact rate coefficients for use in other modules. The geometry is 2-dimensional in cylindrical coordinates assuming azimuthal symmetry. More details about the specific modules are given below.

2.1.1 Electromagnetics Module (EMM)

The frequency domain wave equation for the inductively coupled electric field is solved in the EMM using a discretized finite difference method:

$$\nabla^2 E_\phi(\vec{r}) + \left(\frac{\omega}{c}\right)^2 E_\phi(\vec{r}) = i\omega\mu_0 J_\phi(\vec{r}) \tag{2.1}$$

to produce the time and spatially dependent electric field in the azimuthal direction,

$$E_\phi(\vec{r},t) = E_\phi(\vec{r})\mathrm{Re}(e^{i(\omega t+\delta_E(\vec{r}))}) \tag{2.2}$$

where $E_\phi(\vec{r})$ is the harmonic amplitude of the electric field and $\delta_E(\vec{r})$ is the phase of the electric field. In cases where electron heating is approximated as being solely collisional, the current density is given by

$$\begin{gathered} J_\phi(\vec{r},t) = \sigma(\vec{r})E_\phi(\vec{r},t), \\ \sigma(\vec{r}) = \frac{n_e(\vec{r})e^2}{m_e\nu_m(\vec{r})\left(1+i\frac{\omega}{\nu_m(\vec{r})}\right)} \end{gathered} \tag{2.3}$$

where n_e is the electron density, σ is the conductivity, m_e is the electron mass, and ν_m is the momentum transfer collision frequency. The radial and axial components of the magnetic fields are then obtained from Faraday's law. The instantaneous power deposition is:

$$P(\vec{r},t) = J_{\phi}(\vec{r},t)E_{\phi}(\vec{r},t) \tag{2.4}$$

which can be used as a heating term in the Electron Energy Equation.

For the two-dimensional simulations, the current flowing in the antenna is in the azimuthal direction θ, producing components at the fundamental frequency of the magnetic field in the (r,z) (radius, height) directions and of the electric field, E_θ, in the θ direction. The conduction currents through each turn of the antenna that are used in the solution of the wave equation can be provided by a circuit model, which also provides the fundamental frequency voltages on each turn of the antenna used in the FKM for the solution of Poisson's equation. The antenna is modeled as a discretized transmission line with the geometry of the antenna determining inductance and will be further expanded on in Chapter 3.

2.1.2 Electron Energy Transport Module (EETM)

The primary purpose of the EETM is to solve for the electron energy distribution function $f(\varepsilon, r, \phi)$, which can then be used to produce electron impact rate coefficients $k_e(r,\phi)$ and sources $S_e(r,\phi)$ to be used in the FKPM. Boltzmann's equation for electrons is solved for values of reduced electric field (E/N) in the EETM using a two-term spherical harmonic approximation:

$$\frac{\partial f_e}{\partial t} = -\vec{v}\nabla_r f_e - \frac{e\left(\vec{E}+\vec{v}\times\vec{B}\right)}{m_e}\cdot\nabla_v f_e + \left(\frac{\partial f_e}{\partial t}\right)_{collisions} \tag{2.5}$$

where ∇_r is the spatial gradient, and ∇_v is the gradient in velocity space. Rate coefficients and sources are tabulated as functions of T_e and interpolated in the FKM.

To account for collisionless electron heating and anomalous skin effects in absorption of the coil-launched electromagnetic wave in the plasma, electron currents are calculated in the eMCS and used in the EMM in solution of the wave equation [2]. The solution to the wave equation in

the EMM is performed in the frequency domain, while advancement of pseudoparticle trajectories in the eMCS is performed in the time domain. Electron currents are computed in the eMCS by collecting statistics on the azimuthal component of velocity of the electron pseudoparticles as a function of position and time. These statistics are then Fourier analyzed to provide the harmonic electron current density as a function of position and time,

$$J_\phi(\vec{r},t) = J_\phi(\vec{r})\mathrm{Re}(e^{i(\omega t+\delta_j(\vec{r}))}) \tag{2.6}$$

where $J_\phi(\vec{r})$ is the local harmonic amplitude of the current density and $\delta_j(\vec{r})$ is the phase of the current density. This current density can then used in the EMM to solve the frequency domain wave equation.

2.1.3 Fluid Kinetics Module (FKM)

Continuity, momentum, and energy equations (a fluid representation) are solved in the FKM for all charged and neutral species coincident with the solution of Poisson's equation for the electrostatic potential, Φ. For species *i* with a source term S_i:

$$\frac{\partial N_i}{\partial t} = -\nabla\cdot\vec{\phi}_i + S_i \tag{2.7}$$

$$\begin{aligned}\frac{\partial\vec{\phi}_i}{\partial t} = \frac{\partial(N_i\vec{v}_i)}{\partial t} = &-\frac{1}{m_i}\nabla(kN_iT_i) - \nabla\cdot(N_i\vec{v}_i\vec{v}_i) + \frac{q_i}{m_i}N_i(\vec{E}_s + \vec{v}_i\times\vec{B}) \\ &-\nabla\cdot\bar{\bar{\mu}}_i - \sum_j \frac{m_j}{m_i+m_j}N_iN_j(\vec{v}_i-\vec{v}_j)\nu_{ij}\end{aligned} \tag{2.8}$$

$$\begin{aligned}\frac{\partial N_i\varepsilon_i}{\partial t} = &-\nabla\cdot\bar{\bar{\kappa}}\nabla T_i - p_i\nabla\cdot\vec{v}_i - \nabla\cdot(N_i\vec{v}_i\varepsilon_i) + q_i\vec{\varphi}_i\vec{E} - (\bar{\bar{\mu}}_i\nabla\cdot\nabla\vec{v}_i) \\ &-\sum_{m,j}k_{mij}N_iN_j\varepsilon_i + \sum_{m,j,l}k_{mjl}N_jN_l\Delta\varepsilon_{mjl}\end{aligned} \tag{2.9}$$

where $\vec{\phi}$ is the flux, *N* is the density, $\vec{v}$ is the velocity, *m* is the mass, *T* is the temperature, $\bar{\bar{\mu}}$ is the viscosity, *p* is the pressure, and *ε* is the energy. Poisson's equation is semi-implicitly solved

in the time domain where ρ is the charge density included both surface charging (ρ_m) and charge in the plasma:

$$\nabla\cdot\left[\varepsilon\nabla\Phi(t+\Delta t)\right]=-\rho(t+\Delta t)=-\rho\left(t\right)-\Delta t\left.\frac{\partial\rho}{\partial t}\right|_{t+\Delta t} \qquad (2.10)$$
$$\rho\left(t\right)=\rho_m\left(t\right)+\sum_i q_i N_i(t)$$

q_i is the charge of ion i and N_i is the ion density. Poisson's equation is typically solved using a semi-implicit formulation to bypass limits set by the dielectric relaxation time [3].

For two-dimensional simulations, Φ is solved in the (r,z) plane, providing electrostatic field components E_r, E_z. Electron heating is provided by the harmonic inductively coupled fields E_θ from the EMM. All components of the electrostatic (E_r, E_z) and electromagnetic fields (B_r, B_z, E_θ) are used in the EETM to track the trajectory of secondary electrons from surfaces using Monte Carlo techniques. Complex conductivities are transferred back to the EMM to solve the wave equation. One sweep through the modules is called an iteration of the model.

2.2 Description of the DTS[†]

NP transport and growth were addressed using a 3-dimensional kinetic model, the DTS, embedded in the HPEM. The implementation described here is built on prior versions of the DTS [4,5] and the prior dust particle transport model [6]. The DTS obtains plasma properties from the HPEM, including electric fields, and species densities, temperatures, and momentum flux fields. The precursors to NPs are initialized randomly in the plasma and their trajectories are integrated

[†] Portions of the text that appear in this section were previously published in the paper by S. J. Lanham *et al.*, "Scaling of silicon nanoparticle growth in low temperature flowing plasmas" J. Appl. Phys. **130,** 163302 (2021) [23].

based on the relevant forces: gravitational, electrostatic and inter-particle Coulomb forces, ion drag, viscous fluid drag, thermophoresis and Brownian motion. The forces on NP species i are,

$$\vec{F}_i = M_i\vec{g} + Q_i\vec{E} + \sum_j \vec{F}_{cij} + \sigma_{ion}\vec{\phi}_{ion}\left|\vec{v}_{ion}\right| - \frac{6\pi\mu r_i}{C(Kn)}\left(\vec{v}_i - \vec{u}_f\right)C_D\left(\mathrm{Re}_p\right)\frac{\mathrm{Re}_p}{24} - 6\pi\mu r_i \nu_f K_T \frac{\nabla T}{T_{gas}} + \vec{F}_B \tag{2.11}$$

where $\vec{g}$ the gravitational acceleration, M_i is the mass of the NP, Q_i is the electrical charge of the NP, $\vec{E}$ is the electrostatic electric field, and $\vec{F}_{cij}$ is the Coulombic force between NP species *i* and *j*. The fourth, fifth, sixth, and seventh terms account for the forces due to ion drag, fluid drag, thermophoresis and Brownian motion, discussed below.

The charge on individual NPs is computed by integrating the current to the particle surface due to positive and negative ions, and electrons. The current to NP *i* due to positive ion *j*, I_{ij}^{+}, negative ion *k*, I_{ik}^{-},and electrons I_{ie} are

$$I_{ij}^{+} = \pi r_i^2 N_j^{+} q \sqrt{\frac{2\varepsilon_{Ij}}{m_j}}\left(1 - \frac{q\Phi_i}{\varepsilon_j}\right) \tag{2.12}$$

$$I_{ik}^{-} = \pi r_i^2 N_k^{-} q \sqrt{\frac{8k_B T_{-}}{\pi m_k}}\exp\left(\frac{q\Phi_i}{k_B T_k}\right) \tag{2.13}$$

$$I_{ie} = \pi r_i^2 N_e q \sqrt{\frac{8k_B T_e}{\pi m_e}}\exp\left(\frac{q\Phi_i}{k_B T_e}\right) \tag{2.14}$$

where r_i is the radius of the NP; N_j, N_k and N_e are the densities of positive ion j, negative ion *k* and electrons; ε_j is the kinetic energy of ion *j*; T_k and T_e are the temperatures of negative ion *k* and electrons; m_j, m_k and m_e are the masses of positive ion *j*, negative ion *k* and electrons; k_B is Boltzmann's constant; and Φ_i is the floating electrical potential of NP *i*. These currents result from assuming Orbital Motion Limited (OML) trajectories for positive ions [7,8]. For small NPs (i.e.,

< a few to 10 nm), the currents collected by individual particles have significant stochastic components [9]. In addition to this stochastic charge collection, there is a computational complication. For small NPs when using a continuum approximation, the current flowing to the NP over a typical integrating time step produces less charge than a single electron or ion. Given these conditions, computing NP charge using continuous integration of currents to the particles is problematic.

To address these conditions, a stochastic charging algorithm was implemented. With this algorithm, the charge collected from the current of each ion or electron species during an integration time step is treated as the mean expected value of a Poisson distribution – used to describe discrete, rare events with an unknown variance. The Poisson distribution expresses the probability of discrete events occurring during a fixed time interval, and naturally arises as the limit of the binomial distribution with increasing number of trials. Sampling from this distribution is done using a sequential search algorithm [10] where a random number is generated and compared to the probability of i events occurring (P_i) with a mean μ,

$$P_i = \sum_{k=0}^{i-1} e^{-\mu} \mu^k / k! \quad \text{(i=1,2,...)} \tag{2.15}$$

The algorithm is to generate a random number r = [0,1] and compute the P_i for increasing values of i until $r < P_i$. When the probability of the i^{th} event exceeds the random number, the number of events (N) is returned as N=i-1. The execution time for this algorithm increases with increasing μ, so for μ>5 the Poisson distribution is approximated as Gaussian with a variance equal to the mean. However, for the particle sizes and time steps used in this work, μ is small (typically < 1) and the assumptions needed for sampling from a Poisson distribution are valid. An example output using the stochastic charging algorithm is shown in Fig. 1. The relative fluctuations around the mean particle charge decreases with increasing particle size, corroborating that fluctuations are

less important for larger sized particles. The frequency of oscillations increases with increasing particle size as current to the particle increases in magnitude, with particle charge changing ~1q per ms for a 1 nm NP to charge varying 100s of q per ms for 100 nm particles.

With charge on the NP, Q_i, known, the floating electrical potential of the NP is obtained by assuming that the NP acts as spherical capacitor with capacitance C_i with a surrounding sheath having thickness given by the linearized Debye length, λ_L [11]:

$$\Phi_i = \frac{Q_i}{C_i},\ C_i = 4\pi\varepsilon_0 r_i\left(1+\frac{r_i}{\lambda_L}\right) \tag{2.16}$$

$$\frac{1}{\lambda_L} = \sqrt{\frac{q^2}{\varepsilon_0}\left(\frac{N_e}{k_B T_e}+\sum_k \frac{N_k^-}{k_B T_k}+\sum_k \frac{N_j^+}{2\varepsilon_j}\right)} \tag{2.17}$$

In collisional plasmas, the ion trajectory around the NP predicted by the OML theory may be interrupted by a charge-exchange collision. This collision produces a low energy ion which can be directly collected by the NP, resulting in a higher ion current and less negative ion potential [12]. For the largest particles and highest pressures considered here, this additional ion current could make a contribution, but otherwise these collisional effects are not important.

The numerical mesh used to solve Poisson's equation in the fluid modules of the HPEM for the electric potential has a grid spacing that is much larger than individual NPs. To account for the electrostatic forces between NPs, a particle-particle algorithm was used. Particles interact through their mutual Coulombic forces shielded by the plasma. The shielded electric potential of a single NP is given by a spherically symmetric solution to the Debye Hückel equation [35],

$$\Phi(r) = \Phi_i \frac{r_i}{r}\exp\left[-\frac{(r-r_i)}{\lambda_L}\right] \tag{2.18}$$

The Coulomb force between NP particles i and j at locations separated by distance $R = \left|\vec{r}_i - \vec{r}_j\right|$ is then

$$\vec{F}_{cij}(\vec{r}_i,\vec{r}_j)=\frac{Q_iQ_j}{4\pi\varepsilon_0}\frac{1}{R}\left(\frac{1}{R}+\frac{1}{\lambda_L}\right)\exp\left[-\frac{R-\left(\frac{r_i+r_j}{2}\right)}{\lambda_L}\right]\frac{\left(\vec{r}_i+\vec{r}_j\right)}{R} \tag{2.19}$$

The computational time required to compute the forces between particles has poor scaling of order N^2, so only particle interactions within a few λ_L are calculated. This assumption has been found to be accurate in previous works due to the exponential decay in screening with distance [5]. Particle positions are directly compared and particles within $5\lambda_L$ of each other are saved as pairs in arrays. These particles interact over many time steps while the list of interacting partners is only updated periodically.

The ion-drag force results from ions having a directed velocity approaching, for example, a negatively charged NP, and undergoing a parabolic (positive ion) or hyperbolic (negative ion) orbit about the NP. The change in momentum of the ion due to this orbital motion is imparted to the NP. Since the momenta of positive ions are typically directed towards the boundaries of the plasma, the ion-drag force usually accelerates NPs towards the boundaries of the plasma. In the force due to ion drag, the 4th term in Eqn. 2.11, $\vec{\phi}_{ion}$ is the average ion momentum flux and $|\vec{v}_{ion}|$ is the mean ion speed, both obtained from the HPEM. The ion-dust momentum transfer cross section σ_{ion} is approximated using a semi-analytic equation from the work of Kilgore *et al.* [36]

$$\sigma_{ion}=b^2c_1\ln\left[1+\frac{c_2}{\left(b/\lambda_L\right)^2}\right],\ b=\frac{Q_i^2}{4\pi\varepsilon_0\varepsilon_{ion}} \tag{2.20}$$

The values of c_1=0.9369 and c_2=61.32 are semi-empirical constants from the work of Khrapak *et al.* [37], which were found to agree well with simulation and modeling results [36,38].

The forces due to viscous fluid drag (5th term in Eqn. 2.11) are derived for hard sphere particles from classical thermodynamics [39–41]. The driving force for viscous fluid drag is the

difference between the dust particle velocity ($\vec{v}_i$) and the advective fluid velocity ($\vec{u}_f$). In Eqn. 2.11, Kn is the Knudsen number (mean free path divided by the length scale), Re_p is the particle Reynolds number, and μ is the fluid viscosity.

$$C(Kn) = 1 + Kn(\alpha + \beta)\exp\left(-\frac{\gamma}{Kn}\right)$$
$$C_D(\mathrm{Re}_p)\frac{\mathrm{Re}_p}{24} = 1 + 0.173\,\mathrm{Re}_p^{0.657} + \frac{0.01721\,\mathrm{Re}_p}{1 + 16300\,\mathrm{Re}_p^{-1.09}} \qquad (2.21)$$
$$\mathrm{Re}_p = \frac{2\rho r_i \left|\vec{v}_i - \vec{u}_f\right|}{\mu}$$

The constants used in Eqn. 2.21 are listed in Table 2-I, where α, β, and γ are values which depend on the gas-dust surface interaction, and are measured experimentally.

The thermophoretic force (6th term in Eqn. 2.11) results from the temperature gradient (∇T) in the gas surrounding the NP. In Eqn. 2.11, $\nu_f = \mu/\rho_g$ is the kinematic viscosity (viscosity divided by the mass density of the gas), K_T is given by

$$K_T = \frac{2C_s\left[\left(\kappa_g / \kappa_p\right) + C_t K_n\right]}{\left(1 + 3C_m Kn\right)\left[1 + 2\left(\kappa_g / \kappa_p\right) + 2C_t Kn\right]} \qquad (2.22)$$

where is κ_g is the gas thermal conductivity, κ_p is the particle thermal conductivity, and C_t, C_s, and C_m are coefficients for thermal creep, temperature jump, and velocity jumps. The values used for these constants are also in Table 2-I.

The last force from Eqn. 2.11 is an effective force of Brownian motion due to random collisions with the background gas. This force is more important for smaller particles, ~1 nm where the momentum transfer from individual atoms and molecules can be significant, while decreasing in significance with increasing particle size. The magnitude of the Brownian force is

$$\left\|\vec{F}_B\right\| = \frac{M_g v_{th}\left(\pi r_i^2 \Delta t v_{th} N_g\right)^{1/2}}{\Delta t}, \quad v_{th} = \sqrt{\frac{8k_B T_g}{\pi M_g}} \tag{2.23}$$

where v_{th} is the average thermal speed of the incident gas molecules (mass M_g), and Δt is the integration time step. Once the magnitude of the force is computed, the direction of the force is randomized in polar (θ) and azimuthal (ϕ) directions. The directional components of the Brownian force are then,

$$\begin{aligned} \vec{F}_{B,x} &= \left\|\vec{F}_B\right\| \cos(\theta)\cos(\phi), \\ \vec{F}_{B,y} &= \left\|\vec{F}_B\right\| \cos(\theta)\sin(\phi), \\ \vec{F}_{B,z} &= \left\|\vec{F}_B\right\| \sin(\theta) \end{aligned} \tag{2.24}$$

Several new capabilities were added to the model to address growing dust particles. In previous versions of the DTS, the trajectories of non-growing particles were tracked. Here, the capability to track the mass and diameter of each dust pseudo-particle was added. The time rate of change of mass of NP *i* is given by,

$$\begin{aligned} \frac{dM_i}{dt} &= \sum_j v_j N_j 4\pi r_i^2 S_{c,j} \Delta m_j, \\ v_j &= \sqrt{\frac{8k_B T_j}{\pi m_j}} \end{aligned} \tag{2.25}$$

where the mass of dust particle *i* is M_i having radius r_i. The summation is over all the species j which contribute to dust particle growth, having thermal speed v_j, number density N_j, mass m_j and temperature T_j. The quantity Δm_j is the mass added to the dust particle which is not necessarily equal to the incoming radical mass. The difference would account for example, the desorption of hydrogen from a sticking reaction of SiH with the dust particle. $S_{c,j}$ is the sticking probability for a collision between the dust particle and the dust growth species.

In addition to growth by reactive species, a particle agglomeration algorithm was also added to the DTS which enables two dust particles to combine due to a collision. The algorithm tracks the distance between particle pairs. (This value is conveniently already available from the computation of Coulomb forces.) If the distance is less than the sum of the particle radii, the particles are combined into a single NP. The mass and momentum of the two combining particles are conserved in the new particle. The shape of the new particle remains a sphere with a radius given by the new mass of the combined particle and specified mass density. Since the dust particles are largely negatively charged for the conditions in this work, agglomeration is a rare occurrence.

2.3 Author's Contributions

The main code update featured in this work is the restructuring of the Dust Transport Simulator to allow for particles to have variable mass or size. This was a significant undertaking as previous iterations of the DTS computed forces and particle charge on a grid for static sized particles. The forces were then interpolated based on locations of particles inside of the grid cell. With variable particle size, the forces and charge for each particle need to be directly computed since all quantities are interdependent. The DTS is written in FORTRAN, and the updates needed to perform the research in this work added ≈1,500 lines of code with many more modified to maintain backwards compatibility. Code parallelization was added using OpenMP to compute particle-particle interactions more efficiently – the largest computational bottleneck, improving capabilities from running ~1,000 particles to 10's of thousands of particles depending on the conditions.

Table 2-I. Constants Used in the Calculation of Fluid Drag and Thermophoresis Forces.

Constant	Value	Reference
α	1.227	[19]
β	0.42	[19]
γ	0.85	[19]
C_t	2.20	[18,19]
C_s	1.147	[18,19]
C_m	1.146	[18,19]
k_g	0.1799 $mWcm^{-1}K^{-1}$	[20]
k_p	1240 $mWcm^{-1}K^{-1}$	[20]

2.4 References

[1] M. J. Kushner, J. Phys. D. Appl. Phys. **42,** 194013 (2009).

[2] A. V. Vasenkov and M. J. Kushner, Phys. Rev. E **66,** 066411 (2002).

[3] P. L. G. Ventzek, T. J. Sommerer, R. J. Hoekstra and M. J. Kushner, Appl. Phys. Lett. **63,** 605 (1993).

[4] H. H. Hwang, E. R. Keiter and M. J. Kushner, J. Vac. Sci. Technol. A Vacuum, Surfaces, Film. **16,** 2454 (1998).

[5] V. Vyas, G. A. Hebner and M. J. Kushner, J. Appl. Phys. **92,** 6451 (2002).

[6] S. J. Choi, P. L. G. Ventzek, R. J. Hoekstra and M. J. Kushner, Plasma Sources Sci. Technol. **3,** 418 (1994).

[7] J. E. Allen, Phys. Scr. **45,** 497 (1992).

[8] J. E. Allen, B. M. Annaratone and U. de Angelis, J. Plasma Phys. **63,** 299 (2000).

[9] Chunshi Cui and J. Goree, IEEE Trans. Plasma Sci. **22,** 151 (1994).

[10] A. A. C. Atkinson, S. Journal, R. Statistical, S. Series and C. A. Statistics, J. R. Stat. Soc. Ser. C (Applied Stat. **28,** 29 (1979).

[11] J. E. Daugherty, R. K. Porteous, M. D. Kilgore and D. B. Graves, J. Appl. Phys. **72,** 3934 (1992).

[12] M. Gatti and U. Kortshagen, Phys. Rev. E **78,** 046402 (2008).

[13] J. E. Daugherty, R. K. Porteous and D. B. Graves, J. Appl. Phys. **73,** 1617 (1993).

[14] M. D. Kilgore, J. E. Daugherty, R. K. Porteous and D. B. Graves, J. Appl. Phys. **73,** 7195 (1993).

[15] S. A. Khrapak, A. V. Ivlev, G. E. Morfill and H. M. Thomas, Phys. Rev. E - Stat. Physics, Plasmas, Fluids, Relat. Interdiscip. Top. **66,** 4 (2002).

[16] S. J. Choi and M. J. Kushner, IEEE Trans. Plasma Sci. **22,** 138 (1994).

[17] L. Talbot, R. K. Cheng, R. W. Schefer and D. R. Willis, J. Fluid Mech. **101,** 737 (1980).

[18] G. K. Batchelor and C. Shen, J. Colloid Interface Sci. **107,** 21 (1985).

[19] D. J. Rader and A. S. Geller, Plasma Sources Sci. Technol. **3,** 426 (1994).

[20] R. C. Weast, D. R. Lide, M. J. Astle and W. H. Beyer, *CRC Handbook of chemistry and physics*, CRC Press (1989).

[21] C. Qu, S. J. Lanham, S. C. Shannon, S. K. Nam and M. J. Kushner, J. Appl. Phys. **127,** 133302 (2020).

[22] J. Han, P. Pribyl, W. Gekelman, A. Paterson, S. J. Lanham, C. Qu and M. J. Kushner, Phys. Plasmas **26,** 103503 (2019).

[23] S. J. Lanham, J. Polito, X. Shi, P. Elvati, A. Violi and M. J. Kushner, J. Appl. Phys. **130,** 163302 (2021).

Chapter 3 Fundamental Modeling of Pulsed Low Temperature Inductively Coupled Plasmas

3.1 Introduction

The purpose of this chapter is to characterize pulsed inductively coupled plasmas under conditions that may be seen in plasma material processing reactors. Experiments were conducted by the research group at UCLA, while modeling was by Prof. Kushner's research group at the University of Michigan. Sec. 3.2 details results from a collaboration with the experimental group at UCLA, and is based on the paper by Han *et. al.* [1] where 3D measurements were made in a Lam Research reactor under pulsed operation. This work serves to validate the results from the plasma model and verify the experimental setup. However, the experiments were operated in pure Ar rather than typical electronegative gas mixtures used for processing. Additional modeling was done for Ar/Cl_2 gas mixtures where the transition between different modes of power deposition is emphasized. Sec. 3.3 contains these results, emphasizing power matching during pulsed operation and is based on the publication by Qu *et. al.* [2]. Modeling of pulsed inductively coupled plasmas were primarily done by S. J. Lanham, while power matching and the circuit model was primarily done by C. Qu. Concluding remarks are contained in Sec. 3.2.4 and Sec. 3.3.4 respectively.

3.2 Model Validation Using Three-Dimensional Measurements of a Pulsed Inductively Coupled Plasma Chamber[‡]

Inductively coupled plasmas (ICPs) are extensively used for materials processing and microelectronics fabrication. However, their electromagnetic properties have not been fully characterized. In this regard, we have performed fully three dimensional (3D), time dependent measurements of the magnetic field, electron density, and electron temperature for an ICP sustained in argon in an industrial reactor designed for plasma etching in microelectronics fabrication. These measurements were compared to modeling results. The plasma was generated using pulsed power delivered at 2 MHz by a planar coil. The magnetic field was measured using a three-axis magnetic probe at 15,366 locations throughout the plasma volume during the H-mode portion of the pulse at temporal intervals of 2 ns. A swept Langmuir probe was used to measure plasma parameters at the same locations. The plasma density measurement was calibrated with line-integrated densities obtained using a 96 GHz interferometer. During a single radio frequency (RF) cycle, the 3D current density [derived from $B(\vec{r},t)$] is initially maximum just below the coil and moves downward toward the center of the chamber. Isosurfaces of current are nearly symmetric toroids. The total electric field, space charge field, and inductive electric field were derived and used to calculate the dissipated power, plasma current, and Poynting flux. Computer modeling of the experiment reproduces the phase dependent behavior.

[‡]Results and portions of the text that appear in this section were previously published in the paper by J. Han *et al.*, "Three-dimensional measurements of plasma parameters in an inductively coupled plasma processing chamber" Phys. Plasmas **26**, 103503 (2019). [1]

3.2.1 Introduction

Radio frequency (RF) power is the primary source for generating plasmas for semiconductor materials processing. The two dominant configurations for delivering this power are capacitively coupled plasmas (CCPs) and inductively coupled plasmas (ICPs) [3]. In the ICP configuration, power is electromagnetically delivered by antennas taking the form of external coils. In the stovetop geometry, the coils are flat spirals mounted on an insulating ceramic window which is usually the top of the vacuum system. The coils are driven at frequencies ranging from hundreds of kilohertz to tens of megahertz depending upon the application, pressure, and power. The incident electromagnetic wave from the antenna typically has a dominant component in the azimuthal direction and propagates in the axial direction. The wavelength is usually much longer than either the skin depth or the chamber, and so propagation is in near field. Electrons in plasma, accelerated by the incident RF field, produce a harmonic current, which in turn generates a small magnetic field within the plasma. A key to understanding fundamental plasma transport in these systems is measuring quantities such as the plasma density, magnetic field, internal currents, and electric field throughout the plasma volume. These quantities determine the power deposition profile, which ultimately determines the uniformity of processing.

Investigations of electromagnetic properties of ICPs have been performed over the past two decades. The use of magnetic probes (B-dot), for example, is a well-established method to measure magnetic fields inside ICPs. Piejak et al. [4] used a B-dot probe to measure a single component of the B field in an annular plasma sustained in Ar at pressures of 3-300 mTorr powered by an internal solenoidal coil. They assumed a one-dimensional plasma structure and that an axisymmetric plasma current flows only in the azimuthal direction. With these assumptions, other components of the magnetic field can be derived using Maxwell's equations. In a later work,

Piejak et. al. [5] reports on measurements in a chamber having a stovetop coil similar to an industrial plasma etching reactor. The authors measured the distribution of electromagnetic fields along a vertical line at a fixed radius and showed that B-dot probe measurements in such a system can be erroneous if the physical probe dimensions are too large (e.g., $d_{probe}/d_{chamber} = 0.06$).

Hopwood et al. [6] also investigated one component of the magnetic field in a 13.56 MHz ICP sustained in 5 mTorr Ar using a stovetop coil contained in a "McKenzie bucket" [7] (i.e., the walls were lined with magnets to generate a confining cusp field). Radial scans at three different heights were used to show consistency with the skin depth (1.6-3.6 cm) of ion densities measured using a Langmuir probe. A simple model using Maxwell's equation was used to deduce the electric field from the measured magnetic field.

Using single component magnetic field measurements, El-Fayoumi and Jones [8] made the most thorough measurement inside the volume of the chamber – on a plane consisting of 608 locations. The radial magnetic field was deduced from the axial field measurement using $\nabla \cdot \vec{B} = 0$ while assuming the azimuthal magnetic field to be zero. The experimental data were then fitted to polynomial functions. $\nabla \cdot \mathbf{B} = \mu_0 \mathbf{J}$ was then used to determine a plasma current. The current formed a toroidal ring under the stovetop coil and axially translated several cm away from the coil during a quarter RF cycle.

Using symmetry arguments, Tuszewski [9] found that when operating in oxygen, the magnetic field extended further into the plasma than in Ar, reflecting the lower conductivity and longer skin depth in the attaching molecular gas. Srinivasan et al. [10] studied the effect of current nodes in the antenna. Ding et al. [11] found regions of negative and positive power absorption consistent with nonlocal electron transport and anomalous skin depths. Two components of the magnetic field (B_r and B_z) were measured along one radial and one vertical line by Godyak et al.

[12] in an ICP sustained Ar plasma at pressures of 1-10 mTorr with a stovetop coil driven at 6.78 MHz. The work assumed azimuthal symmetry based on having equally spaced concentric antennas. Using the measured two components of the magnetic field, the current density was calculated by taking derivatives along the line, assuming $\partial / \partial r$ was uniform as a function of height [12]. The current density peaked within 1 cm of the dielectric window adjacent to the antenna and reversed direction in a second layer 6-8 cm from the dielectric. The magnitude and relative phase of the magnetic field, measured by a vector voltmeter, also revealed second harmonic current flowing normally to the main azimuthal current due to the nonlinear effect associated with the rf magnetic field at fundamental frequency [13].

Ostrikov et al. [14] investigated ICPs having a stovetop coil driven at 500 kHz operating in both E- and H-modes. (E-mode refers to conditions where power deposition by electrostatic capacitive coupling from the coil dominates. H-mode refers to conditions where power deposition is dominantly by absorbing the electromagnetic wave produced by the antenna.) They found that the axial magnetic field peaked in the center of the reactor, with the radial magnetic field being maximum under the coil at half radius. They also found a second harmonic contribution of the azimuthal component of magnetic field, which was attributed to nonlinear interactions between the radial and axial magnetic field components.

These previous measurements of properties of low pressure ICPs have provided keen insights into their operation and established many of the fundamental operating principles of low pressure ICPs. However, in most cases, only a subset of plasma properties have been reported and rarely in multiple dimensions due to limitations in diagnostics. Advances in diagnostics now enable simultaneous measurements of nearly all plasma and electromagnetic properties of such ICPs in 3-dimensions (3D). In this work, the radio frequency (RF) magnetic field, plasma density,

and electron temperature were measured in 3D throughout the volume of an ICP sustained in Ar powered by a stovetop coil. The theme of the results presented here is to provide a self-consistent set of 3D measurements for electron temperature, ion density, magnetic field and electric field components, Poynting vector flux, and power deposition, with the goal of providing new or refined insights into operation of ICPs. For example, these 3D measurements show that the plasma density, current density, and Poynting flux have maxima in different locations. Reversals in current density (and regions of negative power deposition) are observed during a single RF cycle and corroborated with modeling results.

The temporal and spatial dependence of the plasma parameters are discussed during one RF cycle after the plasma has reached a steady state during pulsed operation [15]. The experiment was performed in an industrial plasma chamber of the type used for plasma etching which was modified to enable probe access by adding a cylindrical extension below the ceramic window. The antenna and ceramic top were located at the same height as in the commercial device. However, the antenna diameter was reduced by 7 cm in order to investigate physics directly underneath it. The data presented here show the structure of the plasma current and total electric field during an RF cycle. These values were then used to calculate the power deposition in the plasma. The plasma conductivity was calculated from the current density measurements. Computer modeling of the device was performed to help in interpretation of the experimental data. Behavior during the turn-on and decay phases of pulsed operation are left as future work.

This manuscript is structured as follows: the experimental setup and diagnostics are described in Sec. 3.2.2, which also contains a brief description of the model. Measurements of key parameters and quantities derived from them, and computational results, are presented in Sec. 3.2.3. The measurements include plasma density and temperature (Langmuir probe and

microwave interferometer), magnetic field (3-axis magnetic probe), and space charge electric field (emissive probe). The derived quantities are current density ($\frac{1}{\mu_0}\nabla \times \vec{B}$), inductive electric field ($-\frac{\partial \vec{A}}{\partial t}$ or Faraday's law), Poynting flux ($\frac{1}{\mu_0}(\vec{\mathrm{E}} \times \vec{B})$), and conductivity. Our concluding remarks are given in Sec. 3.2.4.

3.2.2 Description of the Experiment and Model

3.2.2.a. Experiment

A schematic of the experimental apparatus is shown in Figure 3-1a, and an image of the experiment is shown in Figure 3-1b. The ICP consists of a cylindrical chamber (height = 17.2 cm and radius = 26 cm) producing argon plasmas at pressures of 10–50 mTorr. A three-turn circular stovetop antenna, mounted on top of a 2.8 cm thick alumina window, was connected to an RF generator operating at a 2 MHz delivering power up to 1 kW. The antenna is wired as two 1.5 turn coils connected in parallel. The coil has a center radius of 18 cm with three turns separated by 1.1 cm and is located at 21.6 cm above the wafer (one cm above the top surface of the dielectric). When producing a plasma with 300W, the peak current in each conductor is approximately 18 A. A Si wafer 15 cm in radius was electrostatically clamped to the cylindrical chuck (radius = 22.75 cm) and cooled with backside helium flow. The top surface of the wafer is at axial location z = 0. The height of the plasma (wafer to the bottom of the ceramic window) is 17.2 cm. A mass flow controller sets the chamber gas pressure measured by convection and Pirani gauges. Unless otherwise noted, experimental data presented in this paper are acquired with a flow rate of 100 sccm. This matched the flow rate used in the simulations. In these experiments, there was no additional bias voltage applied to the substrate.

Probes were inserted from the front (load lock) side of the chamber through a ball valve feedthrough [16] allowing free rotation of the probe shaft through θ and φ spherical coordinates. The probe motion is driven by a 3D drive shown in Figure 3-1b. The stepping motors have embedded controllers and interface to a computer and can position the attachment point of the probe with a linear precision of 10 μm along each drive. The probe tip can be located on a grid within the chamber precise to within 50 μm, although there is up to a 0.5 cm difference between this grid position and chamber coordinates over the full extent of the 3D volume. The rotational limit on the ball valve and position of the port prevent the probe from reaching a region immediately adjacent to its mounting point. This is indicated by missing data in figures showing 2D planes of 3D data. Data were acquired using a 4 channel 2.5 GS/s, 12 bit oscilloscope. The probe motion and data acquisition systems were controlled by a Python program communicating with both through ethernet protocols. The plasma density, electron temperature, plasma potential, and all components of the magnetic field were typically measured on a two- or three-dimensional grid having 1 cm separation between points.

Plasma potential was measured using an emissive probe [17]. The probe consisted a thoriated tungsten filament heated by an isolated power supply with a low capacitance to ground [18]. Prior to making measurements, the probe temperature was adjusted so that the I-V curve of the probe was symmetric. The heater current to the probe was switched off for the duration of the measurement. The off period was typically a few milliseconds, which was measured to be too short a time for the probe emission to decay due to changes in temperature. The probe is capable of tracking changes in plasma potential below a frequency of about 20 MHz. This was verified using a signal generator and an external resistor. The value of the resistor matched $dV/dI|_{I=0}$ obtained by sweeping the probe in its emissive state, which is assumed to be the connection

resistance to the plasma when the probe is floating. During the steady state, the RF component of the plasma potential ranges from a few volts to a few tenths of a volt depending on the antenna power and probe position. Data collected by the probe were then used in calculating the space charge electric field, $\vec{E} = -\nabla\phi_p$.

A cylindrical Langmuir probe made from tungsten (l = 1.43 mm, d = 0.28 mm) was used to measure electron temperature and ion saturation current. Although bi-Maxwellian electron energy distributions have been observed in low pressure argon discharges [19], we found that our measured distributions were well represented by a single temperature Maxwellian. That is, a straight line was a good fit to the log of the probe characteristic. Therefore, we assumed a simple Maxwellian electron energy distribution. The electron temperature (T_e) is determined by fitting an exponential to the I-V curve with ion current subtracted. T_e varies ±0.2 eV throughout the measurement volume, with an average of 3.0 eV during the steady state portion of the pulsed discharge. There was no overall trend to the spatial profile, indicating a uniform T_e. These results agree with previous measurements in similar devices using Thomson scattering [20]. As determined from the emissive probe measurement, RF oscillations in plasma potential are negligible in the bulk of the plasma, being confined by plasma shielding to the region within a few centimeters of the antenna.

The spatial profile of ion saturation current (I_{isat}) was acquired using this Langmuir probe biased at -60 V. The output signal was low-pass filtered at 160 kHz. Since the probe is biased at a voltage much larger than the RF fluctuation of the plasma potential, compensation is not necessary. With the measured uniform temperature, a relative density profile was calculated using $I_{isat} = Ane\sqrt{\frac{kT_e}{M}}$, where A is the area of the probe, M is the ion mass, and e is the elementary charge. We note that relative profiles so obtained were the same for probe bias between -20 V and

-60 V, although the overall magnitudes were different. To eliminate the amplitude ambiguity, we cross-calibrated the measured profiles against the line integral electron density measured by a 96 GHz microwave interferometer. The results discussed in this paper all used this calibration. With a bias of -60 V, the correction factor at 10 mTorr and RF power below 160W was about 20%; at higher power, it dropped to 10%. During a portion of this work, a hairpin probe [21] was also available for the local density measurement. The results are described in a separate publication [22] but closely track with the profiles inferred by the above technique.

A three-axis, single turn magnetic probe [23] (≈4 mm diameter) was used to measure the RF magnetic field produced by the antenna on the same 1 cm spatial grid as the ion saturation current was acquired. The B-dot probe response was calibrated using a Helmholtz coil and a vector network analyzer. The RF magnetic field induces an electric field which, in turn, produces an RF current through the plasma. The data were analyzed by first integrating the three temporal signals recorded from the magnetic probe, as the probe response is proportional to $\partial\vec{B}/\partial t$. Due to the positioning of the ball-valve feedthrough used for the vacuum penetration, the probe position is defined by two angles (θ, ϕ) as shown in Figure 3-1a, and the distance that the probe shaft extends into the chamber. The transformation to Cartesian coordinates inside the chamber is given by

$$\begin{bmatrix} B_x \\ B_y \\ B_z \end{bmatrix} = \begin{bmatrix} \cos\theta\cos\phi & -\sin\theta & \cos\theta\sin\phi \\ \sin\theta\cos\phi & \cos\theta & -\sin\theta\sin\phi \\ \sin\phi & 0 & \cos\phi \end{bmatrix} \begin{bmatrix} B_{xp} \\ B_{yp} \\ B_{zp} \end{bmatrix}, \quad \tan\theta = \frac{y}{(R_p+x)}, \tan\phi = \frac{z}{(R_p+x)} \tag{3.1}$$

where R_p is the distance of the pivot point of the ball valve (slightly past the outer chamber edge) from the center of the chamber. θ is the angle between the probe shaft in the x-y plane and the x axis, and ϕ is the angle from the plane z=0. This definition is convenient for the probe geometry and is notably not quite a spherical coordinate transformation.

The plasma was operated using pulsed power having a pulse repetition frequency of 100 Hz and a duty cycle of 50%, resulting in a power-on period of 5 ms. The current ramp-on and ramp-down times were 50 μs. All quantities were measured after the plasma has reached a quasi-steady state during the power pulse operating in H-mode. The temporal behavior of the optical emission from the plasma was captured with a Si photodiode sensitive to visible light and near infrared. The photodiode has a response time of 1 μs and viewed the center of the plasma.

3.2.2.b. Description of the Model

Properties of the ICP were modeled using the Hybrid Plasma Equipment Model (HPEM) [24]. The HPEM is a simulator that combines modules addressing different physical phenomena in a time slicing manner. The modules used in this investigation are the Electromagnetics Module (EMM), Electron Monte Carlo Simulation (eMCS), and the Fluid Kinetics Module (FKM). Harmonic electromagnetic fields launched from the coil are produced in the EMM by solving the frequency domain wave equation. Continuity, momentum, and energy equations for ions and neutral particles, continuity and momentum equations for electrons, and Poisson's equation for the electric potential are integrated in time in the FKM. RF electric and magnetic fields from the EMM and electrostatic fields from the FKM are then used in the eMCS to advance pseudoparticle trajectories produce electron energy distributions as a function of position including electron-electron collisions. These distributions are then used to produce electron transport coefficients and electron impact rate coefficients for use in other modules. The argon reaction mechanism used in the model is the same as described by Tian et al. [25] The geometry is 2-dimensional in cylindrical coordinates assuming azimuthal symmetry.

To account for collisionless electron heating and anomalous skin effects in absorption of the coil-launched electromagnetic wave in the plasma, electron currents are calculated in the eMCS

and used in the EMM in solution of the wave equation [26]. The solution to the wave equation in the EMM is performed in the frequency domain, while advancement of pseudoparticle trajectories in the eMCS is performed in the time domain. Electron currents are computed in the eMCS by collecting statistics on the azimuthal component of velocity of the electron pseudoparticles as a function of position and time. These statistics are then Fourier analyzed to provide the harmonic electron current density as a function of position and time,

$$J_\phi(\vec{r},t) = J_\phi(\vec{r})\mathrm{Re}(e^{i(\omega t+\delta_j(\vec{r}))}) \tag{3.2}$$

where $J_\varphi(\vec{r})$ is the local harmonic amplitude of the current density and $\delta_j(\vec{r})$ is the phase of the current density. This current density is then used in the EMM to solve the frequency domain wave equation,

$$\nabla^2 E_\phi(\vec{r}) + \left(\frac{\omega}{c}\right)^2 E_\phi(\vec{r}) = i\omega\mu_0 J_\phi(\vec{r}) \tag{3.3}$$

to produce the time and spatially dependent electric field in the azimuthal direction,

$$E_\phi(\vec{r},t) = E_\phi(\vec{r})\mathrm{Re}(e^{i(\omega t+\delta_E(\vec{r}))}) \tag{3.4}$$

where $E_\phi(\vec{r})$ is the harmonic amplitude of the electric field and $\delta_E(\vec{r})$ is the phase of the electric field. In cases where electron heating is approximated as being solely collisional, the current density is given by

$$\begin{aligned} J_\phi(\vec{r},t) &= \sigma(\vec{r})E_\phi(\vec{r},t), \\ \sigma(\vec{r}) &= \frac{n_e(\vec{r})e^2}{m_e\nu_m(\vec{r})\left(1+i\frac{\omega}{\nu_m(\vec{r})}\right)} \end{aligned} \tag{3.5}$$

where n_e is the electron density, σ is the conductivity, m_e is the electron mass, and ν_m is the momentum transfer collision frequency. The radial and axial components of the magnetic fields are then obtained from Faraday's law. The instantaneous power deposition is

$$P(\vec{r},t) = J_\phi(\vec{r},t)E_\phi(\vec{r},t) \tag{3.6}$$

The geometry used in the model is shown in Figure 3-1c. In the model, the ceramic window having a negligible conductivity also serves as a showerhead for injection of argon gas at 100 sccm for a pressure of 10 mTorr. The three turn coil sits a few mm above the window. The Si wafer sits on a metal, grounded substrate surrounded by an alumina electrostatic chuck and a focus ring. Gas is annularly pumped outside the focus ring. The outer boundary of the chamber is grounded. The limit of the experimental diagnostics is shown by the dashed-dotted line.

Since the HPEM is a modular simulator that is intended to address a wide variety of plasma sources, computational parallelization is difficult. In all modules, there are computational branching points invoking different algorithms to address, for example, transport in magnetized or not-magnetized plasmas. This is particularly the case in the eMCS where the transport algorithms are divided into many loops each performing a relatively small amount of work. Parallelizing these smaller loops does not result in significant improvement in performance due to the computational overhead in repeatedly launching (and terminating) these small parallel loops.

Due to the modular nature of the HPEM, obtaining efficient computational parallel performance is challenging. A different parallelization strategy is required for each module (and submodules) which makes parallelization over large numbers of processors impractical. When implemented in parallel using 5-10 processors, as in the cases discussed here, speedups of factors of 3-5 over serial can be obtained. (Using additional processors typically does not improve performance.) To improve parallel performance in the eMCS module, the eMCS was restructured in the following manner.

The eMCS module consists of initialization subroutines (IS), particle trajectory and collisions subroutines (PS), and diagnostic and postprocessing subroutines (DPS). On each call to the eMCS, the IS are called, followed by several calls to the PS. Following each call to the PS,

there is a call to the DPS. Residing within the PS are many smaller loops branches, needed for generality, which slow parallel performance if they are individually made parallel. The restructuring consisted of executing the entire set of PS routines as a parallel thread without any internal parallelization. For example, outside the PS, an array of particle properties is A(i), for the i^{th} particle. Entering into IS, particles and their property arrays are allocated into thread aware arrays, $A_T(i,j)$, where i is the particle number and j is the thread. When executing the PS, parallel threads are launched which separately operate on $A_T(i,j)$ without memory collisions. Upon completion of PS, the A(i) are reconstructed from the $A_T(i,j)$. Since there are still overhead costs with the allocation and reconstruction operations, the restructured eMCS is not efficient when using small numbers of particles. For those conditions, the prior parallelization of individual loops inside PS is more efficient. However, with large numbers of particles, the restructured eMCS is significantly more efficient.

3.2.3 Plasma Properties

The evolution of plasma properties during the power pulse is shown in Figure 3-2. The fill pressure was 10 mTorr. The plasma transitions through the E-mode to H-mode during the first 0.5 ms of the pulse. Subsequently with constant power input in H-mode, the plasma density builds up and reaches a steady state in approximately 2 ms. The initial overshoot visible in the power waveform is due to the controller.

3.2.3.a. Plasma Density

As described above, electron density profiles computed from ion saturation current assuming a uniform spatial electron temperature and calibrated by an interferometer are shown in Figure 3-3. Plasma density peaks in the center of the reactor both radially and vertically, which is

contrary to our expectation that plasma density would be offset toward the top of the device and under the RF antenna where power deposition is maximum. Density contours on an (r,z) plane for three generator powers are shown in Figure 3-4. The maximum density at 300 W 9.0×10^{11} cm^{-3}. Density increases with power, but the position of peak density is nearly independent of power.

The electron density is shown in Figure 3-5 in a 3D perspective; data were acquired at 15,366 spatial locations throughout the volume having separations on a cubic grid of 1 cm. Measurements were made for 64,000 time steps over 269 RF cycles. Several isosurfaces of constant I_{sat} are drawn in Figure 3-5 at 2.3 ms after the start of the power pulse. Unlike other quantities such as the internal electric field, which varies at the 2 MHz frequency, the plasma density at any one location is essentially constant over the RF cycle. The plasma first forms under the coil at the start of the pulse and then moves inward to become the spatial distribution shown in Figure 3-5. This motion takes about 1 ms.

Computed plasma properties (cycle averaged Ar^+ density, electron temperature, and plasma potential) for 300 W power deposition are shown in Figure 3-6. As measured in the experiments, early during the pulse, the plasma density is maximum under the coil and transitions toward the axis. This transition results from two dominant effects. The first is an increase in plasma density which increases the electron thermal conductivity. The higher thermal conductivity enables power deposition that is maximum under the coil to heat electrons throughout the reactor. The second is an increase in the argon metastable density, which assumes a diffusion dominated profile that peaks near the center of the plasma. The lower threshold for multi-step ionization from the Ar^* diminishes the importance of the elevation of the tail of the electron energy distribution function (EEDF) that occurs in the skin depth of the ICP. The predicted electron temperature is relatively uniform, in the bulk plasma within the viewing volume of the experiment, 3.5-3.6 eV,

and elevated to 4.0 eV within the skin depth (outside the experimental view area). This electron temperature is 0.5 eV higher than measured, but within experimental bounds.

3.2.3.b. Magnetic Field and Plasma Current Density

A snapshot of the vector magnetic field at one instant of time is shown in Figure 3-7. The Ar pressure is 10 mTorr, and the generator power is 300 W. The measurements are made at 2 ms after the start of the power pulse when the plasma is in steady state H mode (see Figure 3-2).

The plasma current density is derived from the measured magnetic field using $J = \frac{1}{\mu_0}\nabla \times \vec{B}$. The gradient calculation is performed by either a three-point quadratic Lagrangian interpolation (IDL) or a 1st or 2nd order finite difference method. The three methods give nearly identical results. Currents flow in the azimuthal direction, reversing sign every half-cycle of the 500 ns RF period. Directly under the antenna, this component of the plasma current is 180° out of phase with the antenna current, as expected from Lenz's law. The azimuthal currents are approximately ten times larger than the radial or axial currents. The plasma current density is symmetric about the origin—the radial center of the chamber. The peak antenna current is 37 A distributed over three turns. In contrast, the peak plasma current obtained from spatially integrating the current density is 12 A. This value is consistent with Figure 3-7 where most of the magnetic field lines from the antenna do not intercept the bulk of the plasma.

The azimuthal plasma current density is shown in Figure 3-8 sampled at 4 times during a quarter-cycle of an RF period in a vertical plane. The generator power is 300 W. The images are for t/T_{rf} = 0, 0.13, 0.19, and 0.25, where T_{rf} is the RF period, and were chosen to illustrate the dynamics of the current penetration into the plasma. The dynamics resemble eddy current penetration into a conductor from the external driving current. Since the internal electric field that drives the current changes sign every half cycle, the plasma current directly under the coil reverses

and gains strength as the previous current maximum decays and moves downward. Note that for this figure, the flow rate was reduced to 25 sccm to better emphasize the current penetration, as further discussed in Sec. 3.2.3.d. This current diffusion pattern was seen by Fayoumi [8] and described as "the Ohmic response of the plasma due to an external driving current."

Model predictions for current density as a function of phase for similar conditions are shown in Figure 3-9. The initial phase in this sequence was chosen to align with that of the experiment. Following that alignment, the time between frames is the same as the experiment. The experimental trends of both current reversal and simultaneous regions of positive and negative current densities are also predicted by the model. The origins of the simultaneous regions of positive and negative current densities are twofold. First, the reactive or inertial component of the plasma conductivity, which is proportional to ω/ν_m, introduces a phase delay between the velocity of the electrons (which dominate the current density) and that of the incident electric field. In the limit that $\omega \gg \nu_m$, the plasma conductivity is dominated by reactance, and electron velocities are 90° out of phase with the incident electric field. In the limit that $\omega \ll \nu_m$, the plasma conductivity is dominated by resistance, and electron velocities are in phase with the incident field. The finite response time of the electrons to reversals in the electric field then leads to regions in which current density is opposite to the incident electric field. (To emphasize these reversals, the computed results in Figure 3-9 are plotted on a log-scale, whereas the experimental results are plotted on a linear scale.) These out-of-phase electrons also result in negative power deposition, discussed below.

3.2.3.c. Electric Field

The manner of power transfer from the ICP coil to the plasma is important for understanding the plasma dynamics. For example, in addition to power being deposited in the

plasma, power delivered from the generator is dissipated by the resistance of the coil, radiated into free space, and consumed by eddy losses in the metal of the chamber. To unambiguously determine the power dissipated in the plasma, one should measure the internal electric fields so that $\vec{J} \cdot \vec{E}$ can be volume integrated. Here, we present measurements of the total internal electric field derived from measurement of the magnetic fields (electromagnetic component) and plasma potential (electrostatic component). The total electric field is given by $\vec{E} = -\nabla\phi_p - \frac{\partial \vec{A}}{\partial t}$, where ϕ_p is the electrostatic plasma potential and $\vec{A}$ is the vector potential. We first discuss the electrostatic component.

In the collisional, low temperature plasma represented by this system, charge neutrality is maintained by self-generated ambipolar electric fields, which constrain electron and ion fluxes to surfaces to be equal. The ambipolar electric fields, generally pointing from the center to the boundaries of the plasma, are produced by a small positive space charge in the plasma (leading to the description electropositive plasma). Integration of the ambipolar electric field results in a positive electrostatic plasma potential, ϕ_p, which serves to trap or slow electrons from leaving the plasma and accelerate ions out of the plasma. This electric field is measured using the plasma potential measured by the emissive probe as described above.

The computed ambipolar electrostatic field (as vectors) and plasma potential (as color contours) are shown in Figure 3-10 for an Ar pressure of 10 mTorr and a generator power of 300 W. The electric field is shown on two orthogonal planes, one perpendicular to the wafer and the other parallel to the wafer at a height of 8 cm. The 2 MHz coil frequency was observed on the plasma potential as a 10% ripple, which is produced in part by capacitive coupling and in part by oscillation in the electron temperature during the RF cycle. The maximum plasma potential at the center of the plasma is 17 V. The results from the model predict a maximum plasma potential of

23 V [Figure 3-6c], which aligns with the 0.5 eV higher electron temperature predicted by the model compared to experiment.

The electromagnetic component of the internal electric field is a superposition of the electric field due to the changing RF coil currents, plasma currents, and image currents in the walls. The measured plasma current is in the same direction as the azimuthal electric field. There are no appreciable radial or vertical currents. This implies that the RF electric field, $\vec{E}_{ind}$, is primarily in the azimuthal direction. Since the wall currents can only be estimated, it is difficult to calculate the inductive component of the electric field from $-\frac{\partial \vec{A}}{\partial t}$. Instead, we apply Faraday's law, $\int \vec{E}_{ind} \cdot d\vec{l} = -\frac{\partial}{\partial t} \int \vec{B} \cdot \hat{n} d\vec{A}$, to the azimuthal component E_ϕ from the time derivative of B_z. From the measured time derivative of $\dot{B}_z$, we get

$$E_\phi(r) = \frac{1}{2\pi r} \int_0^r \dot{B}_z(r') 2\pi r' dr' \tag{3.7}$$

E_{ind} results from oscillation in the vector potential that originates from the RF magnetic fields produced by the antenna. The induced electric field in the bulk of the plasma is diminished compared to vacuum conditions because of the shielding effect of induced currents under the antenna. The magnitude of E_{ind} is comparable in the plasma and in vacuum near the top of the reactor where the electromagnetic wave from the coil has not been significantly absorbed. As one moves toward the wafer, the magnitude of E_{ind} decreases over a distance which exceeds the collisionless skin depth, $\delta = c/\omega_p$, where ω_p is the electron plasma frequency. δ is 7 mm in the center of the device and 1.6 cm near the coil. For a fully collisional plasma, $\delta = \sqrt{c/\omega_p \mu_0 \sigma} \approx 3.6$ cm near the coil. There is generally a phase difference between the induced electric field in vacuum with respect to the plasma.

3.2.3.d. Power Deposition

The bulk of the power absorption is localized almost directly under the coil as this is where the image current from the coil is the largest. The time averaged power density inside the plasma calculated using $P = \vec{J} \cdot \vec{E}$ is shown in Figure 3-11a for a pressure of 10 mTorr and a generator power of 300 W. The feedstock gas flow rate affects the plasma current and electric field. At an increased flow rate, while keeping the chamber pressure and input power constant, we observed that plasma currents tended to be higher and more localized near the coil. Increasing the flow rate by a factor of two at constant power and pressure resulted in approximately a 30% increase in peak plasma current and at the same time 30% decrease in internal electric fields. The flow rate does not linearly impact plasma quantities, and further investigations are necessary to determine the effects of flow on other plasma properties (e.g., on metastable densities). The power deposition profiles at a high flow rate mimicked the higher pressure cases shown in Figure 3-11, which similarly tend to localize the power deposition closer to the coil.

The inertial transport that leads to out-of-phase current density also produces instantaneous regions of positive and negative power deposition – regions where net power flows from the field into the plasma and regions where net power flow from the plasma back into the field. Although in most cases, the local, time averaged power deposition is positive, under select conditions, the cycle averaged power deposition can be locally negative. This has been observed by Godyak et al. [27] at 13.56 MHz and 6.78 MHz but not at 3.39 MHz. For our 300 W 10 mTorr argon discharge operating at 2 MHz, computed instantaneous power deposition is shown in Figure 3-12 for the phase during which the striations between positive and negative power deposition are more pronounced. The results are shown for different modes of power deposition and pressures. Local refers to power in the calculation being given by σE^2. Nonlocal refers to power in the calculation

being given by where the current density is kinetically derived from electron trajectories produced in the eMCS. Similar experimental results for instantaneous power deposition are shown in Figure 3-13 for pressures of 10, 50, and 100 mTorr. These results were obtained from instantaneous measured values of J and E and show regions of positive and negative power deposition.

At low pressure with nonlocal power deposition, the out-of-phase electrons produce a wavelike propagation of negative power deposition into the plasma, as shown in Figure 3-12a, similar to the current density shown in Figure 3-8. With ω/ν_m = 0.45-0.5, as derived by the model, the plasma is reasonably collisional while still having reactive properties. The degree to which nonlocal transport affects the negative power deposition is shown in Figure 3-12b, also 10 mTorr, but where current density is given by σE. With σ given by Eqn. 5, the inertial (reactive) component of the conductivity is retained, whereas the nonlocal character is not. The general characteristics of the negative power are retained, whereas the phase at which the negative power is maximum decreases. (This decrease in phase is responsible for the decrease in magnitudes of both positive and negative powers.) With local transport, both the positive and negative power deposition extend over more limited space. With an increase in pressure to 50 mTorr [Figure 3-12c] with local power deposition and ω/ν_m = 0.07-0.08, the region of negative power deposition shrinks and the phase at maximum negative power decreases, commensurate with the dephasing time of the electrons also decreasing. Finally, at 200 mTorr [Figure 3-12d] with ω/ν_m = 0.02, the negative power deposition is nominal, as electrons dephase earlier in the RF cycle compared to the lower pressures having lower collision frequencies.

We note that the negative power dissipation in this experiment is small, much less than one percent of the total. Negative power dissipation is only clearly displayed when experimental data or simulation results are plotted on a log scale as shown in Figure 3-12 and Figure 3-13.

RF power from the generator was calculated by measuring current and voltage at its terminals. These values are substantially in phase, although an exact multiplication over many cycles was performed prior to computing the average value. Power lost in the antenna and the RF delivery system between the generator and plasma is a few percent. To validate these measurements, we placed a 1-turn loop just above the RF antenna, with a resistor in series, while making no other changes to the system. Dissipation in the inductively coupled test circuit is measured by computing I^2R in the absence of plasma, at the same antenna current, with the same "match" settings. The power dissipated in the dummy load arrangement was within a few percent of the reported generator power at all relevant powers. These cross-checks provide confidence in the accuracy of the power being delivered to the plasma.

Once the power density is computed throughout space, we integrate over the volume to compute the measured total power dissipated in the plasma. Resistive losses in the system were estimated by measuring the generator power required to drive the corresponding equivalent coil currents with the chamber evacuated (that is, no plasma). The resistive losses manifest primarily in coil heating and account for 10%-13% of the generator power. Since the viewport of the experiment does not cover the entire volume of the plasma, the model was used to rescale the experimentally derived power deposition to that deposited in the entire reactor.

For example, at 10 mTorr, using nonlocal electron transport, results from the model indicate that the fraction of power deposition observable in the view of the experiment is about 0.7 ± 0.1 of the total (based on the window and positioning uncertainty). The observable experimental power deposition for 10 mTorr and 300 W delivered from the generator is about 112.8 W. With recalibration from the model, the total power deposition in the plasma is then 158.9 ± 17 W. Adding in the resistive power loss of 42.1 ± 2 W produces a total of 201 ± 17 W.

There is an unaccounted power deposition of 99 W or about 33%. We expect that some fraction of the missing power is absorbed by the plasma through capacitive coupling. We measured oscillations in plasma potential using an emissive probe with a bandwidth of 20 MHz and calculated the RF variation in $\vec{E}(\vec{r})$ from $\vec{E} = -\nabla\phi_p$. The estimated power density from capacitive coupling in the volume of the plasma, $P = \sigma E^2$, is few percent of the total or about 10 W. Measurements could not be performed in the sheath directly under the coil, which might account for additional power dissipation by ion acceleration by capacitive electric fields from the coil. However, based on results from the model, we estimate the loss due to ion acceleration under the coil to be about 20 W, which produces a total of about 231 ± 17 W. For the rest the other conditions, we estimated capacitive losses as 10% of the generator power. With the uncertainty in the measurements of about 5%-10%, the majority of power deposition can be accounted for.

3.2.3.e. Poynting Flux and Power Dissipation

Using the complete data for magnetic and electric fields, the Poynting flux, $\vec{S} = \frac{1}{\mu_0}\vec{E} \times \vec{B}$, can be computed. A composite of the experimentally measured plasma density, current density, Poynting flux, and absorbed power during steady state operation is shown in Figure 3-14 for an Ar pressure of 10 mTorr and a generator power of 300 W. Except for the current density which is shown as a peak value, these quantities are averaged over the RF cycle. The plasma density is the largest in the center of the chamber and is not coincident with the plasma current density (grey contours above the red density contours). The Poynting flux originates at the coils and points toward the power deposition region. The maximum absorption is not coincident with the center of the current channel. The Poynting flux averaged over radius as a function of height for the same temporal interval is shown in Figure 3-15. The net Poynting flux briefly points upwards, toward

the coil, twice each cycle. During a complete cycle, the integrated upward Poynting flux is 0.2 of the downward Poynting flux. The cycle averaged Poynting flux is downwards through the lid and estimated to be 90 mW/cm^2, for a total power of 110 W into the surface of the measurement volume. This compares favorably with the computed power in this volume of 113 W. In a purely non-dissipative, reactive plasma where $\omega/\nu_m \gg 1$, the downward and upward directed Poynting fluxes would be symmetric over the RF cycle. There would be no net power deposition in the plasma as electrons remove power from the field on the first half cycle and give back power to the field on the latter half cycle. The differences between the downward and upward directed Poynting fluxes are a measure of the collisional power deposition.

Properties of the Poynting vector obtained with the model are shown in Figure 3-16 for a 300 W plasma sustained at 10 mTorr. The power transport model is nonlocal using the eMCS. The contours show the magnitude of the Poynting vector plotted on a log scale from 0.01-2.5 W/cm^2. The arrows show only the direction (and not magnitude). The results are shown for 4 phases during the RF cycle chosen to demonstrate the change in the direction of the Poynting vectors. The first frame (t/T = 0.41) is when the Poynting vector is maximum pointing downward at 2.5 W/cm^2, delivering power to the plasma. All Poynting vectors with magnitude larger than 10 mW/cm^2 point downwards. At t/T = 0.58, the direction of the Poynting vector near the coils has reversed to point upwards, taking power out of the plasma with a maximum amplitude of 0.9 W/cm^2. At this time, power lower in the reactor continues to flow downward. At t/T = 0.64, the upward directed Poynting vector has its maximum value at 1.4 W/cm^2. Essentially, all Poynting vectors greater than 10 mW/cm^2 are pointed upwards. Finally, at t/T = 0.78, power is again delivered from the antenna to the plasma with downward Poynting vector with a magnitude of 0.8 W/cm^2, while in the fringes of the skin depth, power is still directed upwards.

3.2.3.f. Plasma Conductivity

The electron drift velocity is given by

$$\frac{\partial \vec{v}_d(\vec{r},t)}{\partial t} = \frac{q\vec{E}(\vec{r},t)}{m_e} - \nu_m \vec{v}_d(\vec{r},t) \tag{3.8}$$

With $\vec{v}_d$ and $\vec{E}$, both having a harmonic time dependence $\exp(i\omega t)$, the solution is

$$\vec{v}_d(\vec{r}) = \frac{q\vec{E}(r)}{m_e \nu_m(\vec{r})\left(1+i\frac{\omega}{\nu_m(\vec{r})}\right)} \tag{3.9}$$

and the plasma current density is then $\vec{J}(\vec{r}) = qn_e(\vec{r})\vec{v}_d(\vec{r})$, which results in the plasma conductivity given in Eq. (5). There is a phase difference between $\vec{J}(\vec{r})$ and $\vec{E}(\vec{r})$ due to electron inertia, represented by the imaginary component in the denominator of the conductivity [28,29]. By comparing the measured values of $\vec{J}(\vec{r})$ and $\vec{E}(\vec{r})$, we compute experimental values for the magnitude and phase of the conductivity $\sigma = \left|\frac{J}{E}\right| e^{i\gamma}$. Experimentally, we find the phase difference (γ) varies between 10° and 20° at most locations in the plasma, corresponding to $\nu_m \geq 3\omega$. The phase difference γ is the largest near the top of the chamber in agreement with the simulation, potentially due to nonlocal effects arising in the strong electric field region under the coil. The real part of the conductivity $\mathrm{Re}[\sigma] = |\sigma|\cos(\gamma)$ obtained from experiment and simulation is shown in Figure 3-17. Since both the electric field and current density are small near the bottom and center of the experimental chamber, their ratio develops large errors due to measurement noise, and so the conductivity is evaluated only for r > 3.5 cm, z > 8 cm. The simulations computed the conductivity in the same manner as derived in experiments. The complex electric field was obtained from the solution of Maxwell's equation. The complex current density was obtained from Fourier analysis of trajectories of pseudoparticles in the electron Monte Carlo simulation. Complex conductivity was then computed as $\sigma = \left|\frac{J}{E}\right| e^{i\gamma}$. The spatial profiles for real conductivity

agree within a factor of two, with the differences in the large part due to the difference in ω/ν_m. With this conductivity profile, the collisional skin depth ranges from ten centimeters in the low plasma density region under the coil to a few centimeters where the conductivity is the largest in the center of the plasma. If plasma conductivity strictly obeys Eqn. 5, one expects its spatial dependence to match the electron density, when T_e is spatially uniform, which is generally the case.

The measured conductivity cannot be explained with a simple Ohms law as the electron dynamics are nonlocal. Fast electrons are generated in the narrow sheath under the RF coil and stream downward into the region where the power dissipation is the largest. The electron distribution function is an amalgam of bulk and tail electrons, each coming from different locations. This is what makes the phenomena nonlocal – an electric field applied to one part of the plasma has an influence on the current density elsewhere due to long mean-free-path transport [30]. Changes in conductivity due to the anomalous skin effect have been reported by Kolobov and Economou [31], Lafleur et al. [32], and Cunge et al. [30], with theory initially developed by Weibel [33]. This anomalous transport contributes to the phase difference between electric field and current density that conventional theory attributes solely to local inertial effects of the electrons oscillating in a harmonic field.

3.2.4 Discussion and Conclusions

Understanding the physics of low temperature plasmas and translation of those findings to industrial use requires measurements of fundamental quantities such as magnetic field, total electric field, plasma density and temperature, optimally performed in three dimensions. In this investigation, 3D measurements of these quantities were obtained for the quasi-steady state of a pulsed ICP sustained in argon in an industrial plasma reactor modified to enable probe access.

With these measurements, internal plasma current, power dissipation, and Poynting flux were derived. We found that the peaks of plasma density, current, power deposition, and Poynting flux were not spatially coincident. Although this is an expected result at lower pressures and higher powers where diffusion dominates and electron thermal conductivity is high, at the moderate pressures and power of this investigation, we might expect that plasma density would be more localized closer to the region of power deposition. The measurements imply that either convective noncollisional transport of electrons in the tail of the distribution or rapid thermal conduction, both of which would more uniformly distribute ionization throughout the reactor, retains their influence at these higher pressures and lower power deposition.

From the plasma potential measurement, we derived the electrostatic part of $\vec{E}$ which points away from the center where the electron density is a maximum. From the momentum transfer equation, the divergence of the pressure tensor gives the change of momentum flux due to spatial inhomogeneities. Since the electron temperature is nearly spatially uniform, this inhomogeneity arises from gradients in charge density. The uniformity of T_e indicates a high electron thermal conductivity, since measured power deposition is highly nonuniform.

The volumetric magnetic field measured by three loops oriented in perpendicular directions was used to derive the current density and electromagnetic part of $\vec{E}(r,z)$. These 3D measurements demonstrate and confirm azimuthal symmetry in a cylindrical stove top ICP, symmetries that previously were assumed to apply. Plasma current peaks slightly inwards underneath the antenna, and the peak current density propagates downward. The fact that the current does not penetrate vertically downward in a straight line is due to a nonuniform conductivity. The computed power $P = \vec{J} \cdot \vec{E}$ from probe measurements accounts for 80% of the

generator power. Negative power deposition inside the volume indicates an inertial component of the electron current, and this is further supported by conductivity calculations.

These measurements, and accompanying modeling, have contributed to quantifying physical phenomena necessary to understand fundamental plasma transport in ICP chambers. The measurements here may also contribute to understanding the electron kinetics of other applications such as electric propulsion and the temporal behavior of the electromagnetics in magnetic nozzles [34]. The simultaneous, multi-dimensional, and time-dependent measurements of nearly all pertinent plasma properties have enabled confirmation and clarification of the global mode of operation of ICPs of industrial interest.

3.3 Investigating Mode Transitions in Pulsed Inductively Coupled Plasmas[§]

3.3.1 Introduction

The combined impedance of the plasma reactor and the plasma in low pressure plasma processing for microelectronics fabrication, using both capacitively and inductively coupled plasmas (ICPs), is typically non-linear [35,36]. Common combined impedances can range from 100's of mΩ to 100's of Ω and up to kilo-ohms of reactance. These conditions make it difficult to deliver power to the plasma from conventional power supplies and transmission lines that typically have fixed impedances of 50-75 Ω. The electric field reflection coefficient, Γ_R, is the electric field reflected from the plasma reactor relative to the electric field delivered by the power supply through a transmission line (typically a coaxial cable) to the plasma reactor. The reflection results from the output impedance of the power supply and transmission line differing from that

[§]Results and portions of the text that appear in this section were previously published in the paper by C. Qu *et al.*, "Power matching to pulsed inductively coupled plasmas" J. Appl. Phys. **127**, 133302 (2020). [2]

of the plasma reactor,

$$\Gamma_R = \frac{Z_L - Z_0}{Z_L + Z_0} \tag{3.10}$$

where Z_L is the impedance of the load (in this case, the combined impedance of the plasma reactor and the plasma) and Z_o is the output impedance of the power supply and transmission line [37]. Since Z_L has reactive contributions, Γ_R typically has both real and imaginary components from which both the magnitude and relative phase of the forward and reflected waves can be determined. Typically only the magnitude of reflection $|\Gamma_R|$ is used to characterize matching efficiency.

The usual remedy to maximize power transfer to a plasma processing reactor (and minimize reflection) is to employ an impedance matching network (IMN) between the transmission line and plasma reactor [38–40]. The IMN usually contains reactance (capacitors and inductors) both in series and parallel to the load with the goal of making the input impedance to the IMN be the same as the power supply termination impedance and transmission line impedance. In doing so, the reflection coefficient is minimized. In practice impedance matching is complicated by both the non-linear characteristics of the plasma and the increasingly common use of multiple frequencies and pulsed power. Even if driven with a single frequency, the non-linear response of the plasma to that single frequency power will produce higher harmonics in current, thereby making reproducible impedance matching more challenging [41,42].

The use of pulsed power further complicates matching as the plasma contribution to Z_L can change by orders of magnitude during the pulsed cycle. For example, pulsed ICPs as used in microelectronics fabrication operate at pressures of tens of mTorr in attaching gas mixtures such as Ar/Cl_2 powered with radio frequency (RF) supplies of a few to tens of MHz. The pulsed repetition frequency (PRF), pulses per second, can be hundreds of Hz to tens of kHz. Duty cycle (DC), the fraction of time the power is applied per cycle, can be 10-50%. The end result is that

the electron density at the time the power is applied at the leading edge of the pulse can be as low as 10^8 cm^{-3} whereas later during the pulse, the electron density can exceed 10^{11} cm^{-3} [43,44]. These densities can increase across these three decades during a few to 10s or 100s of μs depending on the power delivery system and reactor design. The reactor contribution to Z_L for an ICP is typically dominated by the positive reactance of the inductance of the antenna, though the antenna will also have resistance.

Z_L for a pulsed ICP has additional dynamics due to the E-to-H (capacitive-to-inductive) transition that occurs during the transient in plasma density at the beginning of a pulsed period [3,45–48]. If the electron density at the beginning of a power pulse is too low, the electromagnetic skin depth, δ_P, may exceed the dimensions of the reactor which then makes inductive coupling of power from the antenna problematic. For these conditions, the antenna simply acts as an electrode which electrostatically and capacitively couples power into the plasma through the dielectric window between the antenna and the plasma [45]. This is the E-mode during which power can be dominantly coupled into the plasma by sheath oscillation (much like a capacitively coupled plasma) with power mainly deposited by ion acceleration from the plasma into the dielectric window under the antenna [48]. During the capacitive E-mode, the reactance of the plasma is negative. As the electron density increases, δ decreases which increases the fraction of power that is inductively coupled until the power is dominantly delivered by electron acceleration in the electromagnetic field within δ of the antenna. This is the H-mode during which the reactance of the plasma is positive. In practice there may be mixed-mode coupling, both E-mode and H-mode during quasi-steady state operation of the ICP [45,46]. The degree of E- and H-mode coupling depends on factors such as the voltage across the antenna, the proximity of antenna to the plasma, the shape of the antenna, gas pressure and composition, and the use of a Faraday shield between

the antenna and plasma [49].

The E-H transition in ICPs has been addressed both experimentally and theoretically [50–58]. When measuring the electron energy distribution (EED), Chung et.al. found that during E-mode, the EED evolves from bi-Maxwellian to Druyvestein-like structure when increasing pressure [59]. During the H-mode, having a significantly larger electron density with a higher rate of e-e collisions, the EED remains essentially as a Maxwellian. To smoothen the severity of the E-H transition, Singh et al. investigated use of a Faraday shield to minimize capacitive coupling from the antenna [49]. When using the Faraday shield, the plasma potential at low power was lower, indicating lower capacitive coupling while the electron density was lower. During H-mode, the antenna current and voltage decreased when using the Faraday shield. Had the plasma been operating purely in H-mode, there would not have been a decrease in current when using the Faraday shield, which then implies that even in H-mode, there was mixed E- and H-mode coupling.

Kempkes et al. investigate the effect of the power modulation on the E-H transition using rectangular and triangular power waveforms [60]. They found that even with smoothly varying power (triangular waveform) abrupt E-H transitions occurred. Kawamura et al. performed 2-dimensional (2D) simulations of E-H transitions in ICPs sustained in Cl_2 [61]. They found ionization instabilities and modulations in electron density attributed to rapid transitions between E- and H-modes.

The E-H transition often displays hysteresis behavior. The transition between the low E-mode electron density to the high H-mode electron density occurs at different powers if increasing power (occurs at a higher power) or decreasing power (occurs at a low power). The power deposition from both inductive and capacitive coupling was theoretically analyzed by Lee et al. [62], who found that the pressure and the dimensions of the reactor affected the power for the E-

H transition. The combined effects of electron density, collision frequency and skin depth of the electromagnetic wave contributes to nonlinear dependence of mode transition on operating conditions. The hysteresis of the E-H transition was experimentally investigated by Daltrini et al. [63]. They suggest that rather than being an intrinsic characteristic of the plasma, the hysteresis behavior can be affected by the power loss in the matching system, suggesting the need to include circuit analysis when investigating these transitions.

The E-to-H transition is another complicating factor in matching pulsed power to the ICP reactor. The change in Z_L due to the E-to-H transition in addition to the reduction in the resistance of the plasma is typically over shorter times than the components in the match box can be changed. The end result is that power delivery cannot be efficiently matched to the plasma reactor during the entire pulsed cycle. The values of components in the match box are typically chosen to match at a particular time during the pulsed cycle – this is called set-point matching. If the match is chosen early in the pulsed period, the E-mode may be emphasized while there is a mismatch during the latter part of the pulsed cycle. If the set-point is late during the pulse period, the E-mode may be suppressed but there is also a longer time to ramp up the plasma density when power is mismatched early in the pulse.

In this section, results from a computational investigation of the dynamics of power matching to pulsed ICPs of the type used in microelectronics processing (etching, deposition) are discussed. A model for the circuit and match box has been employed in a 2-dimensional simulation of the ICP. It was found that under perfect matching conditions, there is a smooth transition between the E- and H-modes, in contrast to several experimental results. This suggests that a sharp transition between modes is not a fundamental plasma transport issue, but rather may be related to power delivery. It was found that when using pulsed power, the power delivery is highly

dependent on the time during the pulse at which the set-point is matched. Matching early in the pulsed period leads to a faster re-ignition of the plasma, while emphasizing E-mode characteristics during the onset of the pulse. There is also poor matching during the H-mode. Matching later in the pulsed period leads to better power delivery overall, at the cost of longer ignition delay. The rapid application of power when operating in E-mode can launch electrostatic waves due to the need to establish a sheath to dissipate the applied voltage. The pulsed duty-cycle, matchbox parameters, and antenna shape play key roles in power matching inductively coupled plasmas.

The model used in this investigation is described in Sec. 3.3.2. Matching to pulsed ICPs with E-H transitions is discussed in Sec. 3.3.3. Concluding remarks are in Sec. 3.3.4.

3.3.2 Description of the Model

This computational investigation was performed using the Hybrid Plasma Equipment Model (HPEM) complemented by a model for the match box. The HPEM is discussed in detail in Chapter 2 and in [24], and so only a brief description will be provided here, including the unique aspects of the circuit calculation. The HPEM consists of modules that address different classes of physical phenomena and exchange information. In this case, we utilized three modules – the Electromagnetics Module (EMM), the Electron Energy Transport Module (EETM), and the Fluid-Kinetics Module (FKM). The frequency domain wave equation for the inductively coupled electric field is solved in the EMM. In this two-dimensional simulation, the current flowing in the antenna is in the azimuthal direction θ, producing components at the fundamental frequency of the magnetic field in the (r,z) (radius, height) directions and of the electric field, E_θ, in the θ direction. The conduction currents through each turn of the antenna that are used in the solution of the wave equation are provided by a circuit model, which also provides the fundamental frequency voltages on each turn of the antenna used in the FKM for the solution of Poisson's equation. Continuity,

momentum, and energy equations (a fluid representation) are solved in the FKM for all charged and neutral species coincident with the solution of Poisson's equation for the electrostatic potential, Φ. In this two-dimensional simulation, Φ is solved in the (r,z) plane, providing electrostatic field components E_r, E_z. Electron heating is provided by the harmonic inductively coupled fields E_θ from the EMM. All components of the electrostatic (E_r, E_z) and electromagnetic fields (B_r, B_z, E_θ) are used in the EETM to track the trajectory of secondary electrons from surfaces using Monte Carlo techniques. Complex conductivities are transferred back to the EMM to solve the wave equation. One sweep through the modules is called an iteration of the model.

The EMM contains a circuit model with which the power supply is interfaced to the plasma reactor. A schematic of the circuit representation of the match box, antenna, reactor, and plasma is in Figure 3-18. The antenna is represented as a discretized transmission line in the circuit model. The physical inductance of the antenna is determined by its overall diameter, height, number of turns, and thickness of the wire. This inductance is divided into 100 discrete series segments, each of which also has an appropriate fraction of the total resistance of the antenna. Each segment n of the transmission line contains a series impedance, Z_{Sn}, consisting of resistance (R_{An}) and physical inductance (L_{An}) of the antenna. Z_{Sn} also contains transformed values of resistance and inductance from the plasma [64]. The transformed impedance of the plasma, Z_T, is [65]:

$$Z_T = \left(\frac{\omega M}{Z_P}\right)^2 \left(-i\omega L_P + R_P\left(1 - i\frac{\omega}{\nu_m}\right)\right), \quad M^2 = k_A L_A L_P$$
$$Z_P^2 = \left(\omega L_P + \frac{\omega}{\nu_m} R_P\right)^2 + {R_P}^2 \tag{3.11}$$

where ω is the radian frequency of the applied power, L_A is the physical inductance of the coil, L_P is the inductance of the plasma, ν_m is the electron momentum transfer collision frequency, R_P is the plasma resistance, and k_A is the antenna transformer coupling coefficient. The effective plasma

resistance R_P is given by

$$R_P = \frac{\int \vec{j}_\theta \cdot \vec{E}_\theta \, d^3 r}{\left(\int \vec{j}_\theta \cdot d\vec{A} \right)^2} \tag{3.12}$$

where the numerator is the volume integrated inductively coupled power and the denominator is the area integrated azimuthal current. The consequences of skin depth and nonlinearities in the plasma are accounted for by the spatial dependence and phase differences between the current and the electric field. From each discrete segment of the transmission line representation of the antenna, a capacitance and series resistance is directed to ground, collectively represented by an impedance Z_{Cn}. The impedance Z_{Cn} represents the capacitive coupling from the antenna through the plasma to grounding. The reactance of Z_{Cn} consists dominantly of the series capacitances of the air gap between the antenna and the dielectric window of the ICP reactor, the window, and the plasma sheath at the surface of the window. The resistance of Z_{Cn} consists of the bulk plasma conducting capacitive current to ground. During execution of the FKM, the impedance of each element Z_{Cn} is determined as follows. For each turn k of the antenna, the voltage amplitude V_{ok} and phase ϕ_{vk} are determined from the circuit model. The voltage $V_k(t) = \mathrm{Re}\left(V_{ok} \exp\left(i\left(\omega t + \varphi_{Vk} \right) \right) \right) = V_{ok} \cos\left(\omega t + \varphi_{Vk} \right)$ is used as a boundary condition on the metal of the antenna for the solution of Poisson's equation in the FKM. Since the antenna is outside the plasma and not touching a conductive surface, the current flowing perpendicular to the surface of the antenna, that is the (r,z) components of current, is purely displacement current. The displacement current flowing out of each turn k of the antenna is computed as an integral over the surface of the antenna having normal $\hat{n}$,

$$I_k(t) = \int \varepsilon_0 \frac{d\left(\vec{E}(t) \cdot \hat{n} \right)}{dt} dA \tag{3.13}$$

where E is the electrostatic electric field produced by the solution of Poisson's equation and ε_k is the permittivity of the material in contact with the antenna. The resulting current is then Fourier analyzed to provide the amplitude I_{ok} and the phase ϕ_{Ik} of the current at the fundamental frequency ω.

The impedance Z_k is then given by

$$Z_k = \frac{V_{ok}}{I_{ok}} \exp\left(i\left(\varphi_{Vk} - \varphi_{Ik}\right)\right) \tag{3.14}$$

The real part of Z_k represents the dissipative resistance (or capacitive power deposition). The imaginary part of Z_k is the reactance. For purely H-mode operation, (ϕ_{vk}-ϕ_{Ik}) tends toward -90° resulting in negligible capacitive power deposition with Z_k being capacitively reactive (negative imaginary). With E-mode contributions, -90° < (ϕ_{vk}-ϕ_{Ik}) < 0, and there is a finite real resistive component. These values of Z_k are then distributed along the transmission line representing the antenna in the circuit model. That is, Z_{Cn} is then a fractional assignment of Z_k to those segments n of the antenna associated with turn k. In a similar way, the total capacitive power is the sum of the power dissipated by each turn of the antenna and is computed as a cycle average of:

$$P_c = \sum_k P_k = \sum_k \frac{1}{\tau_{rf}} \iint \varepsilon_0 V_k(t) \frac{d\left(\vec{E}(t)\cdot\hat{n}\right)}{dt} dA dt \tag{3.15}$$

The power delivered by the power supply is specified as a function of time. This power is delivered into a transmission line between the supply and the match box. Plasma conductivities, P_c and Z_k, are provided by the FKM. Using these values, the circuit equations representing the match box and plasma reactor are solved, which produces antenna currents that are then used in the solution of the wave equation to generate the amplitude $E_\theta(r,z)$ and phase $\phi(r,z)$ of the

azimuthal electric field. The solution of the circuit equations also produces P_A (resistive losses in the antenna coils), P_M (resistive losses in the match box), and Z_M (the input impedance to the matchbox). The power dissipated by inductive coupling in the plasma is:

$$P_I = \int \frac{1}{2} \sigma(\vec{r}) E_\theta^2(\vec{r}) d^3r \tag{3.16}$$

For the purposes of this study, we assumed that inductive power deposition in the plasma is collisional while acknowledging that at low pressures of interest, power deposition has non-local components. The methods described here are completely general and apply to the case of non-collisional heating where kinetic methods are used to derive P_I. With Z_M, we compute the reflection coefficient, Γ, for power delivered by the supply, P_S,

$$\Gamma = \frac{Z_M - Z_0}{Z_M + Z_0} \tag{3.17}$$

We ignored the consequences of the reflected power back to the power supply. In a fully self-consistent solution, we should have the total power dissipation in the system, P_T, as

$$P_T = \left(1 - |\Gamma|^2\right) P_S = P_M + P_A + P_I + P_C \tag{3.18}$$

where P_A is the resistive power dissipated in the antenna and P_M is the resistive power dissipated in the match box. This equality is typically not obtained. Recognizing that E_θ scales linearly with the antenna current and P_I scales with E_θ^2, the current flowing into the match box is renormalized so that the equality for P_T is obtained. With these renormalized values, the circuit and wave equations are again solved. The process is iterated several thousand times to convergence. At the end of this process, the final values of V_k, E_θ, and θ are returned to the FKM and EMM for the next iteration through the modules for time integration of the fluid equations for densities, momenta, and energy, typically for a duration of 100s of ns to 0.5 μs. During this time, amplitudes V_k and E_θ, and the phase θ are not changed.

For a perfect match of P_S to the plasma reactor, we must have $Z_M = Z_0$. For this architecture of the circuit, matching is produced by adjusting C_P and C_S such that $Re(Z_M) = Z_0$ and $Im(Z_M) = 0$. From a procedural perspective, these values can be searched for by varying C_P and C_S to minimize the value of Γ. For select circuit architectures, one can analytically compute Z_M based on the circuit values and solve for the values of C_P and C_S that produce the match ($Z_M = Z_0$). This method of the solution for C_P and C_S is called the perfect match values.

3.3.3 Matching to Pulsed ICPs with E-H Transitions

For computationally investigating the fundamental phenomena of E-H matching, we chose a simple ICP geometry and a relatively small chamber. This layout for an ICP reactor powered by a spiral planar antenna is a standard design used for plasma assisted semiconductor fabrication [35-37]. Industrial systems are typically larger to accommodate wafers up to 30 cm in diameter. Our choice of a smaller chamber for this investigation was based on wanting a fine enough mesh to capture the dynamics of the E-H transitions while also enabling computation of a sufficient number of pulsed periods to reach the quasi-steady stated. The details of our investigation are sensitive to the size and topology of the reactor. For example, antenna and chamber impedance are both functions of size and layout, which would affect the specific values of match box parameters, and necessitate a different termination impedance. The spacing of the antenna from the dielectric window affects capacitive coupling, as discussed below. Having said that, the systematic trends we discuss apply to more complex and larger reactors. For example, we have performed limited studies on industrial size ICP reactors [38] and the systematic trends we discuss here are essentially the same.

A schematic of the reactor is shown in Figure 3-19. The chamber has an internal diameter

of 22.5 cm, height (substrate to window) of 12 cm and is powered by a 3-turn antenna having radii of 2.5, 5.3 and 8.0 cm. The coils have thickness of 0.45 cm and height of 1.15 cm, and sit above the 0.8 cm thick quartz window ($\varepsilon/\varepsilon_0 = 4$) with an air gap of 0.4 cm. The total inductance of the antenna is $L_C = 0.95$ μH. The antenna-plasma coupling coefficient is $k_C = 0.75$. The entire inner surface of the window serves as gas inlet showerhead with the pump port occupying an annulus between 6.9 and 11.1 cm on the bottom of the chamber. A pressure sensor is located in the outer wall 2 cm above the pump port. All other surfaces are grounded metal.

Unless otherwise noted, the gas mixture is $Ar/Cl_2 = 65/35$ at a pressure of 25 mTorr. Ar/Cl_2 gas mixtures are commonly used for conductor etching. The gas inlet flowrate is 200 sccm. The outlet flow rate is adjusted so that the pressure at the sensor is 25 mTorr. As discussed below, our results are sensitive to the conductivity of the plasma at the start of the power pulse, and that conductivity is sensitive to gas mixture. When using pure Cl_2 plasmas, a thermal electron attaching gas, the system can transition to an ion-ion plasma during the afterglow with a negligible electron density. These conditions then require "re-ignition" of the plasma on every power pulse. Although this may in fact be the case for many industrial systems, the re-ignition requirement adds another constraint and complexity. We therefore chose a gas mixture for which there would be significant change in conductivity during the afterglow but not to the degree that re-ignition is required.

The reaction mechanism is the same as discussed in [66]. An important point for the study is that Cl_2 is a thermal electron attaching gas for which the rate coefficient for dissociative electron attachment increases with decreasing electron temperature, T_e. So, for otherwise the same conditions, rates of attachment are small when power is applied during a pulse and T_e is large. Rates of attachment are large when the power is off and T_e is small.

The fixed circuit elements are coil resistance $R_C = 0.1$ Ω, termination impedances $C_T = 100$

nF and L_T = 5 nH, and inductance on match box L_P = 100 nH. The internal resistance of the match box was neglected by setting $R_M = 10^{-6}$ Ω so that P_M is negligible. This allows for the independent study of impedance matching impact on plasma transients. In practice, matching network impedances can have 100s to 1000s of mΩ of real resistance, and consume a significant amount of power delivered by the supply. Typically, these dissipative losses are accounted for in the series elements, where the larger dissipative components tend to reside, and where the current through the elements tends to be higher, as opposed to the shunt components. The inner coil of the antenna was connected to the match box, and the outer coil of the antenna was connected to ground through the series termination components C_T and L_T.

3.3.3.a. Continuous Power Baseline

With the base case values for circuit and operating conditions, the continuous wave (CW) characteristics of the ICP reactor were first investigated as a function of power delivered from the supply. Using perfect match values for C_P and C_S, Γ = 0, and $P_S = P_T$. The electron density, inductive power and capacitive power are shown in Figure 3-20 for a total power deposition of 5 W and 200 W. Note that the capacitive power deposition plotted is actually the time average of the capacitive and resistive (bulk) power deposition. The calculation of local power deposition of $P = \vec{j} \cdot \vec{E}$ is unable to distinguish between the capacitive and resistive heating. Given the spatial distribution and the negative sign of the reactance of Z_k, the capacitive power is clearly dominated by sheath heating at higher total power.

For 5 W, the voltages on the coils (inner to outer) are 147 V, 112 V and 44 V. The total capacitive power is 3.19 W (63.8% of the total), inductive power is 0.86 W (17.2 %), and resistive antenna losses 0.95 W (19%), a power division that indicates E-mode operation. On a relative basis, antenna losses are larger at lower total power due to the higher relative antenna current

required to sustain the plasma. The capacitive component includes contributions from both ion and electron acceleration by the sheath and bulk Joule heating. With the largest voltage and capacitive current from the inner coil, the capacitive heating is maximum under that coil (3.8 mW/cm^3) adjacent to the dielectric with resistive current flowing through the plasma to produce Joule heating of 0.7 mW/cm^3 in the center of the plasma. Sheath heating also occurs along the metal boundaries. With the peak electron density of 6×10^8 cm^{-3}, inductive power deposition extends to the middle of the reactor (electric field skin depth $\delta = 7.4$ cm) with a maximum value of 3 mW/cm^3. The voltages on the 3 coils of the antenna are nearly in phase. However, with different voltage amplitudes and different adjacent sheath thickness, particularly with respect to ground, there is some recirculation of current between the antenna coils that produces a net negative power deposition in the upper outer radius of the reactor.

For 200 W total power, the voltages on the coils (inner to outer) are 334 V, 276 V and 112 V. The total capacitive power is 9.7 W (4.8% of the total), inductive power is 188.2 W (94.1%), and resistive antenna losses 2.1 W (1.1%), a power division that indicates H-mode. With a higher electron density (peak 6.8×10^{10} cm^{-3}) the plasma is more conductive and capacitive heating is largely limited to the periphery of the reactor. The higher plasma density also reduces the electric field skin depth to $\delta = 0.7$ cm.

The capacitive power has a cycled averaged layer of negative power deposition parallel to the dielectric window, in addition to that in the upper right corner, that was not observed at lower power. At the high power, the electron flux directed towards the dielectric is dominated by the ambipolar flux originating from the electron sources produced by inductive coupling. The electron ambipolar flux is retarded by the ambipolar electric field that points from the center of the plasma towards boundaries. This is the same direction as the electric field that produces electron heating

due to expansion of the capacitive sheath under the window. During expansion of the capacitive sheath, power is expended in slowing the ambipolar driven electron flux in addition to accelerating electrons out of the sheath region. This negative power deposition is not observed at the lower power in the absence of the large ambipolar electron flux produced by inductive coupling.

The division of power deposition between capacitive and inductive; and average electron density are shown in Figure 3-21a for P_T = 5-200 W for perfect match conditions and continuous power. The values of C_P and C_S to obtain perfect matches and ionization efficiency are shown in Figure 3-21b. (Ionization efficiency is average plasma density divided by power deposition in the plasma, and is a relative measure of efficiency.) These results are typical of the E-H transition. At low power deposition, the electron density is low, the skin depth is large and sheath is thick. The low electron density and large skin depth reduces (on a relative basis) the inductive power deposition and the thick sheath (on a relative basis) increases the capacitive power deposition. The thicker sheaths produce a larger sheath velocity, and capacitive power deposition scales with the square of the sheath speed. As noted above, for P_T = 5 W, 77% of the power is capacitive and 11% is inductive. The power dissipation by the coil is about 12%. With increasing power deposition, the electron density increases, skin depth decreases and sheath thickness shrinks, all of which contribute to lower capacitive power deposition and higher inductive power deposition. We do not observe a sharp, step-function increase in electron density that can be identified as the E-H transition. The power at which the E-H transition occurs is then somewhat a qualitative judgement. The fraction of power dissipated by inductive coupling exceeds 50% at P_T = 25 W, and exceed 90% at P_T = 140 W. To achieve the perfect match, the values of the matching elements C_P decreases by about 20% and C_S increases by a factor of 2.5.

Over the range of P_T = 5-200 W, the average electron density increases from 2.8×10^8 cm^{-3}

to 2.3×10^{10} cm^{-3}, a factor of nearly 100 increase, for P_T increasing by a factor of 40. A portion of the increase in electron density results from an increase in ionization efficiency, plotted here as the total electron density divided by the total power deposition in the plasma. This efficiency increases by a factor of nearly 3. At low P_T, the fraction of power dissipated by resistive coil and capacitive heating is large. No ionization occurs from coil heating, and the efficiency of ionization by capacitive coupling is low due to ion acceleration in the sheaths, characteristic of the E-mode. The efficiency remains relatively constant until the H-mode begins, at which time the efficiency increases. At high power deposition, a true H-mode occurs, as the majority of power is dissipated by electron heating in the bulk which is intrinsically more efficient at producing ionization.

With there always being a perfect match when changing P_S, there is a relatively smooth transition from dominantly E-mode to dominantly H-mode with increasing power. To obtain this perfect match with increasing power, the value of C_S smoothly increases (33 pF to 155 pF) and C_P smoothly decreases (267 pF to 168 pF). Experimentally, it is often observed that there is a rapid, almost impulsive, increase in electron density with a rapid switch between E-mode and H-mode when a critical power is delivered from the supply. Based on fundamental plasma transport, there is no requirement for such a sharp transition to occur.

In practice, the transition in apparent ionization efficiency may be exacerbated by the difficulty in matching between the E-mode and H-mode. If the circuit is better able to match to the H-mode (positive reactance) than E-mode (negative reactance), then the ionization efficiency will make a rapid and impulsive increase when the H-mode begins to dominate. There may also be heating of electrical components that can change their impedance. Another factor that may influence the apparent ionization efficiency is changes in plasma conditions due to the power deposition. For example, when operating at constant pressure, higher power deposition produces

more gas heating which reduces the gas density and so reduces the electron collision frequency. In chemically active mixtures, more power deposition produces more dissociation and so there are different species with which electrons collide.

To demonstrate these possibilities, two parameterizations were performed. In the first, a parameterization over power (P_T = 5-200 W) was conducted with the match box settings chosen to provide a perfect match at 150 W (C_P = 162 pF, C_S = 135 pF) which then produces mismatches at other powers. The resulting ionization efficiency is shown in Figure 3-22. For these conditions the circuit is mismatched at lower powers, producing a large reflection coefficient, and a corresponding low ionization efficiency. With power increasing towards 150 W, the reflection coefficient decreases, H-mode begins to dominate and so the ionization efficiency increases.

In the results shown in Figure 3-21, the length of time for the simulation was deliberately chosen to be long enough so that the plasma properties came into a quasi-steady state; while being short enough that there was no significant dissociation of the feedstock gases and gas temperature excursions were not significantly different. These conditions correspond to a short residence time of the gas in the plasma, τ_{res}. In this way, a side-by-side comparison of different powers could be performed without the complication of the impact of changing gas temperatures, gas densities and gas compositions on matching. In actual practice, when changing power one does have these complications of gas heating producing rarefaction and different degrees of dissociation of the gas. The parameterization in Figure 3-21 was repeated when computing for a sufficient time that all plasma properties including gas temperature and composition come into a steady state. This would correspond to at large τ_{res}. With the large τ_{res}, for P_T = 5 W, the average gas temperature was T_g = 330 K (for a wall temperature of 325 K) and fractional dissociation of Cl_2 was 1.3%. For P_T = 200 W, T_g = 635 K and fractional dissociation was 27%. The resulting ionization efficiency, also

shown in Figure 3-22, increases by a factor of 4.5 from low to high power. The majority of this increase in efficiency results from the decrease in Cl_2 mole fraction (due to dissociation) and decreases in gas density (gas heating), which then decreases the rate of attachment. These results emphasize the difficulty of performing side-by-side comparisons of E-H behavior when changes in power deposition also change fundamental properties of the plasma in addition to electron density.

3.3.4 Set Point Matching to ICPs

In this section, we discuss matching of a pulsed ICP for the same operating conditions as the CW studies (Ar/Cl_2 = 65/35, 25 mTorr). The standard conditions for pulsed ICP operation were a pulse repetition rate (PRF) of 13.3 kHz (period of 75 μs), duty cycle 35% and forward power delivered from the supply during the power on period of P_S = 250 W. As a base case, we used perfect match conditions by instantly adjusting C_P and C_S to produce Γ=0 throughout the pulse period. The maximum in the plasma potential, the electron density, Cl^- density and positive ion densities are shown in Figure 3-23a during the power pulse and immediate afterglow. The modes of power dissipation are shown in Figure 3-23b. The resistive and reactive components of the impedance Z_L, and perfect matching values of C_P and C_S are shown in Figure 3-23c.

At the beginning of the power pulse, the plasma conditions are essentially an ion-ion plasma where the positive ion density is nearly equal to the negative ion density, $[M^+] \approx [Cl^-] = 4.5 \times 10^{10}$ cm^{-3}. The small electron density at the beginning of the pulse, $n_e = 2 \times 10^8$ cm^{-3} results from Cl_2 being a thermally attaching gas, which reduces the electron density during the afterglow through dissociative electron attachment producing Cl^-. During the power pulse the negative ion density $[Cl^-]$ is relatively constant. With the electron temperature $T_e \approx 2.5 – 3.5$ eV during the power pulse, the thermal dissociative attachments rates are small compared to ionization rates.

The increase in electron density is nearly matched by the increase in positive ion density.

With this low initial electron density, power is initially capacitively coupled. During the first 3 μs, the capacitive power exceeds that of the inductive power and the plasma operates in E-mode. The E-mode is additionally indicated by the oscillation in the plasma potential, Φ_P, with an amplitude as large as 450 V in the same manner as a capacitively coupled plasma. The maximum antenna voltage amplitude (inner turn) is 1080 V. There is some oscillation in the voltage amplitude on the antenna, which is due to the rapid increase in electron density, which changes the plasma impedance sufficiently to lower the antenna voltage, which lowers the electron density which induces an increase antenna voltage. This oscillation is likely magnified by the iterative numerical technique used to link the plasma portion of the simulation with the circuit.

As the electron density increases, the electromagnetic skin depth decreases and sheath under the coils thins, the fraction of capacitive power dissipation decreases. By 5 μs, the electron density is high enough, 1×10^{10} cm^{-3}, and skin depth short enough that power is dominantly inductively coupled and the plasma operates dominantly in H-mode. Due to the proximity of the antenna to the dielectric window, approximately 5% of the total power continues to be capacitively coupled even during H-mode. This is similar to CW operation. In the quasi-steady state during the pulse, the proportion of capacitively coupled power decreases by a few watts but is otherwise nearly constant. Upon termination of the power, both the capacitive and inductive power decrease in nearly the same proportion while remaining in H-mode. The power decreases quickly enough that the electron density does not appreciably change, and so the skin depth remains short enough to allow H-mode operation. This represents a hysteresis-type of behavior. The plasma remains in H-mode during decreasing power at the same power deposition that corresponded to E-mode during the beginning of the pulse.

As the plasma density increases at the leading edge of the power pulse and operation transitions to H-mode, the oscillation in Φ_P decreases to an amplitude of 10-20 V. This modulation of Φ_P is on top of the quasi-dc plasma potential of about 20 V. This dc value of plasma potential results from the ambipolar nature of the plasma transport ($T_e > T_{ion}$, $m_e < m_{ion}$). An indication of purely H-mode operation without capacitive coupling would be quasi-dc plasma potential without significant oscillation. Since the power deposition resulting from E_θ and electron heating are harmonic, there can be harmonic oscillation in T_e and so there would be some small oscillation in Φ_P even in purely H-mode. However, in this case, the majority of oscillation in Φ_P is due to capacitive coupling.

With perfect match conditions, C_P decreases during the power pulse from 290 pF to 160 pF, accompanied by an increase in C_S from 50 pF to 160 pF. The combined load impedance, Z_L (which includes the antenna coil and plasma) has a positive reactance due to the inductance of the antenna. This reactance decreases during the plasma pulse in response to the capacitive component of the antenna current through the plasma. The resistive component increases in response to the power deposition in the plasma.

The impedance of the variable capacitors in RF matching networks is typically changed by a mechanical process (e.g., changing the overlap area between two plates). The speed of the mechanical movement of these variable capacitor systems is largely determined by the driving motors, with end-to-end movement typically on the order of hundreds to thousands of milliseconds. Impedance control algorithms working in conjunction with these mechanical limits will typically produce a tuning transient with a comparable characteristic time. With plasma-induced impedance transients having time scales that are orders of magnitude shorter that what can be achieved by these mechanically driven system, it is typically not possible to change the

values of C_S and C_P rapidly enough to achieve a perfect match throughout the power pulse. Typically set-point matching is employed in which values of C_S and C_P are chosen to minimize Γ at a particular instant during the power pulse. We investigated the consequences of set-point matching. Computationally, this was achieved by selecting values at given times for C_S and C_P from the perfect-match case. For example, plasma reactor properties are shown in Figure 3-24 when values for C_S and C_P were chosen for set-point matches from early to late in the pulse. These times, relative to the start of the power pulse, were 1.5, 3.25, 7 and 21 μs. Since the progression of the plasma prior to the time of the matching point is not exactly the same as for the case with perfect matching, the reflection coefficient at the match point may not be exactly zero.

For a matching point of t_M = 1.5 μs, the reactor properties at the match point are a forward power of 82.7 W and Γ=0.013. The maximum capacitive power of 62.2 W occurs at the match point. The resistive power is 9.6 W and inductive power is 8.5 W, indicating operation in the E-mode. (Note that Γ is finite due to the plasma properties being different than for the perfect match that provided the values of C_S and C_P.) As the plasma density begins to increase, the E-mode dissipates and H-mode begins. With this increase in plasma density, the values of C_S and C_P required to achieve a match deviate from the set-point values. The reflection coefficient then monotonically increases until the H-mode is fully established at t = 6-7 μs, after which Γ is relative constant at 0.5. At the end of the pulse, the electron density is 1.15×10^{10} cm^{-3} compared to the perfect match value of 2.4×10^{10} cm^{-3}. This decrease in electron density is due to the reduction in power deposition following that Γ = 0.5.

As t_M increases, the peak capacitive power decreases, there is a larger delay in the onset of inductive power deposition and the maximum inductive power increases, as shown in Figure 3-25. The delay in onset of the H-mode results from there being less ionization produced during

the E-mode. With a larger t_M, there is a larger mismatch that produces a larger Γ early in the pulse, which reduces power deposition and ionization. For example, for t_M = 2.5 μs, the peak capacitive power of P_C = 70 W occurs at 2 μs when the inductive power is P_I = 41 W and Γ=0.03. Just prior to the end of the maximum delivered power at 23 μs, P_C = 9.3 W, P_I = 108 and Γ=0.46. For t_M = 21 μs, the peak capacitive power of P_C = 21 W occurs at 2.6 μs when the inductive power is P_I < 1 W and Γ = 0.76. At 23 μs, P_C = 12 W, P_I = 235 and Γ < 0.001. For t_M > 7 μs, the set-point values of C_S and C_P are well matched to the H-mode, and so Γ < 0.01 for t > 10-15 μs for the remainder of the power pulse. The electron density at the end of the power pulse is nearly that of the perfect match.

3.3.4.a. Matching for Different Duty Cycles

Matching early during the power pulse is sensitive to the electron density at the onset of power, and this is particularly problematic in thermally attaching gas mixtures such as Ar/Cl_2. During the inter-pulse period, the electron temperature decreases, which increases the rate of attachment and increases electron loss. The lower electron density at the onset of power for the next pulse makes the system appear to be more capacitive to the matching network. This sensitivity can be demonstrated by varying the duty cycle of the pulsed power.

For the same peak power during the power pulse, a shorter duty cycle translates to lower average power deposition and less fractional dissociation of Cl_2. The larger density of Cl_2 results in more attachment during a longer inter-pulse period, resulting in a lower initial electron density at the beginning of the next pulse. For example, the electron density and plasma potential Φ_P during the pulsed period are shown in Figure 3-26 for different duty cycles (25% to 65%). Note that the time scales are shifted in Figure 3-26b by increments of 10 ns. in order to show the plasma

potentials more clearly. The electron density at the beginning of the pulsed cycle is 1×10^8 cm^{-3} for a duty cycle of 25% and 1×10^9 cm^{-3} for a duty cycle of 65%. The magnitude of oscillation of Φ_P indicates the severity of capacitive coupling.

When varying duty cycle, the same set-point match is used corresponding to t_M = 7 μs and a duty cycle of 35%. Duty cycles shorter than 35% produce smaller initial electron densities. However, the system already starts in the E-mode, and so there is little change in the oscillation of the Φ_P. Increasing duty cycle increases the initial electron density, which enables some H-mode coupling early during the pulse. This H-mode coupled power reduces the power coupled into the E-mode which then reduces the oscillation in Φ_P. This reduction in capacitive power does come at a cost of increasing the reflection coefficient. At the time of the nominal match conditions for a duty cycle of 35%, the reflection coefficient at t = 7 μs is Γ = 0.01. For a 25% duty cycle, is Γ = 0.02 (still small) whereas for a duty cycle of 65%, the reflection coefficient is Γ = 0.08.

3.3.4.b. Ion Energy Distributions on Dielectric Window During E-mode

A consequence of early matches that allow significant power into the E-mode is large ion fluxes incident onto the dielectric window while there is still significant oscillation in the plasma potential. These conditions produce energetic ions onto the window which can result in sputtering and erosion. For example, the ion energy distributions (IEDs) incident onto the window with a duty cycle of 25% are shown in Figure 3-27. At the beginning of the pulse, the plasma potential rises from about 10 V when the sheath beneath the window is thick. The resulting IED is largely thermal with an extended tail. As the plasma density increases, which thins the sheath, and plasma potential increases with the capacitive coupling, the IED extends to as high as 200 eV, for a plasma potential peaking at 375 V during the E-mode. The maximum in the IED does not directly

correspond to the maximum in plasma potential due to the locations within the thick sheath that ions are produced and due to the transient charging of the dielectric. As the H-mode is established and the plasma potential decreases, the maximum energy of the IEDs also begins to decrease. By the end of the power pulse, the peak of the IED occurs at 18 eV. In the afterglow where the plasma potential decreases below 10 V, the peak in the IED occurs at 5 eV.

When matching early in the pulse, capacitive coupling is emphasized, there is more power dissipated in ion acceleration and there are more energetic of ions incident on all inside surfaces of the reactor, and on the window in particular. These energetic ions could be potentially damaging to the window and other surfaces. These energetic fluxes are then another consideration in choosing an early match. Having said that, even with t_M being small, the E-mode dissipates before the plasma density reaches its maximum value. As such, the flux of energetic ions produced by capacitive coupling may not be large, thereby reducing the likelihood for damage.

3.3.4.c. Antenna Placement

The capacitance between the antenna and the plasma consists of at least three series components – the capacitance of the air gap between the antenna and window, the capacitance of the window and the capacitance of the sheath. In practice, the capacitance of the antenna-window gap is more variable than that of the window. For example, placement of the antenna after maintenance must be extremely precise to replicate the capacitance of the antenna-window gap. The variable capacitance of the antenna-window gap then translates into variability in the plasma.

To demonstrate the sensitivity of matching pulsed ICPs to the placement of the antenna, the following procedure was followed. The gap between the bottom of the flat antenna and the window was varied from $d = 0$ (in contact with the window) to 8.2 mm. For each gap, calculations were first performed with perfect matching. The values of C_P and C_S for each gap size were then

chosen as the perfect match values at t_M = 20 μs. The simulations for gaps sizes of d = 0 – 8.2 mm were then repeated with these fixed values C_P and C_S. The resulting capacitive power P_C and inductive power P_I during the power pulse are shown in Figure 3-28.

With increasing values of the gap, d, the series capacitance of the gap-window pair decreases. With d = 0 (maximum capacitance), E-mode power is dissipated at the leading edge of the power pulse. This capacitive power produces ionization, which then enables the inductive power to begin earlier leading to an onset of the H-mode. As the gap size d increases, the series capacitance also decreases. This decrease in capacitance of the gap limits current, then decreases the E-mode power at the leading edge of the power pulse and increases the reflection coefficient. With lower E-mode power deposition, the increase in electron density is slower. This slow rate of increase in electron density means that more time is required for the electron density to increase to the point that inductive power dominates and the H-mode begins. During the quasi-steady state portion of the pulse where the circuit is well matched to the plasma, the small values of d allow for larger capacitive power deposition, which then reduces the inductive power deposition.

For all values of the antenna-window gap, there is nearly a perfect match late in the pulse – all forward power is dissipated either in the plasma or in the antenna. However, the manner of deposition, fraction of power dissipated as P_C and P_I, is sensitive to the height of the antenna above the window. In results not shown here, there is a similar dependence on the flatness of the antenna. An antenna that may be mounted at a small angle with respect to the window can be perfectly matched, however the fractions of power dissipated as P_C and P_I are a function of the orientation of the antenna. Reproducing performance when replacing an antenna requires both ensuring a match and also reproducing the fraction of power separately dissipated as P_C and P_I. In the case of pulsed plasmas, the power waveforms should also be reproduced.

3.3.4.d. Electrostatic Waves at Onset of E-mode

For thermally attaching gas mixtures, as in the Ar/Cl_2 mixture used in this investigation, the onset of the E-mode at the leading edge of the power pulse produces an impulsive perturbation to the plasma that generates electrostatic waves. At the beginning of the power pulse, the plasma is essentially an ion-ion plasma with the positive and negative ion densities greatly exceeding the electron density. For example, for the base-case at the end of the afterglow, the positive and negative ion densities adjacent to the window are essentially equal at 3.4×10^{10} cm^{-3} whereas the electron density is 2×10^{8} cm^{-3}. The charge density (units of elementary charge, $q = 1.6 \times 10^{-19}$ C) is -2.5×10^{4} cm^{-3}. There essentially is no sheath as both positive ions have largely thermalized to the same temperature during the afterglow and the ions have nearly the same mobilities.

When the power is applied, a large voltage is generated across the antenna and capacitive coupling to the plasma occurs. The response of the plasma is to attempt to form a sheath to dissipate the capacitive voltage drop. During the first few RF cycles, the sheath is most easily formed by accelerating electrons adjacent to the dielectric into the plasma to produce a positive space charge region. During these first few cycles, the far more numerous positive and negative ions are nearly immobile and do not significantly separate to produce the charge density needed to create the sheath. With each half cycle, electrons are expelled from and attracted to the dielectric. The end result is launching of electrostatic waves into the ion-ion plasma.

The electron and charge density are shown in Figure 3-29 during the first 6 cycles of the power pulse for the base-case with a match point of $t_M = 1.5$ μs. These conditions were chosen to emphasize the initial E-mode coupling for demonstration purposes. The electron density is shown as color-contours. The charge density ρ (units of elementary charge/cm^3) is shown with numerical labels with a line for $\rho = 0$ indicating a sign change in local charge density. As the power increases

at the beginning of the pulse, the voltage on the coils increases with each successive RF cycle. Electrons adjacent to all surfaces in contact with the plasma are expelled into the plasma in an attempt to form a sheath. This expulsion is most pronounced under the window adjacent to the coils but also occurs along the side walls and substrate. The expulsion first produces an electrostatic wave having $\rho < 0$. Since the electron density is 2-orders of magnitude less than the positive and negative ions, this wave can propagate through the plasma without significantly perturbing the overall charge balance. The anodic half of the cycle launches a positive electrostatic wave. With each cycle, a new wave is launched, producing layers of alternating charge propagating into the plasma. The waves appear to emanate from under the inner and middle coils where the voltage is the largest and the largest amount of charge must be expelled to form the sheath.

In time, the electron density increases and positive space charge sheath is formed under the dielectric while the initial electrostatic waves collisionally dissipate. The waves soon become chaotic (not shown) due to the disparity in coil voltages, each with slightly different phases. The oscillating voltage on each coil launches what appears to be a cylindrically expanding electrostatic wave of different magnitude. These individually expanding waves are close enough in phase that their sum appears to have only a slight curvature. However, on successive pulses, the disparity in voltage between the coils increases, producing expanding waves which intersect and become chaotic before dissipating.

These electrostatic waves will occur in any highly electronegative system in which a sharply rising negative voltage is applied to a surface. For example, in pulsed plasma doping (P^2LAD) systems, a multi-kV negative, nearly step-function pulse is applied to the substrate to accelerate ions into the wafer for shallow junction implantation [67]. Simulations of P^2LAD

systems predict similar electrostatic waves, albeit more soliton-like due to the single transient voltage [68]. In the ICP systems discussed here, the amplitude and duration of the waves are small, and so the effects on processing (e.g., etch rate or uniformity) are likely not large. Their effects on diagnostics and sensors could be problematic, particularly if the waves are not reproducible pulse-to-pulse.

3.3.5 Concluding Remarks

Power dissipation in CW and pulsed electronegative inductively coupled plasmas sustained in Ar/Cl_2 mixtures and the consequences of impedance matching were computationally investigated. During a pulsed cycle, the modulation in electron density determines the mode of power deposition – capacitive (E-mode) at low electron density where the electromagnetic skin depth is large and inductive (H-mode) at high electron density where the electromagnetic skin is small. Even with perfect power transfer from the supply to the plasma, there is a natural E-H mode transition that occurs at the beginning of the pulsed period.

When considering matching, the increase in plasma density and spatial distribution of the plasma changes the impedance of the plasma reactor during pulsing, which then changes the matching requirements to deliver power from the supply. Since components in the match box are typically fixed during the pulsed period, components in the match box are set to match the plasma at particular time during the pulsed period. If the match box is chosen to match the impedance at the onset of the power pulse, E-mode is emphasized and a fast plasma ignition is expected due to efficient power deposition during power ramp-up. However, the tradeoff is a high power reflection coefficient during the majority of the power-on period as a consequence of the impedance mismatch to the H-mode plasma. In contrast, matching the higher power H-mode produces more net power transfer from the supply to the plasma, but delays the onset of the H-mode due to the

mismatch of power in the E-mode.

Duty cycle during pulsing has important implications on power matching. In general, the shorter the duty cycle, the lower the electron density at the beginning of the next power pulse. This is particularly the case for mixtures using gases that attach thermal electrons, such as Cl_2. The lower electron density with a shorter duty cycle promotes E-mode operation at the start of the next power pulse.

In highly electronegative gases, the plasma at the beginning of the power pulse is essentially an ion-ion plasma. The impulsive application of power in a purely an E-mode results in launching of electrostatic waves during the leading RF cycles. The response of the plasma to the high voltage on the antenna during the E-mode is to form a sheath. The electrostatic waves result from the expulsion of the remaining electrons from nearby surfaces in an attempt to form a sheath. These waves are more severe when the afterglow is long and electronegativity is high.

Capacitance is largely a function of geometry and so the capacitance between the antenna and the plasma is a function of the gap length between the coil and dielectric window. A big gap produces a small capacitance and decreases the capacitive power that can be deposited during the E-mode. That decrease in power reduces the initial increase in electron density which then delays the onset of the H-mode.

Power matching to transient systems will be challenging so long as the matching requires mechanical changes in components. These mechanical changes simply cannot be made rapidly enough to track the change in plasma impedance. As pulsed plasmas become even more prevalent in semiconductor manufacturing, advanced matching techniques, such as frequency tuning, will be required to minimize mode transitions and instabilities.

3.4 Figures

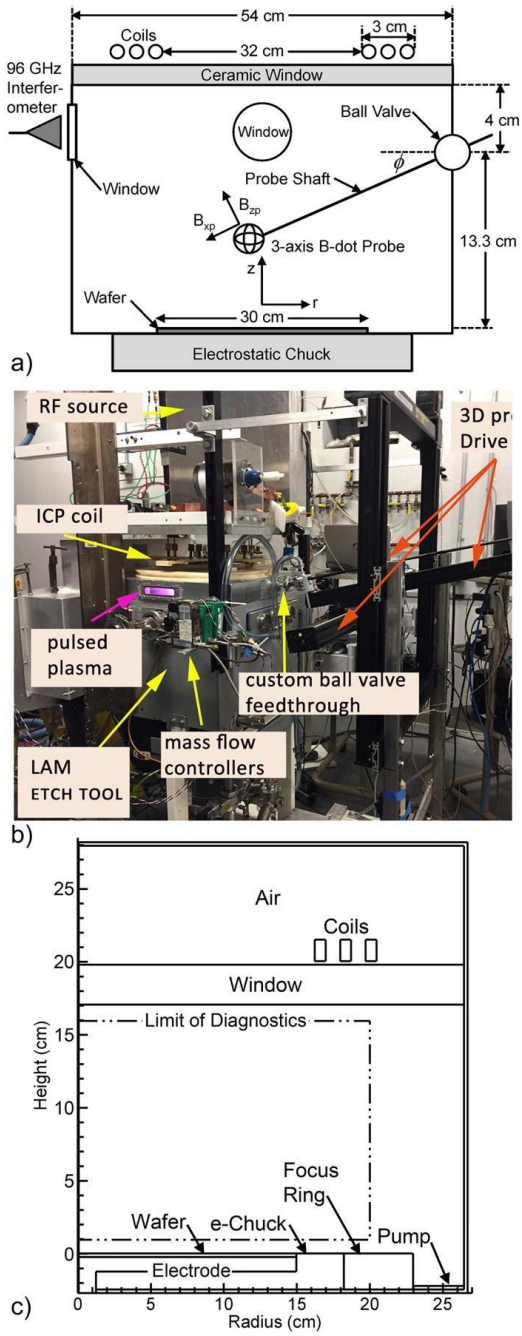

Figure 3-1. Overview of the experimental setup and model geometry. (a) Schematic of the experimental chamber (not to scale). The probe shaft is capable of rotation and translation with the ball valve as the pivot point so that the probe tip can move in three dimensions inside the chamber. Here, B_{xp} is the x component of the magnetic field in the frame of the probe. (b) Photo of the experimental apparatus. When in use, the interferometer is positioned at the rectangular window through which the "pulsed plasma" is viewed. This window is 90° from the ball valve port. (c) Schematic of the cylindrically symmetric computational geometry.

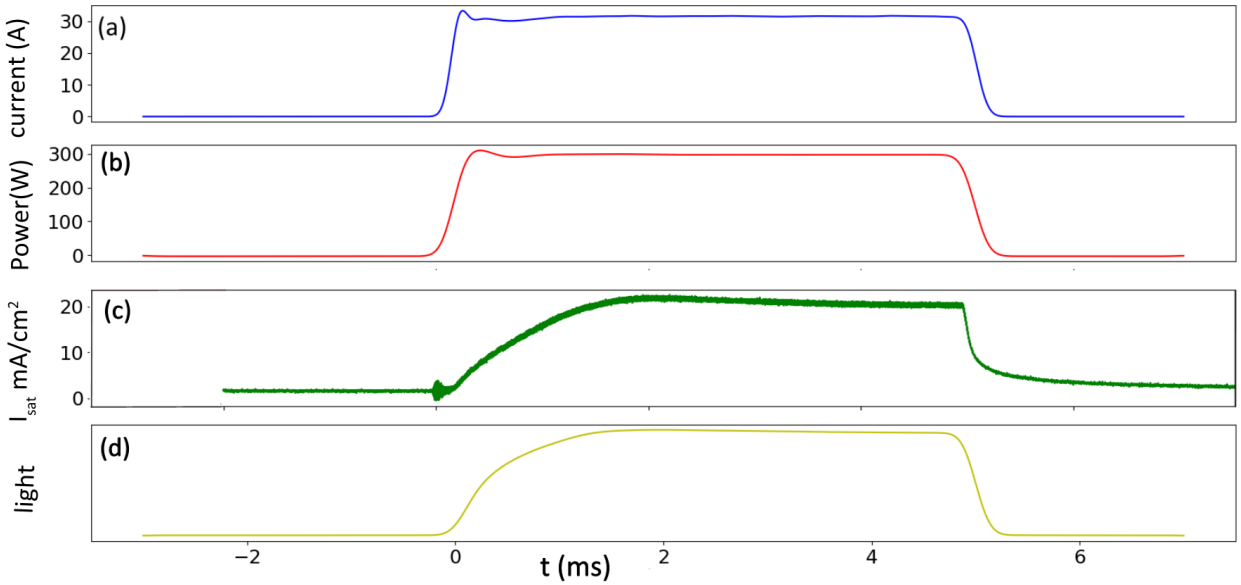

Figure 3-2. Plasma properties during a pulsed cycle. (a) Current in the 3-turn RF antenna. (b) Power from the RF generator. (c) Ion saturation current measured by the Langmuir probe located at z = 12 cm, r = 0 cm. (d) Photodiode signal measuring optical emission positioned at a window facing the center of the plasma. The slower decay in I_{sat} compared to the optical signal indicates more rapid thermalization of the electron temperature than losses of ions by diffusion to the walls.

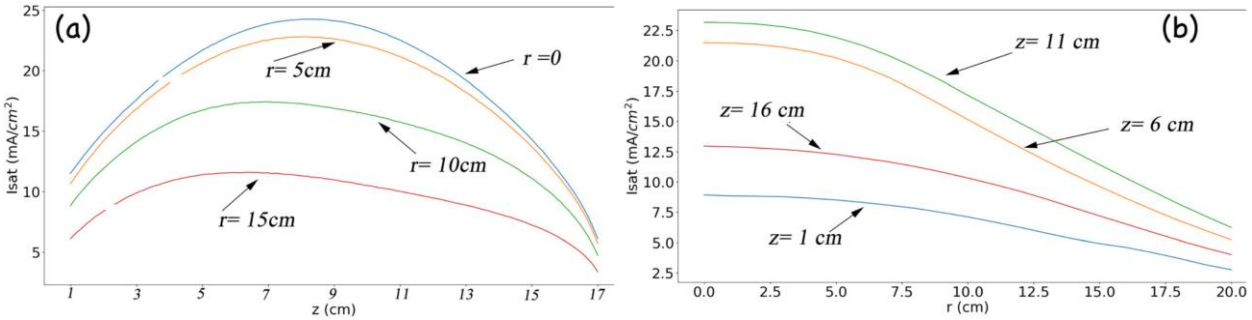

Figure 3-3. Measurements of plasma density for Ar 10 mTorr and a generator power of 300 W. (a) Density as a function of height above the wafer at different radii. (b) Density as a function of radius at different heights.

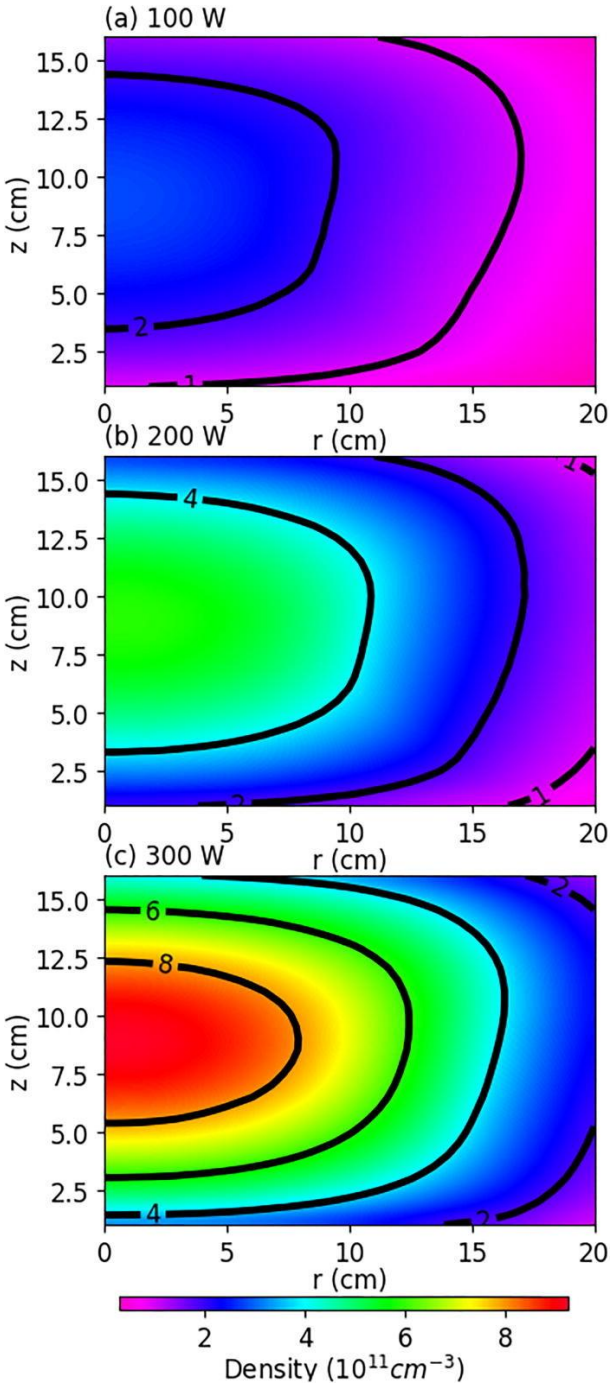

Figure 3-4. Electron density in an (r,z) plane for three generator powers. The density is evaluated from the interferometer calibrated I_{sat} assuming uniform $T_e = 3$ eV. The edge of the wafer is at r = 15 cm.

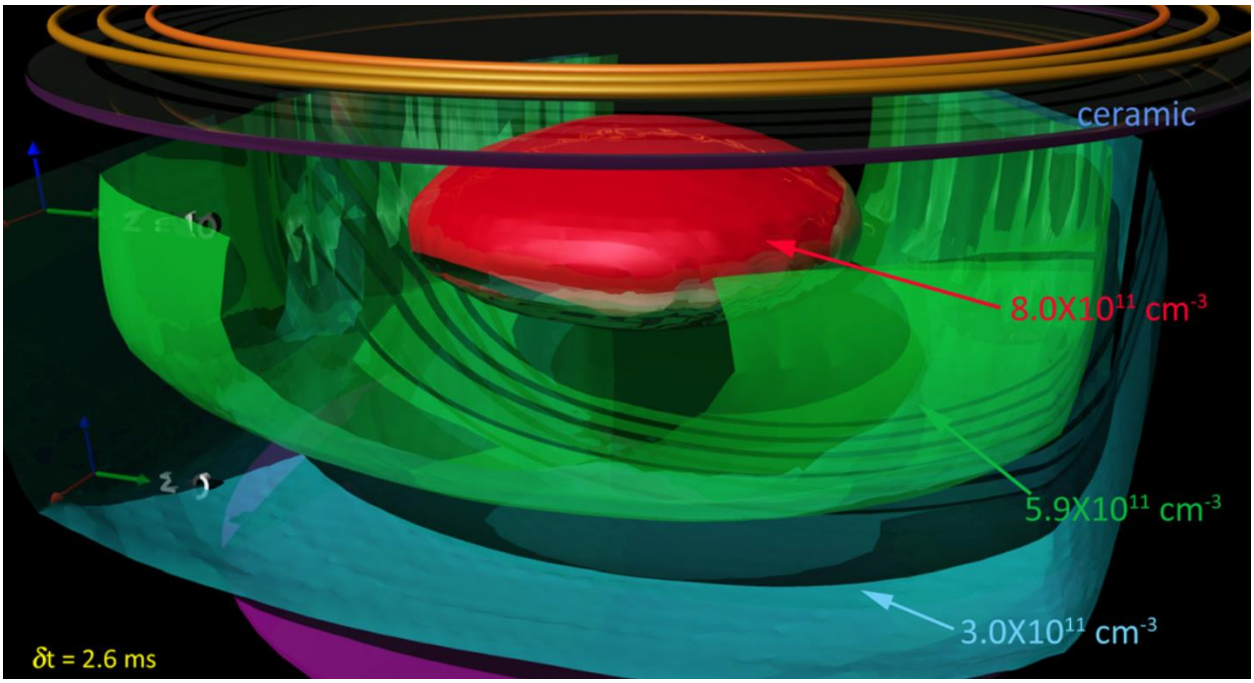

Figure 3-5. 3D measurement of electron density derived from ion saturation current shown as nested isosurfaces. Data were acquired 2.6 ms into the 300 W power pulse. The wafer is drawn to scale to guide the eye. The maximum electron density at this time (red surface in center) is 8×10^{11} cm^{-3}.

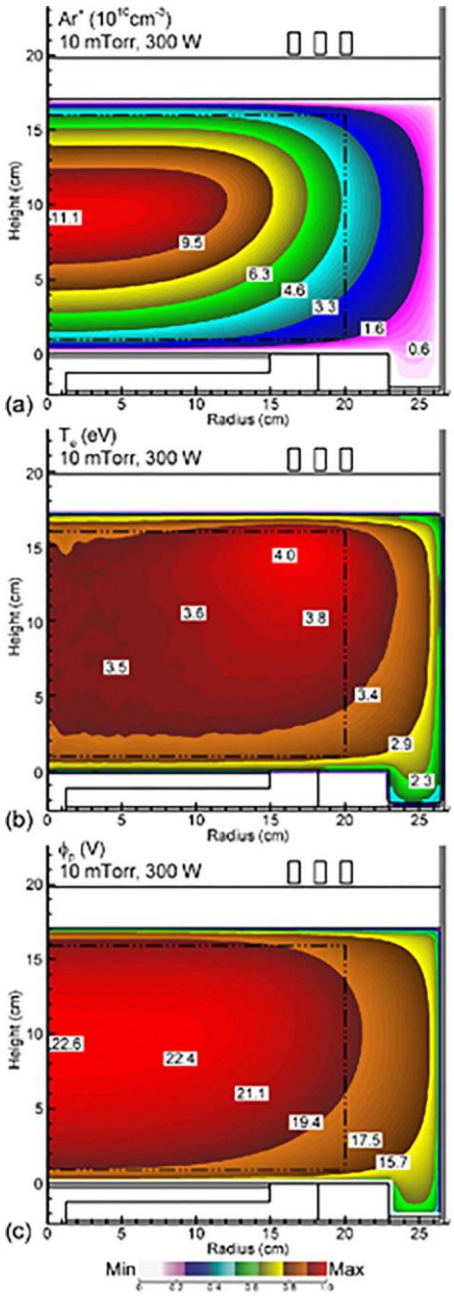

Figure 3-6. Plasma properties predicted by the model for the ICP sustained in argon at 10 mTorr and 300 W. (a) Ar^+ density (contours have units of 10^{10} cm^{-3}), (b) electron temperature, and (c) plasma potential. The dashed-dotted line represents the experimental viewing area.

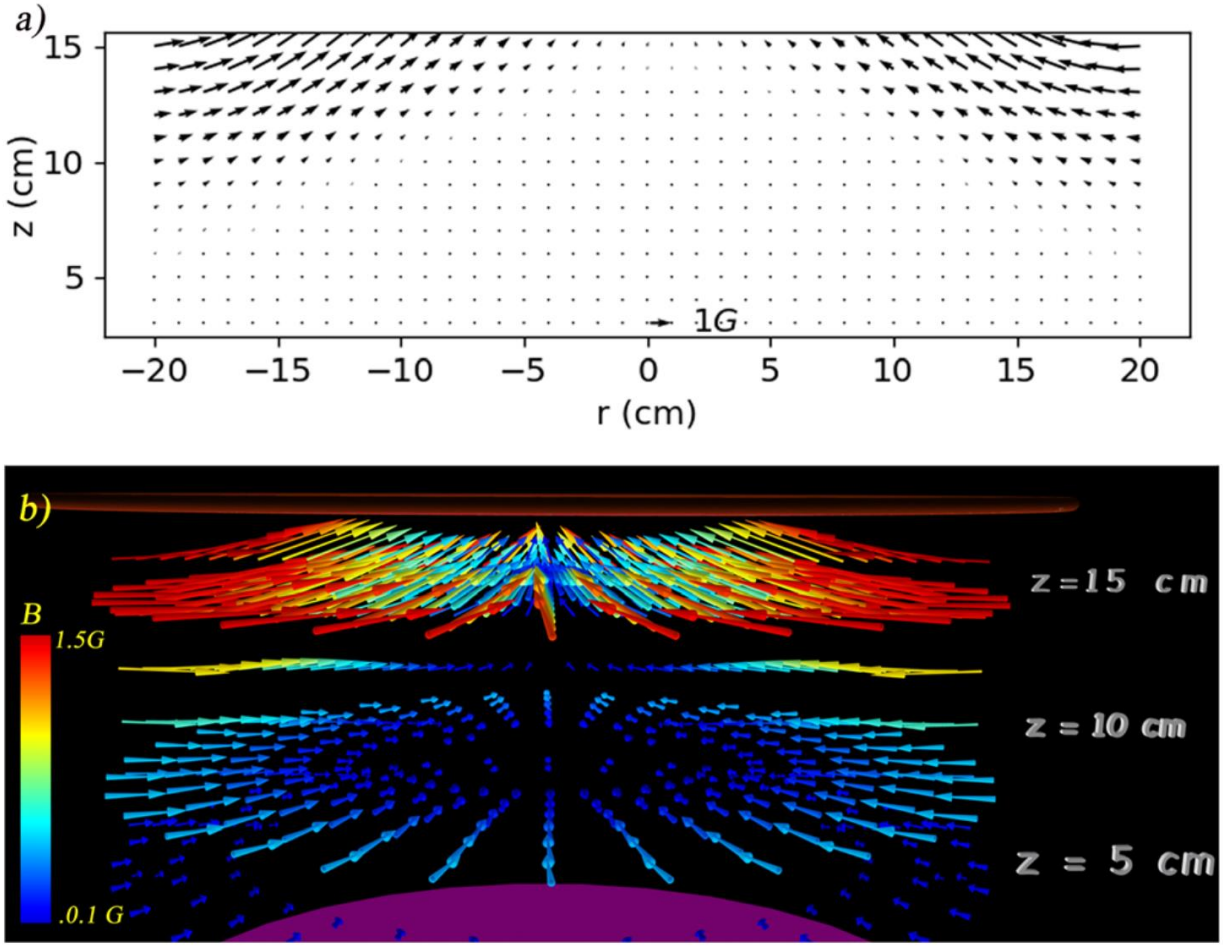

Figure 3-7. Measured magnetic field during the steady state plasma. (a) 2D vector plot ($r \leq 20$ cm). The fiducial arrow represents a magnitude of 1 G. Note the coil is centered at 18 cm. (b) 3D vector plot ($r \leq 15$ cm). The coils and wafer are drawn to scale to aid the eye. The largest arrow drawn in red is $|B| = 1.5$ G.

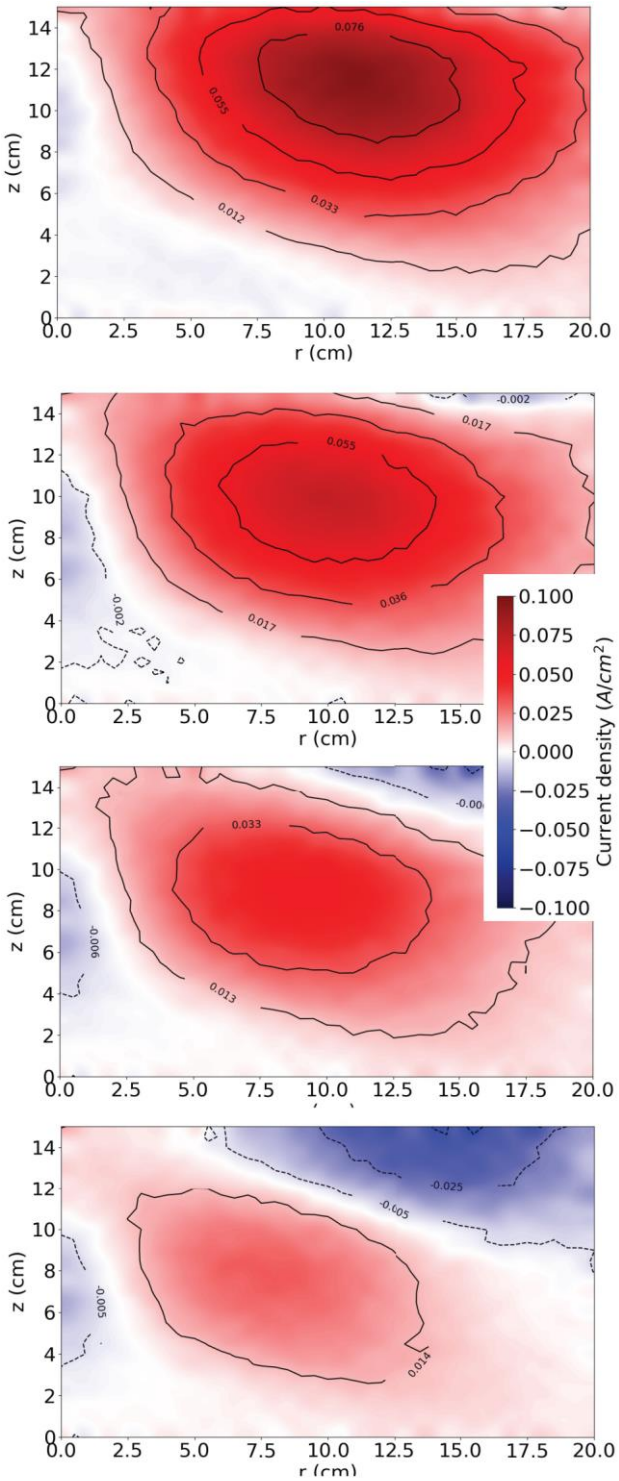

Figure 3-8. Plasma current density (A/cm^2) in a vertical (r,z) plane at four times during the RF cycle. The Ar pressure is 10 mTorr, and the generator power is 300 W. The images from top to bottom are at times, t/T_{rf} = 0, 0.13, 0.19, and 0.25, respectively. The internal current forms below the coil (z = 21.6 cm and r = 16.0 cm) and moves down and toward the center of the chamber. The reverse current (shown in blue) forms as the current in the center fades away.

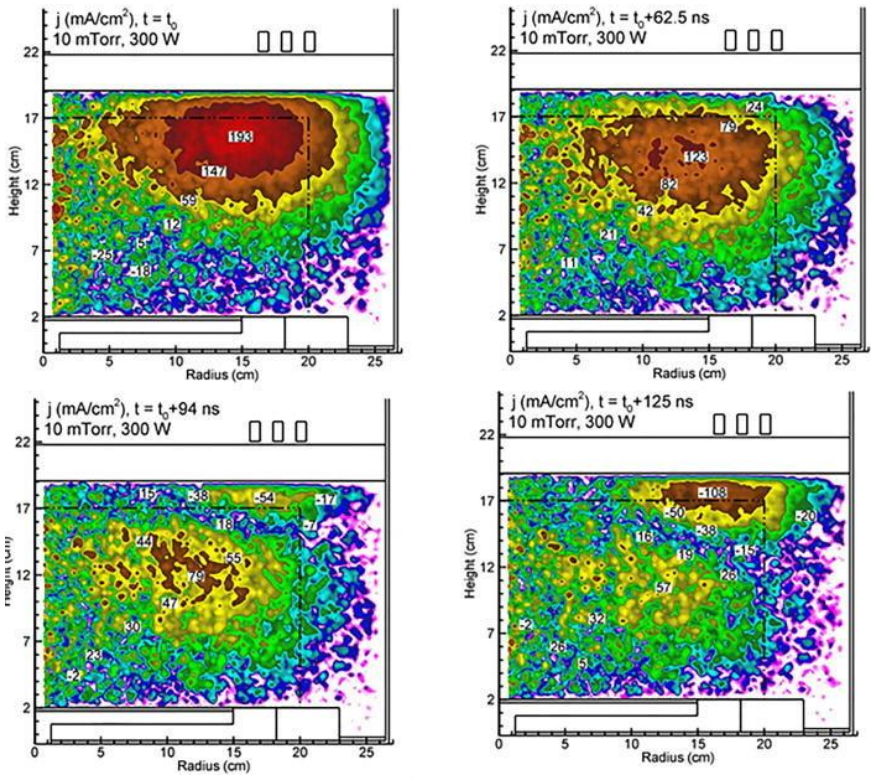

Figure 3-9. Plasma current density in (mA/cm^2) plotted on a log scale at four times during the RF cycle, aligning with the experimental results in Figure 3-8. The Ar pressure is 10 mTorr, and the power deposited in the plasma is 300 W. The images are (a) t_0, (b) t_0 + 62.5 ns, (c) t_0 + 93.75 ns, and (d) t_0 + 125 ns. The dashed-dotted line is the experimental view.

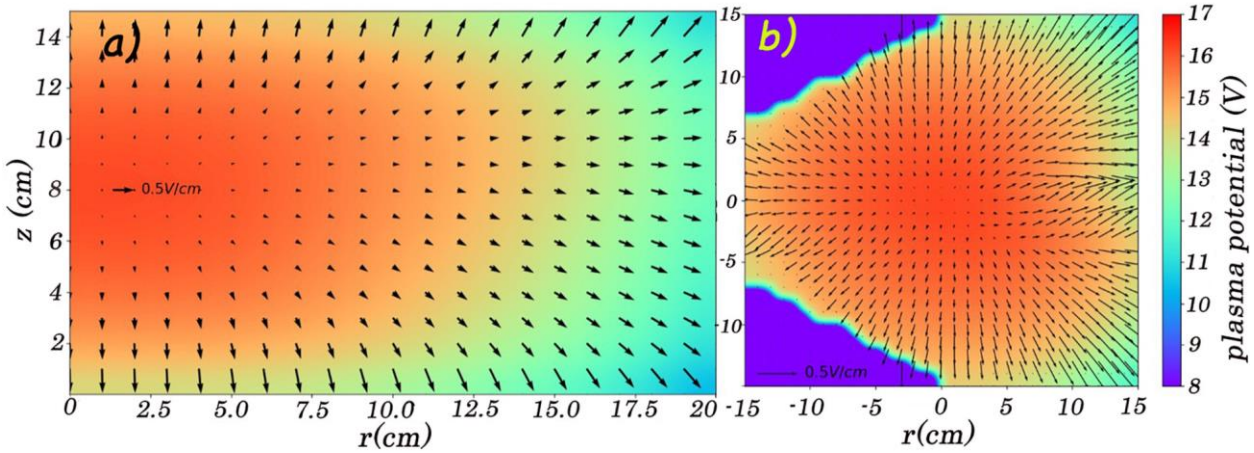

Figure 3-10. Space charge electric field vectors calculated from measurements of the plasma potential (shown as flood contours) obtained by using an emissive probe for an Ar pressure of 10 mTorr and a generator power of 300 W. (a) E_x-E_z vectors on a plane centered at $y = 0$ where $r = 0$ corresponds to the center of the wafer. (b). E_x-E_y vectors on a plane-parallel to the wafer at an intermediate height, $z = 8$ cm.

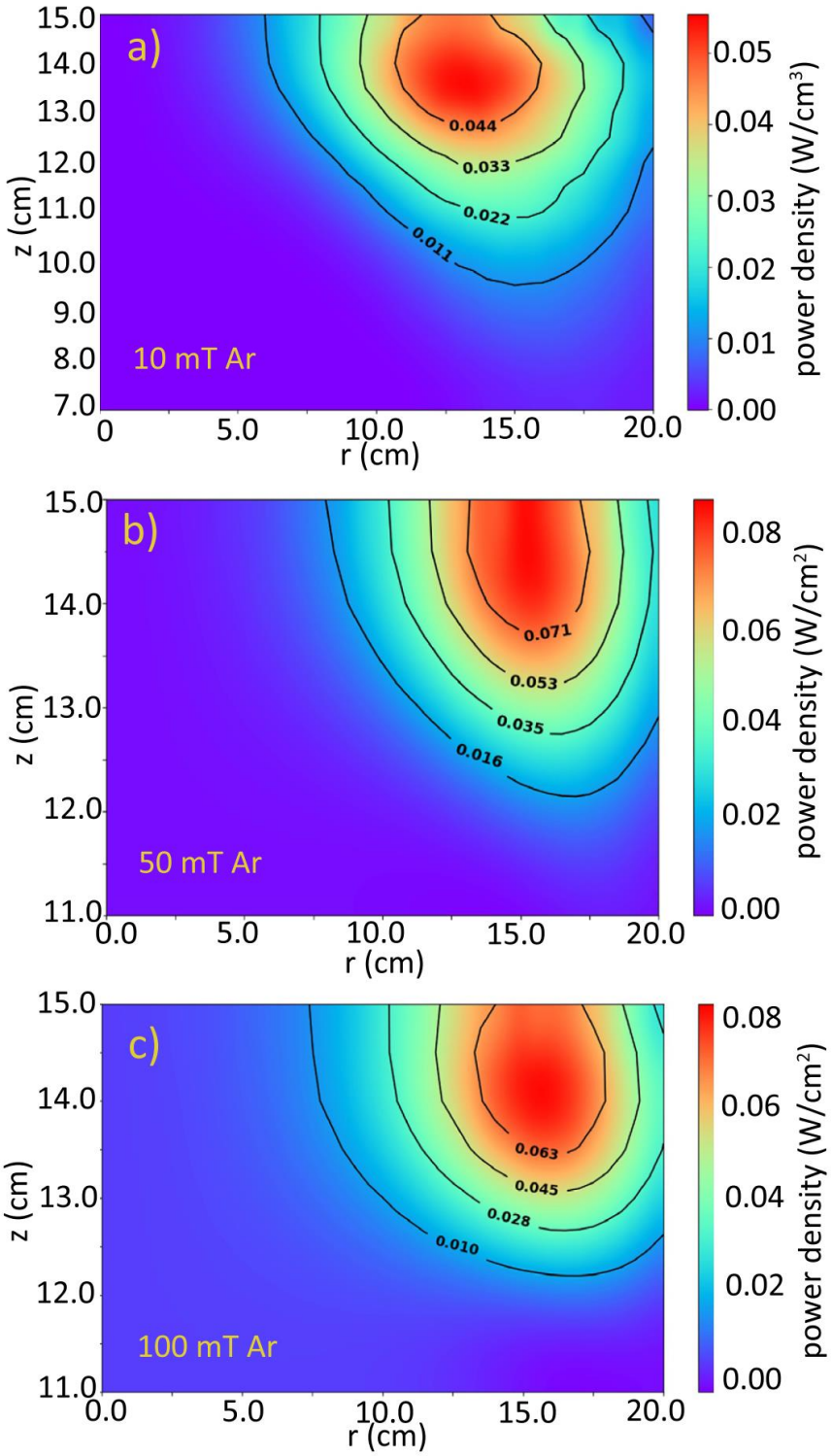

Figure 3-11. Time averaged power density (W/cm^3) calculated from $P=J\rightarrow\cdot E\rightarrow$P=J→·E→ for Argon pressures of (a) 10 mTorr (with an extended vertical axis), (b) 50 mTorr, and (c) 100 mTorr. The powers are plotted as a function of height and radius with the center of the wafer at r = 0. The mean coil radius is 18 cm, and the bulk of the power absorption occurs a few centimeters inward in radius and just under the top ceramic.

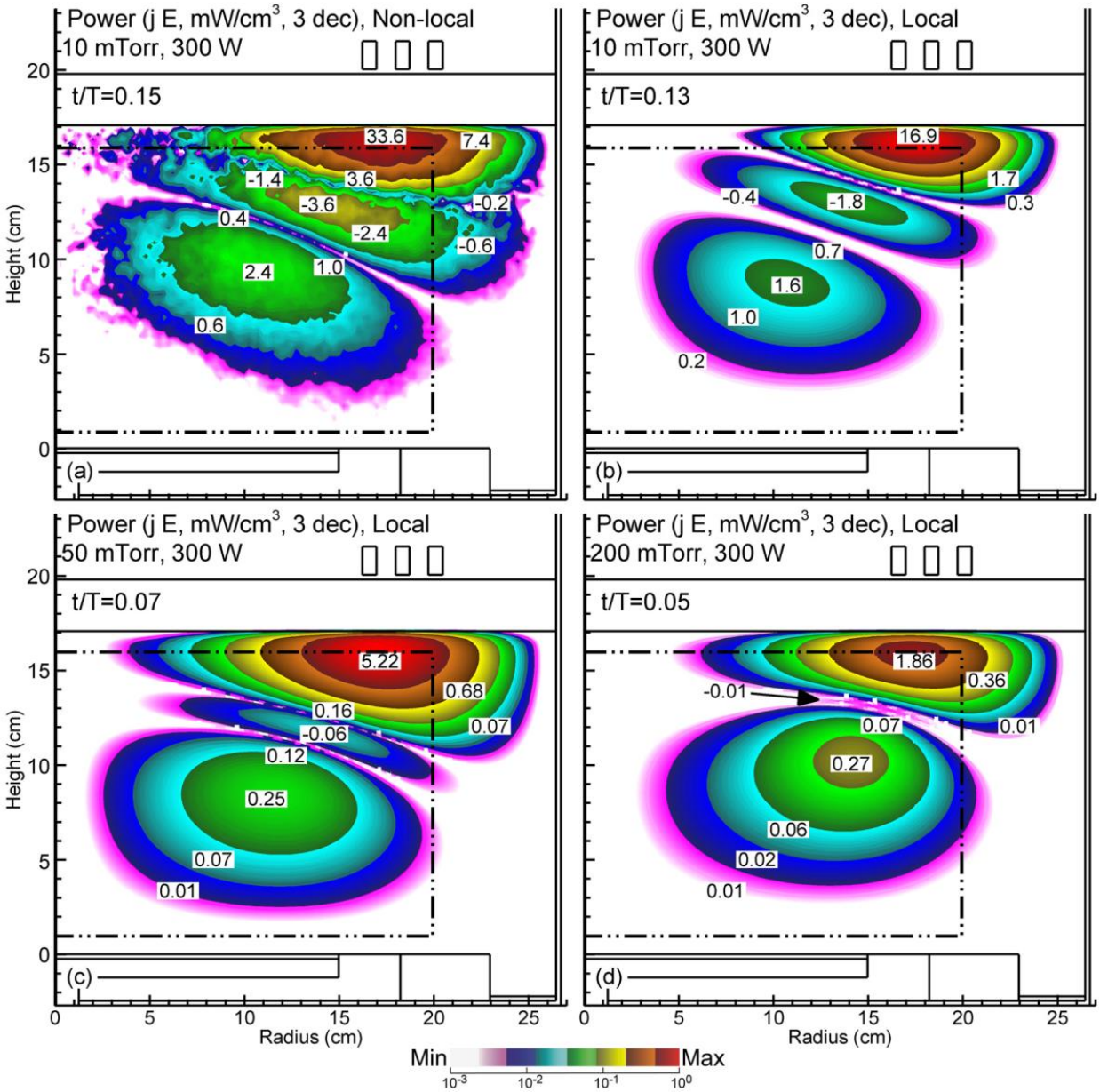

Figure 3-12. Computed instantaneous power deposition for argon with 300 W of in-plasma power with the time in each cycle indicated. Color contours are power deposition plotted over 3 decades. Contour labels are in units of mW/cm^3. (a) 10 mTorr with nonlocal power deposition computed with the eMCS. (b) 10 mTorr, (c) 50 mTorr, and (d) 200 mTorr with local power deposition. The dotted-dashed line is the experimental view.

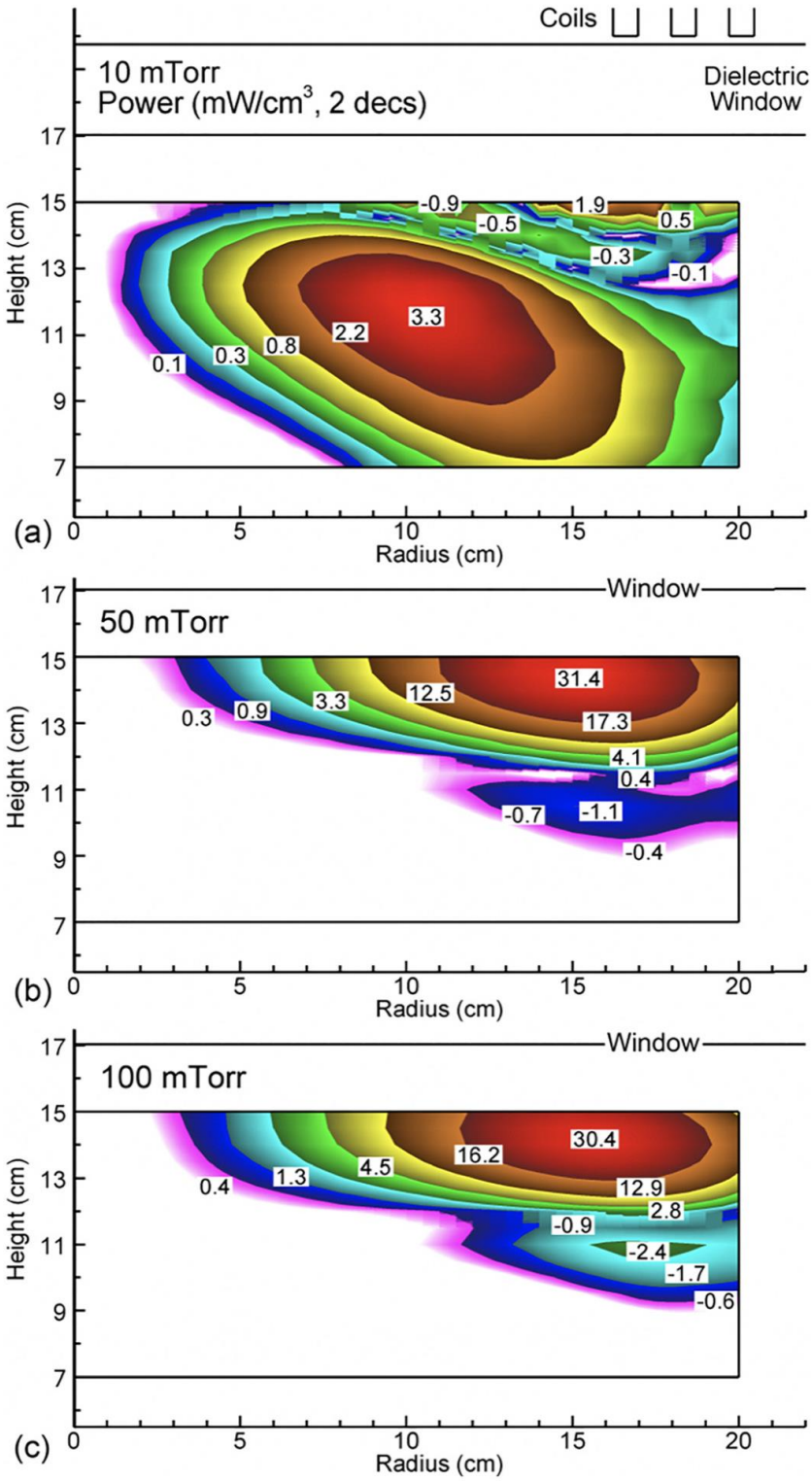

Figure 3-13. Experimentally measured instantaneous power deposition (mW/cm^3) for argon at pressures of (a) 10 mTorr, (b) 50 mTorr, and (c) 100 mTorr at 300 W. The phase of each image was chosen to emphasize the negative power deposition.

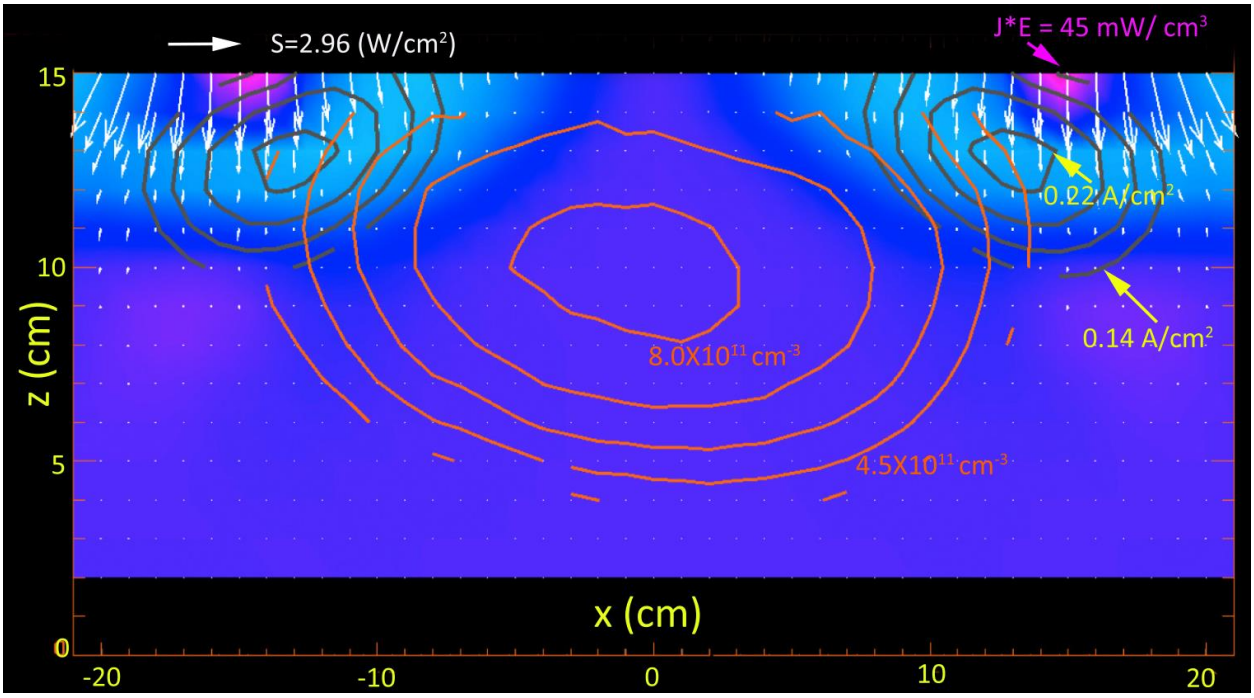

Figure 3-14. Contours of plasma density (red), shaded contours of plasma dissipation. The Poynting flux is shown as white arrows and the plasma current density as brown contours. Values are shown for an Ar pressure of 10 mTorr and a generator power of 300 W.

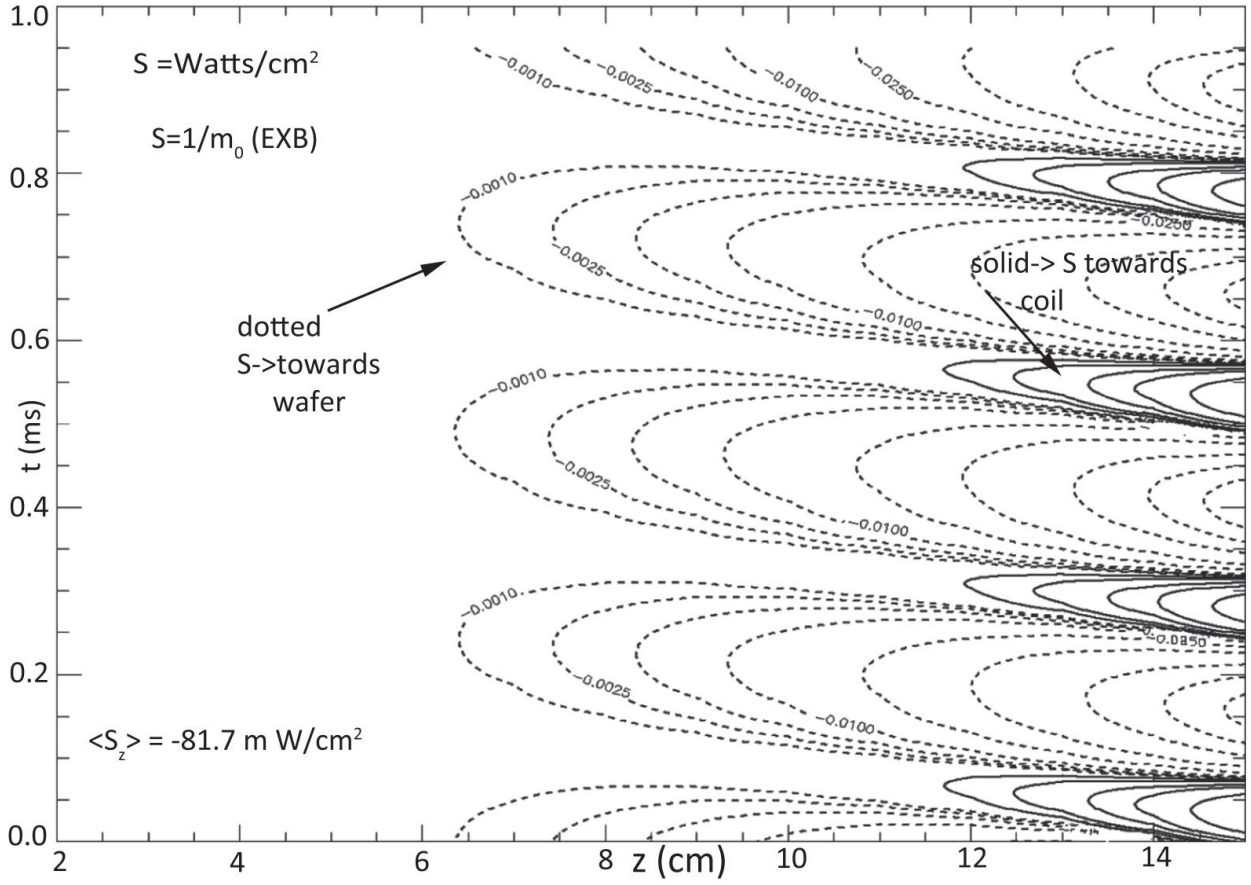

Figure 3-15. Poynting flux averaged over radius and as a function of height above the wafer. The solid curves depict power directed upwards toward the coil. The dashed lines indicate power flow toward the wafer. In the presence of plasma, they are not symmetric. The downward Poynting flux averaged over the two cycles shown is −81.7 mW/cm^2. The largest downward flux is −496 mW/cm^2, and the largest upward Poynting flux is 201.0 mW/cm^2.

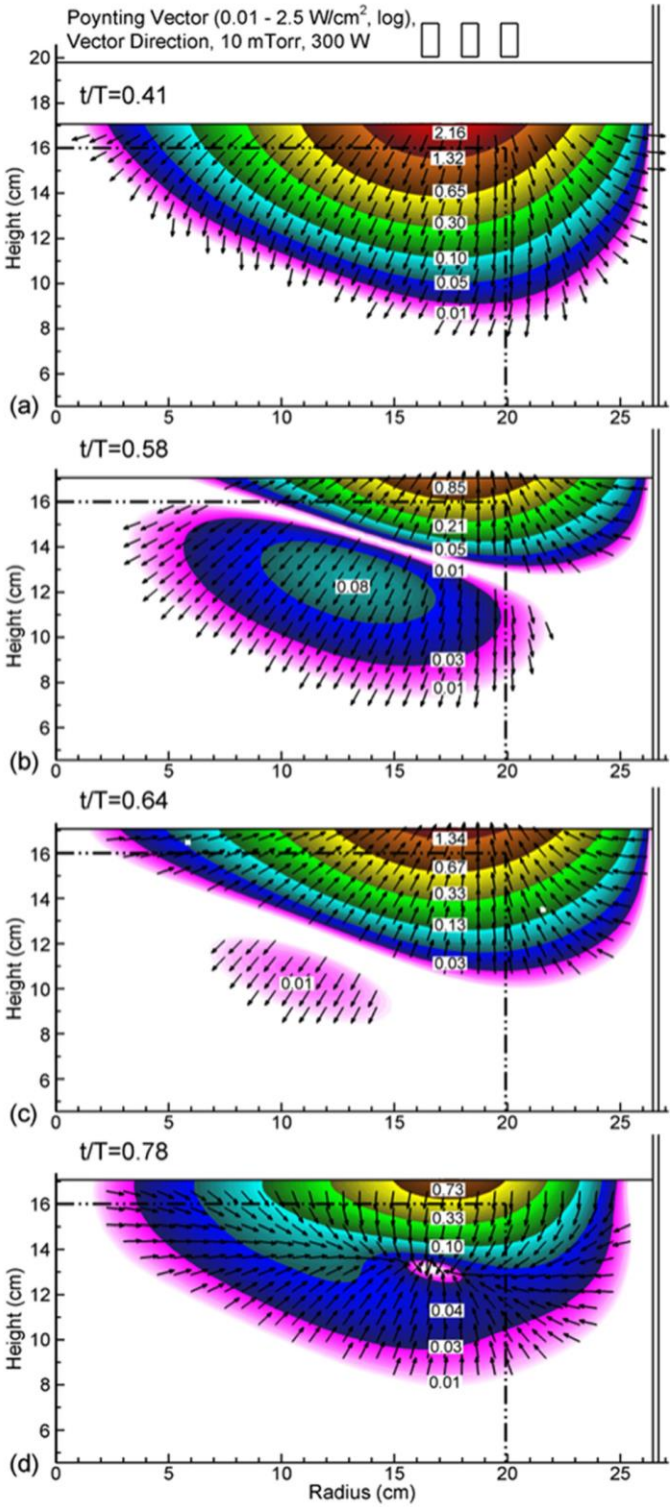

Figure 3-16. Magnitude of Poynting vector (W/cm^2) and direction of vector for different times during the RF cycle. (a) t/T = 0.41, (b) 0.58, (c) 0.64, and (d) 0.78. Plasma conditions are Ar, 10 mTorr, 300 W. The contours are plotted on a log scale (0.01–2.5 W/cm^2). The arrows have constant length to show direction only.

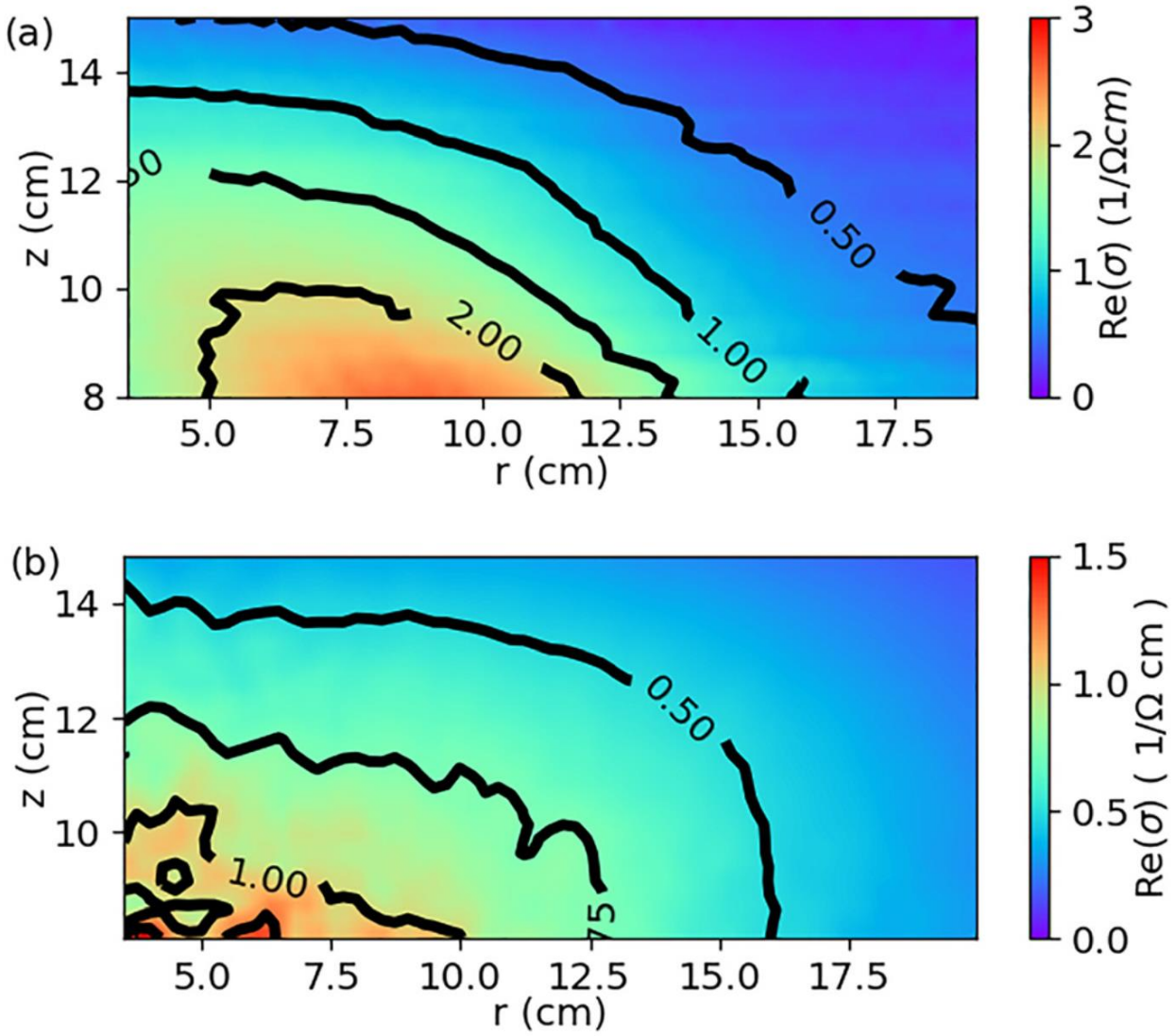

Figure 3-17. Real component of the conductivity throughout the plasma (1/Ω-cm) obtained from (a) experimental values of J and E and (b) simulation results computed in the same fashion.

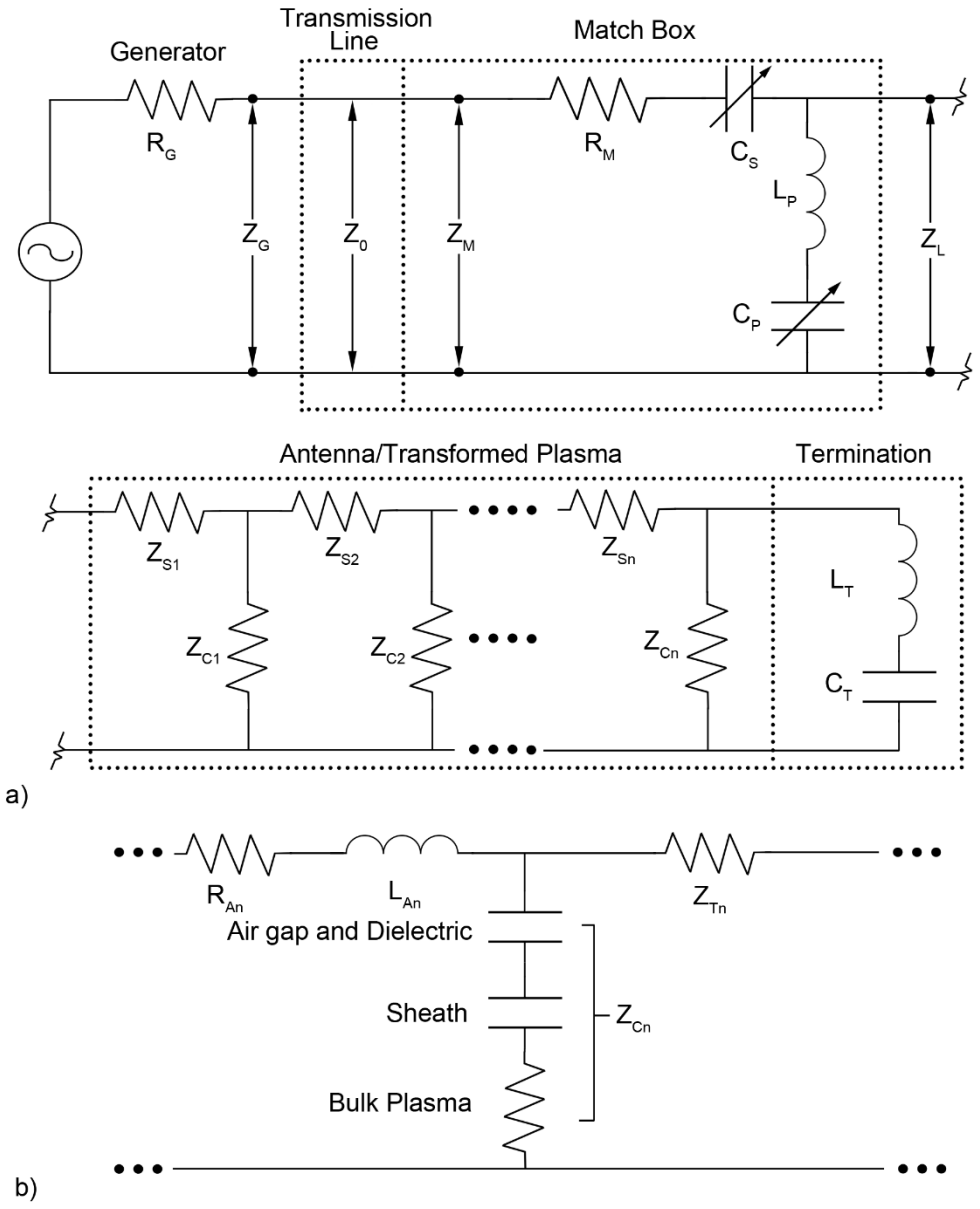

Figure 3-18. Circuit schematic a) The circuit consists of impedances of the power generator, transmission line, matchbox, antenna, plasma, and termination circuit components. The antenna and transformed plasma impendances area represented by a discrete transmission line with each segment have having serial impedance Z_{sn} and parallel impendance due to capactive coupling, Z_{cn}. b) The Z_{sn} components consist of the physical resistance (R_{An}) and inductance (L_{An}) of the antenna, and the transformed impedance (resistance and inductance) of the plasma, Z_{Tn}. The impedance due to capacitive coupling, Z_{cn}, has components due to the air gap and dielectric, sheath and bulk resistance of the plasma.

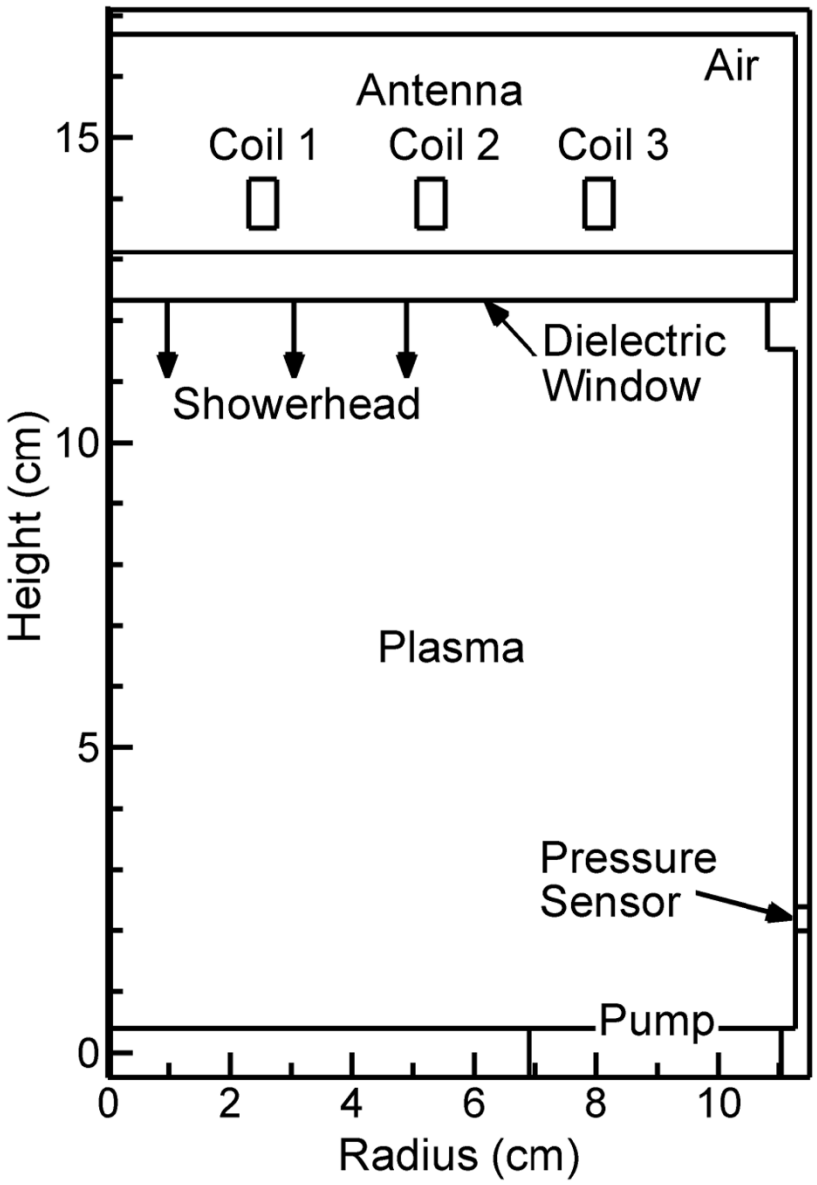

Figure 3-19. Geometry of the cylindrically symmetric ICP reactor.

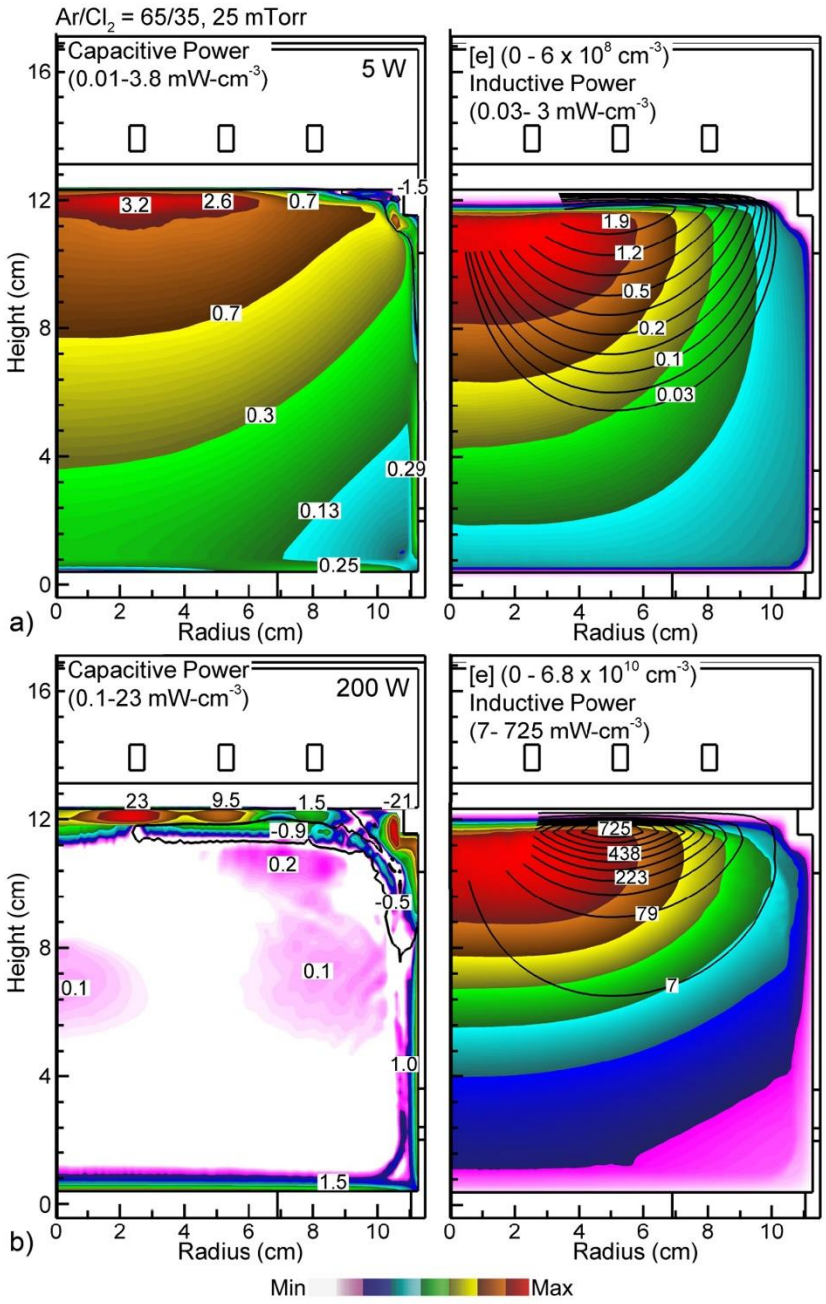

Figure 3-20. Capacitive and inductive power deposition, and electron density when plasma is sustained with at total continuous power of a) 5 W and b) 200 W. (Ar/Cl_2 = 65/35, 25 mTorr.) The match is perfect. The capacitive power is shown as color contours with a line separating positive and negative values. Contour labels are mW/cm^3. Electron density is shown as color contours. Inductive power deposition is shown as contour lines with labels in mW/cm^3. The contour lines are blanked near the axis to enable clear view of the sheath formed under the powered coil.

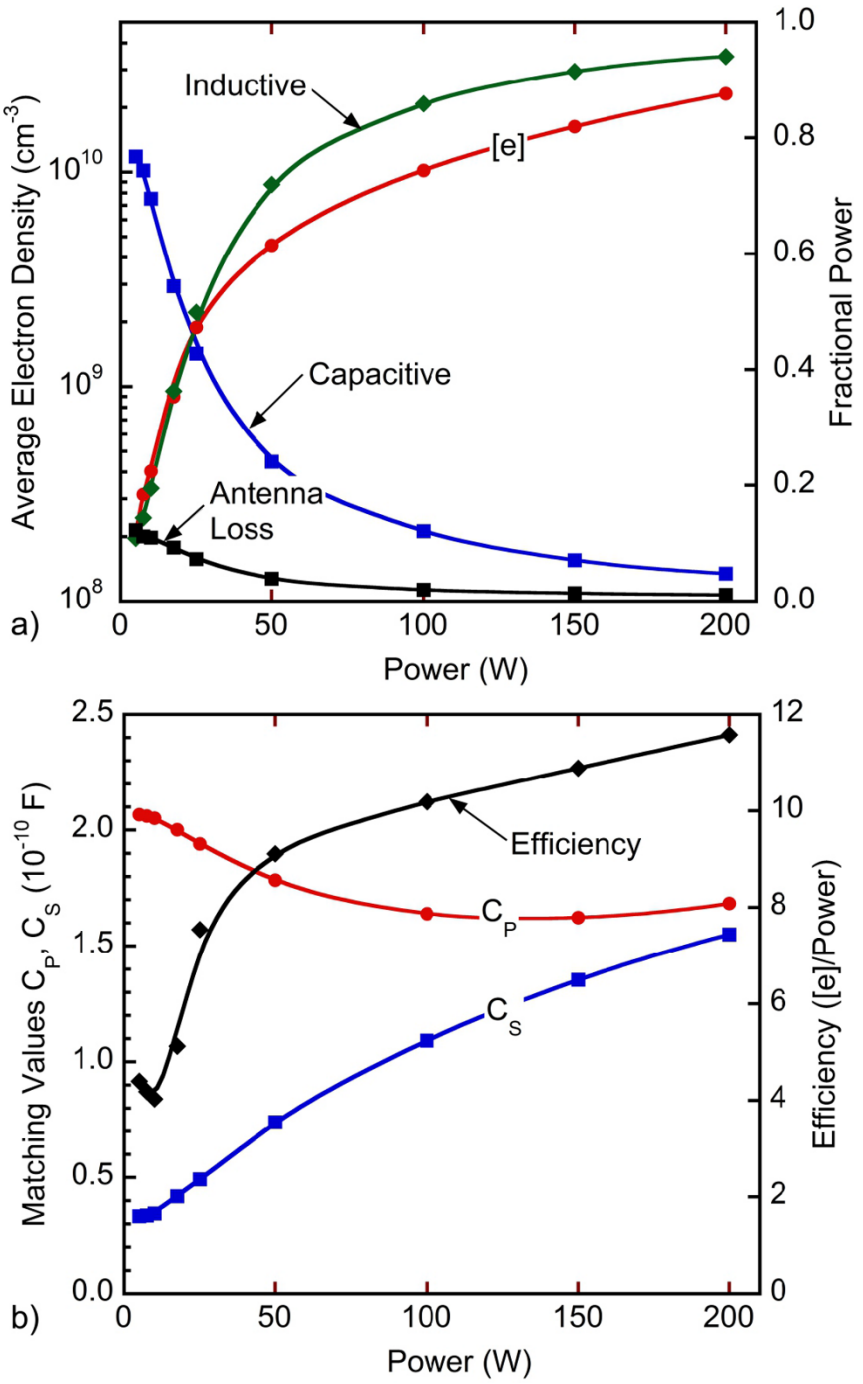

Figure 3-21. Plasma and circuit properties as a function of CW power deposition for perfect matching (Ar/Cl_2 = 65/35, 25 mTorr). a) Electron density and fraction of power deposition due inductive H-mode, capacitive E-mode and antenna heating. b) Analytical solutions for C_P and C_S for a perfect match and the ionization efficiency. The ionization efficiency is total electron density divided by power deposition in the plasma, and is a relative measure of efficiency.

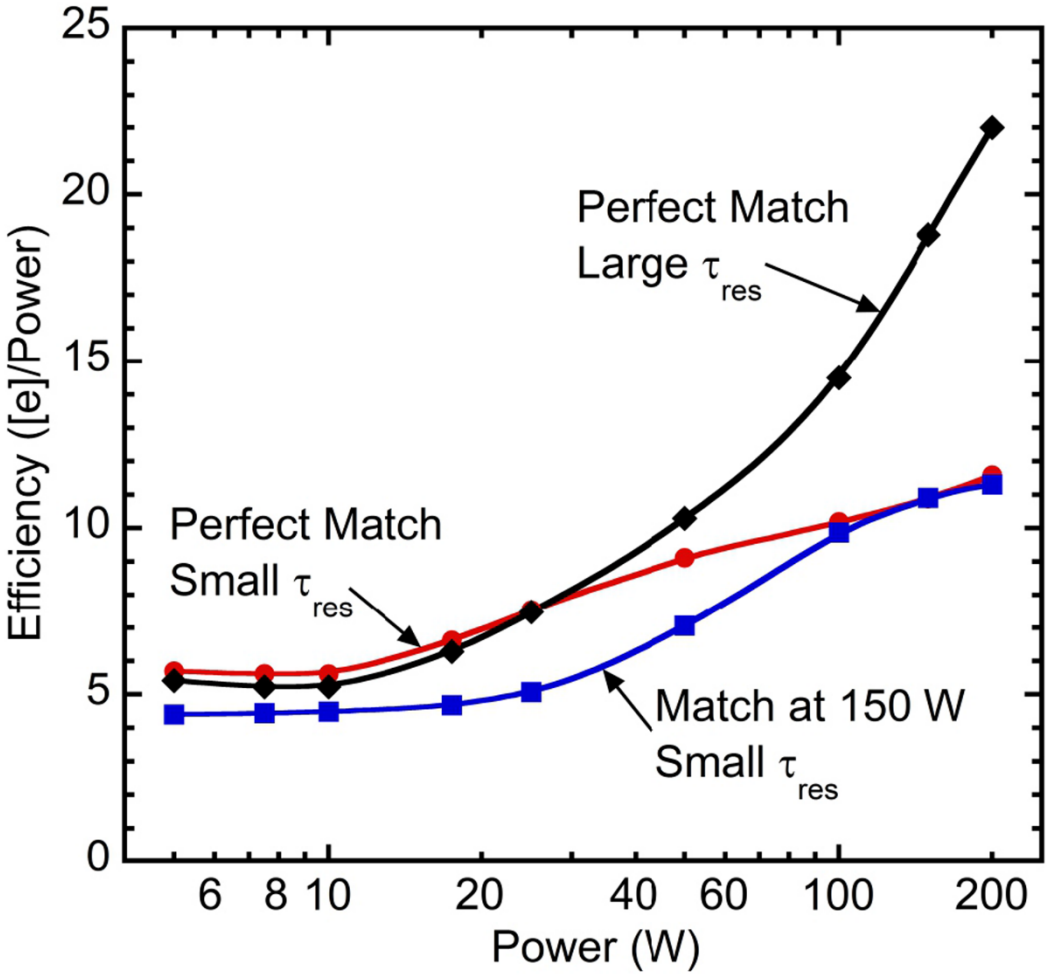

Figure 3-22. Ionization efficiency as a function of cw power (Ar/Cl_2 = 65/35, 25 mTorr). Cases are shown for perfect matches for small and large residence time (τ_{res}) and with circuit values for a perfect match at 150 W with small τ_{res}. The ionization efficiency is total electron density divided by power deposition in the plasma, and is a relative measure of efficiency.

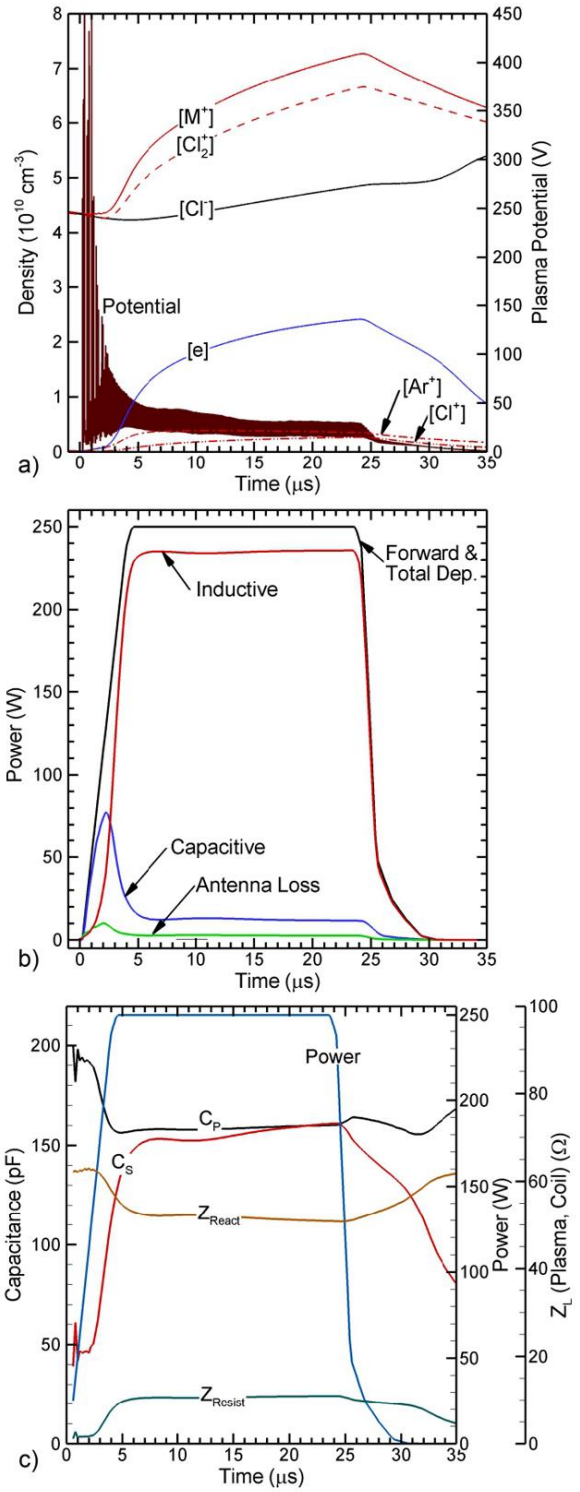

Figure 3-23. Plasma and circuit values for a pulsed ICP with perfect matching. a) Electron and ion densities, and plasma potential, b) modes of power deposition and c) C_P and C_S for perfect match conditions, and reactive and resistive components of the impedance Z_L. The pulse repetition frequency is 13.3 kHz, duty cycle of 35% and forward power during the pulse is P_S=250 W, shown in c).

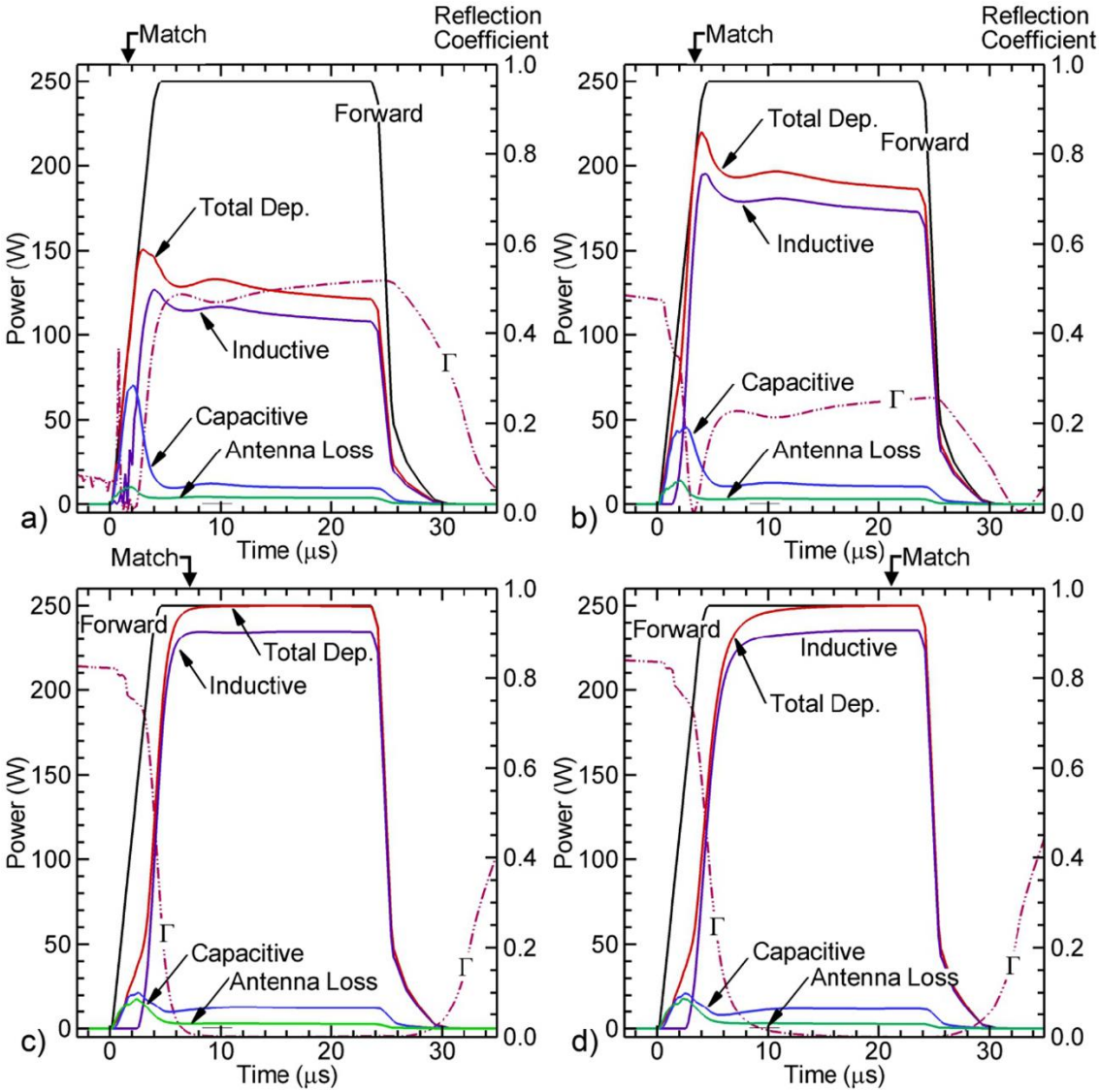

Figure 3-24. Modes of power deposition, total power deposition and power reflection coefficient Γ when C_P and C_S are chosen to match at t_M = a) 1.5, b) 3.25, c) 7 and d) 21 μs into the pulse. (Ar/Cl_2=65/35, 25 mTorr, PRF = 13.3 kHz, DC = 35%, P_S = 250 W.)

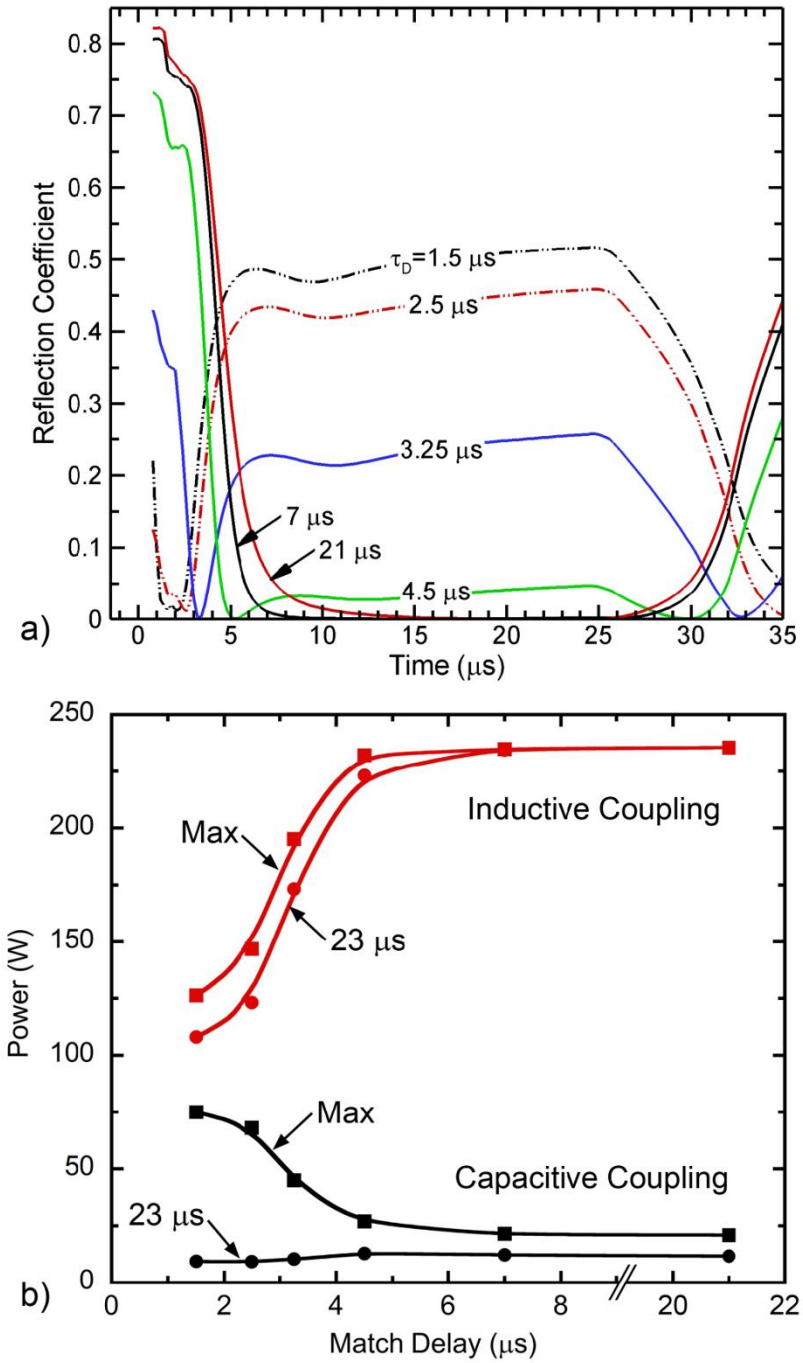

Figure 3-25. Circuit values and power deposition as a function of matching time. a) Power reflection coefficients through one pulsed period when matching at different t_M. b) Inductive and capacitive power at their maximum value and at the end of pulse (t = 23 μs) with varying match time t_M. (Ar/Cl_2 = 65/35, 25 mTorr, PRF = 13.3 kHz, DC = 35%, P_S = 250 W.)

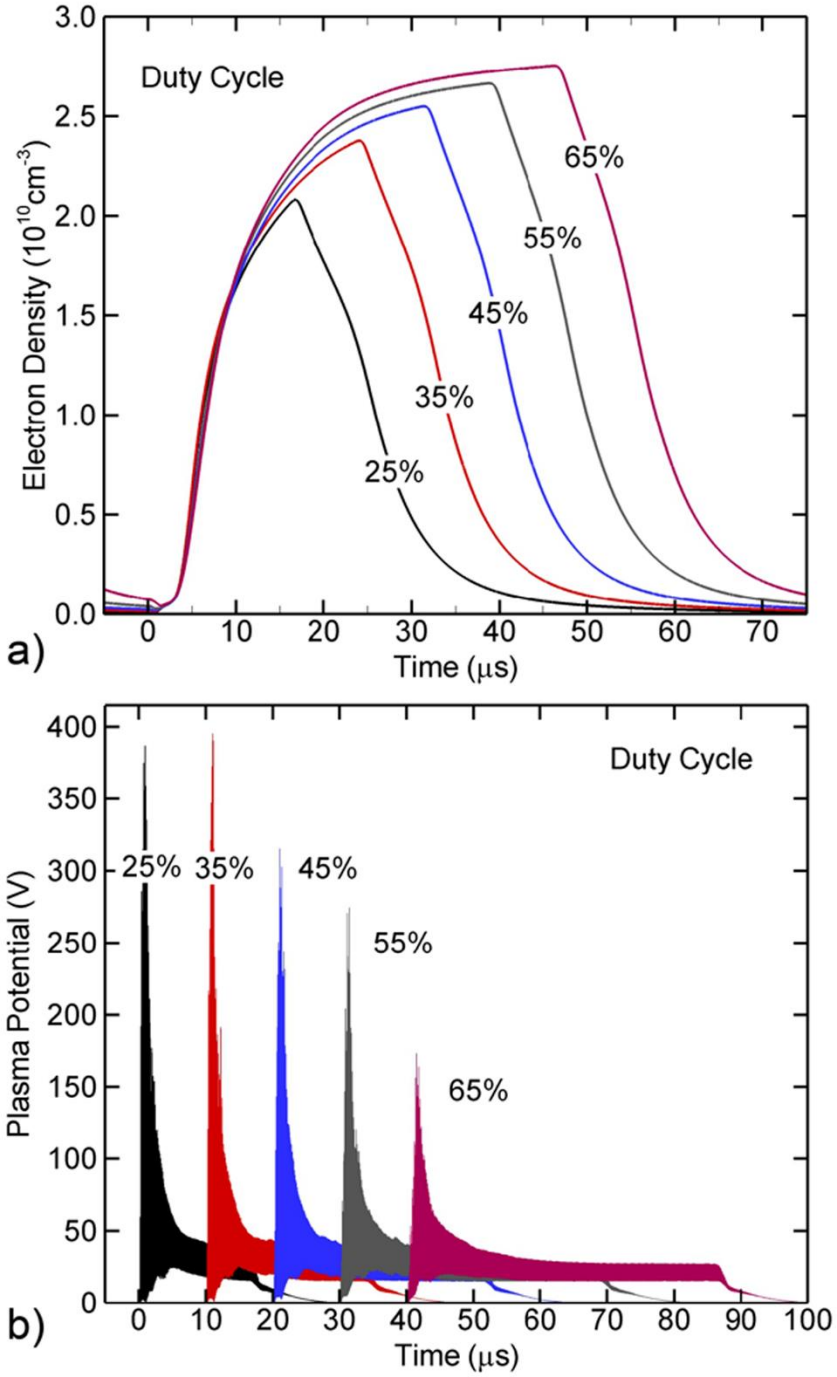

Figure 3-26. Plasma properties when varying duty cycle (25 to 65%) during a pulsed period. The circuit match values correspond to a duty cycle of 35% with the match time at t_M = 7 μs. a) Electron density and b) plasma potential. For clarity, the plots for plasma potential have been shifted by increments of 10 ns. (Ar/Cl_2=65/35, 25 mTorr, PRF = 13.3 kHz, P_S = 250 W)

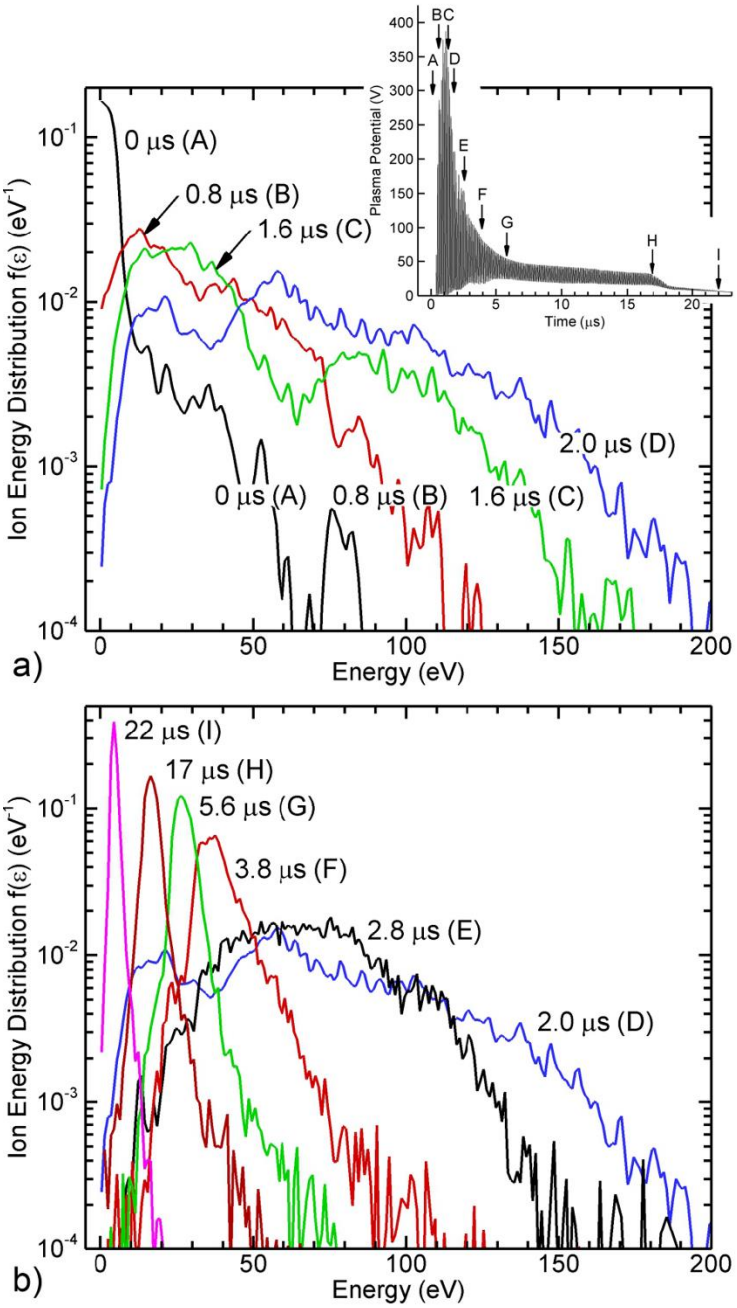

Figure 3-27. Ion energy distribution (IED) incident onto the dielectric window at different times during the pulse. a) 0-2.0 μs, and b) 2.0-22 μs. The inset shows the plasma potential. The labels A-H are the locations in the pulsed cycle at which the IEDs are plotted. (Ar/Cl_2 = 65/35, 25 mTorr, PRF = 13.3 kHz, DC = 25%).

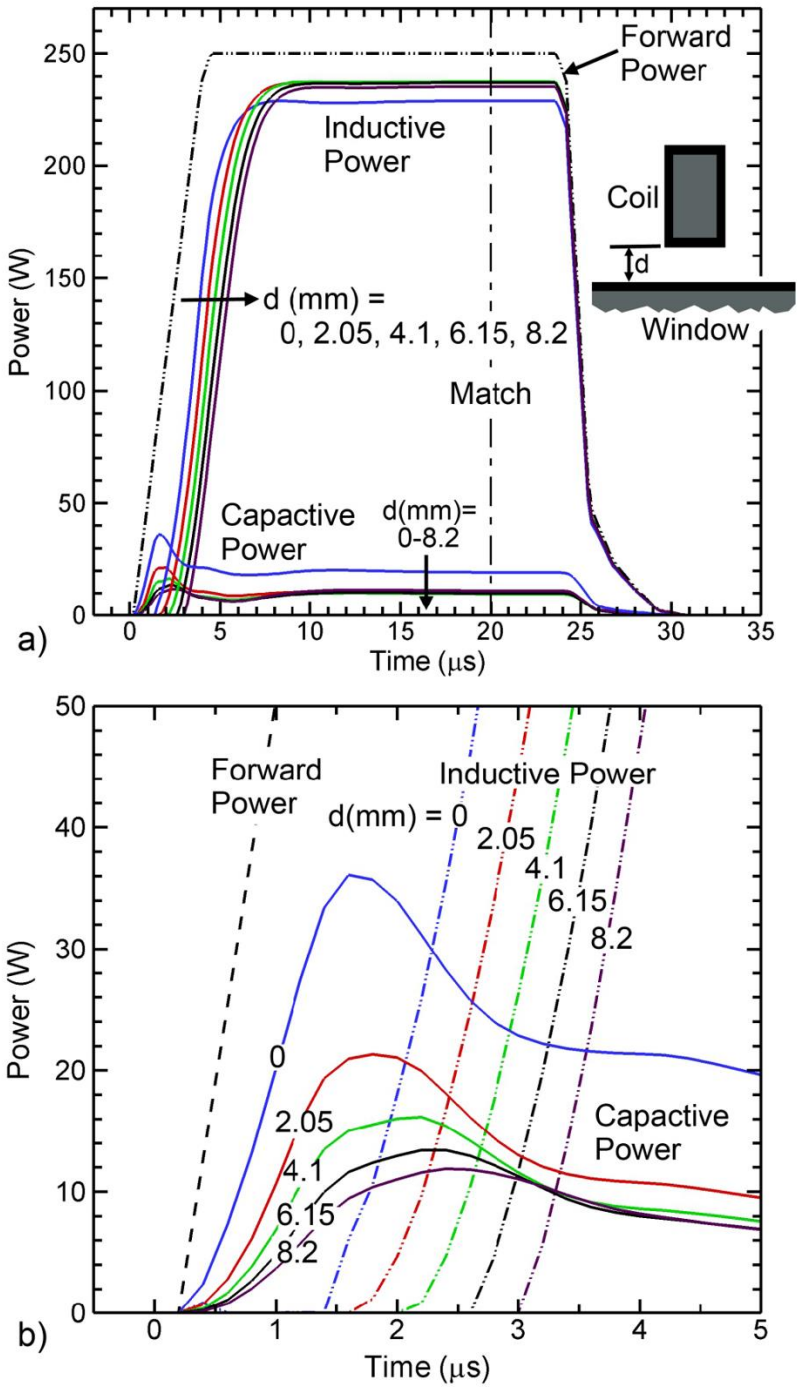

Figure 3-28. Inductive and capacitive power deposition for different gaps, d, between the coils and the top of the dielectric window. Heights range between d = 0 to 8.2 mm. a) Power over the entire power-on period and b) power during the first 5 μs. The circuit match values correspond to the match time t_M = 20 μs. (Ar/Cl_2 = 65/35, 25 mTorr, PRF = 13.3 kHz, DC = 35%, P_S = 250 W.)

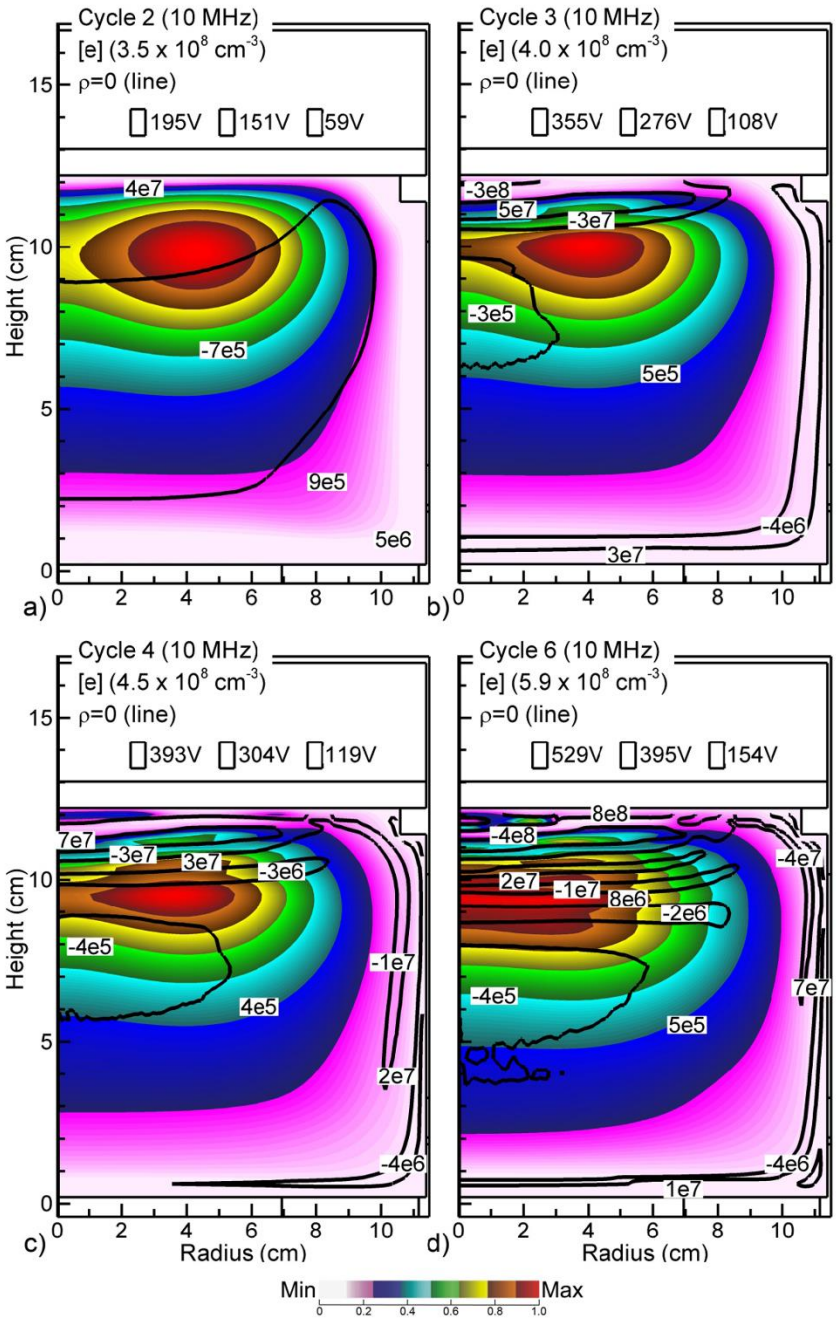

Figure 3-29. Electron density (color contours) and charge density over the first few RF cycles of a pulsed period. a) 2nd, b) 3rd, c) 4th and d) 6th cycles. The circuit match values correspond to the match time t_M = 1.5 μs. The charge density ρ is shown by labels in units of q (1.6×10^{-19} C)/cm^3 with a line denoting ρ = 0. (Ar/Cl_2 = 65/35, 25 mTorr, PRF = 13.3 kHz, DC = 35%, P_S = 250 W). The impulsive power deposition launches electrostatic waves.

3.5 References

[1] J. Han, P. Pribyl, W. Gekelman, A. Paterson, S. J. Lanham, C. Qu and M. J. Kushner, Phys. Plasmas **26,** 103503 (2019).

[2] C. Qu, S. J. Lanham, S. C. Shannon, S. K. Nam and M. J. Kushner, J. Appl. Phys. **127,** 133302 (2020).

[3] M. A. Lieberman and A. J. Lichtenberg, *Principles of Plasma Discharges and Materials Processing*, John Wiley & Sons, Inc. (2005).

[4] R. Piejak, V. Godyak and B. Alexandrovich, J. Appl. Phys. **78,** 5296 (1995).

[5] R. Piejak, V. Godyak and B. Alexandrovich, J. Appl. Phys. **81,** 3416 (1997).

[6] J. Hopwood, C. R. Guarnieri, S. J. Whitehair and J. J. Cuomo, J. Vac. Sci. Technol. A Vacuum, Surfaces, Film. **11,** 147 (1993).

[7] R. Limpaecher and K. R. MacKenzie, Rev. Sci. Instrum. **44,** 726 (1973).

[8] I. M. El-Fayoumi and I. R. Jones, Plasma Sources Sci. Technol. **7,** 162 (1998).

[9] M. Tuszewski, Phys. Plasmas **5,** 1198 (1998).

[10] S. Srinivasan, J. Marquis, L. Pratti, M. H. Khater, M. J. Goeckner and L. J. Overzet, Plasma Sources Sci. Technol. **12,** 432 (2003).

[11] Z. F. Ding, B. Sun and W. G. Huo, Phys. Plasmas **22,** 063504 (2015).

[12] V. A. Godyak and R. B. Piejak, J. Appl. Phys. **82,** 5944 (1997).

[13] V. A. Godyak, R. B. Piejak and B. M. Alexandrovich, Phys. Rev. Lett. **83,** 1610 (1999).

[14] K. Ostrikov, E. Tsakadze, S. Xu, S. V. Vladimirov and R. Storer, Phys. Plasmas **10,** 1146 (2003).

[15] P. Subramonium and M. J. Kushner, J. Appl. Phys. **96,** 82 (2004).

[16] D. Leneman and W. Gekelman, Rev. Sci. Instrum. **72,** 3473 (2001).

[17] J. P. Sheehan and N. Hershkowitz, Plasma Sources Sci. Technol. **20,** 063001 (2011).

[18] M. J. Martin, J. Bonde, W. Gekelman and P. Pribyl, Rev. Sci. Instrum. **86,** 053507 (2015).

[19] J. Y. Kim, H.-C. Lee, D.-H. Kim, Y.-S. Kim, Y.-C. Kim and C.-W. Chung, Phys. Plasmas **21,** 023511 (2014).

[20] T. Hori, M. D. Bowden, K. Uchino, K. Muraoka and M. Maeda, J. Vac. Sci. Technol. A Vacuum, Surfaces, Film. **14,** 144 (1996).

[21] R. L. Stenzel, Rev. Sci. Instrum. **47,** 603 (1976).

[22] X. Fan, Y. Wug, J. Han, P. Pribyl and T. Carter, Rev. Sci. Instrum. **91,** 113502 (2020).

[23] R. L. Stenzel, Phys. Fluids **19,** 857 (1976).

[24] M. J. Kushner, J. Phys. D. Appl. Phys. **42,** 194013 (2009).

[25] P. Tian and M. J. Kushner, Plasma Sources Sci. Technol. **24,** 034017 (2015).

[26] A. V. Vasenkov and M. J. Kushner, Phys. Rev. E **66,** 066411 (2002).

[27] V. A. Godyak and V. I. Kolobov, Phys. Rev. Lett. **79,** 4589 (1997).

[28] G. G. Lister, Y. -M. Li and V. A. Godyak, J. Appl. Phys. **79,** 8993 (1996).

[29] V. A. Godyak, R. B. Piejak, B. M. Alexandrovich and V. I. Kolobov, Phys. Rev. Lett. **80,** 3264 (1998).

[30] G. Cunge, B. Crowley, D. Vender and M. M. Turner, J. Appl. Phys. **89,** 3580 (2001).

[31] V. I. Kolobov and D. J. Economou, Plasma Sources Sci. Technol. **6,** R1 (1997).

[32] T. Lafleur, P. Chabert, M. M. Turner and J. P. Booth, Phys. Plasmas **20,** 124503 (2013).

[33] E. S. Weibel, Phys. Fluids **10,** 741 (1967).

[34] J. Y. Kim, J. Y. Jang, K. S. Chung, K.-J. Chung and Y. S. Hwang, Plasma Sources Sci. Technol. **28,** 07LT01 (2019).

[35] P. Chabert, J. L. Raimbault, J. M. Rax and M. A. Lieberman, Phys. Plasmas **11,** 1775 (2004).

[36] J. T. Gudmundsson and M. A. Lieberman, Plasma Sources Sci. Technol. **7,** 83 (1998).

[37] K. Kurokawa, IEEE Trans. Microw. Theory Tech. **13,** 194 (1965).

[38] S. Xu, K. N. Ostrikov, Y. Li, E. L. Tsakadze and I. R. Jones, Phys. Plasmas **8,** 2549 (2001).

[39] F. Schmidt, J. Schulze, E. Johnson, J.-P. Booth, D. Keil, D. M. French, J. Trieschmann and T. Mussenbrock, Plasma Sources Sci. Technol. **27,** 095012 (2018).

[40] J. Franek, S. Brandt, B. Berger, M. Liese, M. Barthel, E. Schüngel and J. Schulze, Rev. Sci. Instrum. **86,** 053504 (2015).

[41] T. Mussenbrock, R. P. Brinkmann, M. A. Lieberman, A. J. Lichtenberg and E. Kawamura, Phys. Rev. Lett. **101,** 085004 (2008).

[42] J. Schulze, B. G. Heil, D. Luggenhölscher, R. P. Brinkmann and U. Czarnetzki, J. Phys. D. Appl. Phys. **41,** 195212 (2008).

[43] L. Liu, S. Sridhar, V. M. Donnelly and D. J. Economou, J. Phys. D. Appl. Phys. **48,** 485201 (2015).

[44] C. Xue, D.-Q. Wen, W. Liu, Y.-R. Zhang, F. Gao and Y.-N. Wang, J. Vac. Sci. Technol. A Vacuum, Surfaces, Film. **35,** 021301 (2017).

[45] T. Wegner, C. Küllig and J. Meichsner, Plasma Sources Sci. Technol. **26,** 025006 (2017).

[46] T. Wegner, C. Küllig and J. Meichsner, Plasma Sources Sci. Technol. **26,** 025007 (2017).

[47] J. Wang, Y. Du, X. Zhang, Z. Zheng, Y. Liu, L. Xu, P. Wang and J. Cao, Phys. Plasmas **21,** 073502 (2014).

[48] P. Chabert and N. Braithwaite, *Physics of Radio-Frequency Plasmas,* Cambridge University Press (2011).

[49] S. V. Singh and C. Pargmann, J. Appl. Phys. **104,** 083303 (2008).

[50] T. Gans, M. Osiac, D. O'Connell, V. A. Kadetov, U. Czarnetzki, T. Schwarz-Selinger, H.

Halfmann and P. Awakowicz, Plasma Phys. Control. Fusion **47,** A353 (2005).

[51] G. Cunge, B. Crowley, D. Vender and M. M. Turner, Plasma Sources Sci. Technol. **8,** 576 (1999).

[52] M.-H. Lee and C.-W. Chung, Plasma Sources Sci. Technol. **19,** 015011 (2010).

[53] M. M. Turner and M. A. Lieberman, Plasma Sources Sci. Technol. **8,** 313 (1999).

[54] T. Czerwiec and D. B. Graves, J. Phys. D. Appl. Phys. **37,** 2827 (2004).

[55] T. Wegner, C. Küllig and J. Meichsner, Plasma Sources Sci. Technol. **24,** 044001 (2015).

[56] P. Chabert, A. J. Lichtenberg, M. A. Lieberman and A. M. Marakhtanov, Plasma Sources Sci. Technol. **10,** 478 (2001).

[57] U. Kortshagen, N. D. Gibson and J. E. Lawler, J. Phys. D. Appl. Phys. **29,** 1224 (1996).

[58] E. Despiau-Pujo and P. Chabert, Plasma Sources Sci. Technol. **18,** 045028 (2009).

[59] C. Chung and H.-Y. Chang, Appl. Phys. Lett. **80,** 1725 (2002).

[60] P. Kempkes, S. V. Singh, C. Pargmann and H. Soltwisch, Plasma Sources Sci. Technol. **15,** 378 (2006).

[61] E. Kawamura, M. A. Lieberman, A. J. Lichtenberg and D. B. Graves, Plasma Sources Sci. Technol. **21,** 045014 (2012).

[62] M.-H. Lee and C.-W. Chung, Phys. Plasmas **13,** 063510 (2006).

[63] A. M. Daltrini, S. A. Moshkalev, T. J. Morgan, R. B. Piejak and W. G. Graham, Appl. Phys. Lett. **92,** 061504 (2008).

[64] M. J. Kushner, W. Z. Collison, M. J. Grapperhaus, J. P. Holland and M. S. Barnes, J. Appl. Phys. **80,** 1337 (1996).

[65] R. B. Piejak, V. A. Godyak and B. M. Alexandrovich, Plasma Sources Sci. Technol. **1,** 179 (1992).

[66] P. Tian and M. J. Kushner, Plasma Sources Sci. Technol. **26,** 024005 (2017).

[67] S. . Felch, Z. Fang, B.-W. Koo, R. . Liebert, S. . Walther and D. Hacker, Surf. Coatings Technol. **156,** 229 (2002).

[68] A. Agarwal and M. J. Kushner, J. Appl. Phys. **101,** 063305 (2007).

Chapter 4 Effects of a Chirped Bias Voltage on Ion Energy Distributions in Inductively Coupled Plasma Reactors[**]

The metrics for controlling reactive fluxes to wafers for microelectronics processing are becoming more stringent as feature sizes continue to shrink. Recent strategies for controlling ion energy distributions to the wafer involve using several different frequencies and/or pulsed power. Although effective, these strategies are often costly or present challenges in impedance matching. With the advent of matching schemes for wide band amplifiers, other strategies to customize ion energy distributions become available. In this paper, we discuss results from a computational investigation of biasing substrates using chirped frequencies in high density, electronegative inductively coupled plasmas. Depending on the frequency range and chirp duration, the resulting ion energy distributions exhibit components sampled from the entire frequency range. However the chirping process also produces transient shifts in the self-generated dc bias due to the reapportionment of displacement and conduction with frequency to balance the current in the system. The dynamics of the dc bias can also be leveraged towards customizing ion energy distributions.

4.1 Introduction

Inductively coupled plasma (ICP) reactors are extensively used in plasma materials

[**]Results and portions of the text that appear in this chapter were previously published in the paper by S. J. Lanham *et al.*, "Effects of a chirped bias voltage on ion energy distributions in inductively coupled plasma reactors" J. Appl. Phys. **122,** 083301 (2017).

processing for microelectronics fabrication [1–3]. The typical operating conditions use a radio-frequency (rf) biased substrate with the goal of separately controlling the flux of reactive ions and radicals to a wafer with the inductively coupled source, and the energy of incident ions with the substrate bias. The magnitude of the fluxes determine the rate of processing, while controlling the incident ion energy distributions (IEDs) onto the wafer determines the etch selectivity required for control of the critical dimension (CD). Many strategies have been investigated to control IEDs, including adding a boundary electrode [4], using tailored voltage waveforms [5–8], multiple frequencies [9–12], and pulsing [13–17]. When using multiple frequencies at multiple harmonics, the electrical asymmetry effect enables further customization of IEDs through, in part, control of the self-generated dc bias [18–20]. In plasma chambers, a dc bias forms due to the asymmetry in collection of current between the powered and grounded electrodes to balance the flow of current. This self-generated dc bias was recently shown to oscillate in a controllable manner using tailored voltage waveforms with slightly off-harmonic high frequencies in capacitively coupled plasmas, while retaining favorable properties such as constant ion flux to the substrate [21]. Since the return currents in ICP reactors include both conduction current to the substrate and displacement current through the dielectric window beneath the antenna, dc bias formation is less straight forward than in capacitively coupled plasmas [22–24].

The width in energy of an IED striking the surface of an rf biased substrate can be controlled by the ratio of the rf period compared to the time required for the ion to cross the sheath [25,26]. For low bias frequencies (long periods), ions transiting through the sheath in a small fraction of an rf period arrive with energies dependent on the phase and voltage of the bias when the ion enters the sheath. These conditions lead to dual peaked IEDs. For high bias frequencies (short periods), ions transiting through the sheath over many rf periods arrive at the substrate with

a narrower distribution centered about the average sheath potential – the difference between the plasma potential and dc bias – resulting in a single peaked IED. However, for intermediate frequencies both the number of rf cycles to transit through the sheath and phase dependence can affect ion energy distributions. This scaling in part motivates the use of multiple bias frequencies to customize the IEDs. To some degree, the IEDs will be super-positions of broad IEDs produced by low frequencies and narrow IEDs by high frequencies.

A "chirp" is where the frequency of a sinusoidal or repetitive waveform is linearly varied over time (see Fig. 4-1). For example, a purely linear chirp will vary the frequency between f_0 and f_1, the initial and final frequencies, over a time τ to sweep across frequencies. For an initial phase φ_0, a repetitive amplitude of the chirped signal is:

$$a(t) = \sin\left[\phi_0 + 2\pi t\left(f_0 + \frac{(f_1 - f_0)\,\mathrm{mod}(t,\tau)}{\tau}\right)\right] \tag{4.1}$$

A chirped bias voltage provides an opportunity to customize IEDs by taking advantage of the variation in the energy width of the IEDs as a function of frequency, with an added level of control of the dwell time of the bias at any given frequency. If the range of frequencies or chirp periods is moderate, it may be possible to use a single amplifier and simple impedance matching circuitry, while achieving the advantages of using separate frequencies, power supplies and matching networks.

In this work, results from a computational investigation of controlling IEDs onto wafers using a chirped substrate bias in a high plasma density, electronegative ICP are discussed. In particular, the impact of the transient frequency during chirping on the self-generated dc bias and on the IEDs is quantified. Sweeping frequencies causes the blocking capacitor on which the dc bias resides to continually charge and discharge, shifting the ion energies striking the wafer from

what would be obtained from the equivalent constant continuous wave (cw) frequency. A chirped frequency can be used to control the dc bias and to customize IEDs.

Descriptions of the computational models used in this work are discussed in Sec. 4.2. In Sec. 4.3, results from studies of basic chirped bias waveforms and how changes in operating conditions affect IEDs are discussed. The concept of customized chirping is then demonstrated to craft custom frequency waveforms. Concluding remarks are in Sec. 4.4.

4.2 Description of the Model

The Hybrid Plasma Equipment Model (HPEM) was used to investigate the consequences of a chirped bias voltage in an ICP reactor. The HPEM is a two-dimensional fluid hydrodynamics computer model for low temperature plasmas, and the specific details can be found elsewhere [27]. HPEM executes by having separate modules which address different classes of physics. In this work, the Electromagnetics Module was used to determine the inductive electric fields for a specified input power. An electron Monte Carlo simulation within the Electron Energy Transport Module (EETM) was used to track electrons produced by secondary emission from surfaces. The Fluid-Kinetics Poisson Module (FKPM) was used to separately solve continuity, momentum, and energy equations for all heavy particle species, and a drift-diffusion formulation for electrons. A semi-implicit form of Poisson's equation was used to solve for electrostatic fields. An electron energy conservation equation was used to obtain an effective electron temperature based on absorbed power and electron collisional losses. Stationary solutions of Boltzmann's equation provided electron impact rate coefficients and transport coefficients as a function of effective electron temperature. The Plasma Chemistry Monte Carlo Module (PCMCM) was used to calculate ion energies incident onto a wafer by tracking ion pseudoparticles, influenced by electric

fields and collisions, binning the resulting flux by energy and incident angle [Ion Energy and Angular Distributions (IEADs)].

The base case uses a chirped frequency of 2 – 20 MHz, repeated every 30 μs. To work within the HPEM framework, the chirped waveform was approximated by using steps of the lowest frequency harmonics, shown in Fig. 4-2. The bulk plasma properties in high plasma densities systems, such as ICPs, are weak functions of the bias for moderate bias voltages. So to speed computational convergence, the model is first run with only the ICP power until a steady state is achieved. The chirped bias is then turned on, and a sufficient number of chirped periods are computed to achieve a pulse-periodic steady state.

4.3 Chirped Substrate Bias

The simulations in this study were performed for the ICP reactor schematically shown in Fig. 4-3a. This reactor features a four-turn planar coil antenna that delivers purely inductive power. An Ar/Cl_2 = 80/20 gas mixture flows into the reactor through the inlet at 600 sccm. The reaction mechanism used is the same as that described by Tian et al. [28] with the exception that radiation transport was not included here. The basic circuit consists of the chirped bias power being applied to the metal substrate through an intervening blocking capacitor, a dielectric wafer functionally acting as a lossy capacitor on the substrate, the sheath above the wafer acting as a capacitor, the plasma acting as an impedance and the sheath against the grounded metal wall and alumina window. Conduction current flowing out of the power supply returns to ground through the metal walls in contact with the plasma or as displacement current flowing through the quartz window which terminates on ground on the opposite side of the window. The dc bias forms on the blocking capacitor to balance the current flowing through the substrate and that returning to ground

elsewhere. These flows of current are natural outcomes of the simulation by computing fluxes of charged particles and time variations of electric fields at surfaces, and are calculated by performing integrals of the conduction and displacement current densities entering the surface of metals. Although the majority of voltage that balances the currents resides on the blocking capacitor, the wafer and sheaths also hold some charge.

4.3.1 Base Case

The ICP reactor was operated with 900 W of inductive power, with a chirped bias waveform having an amplitude of 150 V and frequency excursion of 2 to 20 MHz repeated every 30 μs. (The increasing frequency during the chirp is called the *ascending chirp*.) Computed plasma properties are shown in Fig. 4-3b and 4-3c after operating without a bias to approximate convergence, then applying 5 chirped bias cycles which was sufficient to achieve a pulse-periodic steady state. The electron density reaches a maximum of 3.7×10^{11} cm^{-3}, slightly off-axis which reflects the maximum in the inductive power deposition beneath the coils. In this electronegative, molecular gas mixture, electron losses occur both in the volume by dissociative electron attachment to Cl_2 and dissociative recombination with Cl_2^+, as well as diffusion to the walls. The electron temperature, T_e, reaches a maximum of 3.2 eV beneath the coils, decreasing to 2.6 eV near the pump port. The plasma properties do not significantly vary over a chirped period since the majority of the power deposition from the bias is expended in ion acceleration. However the amount of capacitive power does change with frequency during the constant voltage chirp. The minimum capacitive power occurs at the beginning of the chirp – 200 W when the bias is 2 MHz. Near the end of the chirped period, the capacitive power is 300 W when the bias is 20 MHz.

The IEADs at various times (collected over a 0.5 μs time period) during the chirped period are shown in Fig. 4-4 for Ar^+. At the beginning of the chirp with lower frequencies, ions are

extracted with bimodal peaks in energy, with the high energy peak emphasized. At the beginning of the chirp (t = 0), ions having energies as large as 260 eV are extracted, characteristic of the low frequency (2 MHz) [26]. During the chirp, the peak energy decreases while the minimum energy increases, reflecting the increasing frequency which shortens the rf cycle and so drives the IEADs towards being single peaked.

IEDs averaged over the chirped cycle are shown in Fig. 4-5 for Ar^+, Cl^+, and Cl_2^+. To give context to these results, IEDs are also shown in Fig. 4-5 when holding the bias at a constant frequency for the same conditions (2, 10, and 20 MHz with 150 V amplitude). The trends in the IEDs for increasing ion mass at higher frequencies show decreasing energy between the peaks due to their longer transit time through the sheaths. At 2 MHz, the IEDs are nearly identical for all ions, which suggests that the ion transit time through the sheath is shorter than the rf period for all masses, and so the IEDs are dominantly dependent on the time which the ion enters the sheath. The IEDs for Ar^+ will be discussed in detail and used to compare trends to other conditions.

For the constant frequency cases, the IED for 10 MHz extends to the highest energy. This is caused by a combination of a decrease (more negative) dc bias, -60 V, combined with the more extended IED that is produced at lower frequencies. (See Fig. 4-6.) Although one might expect a more extended IED at 2 MHz, the dc bias is only -24 V at this frequency. The steady state dc bias results from balancing the rf cycle averaged current through the powered electrode with that returning to ground. A negative bias indicates that in the absence of the bias, more current would be collected on the powered side of the circuit. In parallel plate capacitive systems, these differences in currents are typically a result of the powered and grounded metal surfaces having different areas. If the area of the grounded electrode is greater than that of the powered electrode, the blocking capacitor should naturally charge to a negative voltage. In this system, the accounting

of currents is complicated by much of the return current to ground passing as displacement current through the dielectric window, which scales directly proportional to frequency. For example, changing the bias frequency from 2 to 20 MHz increases the displacement current through the window by an order of magnitude, making the system appear more asymmetric and creating a more negative dc bias for higher frequency. The displacement current is more sensitive to frequency than the combination of conduction and displacement current that returns to ground at the walls of the chamber. The energy between the peaks in the IEDs decreases with increasing frequency due to ion transit times through the sheath that can span multiple rf periods. For the 10 MHz case, the dc bias decreases at a faster rate than the peaks come together, leading to higher energy ions.

The IEDs for the chirped case has characteristics of the low and high frequency cw bias cases. The IEADs resulting from the ascending chirp sampled over 0.5 μs when the bias is at 2, 10 and 20 MHz are compared to IEADs produced with constant frequency biases in Fig. 4-7. Over the chirped period, the IEAD transitions from having low and high energy peaks (as the 2 MHz case) to peaks closer together in energy (characteristic of 20 MHz). However, the chirped IEAD has a higher energy tail compared to any of the cw cases. This high energy tail results from the transient nature of the "dc" bias when chirping, as shown in Fig. 4-6. The dc bias changes in times given by the effective RC time constant in response to the change in currents over an rf cycle to the powered and grounded surfaces. For this geometry, higher frequencies produce a more negative dc bias. At the end of the chirped period with 20 MHz excitation, the negative bias is becoming even more negative. The frequency changes to 2 MHz at the beginning of the next chirped period, a frequency which for continuous excitation would produce a more positive bias. However, the more negative dc bias produced by the high frequency persists into the part of the

chirp that has low frequency as the RC time constant for these conditions is approximately 25 μs. The end result is that the 2 MHz portion of the chirp that naturally produces an IED that extends to higher energy has an abnormally more negative dc bias compared to the cw case. This abnormally more negative dc bias enables the IED to extend to even higher energy. With the chirp now at low frequency, the dc bias begins to become more positive.

The remainder of the IEAD generally has less structure than the IEADs obtained with single frequencies, though this is not a universal trend. For example, the IEAD with chirping for Cl_2^+ retains some semblance of two-peaks, indicating that the IEADs for the heavier ion are less sensitive to changes in frequency due to their longer sheath crossing time.

The base case uses an ascending chirped frequency from 2 to 20 MHz (150 V). The dc bias is sensitive to the rate of change of the applied frequency and the change in frequency from high to low at the end of the chirp. A *descending chirp* – chirping from 20 to 2 MHz, as shown in Fig. 4-8a – should then produce a different sequencing of the dc bias. Reversing the bias frequency from ascending to descending modifies the IEDs, particularly at high energies, as shown in Fig. 4-8b. The descending chirp produces an IED having a lower maximum energy. With the ascending chirp the dc bias is most negative when the highest frequency (20 MHz) changes to the lowest frequency (2 MHz). The lowest frequency naturally produces the broadest bimodal distribution function (2 MHz). The combination of large dc bias and bimodal IED produces a larger maximum in ion energy.

The descending chirp has the opposite trend in dc bias. The dc bias is most positive at the end of the chirped period at the lowest frequency (2 MHz), as shown in Fig. 4-8c, at which time the chirp switches to the highest frequency (20 MHz) which naturally produces the narrowest IED with a single peak. The dc bias immediately becomes more negative in response to the higher

frequency. However the more positive dc bias persists beyond the switch in frequency, decreasing the ion energies when the 20 MHz is applied. These trends for IEADs are shown in Fig. 4-7. The IEAD at 20 MHz for the descending chirp (Fig. 4-7c) has a maximum energy that is ≈40 eV smaller than that for 20 MHz for the ascending chirp. This difference is equal to the increase in dc bias for the descending chirp. The shift in the average energy of the IEADs for ascending and descending chirps in Fig. 4-7 for the same frequency is largely a result of the opposite trending dynamics of the dc bias.

4.3.2 Source Power

The effect of varying the ICP source power was investigated for the base case ascending chirped waveform for Ar^+ over the range of 600 – 1,200 W. The resulting IEDs are shown in Fig. 4-9 for constant bias frequencies of 2 MHz and 20 MHz, and the ascending chirped waveform. The maximum electron density increases from 1.6×10^{11} cm^{-3} for 600 W to 5.9×10^{11} cm^{-3} for 1,200 W with the same general spatial trends. The electron temperature was largely unaffected by these changes in inductive power, which partly results from the high flowrate that minimizes the amount of dissociation of Cl_2 by replenishing the feedstock. The dominant change with increasing power is the thinning of the sheath, which then broadens the energy range of the IEDs, particularly at the higher constant frequency. The broadening of the IEDs with thinning of the sheath is tempered by a decrease in dc bias with increasing power, shown in Fig. 4-10.

The IEDs for chirping the bias frequency with different ICP powers are shown in Fig. 4-9c. With chirping the frequency, the relative flux of ions with lower energies increases and at high energy decreases with increasing power. These trends largely result from the change in dc bias with source power, shown in Fig. 4-10. As with the fixed frequency, increasing source power produces an increase in dc bias (to less negative values). These trends in dc bias have been

experimentally [29] and analytically [30] investigated, and are attributed to increased capacitance of the ion sheath above the wafer. A more negative dc bias for the 600 W case results in ions generally being extracted with higher energy. Since the magnitude of the flux to the wafer scales with ICP power, the low flux at 600 W produces a less transient dc bias.

4.3.3 Blocking Capacitor Size

With continuous excitation for a fixed frequency in the steady state, the dc bias is not a function of the size of the blocking capacitor. The initial transient to the steady state bias does depend on the size of the blocking capacitor due to the larger RC time constant. However, the final dc bias should not depend on the size of the blocking capacitor. With the repeating, chirped frequency bias, the system is driven by what is a functionally dynamic pulsed bias – the system is never in a steady state. If these transients have times that are commensurate with the RC charging time of the blocking capacitor, the resulting dc bias will also have modulation. These trends are shown in Fig. 4-11 where IEDs and dc bias are shown for values of the blocking capacitor of 10 nF to 1 μF. The bulk plasma properties were essentially unchanged from the base case shown in Fig. 4-3. The energies at which the peaks occur in the IEDs are consistent for all blocking capacitor values. The main difference between the IEDs is the slope at high energies – a steep slope for the responsive 10 nF blocking capacitor case, and a shallower slope for the 1 μF blocking capacitor.

The differences in IEDs are caused by differences in the transient dc bias. The 10 nF blocking capacitor has a short enough response that its transient dc voltage nearly spans the range of the dc biases produced by the cw 2 and 20 MHz voltages. The dc bias at a given frequency is close to that for the cw bias. For the large blocking capacitor (1 μF), the response is long enough that the dc bias is relatively constant over a chirped period, an average of the currents collected between 2 MHz and 20 MHz. The excursion in dc bias is least negative at high frequency at the

end of the chirp for the 1 μF capacitor and most negative for low frequency at the beginning of the chirp. These trends account for the IED being more highly populated at high energy with 1 μF capacitor. On the other hand, the dc bias for the 10 nF blocking capacitor quickly responds upon starting the low frequency part of the chirp. The bias quickly increases towards more positive values while the frequency is low, thereby reducing the ion flux at high energy.

4.3.4 Custom Frequency Waveforms

Chirping is typically performed with a linear ramp between minimum and maximum frequencies. However, a more general form of chirping is a waveform of frequencies, which might be used to achieve a desired shape of the IEAD. For example, the chirped-waveform shown in Fig. 4-12a was used to demonstrate the possible utility of this method. The waveform consists of chirping between two frequencies while holding the upper and lower frequencies for a specific time. In this case, the 2 MHz and 20 MHz are held constant for 11 μs with a linear chirp between them lasting 4 μs, for a period of 30 μs. The IEADs collected at different times during the chirp are shown in Fig. 4-12b. The IEDs averaged over the chirp, and dc bias during the chirp are shown in Fig. 4-13. The IEADs at point 1 and 4 are at the same frequencies, as are the IEADs at points 2 and 3. However, the predicted ion energies shift by ≈40 eV when going from the leading to the trailing edge of the chirp for 2 MHz, and shift by ≈20 eV for 20 MHz between the beginning and end of its portion of the waveform. These shifts result from the dynamics of the dc bias, which is most negative at the end of the high-frequency plateau in the chirp.

If not for the response of the dc bias, the chirp averaged IEDs should dominantly be a function of the integral of the ion flux arriving at the wafer for each frequency component. Custom frequency waveforms were investigated by varying the time for which the high-and-low frequencies are held constant, producing cycle times of 10 to 50 μs. These waveforms and the

resulting IEDs are shown in Fig. 4-14. The IEDs are most sensitive to the longer dwell time at the low frequency, with longer dwell time at the low frequency corresponding to larger low-energy peaks in the IEDs. The lack of corresponding large high energy peaks stems from the dynamics of the dc bias, shown in Fig. 4-14c. For the 10 μs cycle time, the dc bias oscillates very little over the chirp period, while the longer cycle times enable the dc bias to nearly reach the steady-state limits of the cw cases. It could prove beneficial to customizing IEDs to control the range over which the dc bias oscillates. Operating with different cycle times enables control over the proportion of the IEDs in the high and low energy peaks, while keeping the energy of the peaks essentially unchanged. This could be valuable for other gases with more complicated etching mechanisms, such as C_4F_8 [31], which benefit from a controllable distribution of ions having both low and high energies.

4.4 Concluding Remarks

A computational investigation has been used to assess the ability to control IEADs using chirped substrate biases. Chirped substrate biases produce customizable IEADs incident on the substrate due to both the integral of IEADs produced by different frequency components and due to their being a dynamic self-generated dc bias. Using different bias frequencies can change the effective asymmetry of the system, producing shifts in the dc bias that forms to balance the current. By sweeping the applied frequency, the potential drop across sheaths differs compared to the expected value for constant frequency due to transients in the dc bias on time scales of the RC time constant.

One potential use for a chirped bias frequency would be when a mix of high and low energy components in the IEADs is desired. Operating with a single frequency leaves little flexibility in

this regard since the dc bias and ion energy distribution are, to some degree, predetermined for a given set of plasma operating conditions. For a constant 2 MHz frequency with the operating conditions in this work, the majority of ions are extracted at low energies. Using a chirped frequency could be one method to tune the low energy peak in the IED while having a minimal impact on the plasma. Chirped frequencies have many of the advantages of using multiple fixed frequencies for biasing the substrate with perhaps the additional feature of dynamic dc biases.

4.5 Figures

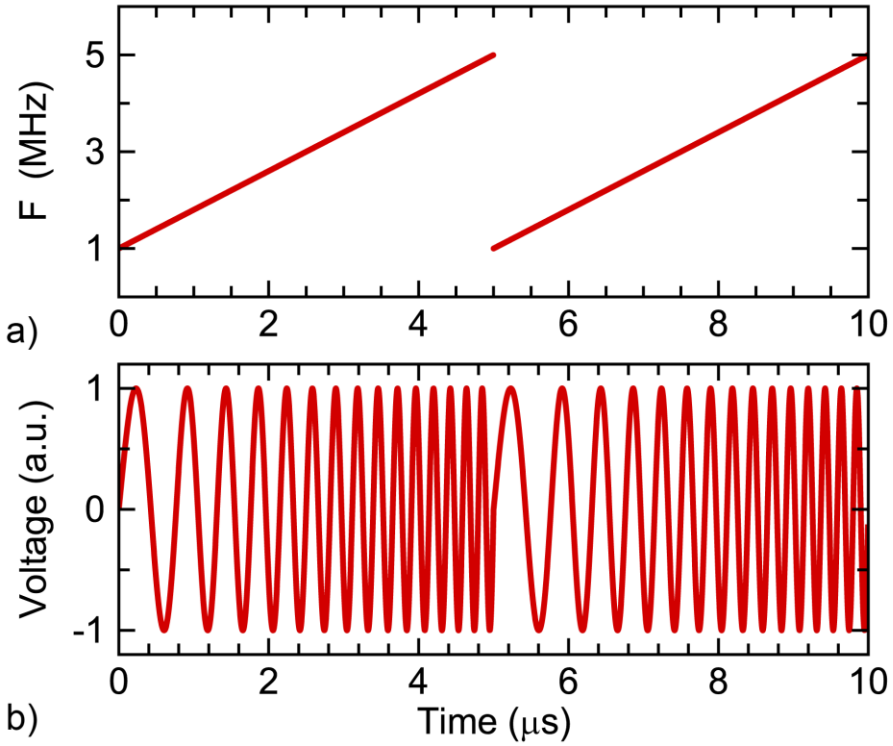

Figure 4-1. A linear chirp is shown in a), where the frequency increases from 1 to 5 MHz, repeating every 5 μs, and b) the resulting rf voltage signal (arbitrary units).

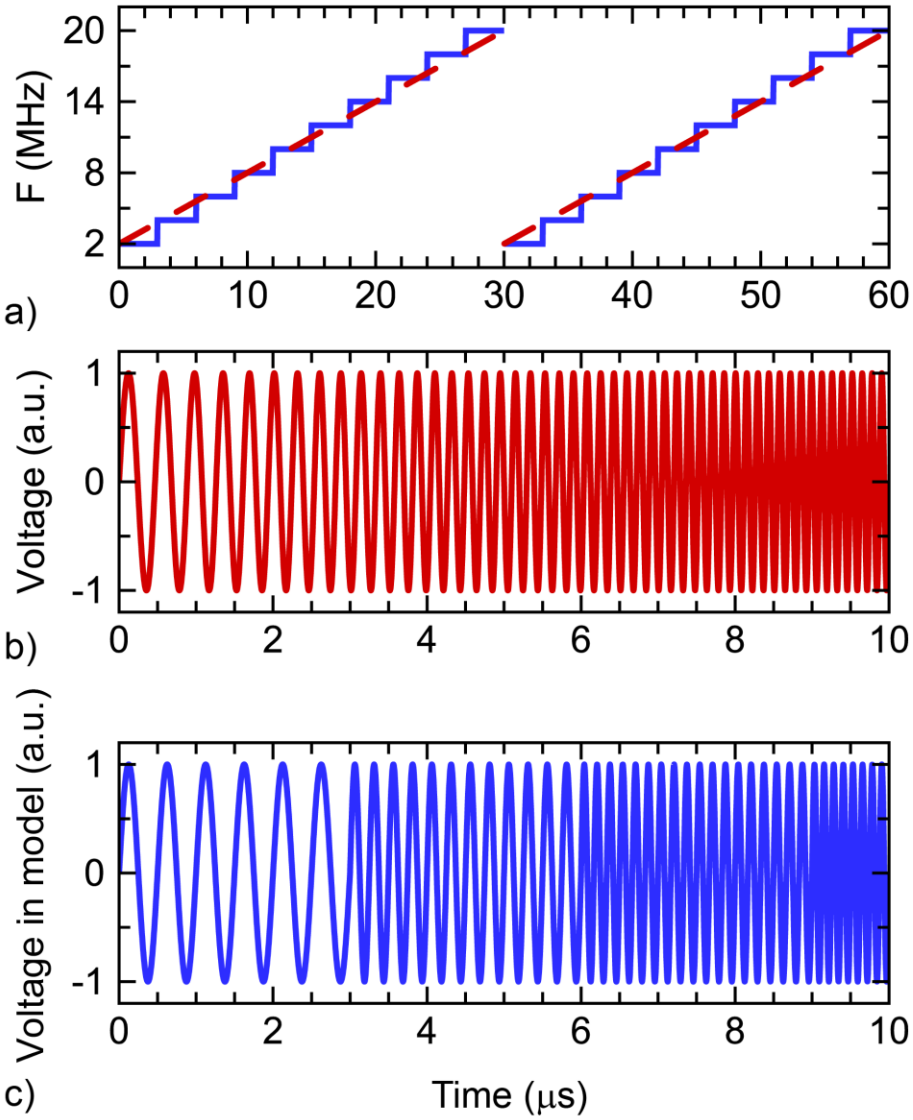

Figure 4-2. Typical voltage and frequency waveforms. a) Chirped frequencies used in this work (blue) are shown compared to a true linear chirp (red), 2-20 MHz repeated every 30 μs. This simplification can be checked by comparing the chirp in Fig. 4-1a to the true voltage waveform (arbitrary units), shown in b), to the simplified voltage waveform in c).

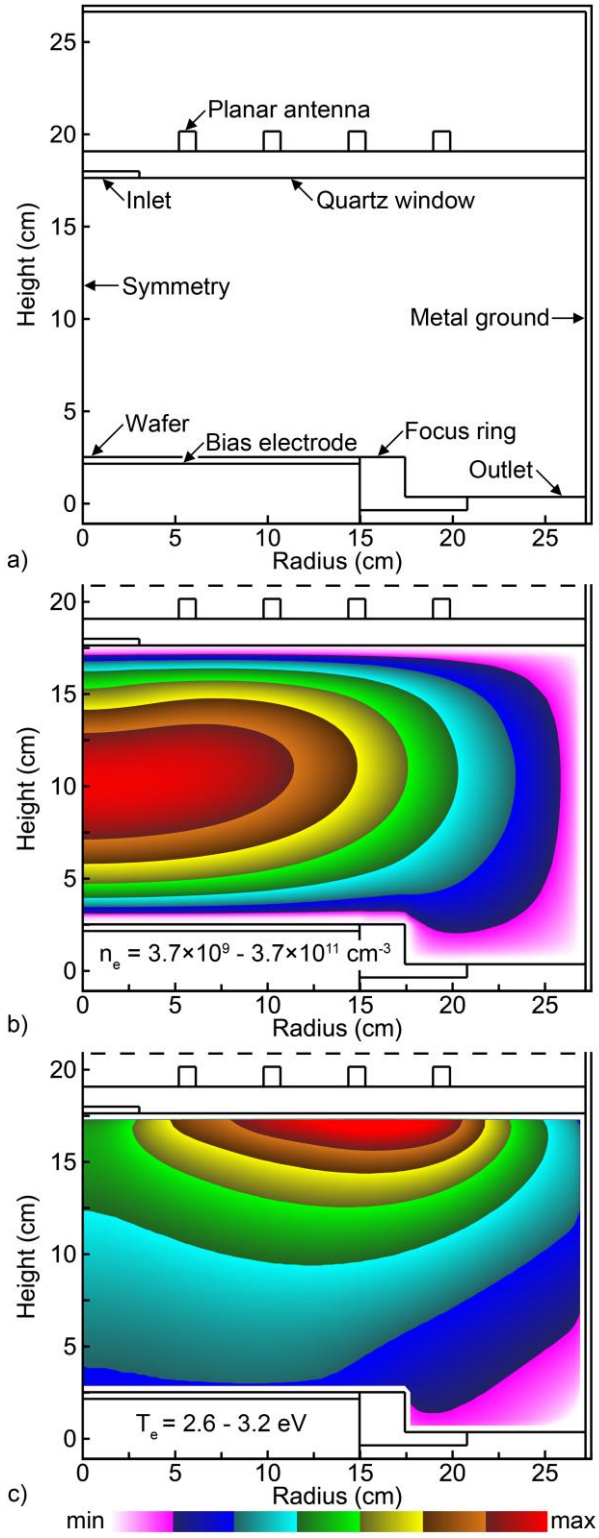

Figure 4-3. Plasma parameters for the base case. a) Schematic of the cylindrically symmetric ICP chamber used in the model. Computed b) n_e, having a maximum density 3.7×10^{11} cm^{-3} and c) T_e over the range of 2.6 - 3.2 eV. n_e and T_e are essentially constant over the chirped period.

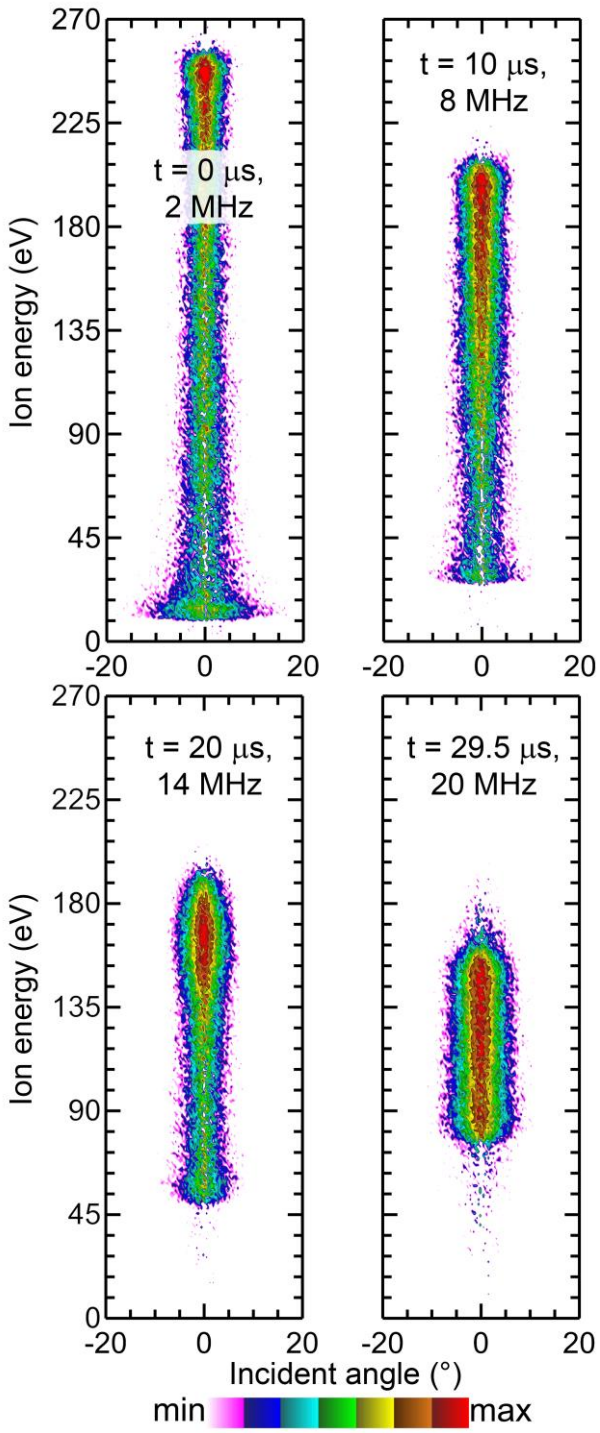

Figure 4-4. Ion Energy and Angular Distributions for Ar^+ sampled over 0.5 μs at times during the chirp period with the frequencies noted for each time. The IEADs exhibit a general decrease in peak ion energy and increase in minimum ion energy as the frequency increases over the chirp.

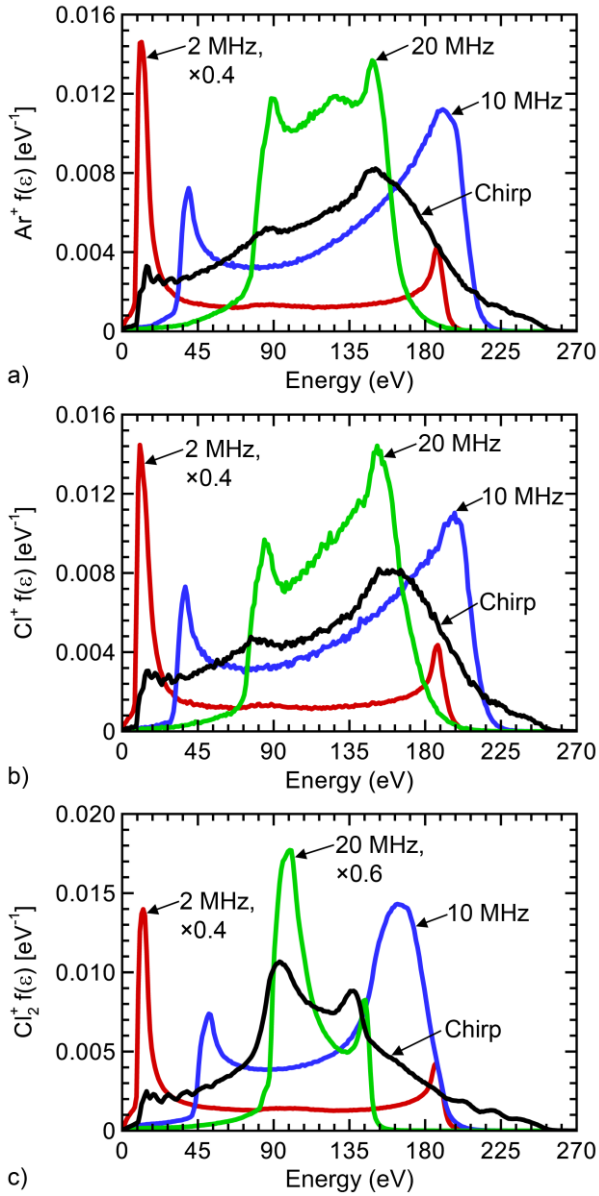

Figure 4-5. Time averaged IEDs for the base chirped case for a) Ar^+, b) Cl^+, and c) Cl_2^+. The chirped results (black) are compared to IEDs produced with constant frequency: 2 MHz (red), 10 MHz (blue), and 20 MHz (green).

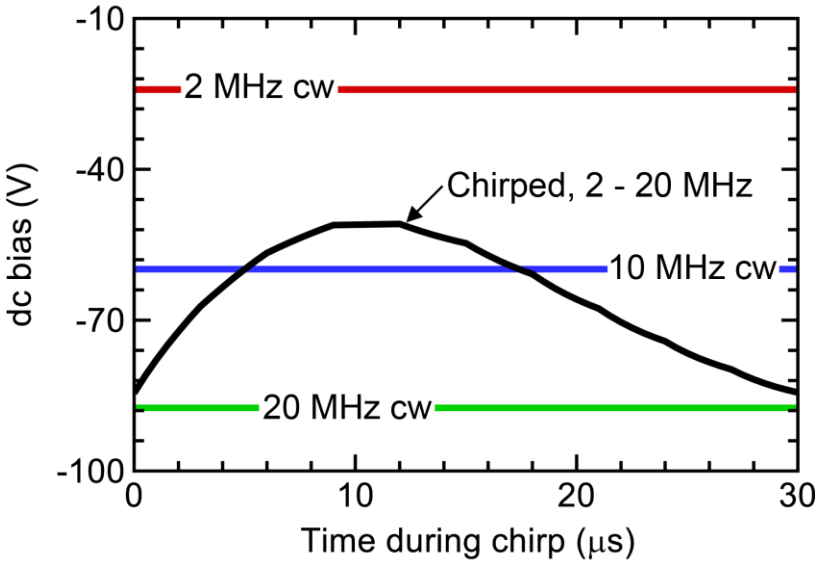

Figure 4-6. Transient dc bias on the blocking capacitor for the chirped case (black), compared to constant frequency cases: 2 MHz (red), 10 MHz (blue), and 20 MHz (green). The dc bias is dynamic when using a chirp.

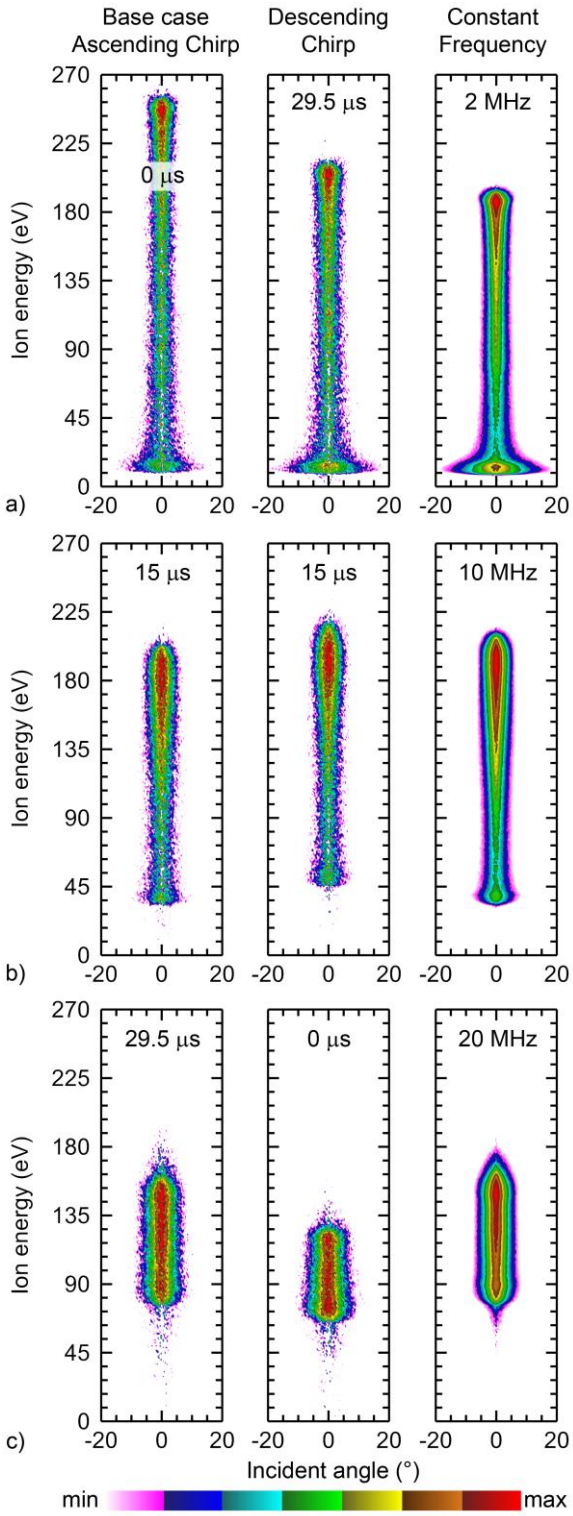

Figure 4-7. Time resolved IEADs for Ar^+ for the base case having an ascending chirp (column 1) and a descending chirp (column 2), compared to the IEAD produced with a constant frequency (column 3). The IEADs are shown at the same frequencies, a) 2 MHz, b) 10 MHz and c) 20 MHz. Note that these IEADs then correspond to different times during the chirp cycle for the ascending and descending chirps (noted in each frame).

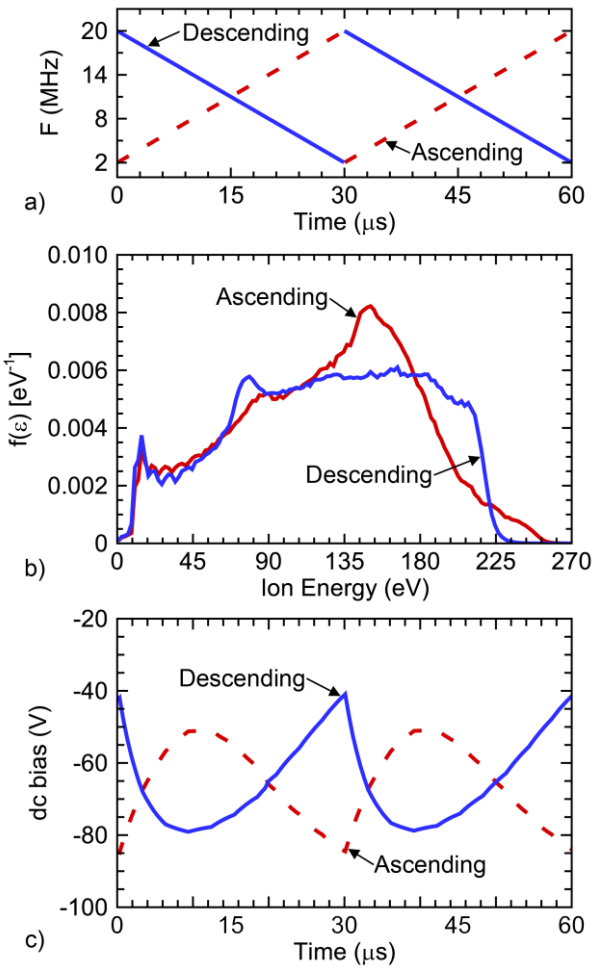

Figure 4-8. Comparisons of ascending and descending chirps for base case conditions. a) Frequencies for ascending and descending chirps. b) Time averaged IEDs for Ar^+ and c) dc bias. The differences in IEDs result from contrasting transients in the dc bias.

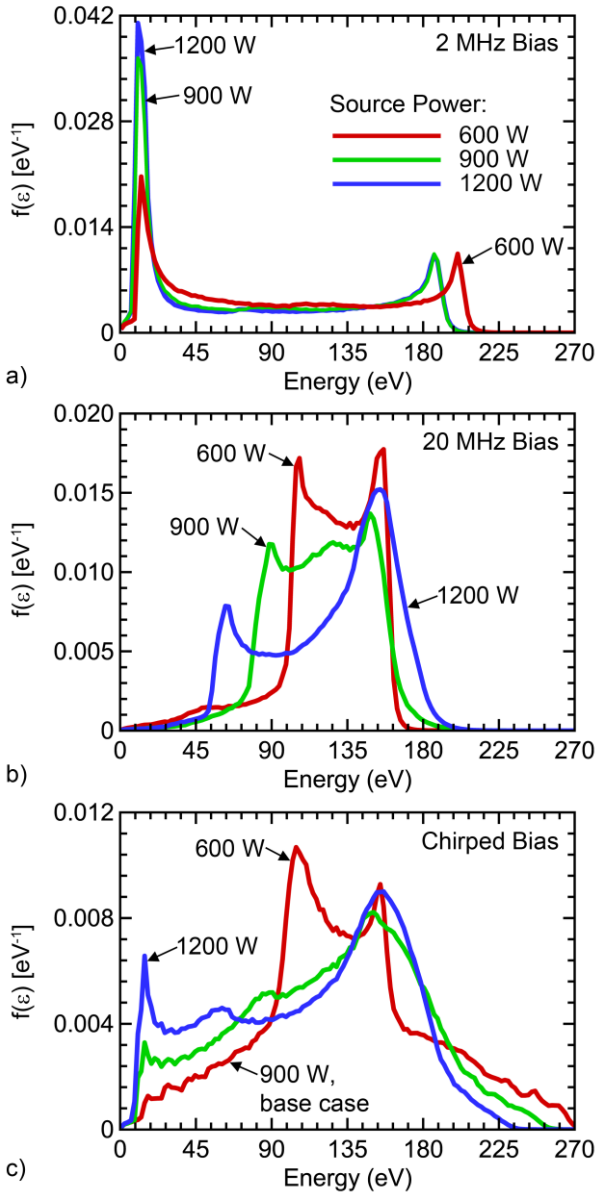

Figure 4-9. IEDs for Ar^+ as a function of ICP source power (600 - 1200 W) for different bias waveforms: a) 2 MHz, b) 20 MHz, and c) ascending chirp (2-20 MHz) with V_{rf} = 150 V.

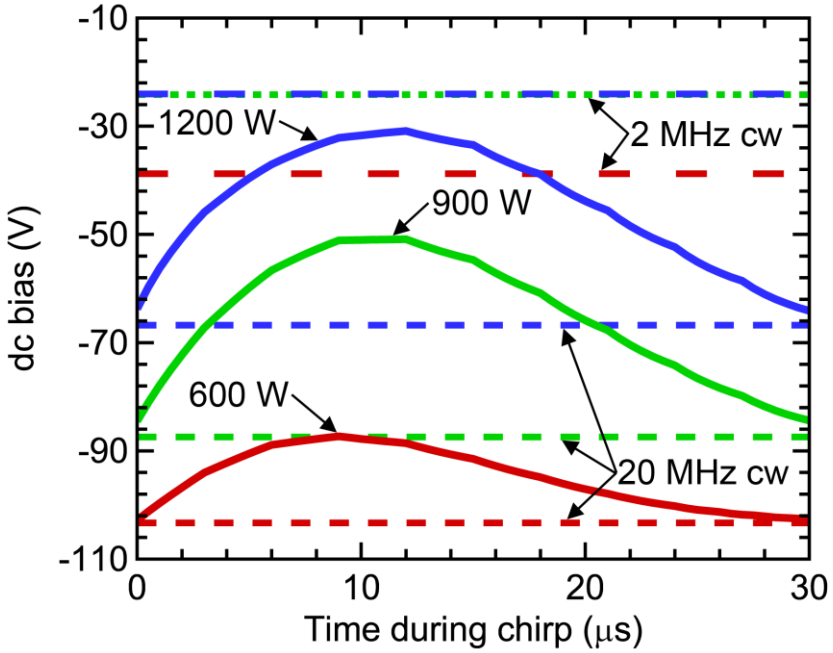

Figure 4-10. dc bias on the blocking capacitor as a function of source power (600 - 1200 W) for 2 MHz, 20 MHz, and an ascending chirped substrate bias (2 - 20 MHz).

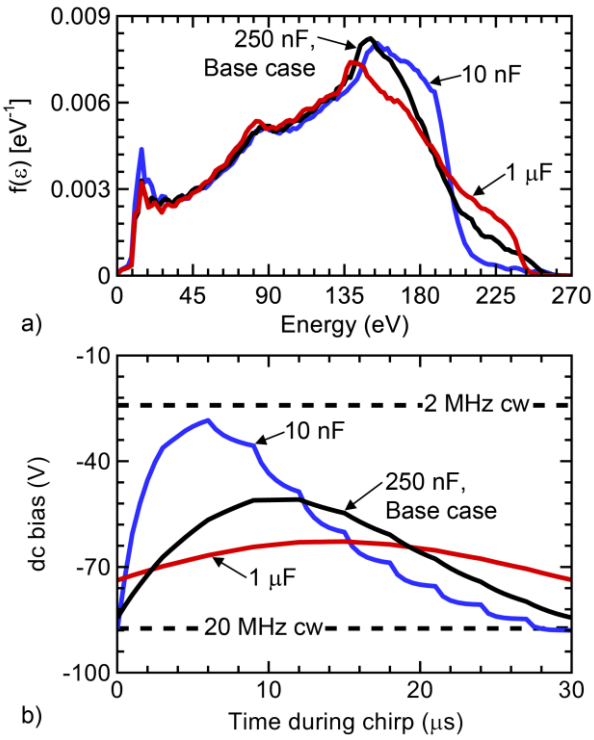

Figure 4-11. Plasma properties for the ascending chirp (150 V, 2 - 20 MHz, repeated 30 μs) as a function of blocking capacitor sizes: 10 nF, 250 nF (base case), and 1 μF (red). a) IEDs for Ar^+ and b) dc bias. The dc bias oscillates between the values set by the cw extreme frequencies without reaching a steady-state value. The dc bias for the smaller capacitor approaches these extreme values.

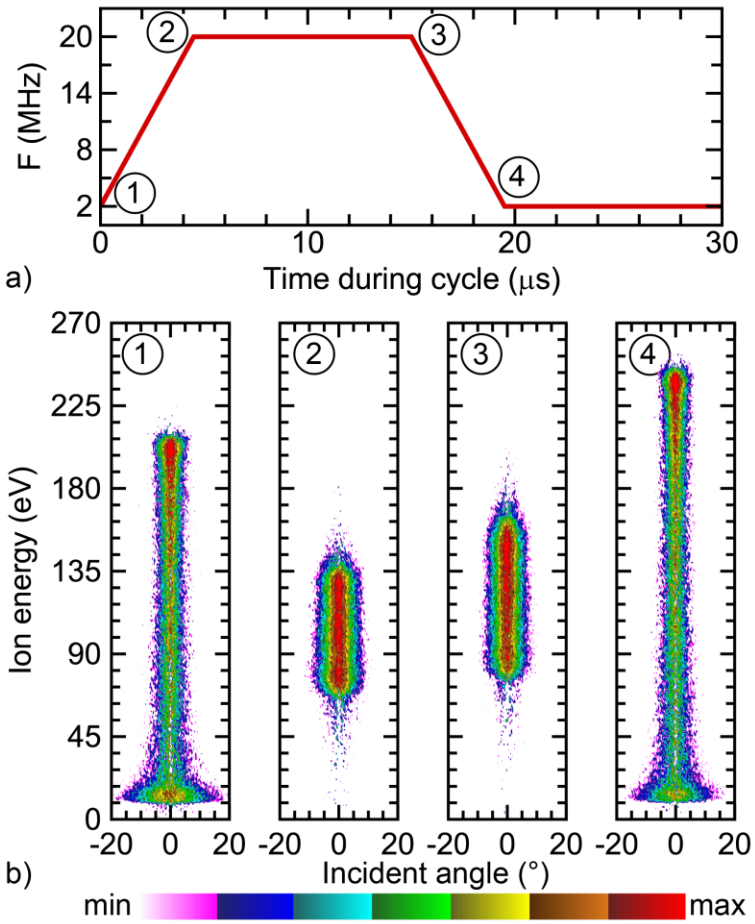

Figure 4-12. A custom chirp waveform for customizing IEADs. a) Frequency of custom chirped waveform and b) IEADs for Ar^+ sampled over 0.5 μs at times during this repeated period. Ion energies shift in energy even when the same frequency is applied (points 1 and 4 for 2 MHz; and points 2 and 3 for 20 MHz) due to the dynamics of the dc bias.

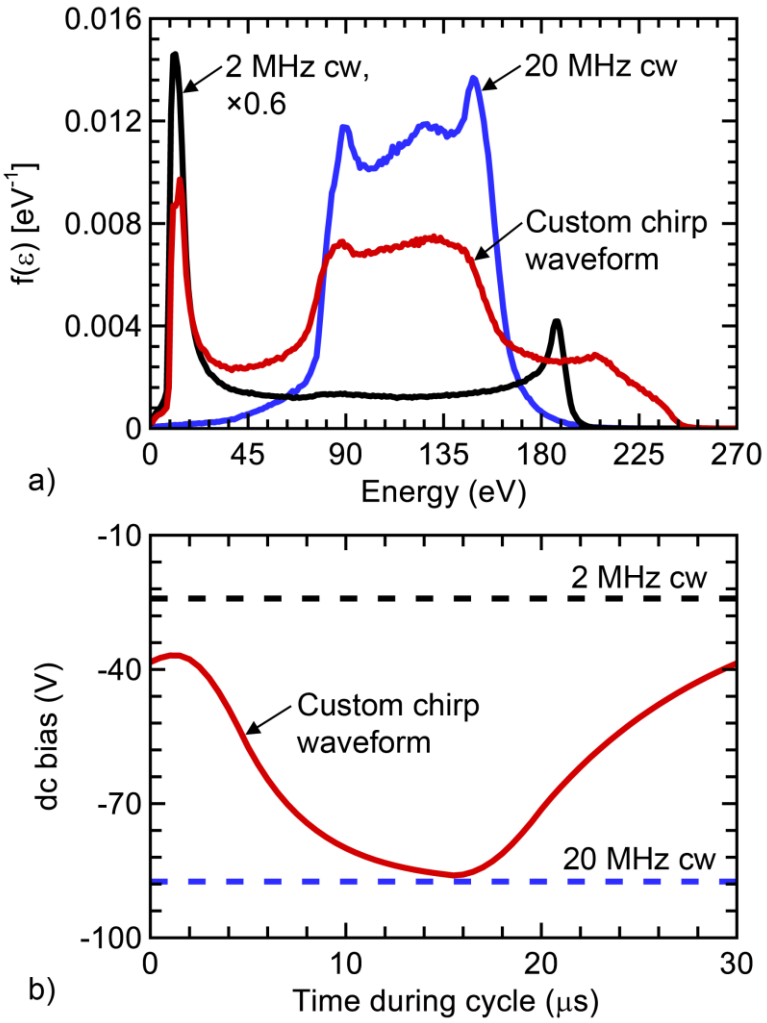

Figure 4-13. Plasma properties for the custom chirp waveform. a) Time averaged IEDs for Ar^+ for the 30 μs custom frequency waveform compared to IEDs for constant frequencies (2 MHz and 20 MHz). b) Transient bias on the blocking capacitor, producing shifts in the IEDs for the same frequencies.

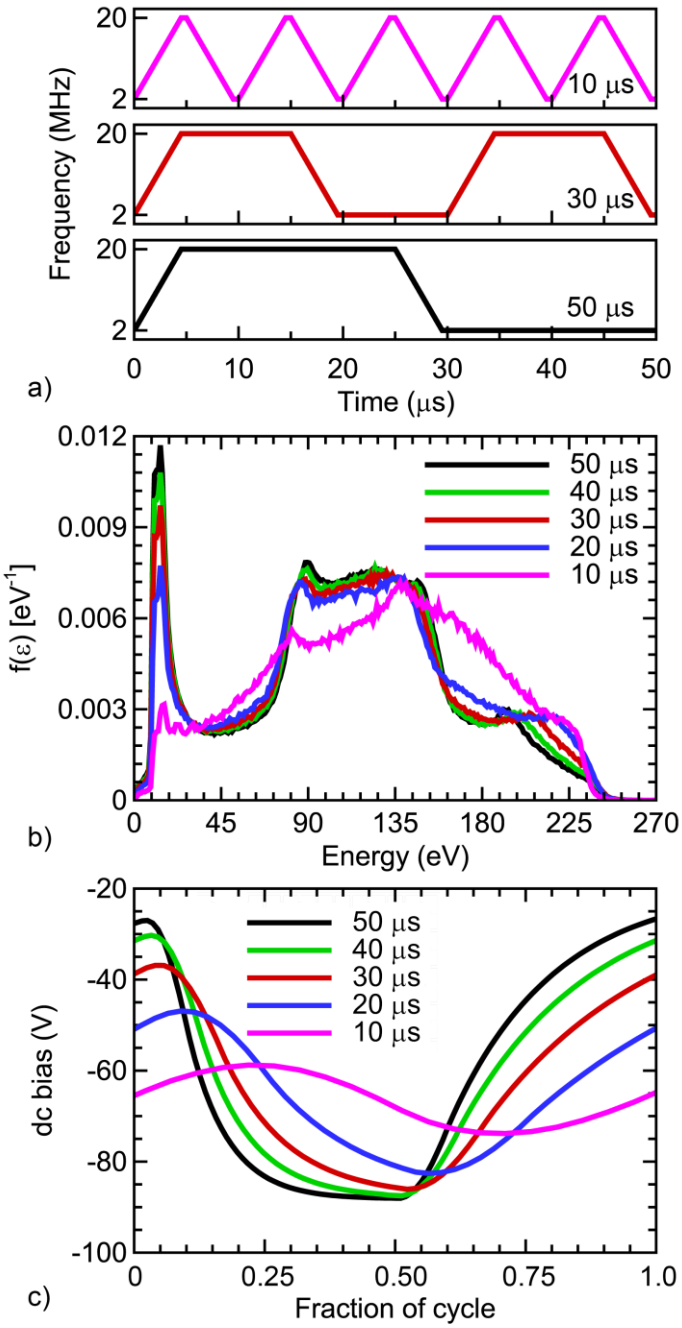

Figure 4-14. Selection of custom frequency waveforms. a) Custom frequency waveforms varying the time spent holding the extreme frequencies by the length of the chip period. b) IEDs for Ar^+ for different chirp periods of 10 μs to 50 μs (varying times holding the extreme frequencies). c) The transient dc bias for chirp periods 10 μs to 50 μs. Holding the extreme frequencies for less time results in a less transient dc bias.

4.6 References

[1] J. Hopwood, Plasma Sources Sci. Technol. **1,** 109 (1992).

[2] D. J. Economou, Thin Solid Films **365,** 348 (2000).

[3] V. M. Donnelly and A. Kornblit, J. Vac. Sci. Technol. A Vacuum, Surfaces, Film. **31,** 050825 (2013).

[4] H. Shin, W. Zhu, L. Xu, V. M. Donnelly and D. J. Economou, Plasma Sources Sci. Technol. **20,** 055001 (2011).

[5] S.-B. Wang and A. E. Wendt, J. Appl. Phys. **88,** 643 (2000).

[6] P. Diomede, D. J. Economou and V. M. Donnelly, J. Appl. Phys. **109,** 083302 (2011).

[7] T. Lafleur, Plasma Sources Sci. Technol. **25,** 013001 (2016).

[8] A. Derzsi, B. Bruneau, A. R. Gibson, E. Johnson, D. O'Connell, T. Gans, J.-P. Booth and Z. Donkó, Plasma Sources Sci. Technol. **26,** 34002 (2017).

[9] P. C. Boyle, A. R. Ellingboe and M. M. Turner, J. Phys. D. Appl. Phys. **37,** 697 (2004).

[10] V. Georgieva and A. Bogaerts, J. Appl. Phys. **98,** 23308 (2005).

[11] S. H. Lee, P. K. Tiwari and J. K. Lee, Plasma Sources Sci. Technol. **18,** 025024 (2009).

[12] J. Schulze, E. Schüngel, Z. Donkó and U. Czarnetzki, Plasma Sources Sci. Technol. **20,** 015017 (2011).

[13] A. Agarwal, P. J. Stout, S. Banna, S. Rauf, K. Tokashiki, J.-Y. Lee and K. Collins, J. Appl. Phys. **106,** 103305 (2009).

[14] S. Banna, A. Agarwal, G. Cunge, M. Darnon, E. Pargon and O. Joubert, J. Vac. Sci. Technol. A Vacuum, Surfaces, Film. **30,** 040801 (2012).

[15] M. Brihoum, G. Cunge, M. Darnon, D. Gahan, O. Joubert and N. S. J. Braithwaite, J. Vac. Sci. Technol. A Vacuum, Surfaces, Film. **31,** 020604 (2013).

[16] C. Petit-Etienne, M. Darnon, P. Bodart, M. Fouchier, G. Cunge, E. Pargon, L. Vallier, O. Joubert and S. Banna, J. Vac. Sci. Technol. B, Nanotechnol. Microelectron. Mater. Process. Meas. Phenom. **31,** 011201 (2013).

[17] D. J. Economou, J. Phys. D. Appl. Phys. **47,** 303001 (2014).

[18] B. G. Heil, U. Czarnetzki, R. P. Brinkmann and T. Mussenbrock, J. Phys. D. Appl. Phys. **41,** 165202 (2008).

[19] J. Schulze, E. Schüngel, U. Czarnetzki, M. Gebhardt, R. P. Brinkmann and T. Mussenbrock, Appl. Phys. Lett. **98,** 31501 (2011).

[20] T. Lafleur, P. Chabert, M. M. Turner and J. P. Booth, Plasma Sources Sci. Technol. **22,** 065013 (2013).

[21] B. Bruneau, T. Lafleur, J.-P. Booth and E. Johnson, Plasma Sources Sci. Technol. **25,** 025006 (2016).

[22] R. J. Shul, G. B. McClellan, S. A. Casalnuovo, D. J. Rieger, S. J. Pearton, C. Constantine, C. Barratt, R. F. K. Jr., C. Tran and M. Schurman, Appl. Phys. Lett. **69,** 1119 (1996).

[23] J.-H. Kim, Y.-H. Shin and K.-H. Chung, Thin Solid Films **435,** 288 (2003).

[24] H.-C. Lee, M.-H. Lee and C.-W. Chung, Appl. Phys. Lett. **96,** 71501 (2010).

[25] A. Metze, D. W. Ernie and H. J. Oskam, J. Appl. Phys. **65,** 993 (1989).

[26] E. Kawamura, V. Vahedi, M. A. Lieberman and C. K. Birdsall, Plasma Sources Sci. Technol. **8,** R45 (1999).

[27] M. J. Kushner, J. Phys. D. Appl. Phys. **42,** 194013 (2009).

[28] P. Tian and M. J. Kushner, Plasma Sources Sci. Technol. **26,** 024005 (2017).

[29] T. Fukasawa, T. Nouda, A. Nakamura, H. Shindo and Y. Horiike, Jpn. J. Appl. Phys. **32,** 6076 (1993).

[30] A. Aanesland, C. Charles, R. W. Boswell and M. A. Lieberman, Phys. Plasmas **12,** 103505 (2005).

[31] I. R. Saraf, M. J. Goeckner, B. E. Goodlin, K. H. R. Kirmse, C. T. Nelson and L. J. Overzet, J. Vac. Sci. Technol. B, Nanotechnol. Microelectron. Mater. Process. Meas. Phenom. **31,** 11208 (2013).

Chapter 5 Particle Trapping Theory and Model Validation[††]

Low-pressure nonthermal flowing plasmas are widely used for the gas-phase synthesis of nanoparticles and quantum dots of materials that are difficult or impractical to synthesize using other techniques. To date, the impact of temporary electrostatic particle trapping in these plasmas has not been recognized, a process that may be leveraged to control particle properties. Here, we present experimental and computational evidence that, during their growth in the plasma, sub-10 nm silicon particles become temporarily confined in an electrostatic trap in radio-frequency excited plasmas until they grow to a size at which the increasing drag force imparted by the flowing gas entrains the particles, carrying them out of the trap. We demonstrate that this trapping enables the size filtering of the synthesized particles, leading to highly monodisperse particle sizes, as well as the electrostatic focusing of the particles onto the reactor centerline. Understanding of the mechanisms and utilization of such particle trapping will enable the design of plasma processes with improved size control and the ability to grow heterostructured nanoparticles. Separate experiments were conducted at the University of Minnesota from Prof. Kortshagen's group, and at Washington University at St. Louis from Prof. Thimsen's research group. Reactor scale modeling of the coupled plasma and nanoparticle system was done at the University of Michigan from Prof. Kushner's research group. A separate computational model was developed at the University of Minnesota for additional theoretical insight.

[††]Results and portions of the text that appear in this chapter were previously published in the paper by Z. Xiong *et al.*, "Particle trapping, size-filtering, and focusing in the nonthermal plasma synthesis of sub-10 nanometer particles" J. Phys. D: Appl. Phys. **55,** 235202 (2022).

5.1 Introduction

The term dusty plasma refers to a weakly ionized gas containing solid particulates [1,2]. Over the past two decades, nonthermal dusty plasmas in low pressure flowing systems have become critically important sources for the synthesis of nanoparticles and quantum dots [3–8]. In these plasmas, energetic plasma electrons decompose molecular gaseous precursors, producing radicals, which lead to the nucleation and growth of nanoparticles. Based on the extreme nonequilibrium in these plasmas, with the temperature of electrons (several eV) exceeding the temperature of the gas atoms and plasma ions (near ambient) by about two orders of magnitude, dusty plasmas offer the ability to synthesize crystalline nanoparticles even of high melting point, including covalently bonded materials. This capability is due to the selective heating of nanoparticles to temperatures far above the gas temperature [8] which enables the synthesis of nanocrystals that are commonly inaccessible to liquid phase synthesis [9–11]. Once the nanoparticles growing in the plasma reach a certain minimum size, they acquire a negative charge based on the higher mobility of free plasma electrons compared to that of plasma ions which suppresses agglomeration of larger nanoparticles as a result of the resulting Coulombic repulsion [12,13]. This mechanism is widely credited with the ability of plasmas to produce nanoparticles with much more monodisperse size distributions than other gas-phase approaches [8].

Dust particles immersed in plasmas are subject to a variety of forces, including electrostatic, gas and ion drag, thermophoresis, Brownian motion, and gravity [14–22]. The relative magnitude of each force depends on the size of the particle and the plasma conditions. The plasmas of interest here are produced by application of radio frequency (RF) voltages, typically sustained in cylindrical reactors of up to a few cm in diameter and 10-15 cm length, operating at pressures of a few Torr with nominal power deposition of up to about 50 W. The electrostatic

force originates from the negative charge acquired by dust grains and the electric fields in the plasma. These electric fields are either ambipolar in nature, self-generated to confine the highly mobile electrons in a way that the plasma bulk is charged slightly positively compared to the surrounding reactor walls, or due to applied voltages, which for the plasmas of interest produce moderate electric fields of only a few V-cm^{-1} in the bulk plasma and hundreds of V-cm^{-1} in the bounding sheaths. In dusty plasmas containing micron-sized particles, particles can carry many thousands of elementary charges and electrostatic forces produced by the RF sheaths at the plasma boundary can be strong enough to balance the gravitational and ion drag forces, leading to particle levitation and trapping close to the plasma boundary sheath [2,23]. In semiconductor processing, this trapping of particles was recognized as a problem as early as the 1990s [24], as dust particles that form during plasma processing can accumulate in these electrostatic particle traps and then drop onto the wafer being processed after the plasma is turned off.

Plasma reactors used for nanoparticle synthesis are fundamentally different from reactors used in semiconductor processing and those typically used to study the fundamental properties of dusty plasmas which are parallel plate, capacitively coupled systems [3,4,25,26]. As noted above and shown schematically in Fig. 5-1a, the plasmas typically used for nanoparticle synthesis are based on tubular laminar flow reactors, in which a plasma is excited either by capacitive or inductive coupling of RF power. Gas flow rates are commonly large so that the gas residence time in the reactor is on the order of milliseconds in order to limit particle growth to the nanometer size range.

For nanometer-sized particles, gravity does not play a significant role. Trapping, if it were to occur, would be the result of the balance between the electrostatic force and opposing forces such as the drag of the flowing neutral gas, the ion drag, and the thermophoretic force [14,27]. In

this context, trapping refers to nanoparticles which are temporarily quasi-stationary within the reactor and which continue to grow by reactions with radicals while in the trap. Particles are, indeed, collected as they flow out of the reactor so any trapping would be temporary or dynamic. However, to date, the likelihood and leveraging of particle trapping in the synthesis of nanoparticles with diameters of less than tens of nm has not been either realized or acknowledged. This lack of acknowledgement has resulted mainly from two reasons:

• The high concentration of nanoparticles during particle nucleation: during the initial nanoparticle nucleation event, the concentration of nanoparticles of less than a few nm in diameter commonly can exceed that of positive ions and plasma electrons by more than an order of magnitude [13]. These conditions imply that the average charge of nanoparticles in a plasma is less than one elementary charge. While the nanoparticle charge fluctuates stochastically due to the random collection of electrons and ions [12], nanoparticles are neutral for a significant fraction of time while in the plasma. (Large particles with sizes exceeding many tens of nm will be permanently negatively charged.) With particles of a few nm being neutral for long periods of time, they would presumedly not be subject to electrostatic trapping while still being subject to neutral drag and thermophoretic forces.

• In many studies, it has been found that the average nanoparticle size correlates nearly linearly with the residence time of particles in the plasma (and inversely with the gas flow velocity) [28]. These observations have been interpreted to mean that particles, while growing, travel through the reactor with the gas flow akin to a plug flow reactor and that the particle position in the reactor varies with time in a linear fashion. These processes are schematically shown in Fig. 5-1b and 5-1c.

There have been limited reports of nanoparticle trapping during plasma synthesis. Nanoparticle trapping was observed in a laminar flow reactor with small gas flow speeds through the tube geared towards synthesizing large nanocrystals of several tens of nanometers in diameter [29]. This observation, a priori, was not inconsistent with the above reasoning because such large nanoparticles carry several tens of elementary charges and, in spite of stochastic charge fluctuations, are likely negative all of the time. Furthermore, the gas drag that acts to remove particles from the electrostatic traps was small due to the low flow speeds. A recent simulation study was the first to point to the possibility of trapping even of particles even in the sub-10 nm regime [30]. While these simulations did not model the high particle concentrations that are present in actual synthesis reactors, they clearly indicated that even small particles that are electrically neutral for a fraction of their time in the plasma can experience trapping.

The present study provides the first experimental evidence, with computational verification, of the trapping of sub-10 nm particles during particle synthesis and introduces a new paradigm of utilizing trapping in nonthermal plasma synthesis for the size filtering of nanoparticles. The demonstration system is the growth of Si nanoparticles using Ar/SiH_4 gas mixtures in RF sustained plasmas at pressures of 1.1-6.5 Torr and powers of 5-20 W. Trapping was independently observed in multiple different reactor set-ups by two different research groups using different experimental techniques to analyze the presence of trapped particles. Experimental results were interpreted based on parametric Monte Carlo simulations and verified with full scale plasma reactor simulations.

5.2 Experimental Approach and Reactors

In situ detection of trapped sub-10 nm particles poses great difficulties. For larger particles, visible laser light scattering (LLS) is widely used [2,23]. However, the scattered intensity for LLS rapidly becomes untenably small as the particle size is reduced. In particular, the Rayleigh scattering cross section scales with the sixth power of the particle diameter [31]. To overcome this unfavorable scaling, the only in situ detection method that we know of and that provides good sensitivity for particles smaller than 10 nm, is a destructive method—laser induced particle explosive evaporation (LIPEE) [32]. In this method, the diagnostic is not elastically scattered laser light, but rather the thermal glow from particles that are suddenly heated and evaporated by a pulsed laser. This LIPEE method has not been widely used in the dusty plasma literature since it was reported in 1994. This lack of use is perhaps due to the equipment that is required, which includes a powerful pulsed ultraviolet laser along with sensitive high-speed optical detection. For these reasons, our approach relies not on in situ detection of the particles, but instead on ex situ measurements.

Our experimental approach is based on the scheme detailed in Fig. 5-1 utilizing a time-resolved measurement of the particle mass at the exit of the reactor. For simplicity, we neglect in this figure the influence of radial losses of particles and chemical precursors, which occurs in an actual reactor, but will not significantly affect the argument that we present. If particle trapping during synthesis does not occur, the currently predominant view, particles move through the reactor with time in a linear fashion following the gas flow (Fig. 5-1b and 5-1c) while growing by reactions with the locally available precursor radicals. When radial losses are neglected, the particle mass density, defined by the mass density of the forming nanoparticles and that of the unreacted precursor, is constant along the reactor (Fig. 5-1d). Towards the exit of the reactor, the

majority of the mass that has been transformed into particles can be collected and their mass measured. If the plasma is turned off, particle formation ceases and the collection of particles ceases after one gas transit time through the reactor following the moment of plasma turn-off (Fig. 5-1e).

Particle trapping significantly changes this picture. If nanoparticles are temporarily trapped, their motion through the plasma reactor is no longer linear in time (Fig. 5-1f and 5-1g). Particles are temporarily confined in a trapping zone but continue to grow due to the presence of the radical precursors. The electrostatic trapping force is roughly proportional to the particle diameter. However, in the Knudsen number range of relevance to low pressure plasmas, the gas drag force is proportional to the square of the particle diameter [33]. As a result, particles will be forced from the trap once they reach a critical size when drag by the gas flow dominates. However, since particles are temporarily stopped in their motion through the reactor, the particle mass density within the trapping zone exceeds that of the particles outside the trapping region (Fig. 5-1h). If the plasma is turned off and the particle mass at the reactor exit is measured, the trapped particles will appear as a peak in the particle mass leaving the reactor after the plasma is turned off (Fig. 5-1i).

To evaluate these two scenarios, three different plasma reactors were designed using different experimental methodologies to measure the particle mass leaving the reactor over time. The reactors are shown schematically in Fig. 5-2. The first reactor was resident at the University of Minnesota (UMN1). The plasma was generated by applying capacitively coupled RF power (frequency 13.56 MHz) to the quartz tubular reactor with 2.5 cm external diameter (2.2 cm internal diameter) and 20 cm length. The power was applied with a pair of ring electrodes 1 cm wide and separated by 2 cm at their centers. The operating conditions for the base case are an RF power of 20 W, flow rate of Ar/He/SiH_4 = 30/4.75/0.25 sccm and gas pressure of 1.1 Torr.

The nanoparticle cloud resulting from plasma synthesis was sent through a slit-shaped nozzle (0.5 mm × 12 mm) at the reactor exit and focused into a curtain-shaped beam of nanoparticles. These particles were deposited on a glass or silicon substrate that was translated through the nanoparticle beam at a constant velocity by a linear direct current (DC) servomotor.

The deposited particle mass was evaluated by measuring optical absorption of the particles deposited on a transparent glass substrate moving at a constant speed of 5 mm-s^{-1}. The plasma was turned off during the substrate translation to collect both particles leaving the reactor in steady state operation and trapped particles. The substrate with deposited silicon nanoparticles was then placed on one exit port of a Labsphere 10 cm integrating sphere, illuminated with a light emitting diode (LED) emitting at 390 nm, and imaged using a digital camera (NIKON D7100). Raw files were converted to 16-bit TIFF format and the transmitted light intensity was measured as line intensity plots in ImageJ, using a bare glass substrate as a baseline. Absorbance was obtained as $A = -\log(I_t/I_0)$, where I_t is the transmitted light intensity and I_0 is the incident light intensity.

The delay time of the arrival of the trapped particles at the substrate after turning off the plasma was measured by a 240 frames-per-second camera (iPhone 12, Slo-mo mode). Accuracy of the arrival time was estimated as ±1 frame (1/240 s). The axial trapping position was determined by multiplying the arrival time by the gas flow velocity, which was determined by fitting particle arrival times versus the different axial positions of the electrode pair.

A second reactor similar in design to UMN1, also resident at the University of Minnesota was used to evaluate the consequences of particle growth on precursor density and deposition on the walls of the reactor. This reactor, UMN2, was a quartz tubular reactor having two diameters. The power was applied to the narrower portion of the tube, 0.7 cm internal diameter. The tube expanded downstream to 2.2 cm internal diameter. The plasma conditions were a gas pressure of

0.8–0.9 Torr and gas mixture of Ar/He/SiH_4 that was varied from 30/6.65/0.35 sccm to 30/13.3/0.7 sccm. RF power of 50 W was applied to a pair of 1 cm wide electrodes, separated by 2 cm center-to-center, that was located 2 cm upstream of the tube expansion.

The third reactor was resident at Washington University in St Louis (WUSTL). Similar to the UMN1 reactor, the plasma was generated by applying capacitively coupled RF power (frequency 13.56 MHz) to the quartz tubular reactor with 3.2 cm internal diameter. The power was applied with a pair of aluminum ring electrodes 1.4 cm wide and separated by 2.65 cm at their centers. The operating conditions for the base case are an RF power of 5 W, flow rate of Ar/He/SiH_4 = 51/0.991/0.009 sccm and gas pressure of 6.5 Torr. Following the reactor, 2.7% of the total flow was diverted to a quartz crystal microbalance (QCM) impactor. A 150 μm orifice was used to impact synthesized particles onto the quartz crystal. The mass loading on the quartz crystal was determined using the Sauerbrey equation [34]:

$$\Delta m = -\Delta f \left(\frac{A\sqrt{\rho_q \mu_q}}{2 f_o^2} \right) \tag{5.1}$$

where Δm is the change in the mass loading of the quartz crystal, Δf is the change in the quartz crystal resonance frequency A is the effective crystal area (6.5 mm), ρ_q is the density of the quartz crystal (2.65 g-cm^{-3}), μ_q is the shear modulus of the quartz crystal (2.95×10^{11} g-cm^{-1}s^{-2}), and f_o is the resonant frequency of the fundamental mode of the quartz crystal (6 MHz).

Transmission electron microscope (TEM) imaging of the collected particles was performed using an FEI Talos F200x operating at an accelerating voltage of 200 kV as well as an FEI Tecnai T12 operating at 120 kV. To determine particle size distributions, nanoparticles were deposited directly onto thin holey carbon coated Cu TEM grids translated under the curtain-shaped particle

beam in reactor UMN1. The diameters of 300 particles were then measured with ImageJ and their size distribution fit to a log-normal size distribution.

5.3 Observations of Nanoparticle Trapping

Silicon nanoparticles deposited on a silicon substrate translated with constant velocity under the exit nozzle of the UMN1 reactor are shown in Fig. 5-3a. Initially, the particle deposition is essentially uniform (except for some nonuniformities caused by the not entirely constant speed of the motor drive). After turning off the plasma and emptying of the electrostatic trap, the deposition of a significantly larger amount of particles was observed corresponding to the arrival of trapped particles, consistent with the scenario described in Fig. 5-1f–i. After the arrival of the trapped particles, the deposition of additional particles was observed corresponding to particles that were upstream of the trapping zone when the plasma was turned off. The curvature of the deposition in vertical direction is assumed to be caused by the laminar flow in the reactor with there being little slip at the surface of the tube. These conditions result in the gas close to the reactor wall to have a lower flow speed than at the center of the tube. The amount of mass corresponding to the trapped particles is about five times that of the particles leaving the reactor in steady state, shown in Fig. 5-3b. The experiment was repeated for three different axial positions of the electrodes that would in turn determine the location of the electrostatic trap. From the delay of the arrival of the trapped particles with respect to the moment of plasma turn-off, the gas flow velocity was determined which then enabled the computation of the axial position of the trapped particles. As shown in Fig. 5-3c, the trapping zone is located about 1.6 cm below the powered top electrode.

Results from the WUSTL plasma reactor, which was operated at significantly higher pressure than the UMN1 reactor, are shown in Fig. 5-3d and 5.3e. In this reactor, the arrival of

particles after leaving the reactor was significantly delayed due to the low flow rate in the gas lines leading to the QCM. A significant increase in the deposited mass after plasma turnoff, indicative of the arrival of trapped particles, is shown in Fig. 5-3c. The mass deposition rate after the plasma was turned off was almost two orders of magnitude larger than the deposition rate during the steady-state plasma on phase, as shown in Fig. 5-3e. This result suggests that the particle mass density in the particle trap is about a factor of 100 times larger than that outside of the trap. These results demonstrate that plasma parameters such as pressure and flow rates can be used to control the amount of particle mass that is trapped compared to that leaving in steady state.

It is also instructive to consider the deposition of a silicon film on the reactor walls, which occurs in actual reactors as an unwanted loss process of radicals, but was neglected in our simplified argument illustrated in Fig. 5-1. The silicon film deposition in a third plasma reactor, similar in design to the UMN1 reactor, which is typically used for the synthesis of sub-5 nm silicon particles, is shown in Fig. 5-4. For the higher flow rates associated with silicon nanocrystal formation ($Ar/He/SiH_4$ = 50/13.7/0.7 sccm), the deposition of a silicon film on the reactor walls is limited to the region upstream of the electrodes. If the silane precursor flow rate is lowered to a level that particle nucleation does not occur ($Ar/He/SiH_4$ = 50/6.65/0.35 sccm), and no particles are collected, the silicon film deposition is observed both upstream and downstream of the RF electrodes. These observations are consistent with the hypothesis that nanoparticles are trapped close to the RF electrodes at the higher silane flow rate. The trapped particles likely act as a sink for the silane precursor that leads to an almost complete precursor consumption in the region upstream and up to the RF electrodes. In the case of the lower silane flow, no particles form and the strong precursor sink around the electrodes is removed, leading to silicon deposition also downstream of the electrodes.

5.4 Evidence of Size Filtering

The sole observation of particle trapping during nonthermal plasma synthesis may be viewed as an interesting outcome of the plasma dynamics. However, its importance is significantly deeper because particle trapping acts as an inherent size filter in the plasma synthesis as particles need to reach a certain critical size before they can escape the particle trap. This concept is demonstrated in Fig. 5-5a which shows a TEM image of particles that are leaving the reactor in steady state operation. These are the particles that were trapped and grew to a size so that the gas drag overcame the electrostatic trapping force and liberated the particles from the trap. More than 300 particles were counted and their size distribution fit with a log-normal distribution with a mean size of 7.4 nm and a geometric standard deviation of 1.17. This geometric standard deviation is typical for nonthermal plasma synthesis but significantly smaller than those achieved in other gas-phase syntheses where nanoparticles are neutral and not prevented from agglomerating [35,36]. Particles shown in Fig. 5-5b were collected after the plasma turn-off and are representative of the trapped particle deposit shown in Fig. 5-3a. These particles exhibit a significant population of smaller particles that is not present in the particles that are collected in steady state. Accordingly, the log-normal size distribution of trapped particles has a mean size of 6 nm and a geometric standard deviation of 1.39. To our knowledge, this is the first demonstration of trapping acting as a size filter during the nonthermal plasma synthesis of sub-10 nm particles. Understanding this aspect may open new routes to designing plasma processes with even better size and composition control.

5.5 Parametric Monte Carlo Simulation of Particle Trapping

Particle charge and particle trajectories were simulated with a one-dimensional Monte Carlo code implemented in MATLAB, which is available in the supplemental material of the published article [37]. In this simulation, pseudoparticles of a specified diameter are initiated at the entrance to the plasma reactor. Their size is kept constant during the simulation. The simulation is based on the assumption that the plasma is quasi-neutral. Due to the large concentration of nanoparticles in the physical system, the vast majority of electrons resides on the particles. However, in our simulation, a single nanoparticle is simulated at a time; hence, the effect of the electron attachment to nanoparticles is parametrically represented by an electronegativity n_i/n_e, with n_i the positive ion density and n_e the free electron density. In nanoparticle forming argon-silane plasmas it has been observed that n_i often exceeds n_e by about two orders of magnitude, and that the density of negative ions is on the same order as n_e [38], because negative ions are consumed in particle nucleation. Hence, the charging of nanoparticles is described by the collection of electrons and positive ions, while negative ions are neglected.

The nanoparticle trajectories are integrated in time accounting for the gas drag force and electrostatic force until particles leave the reactor. Hence, an important input for this simulation is the time-averaged axial electric field profile, as the nanoparticles are too massive to follow the instantaneous RF electric field. An approximate electric field profile was derived by performing Comsol simulations for a pure argon plasma. The time averaged electric field derived from these simulations was approximated by the simplified profiles. The simulation ran cyclically with a time step Δt of 100 ns. At every time step, a new position and charge for a particle was calculated. The initial particle had no charge and had a position of 10 cm from the outlet. Orbital motion limited theory [39] was then used to calculate collision frequencies of the particle with ions and electrons

[40]. A specific event (collision with an ion or an electron) was chosen according to random Monte Carlo sampling. The Störmer–Verlet method [41] was applied to determine the particle trajectory, and a single Monte Carlo simulation was run for 5×10^6 timesteps.

Results of the model are shown in Fig. 5-6. With the exception of the results shown in Fig. 5-6f, simulations were performed for a typical positive ion density n_i of 5×10^{11} cm^{-3} and a free electron density n_e of 5×10^9 cm^{-3} resulting in an electronegativity $n_i/n_e = 100$. This degree of electronegativity is consistent with previous work on dusty plasmas forming silicon particles [42,43]. Plasma electrons can dissociatively attach to silane or directly attach to radicals to form negative SiH_x^- ions and attach to the nanoparticles, whose density can exceed the positive ion density. The fraction of time that nanoparticles of three different sizes are in a certain charge state is shown in Fig. 5-6a. Particles with a diameter of 1 nm are neutral or positively charged 78% of the time, while larger 5 nm particles are neutral 31% of the time. As a result of the long times that particles are neutral, one might conclude that small nanoparticles may not be trapped in the plasma.

The typical charging times are compared with the gas transit time through trapping region in Fig. 5-6b, defined by the pink shaded region in Fig. 5-6c with a length of about 1 cm. In this region, the electrostatic force opposes the gas drag force and increases up to a maximum at z = 4 cm. Particle charging is so fast that neutral particles are likely to become negatively charged again before they are convected out of the trapping zone. As a result, particles remain trapped, even if they are charged negatively only for a fraction of the time.

The trapping of particles in spite of their transient neutral states is demonstrated by the results in Fig. 5-6d, which shows the axial locations of 1, 3 and 5 nm particles with time for a gas flow velocity of 100 cm-s^{-1}. The smallest 1 nm particles enter the trapping zone and their position fluctuates in the axial direction as the particle charge changes. This is shown in the inset in Fig.

5-6d, where particles follow the gas flow when they are neutral, but are drawn upstream again when they acquire a negative charge. For these conditions, 1 nm particles remain trapped indefinitely. Somewhat larger 3 nm sized particles behave similarly, but they assume a position deeper in the particle trap because they require a larger electrostatic force to balance the gas drag force. Particles with a 5 nm diameter are not confined in the trap. The particles are slowed down by the electrostatic force, but the force is insufficient to trap the particles. In an actual plasma reactor, the particle size does not remain constant, but particles grow due to the deposition of precursor. This means that the smallest particles are initially trapped at the top of the trap at the smallest electric fields. As particles grow, they sink deeper into the trap where the electric field increases. Finally, the electric field will be insufficient to balance the increasing gas drag and particles will be released from the trap.

The influence of gas flow velocity on the critical size for particle detrapping is shown by the results in Fig. 5-6e. Since the gas drag force acting on trapped particles scales linearly with the gas flow speed, the critical size above which trapping does not occur varies inversely with the gas flow speed. The simulations reproduce the often observed linear dependence of particle size with the gas residence time in the reactor. However, the simulations suggest that the important time is not the residence time of the gas in the reactor but the extended time spent in the particle trap that allows particles to grow to larger sizes before leaving the trap.

The effect of plasma electronegativity on the critical size for detrapping is illustrated by the results in Fig. 5-6f. As electronegativity in the plasma is reduced, the critical size for detrapping increases. This is due to the increased electron density at reduced plasma electronegativity, which produces more negatively charged particles and thus enhances

electrostatic confinement. Both the impact of gas flow velocity and plasma electronegativity may be important parameters for designing trapping conditions in the plasma.

5.6 Full Scale Reactor Simulations of Particle Growth and Trapping

The nanoparticle and plasma dynamics leading to trapping and de-trapping of particles are functions of the spatially dependent electrostatic fields, gas flow, and particle growth rates. To investigate the influence of these processes, a two-dimensional plasma reactor model with an embedded three-dimensional nanoparticle trajectory and growth model were employed. The combination of the plasma reactor model, the hybrid plasma equipment model (HPEM), and the nanoparticle trajectory model, the dust transport simulator (DTS) are described in detail in [30]. The HPEM provides self-consistent electric fields, gas flow profiles, gas temperatures, charged particles fluxes, and radical fluxes. The DTS uses these values to predict the trajectories, statistical charging and trapping of growing nanoparticles while including all of the pertinent forces (electrostatic, fluid drag, ion drag, thermophoresis, gravity, Brownian motion, and particle-particle Coulomb force).

The HPEM/DTS was used to simulate the process conditions of a low pressure reactor similar to UMN1 described above, with the cylindrical model geometry shown in Fig. 5-7a. The reactor length is 90 mm and diameter 20 mm with powered and grounded ring electrodes, and gas flowing left-to-right. The pressure was 1 Torr, the gas flow rate 75 sccm, the gas mixture $Ar/He/SiH_4$ = 99/0.9/0.1, and the capacitively coupled power deposition at a frequency of 10 MHz is 10 W. The electron density, electron temperature, electric potential, electric field vectors (with electric field and potential on axis) averaged over an RF cycle, are shown in Fig. 5-7. The electron density has a maximum value of 1.3×10^{11} cm^{-3} on axis at the position of the powered electrode.

Due to the high conductivity of the plasma, the electron temperature is fairly constant in the bulk plasma, 3.2-3.7 eV, while extending above 10 eV in the sheath at the powered electrode. The amplitude of the applied RF voltage is 680 V with a self-generated DC bias on the tube wall of −217 V, which results in a maximum in the time averaged electric potential of 182 V. However, again due to the high conductivity of the plasma, the time averaged voltage drop across the bulk of the plasma is <10 V. This results in electric fields of hundreds of V-cm^{-1} that are dominantly pointing outwards (confining for negative particles) at the boundaries of the plasma. The electric field along the axis at which particles are trapped is only a few V-cm^{-1}.

Predictions of trapping locations for 1 and 3 nm particles are shown in Fig. 5-7f–i. The 1 nm particles have trapping locations on axis that are nearly at the maximum of the plasma potential (see Fig. 5-7e). This focusing of the particles onto the axis results from radial electric fields which predominantly point outwards, thus accelerating particles radially inwards. The trapping locations are strewn along the axis for about 1 cm, a result of the charging and discharging of the particles. When the particles discharge to be neutral, they drift downwards with the gas flow. When the particles recharge negatively, they drift back towards the maximum in the plasma potential. The 3 nm particles are also trapped on axis, though at a location further downstream beyond the maximum in the potential. The larger particles are more susceptible to the fluid drag forces and become trapped where the axial electric field provides a sufficient force to counter the fluid drag, approximately 1 V-cm^{-1}, which occurs downstream of the trapping location of the 1 nm particles. The trapping sites are strewn along the axis for more than 1 cm.

The average locations for particle sizes of 1–10 nm as a function of time are shown in Fig. 5-7h. A horizontal line (constant location) indicates that the particles are trapped. Particles falling below 1 cm are not trapped and exit the reactor. For the simulated conditions, de-trapping occurs

for particle sizes of greater than about 4 nm when the neutral gas flow drag exceeds the ability of the plasma to electrostatically confine the particles. The trapping locations are at lower axial locations for larger particles where the confining axial electric fields are larger, as indicated in Fig. 5-7e. The trends from the Monte Carlo simulations (Fig. 5-6) and those from the full two-dimensional simulations (Fig. 5-7) are in good agreement with each other, and with the experiments.

5.7 Concluding Remarks

In this contribution, we showed through experiments performed on multiple plasma reactors as well as simulations with different levels of completeness that particle trapping through electrostatic forces does occur during the synthesis of sub-10 nm particles, a phenomenon that has generally not been recognized to date. We demonstrated that particles are trapped even if they are neutral for the majority of time that they spend in the trapping region due to a cycle of particles discharging and recharging. In actual plasma reactors, particles enter the trapping region and are spatially confined while growing through the continued accretion of precursor. Once particles reach a critical size such that the gas drag is sufficiently strong to overcome the electrostatic trapping force, particles are released from the trap. This critical size required for de-trapping narrows the collected particle size distribution since particles smaller than the critical size are confined and those that grow to larger than this critical size can escape and exit the reactor in steady state operation. Our numerical simulations suggest that the radial electric fields present in the particle trap lead to a focusing of the released particles onto the reactor centerline.

The observations reported here may establish a new paradigm for control of the nonthermal plasma synthesis of sub-10 nm particles. A better understanding of the trapping mechanism will

enable a better control over particle sizes and more monodisperse size distributions than has been possible to date. The existence of trapping is of particular importance for the design of reactors for core–shell heterostructure nanoparticles [10,44–46]. A better understanding of trapping will enable researchers to design plasma processes in which nanoparticles are either trapped or not trapped in the shell growth region. This will enable enhanced control over the range of core/shell diameter ranges than has been achieved at present. Moreover, the understanding of the particle focusing onto the centerline of the reactor is another important insight for the growth of heterostructure particles as it implies that all particles essentially experience the same growth conditions in the reactor, in spite of the parabolic flow velocity profile expected for laminar flow reactors.

However, the current study also leaves several open questions, such as whether particle trapping is a universal phenomenon or whether it is dependent on the nanoparticle material. For high gas flow rates most particles may not be trapped because the critical size for particles to be released from the trap by the gas drag decreases with increasing flow rates. There may also be electric field configurations in the plasma that do not support trapping. It is also not clear whether nanoparticles of insulators, semiconductors, or metals will be equally trapped as their charge states depend on their capacitance and secondary emission processes, and so depend on the materials work function or dielectric properties. These issues will need to be clarified to fully take advantage of particle trapping in nanoparticle synthesis as a design parameter. However, the current study demonstrates that gas flows and electric fields can be designed to utilize particle trapping to control particle sizes and size distributions.

5.8 Figures

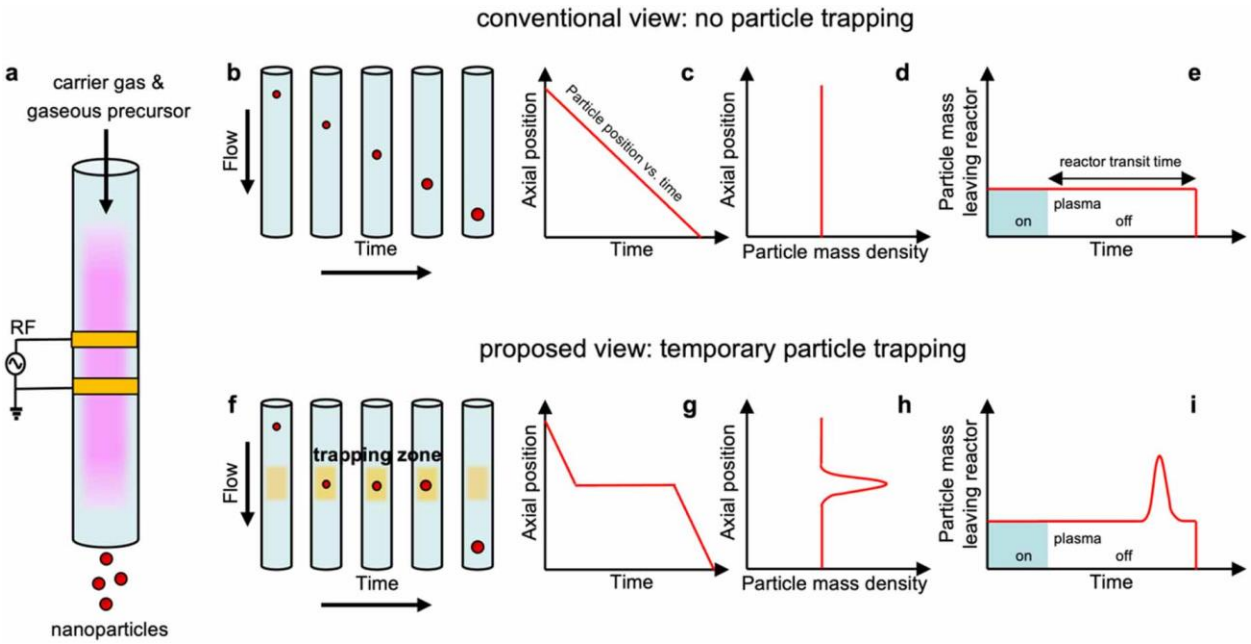

Figure 5-1. Overview of two scenarios of particle growth in nonthermal plasmas without and with particle trapping. (a) Schematic of laminar flow plasma reactor for nanoparticle synthesis. (b)-(e) Scenario without particle trapping and (f)-(i) with particle trapping. In the untrapped scenario (b)-(e) the particles flow through the reactor at a constant velocity as they continue to grow by reactions with radicals. Under the assumption of negligible radial losses to the reactor walls, the particle mass density, defined as the mass density of particles and unreacted precursor, is therefore constant along the reactor. When the plasma is extinguished, particle mass leaves the reactor at a constant rate until one transit time after the plasma turn-off. In the trapped scenario (f)–(i), the particles become temporarily trapped while continuing to grow, leading to a locally enhanced mass density in the trapping zone. When the plasma is turned off, removing the trap, this larger mass density is released and will appear as a peak in the rate of particle mass leaving the reactor.

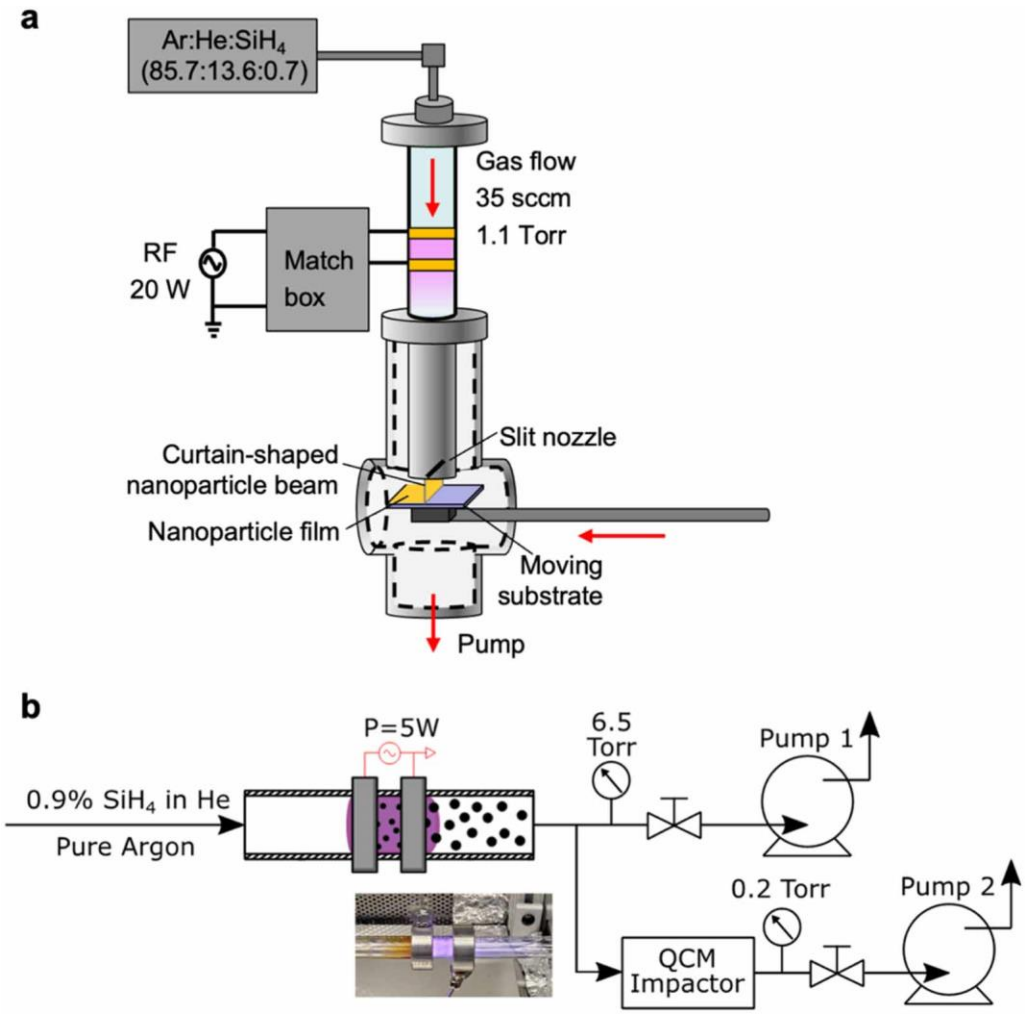

Figure 5-2. Schematics of two of the three plasma reactors used to investigate particle trapping. (a) Schematic of the UMN1 plasma synthesis reactor used to deposit silicon nanocrystals on a moving substrate. The deposited particle mass is analyzed by studying the optical absorbance of the particles on the substrate. (b) Schematic of the WUSTL plasma synthesis reactor. In this reactor, particle mass leaving the reactor is directly measured using a QCM.

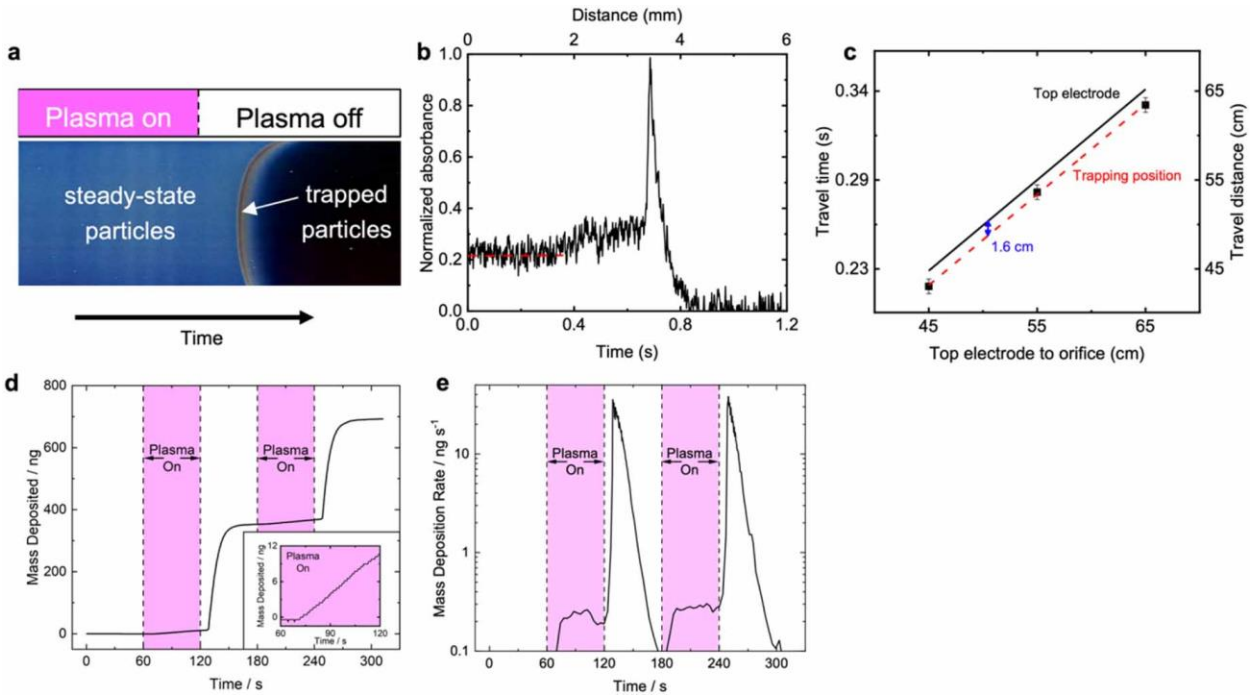

Figure 5-3. Experimental results demonstrating particle trapping in the synthesis of sub-10 nm silicon particles. (a)–(c) Results from the UMN1 reactor. (a) Photograph of particles deposited on a silicon substrate (to enable better photographic imaging) moving at constant speed below the reactor exit showing the deposition peak associated with trapped particles. (b) Absorbance of 390 nm light by silicon nanoparticles on the translated glass substrate. (c) Position of trapped particles derived from arrival time of particles after plasma turn-off for three different electrode positions. (d), (e) Results from WUSTL plasma reactor. (d) Particle mass deposited on a QCM over time and (e) particle mass deposition rate.

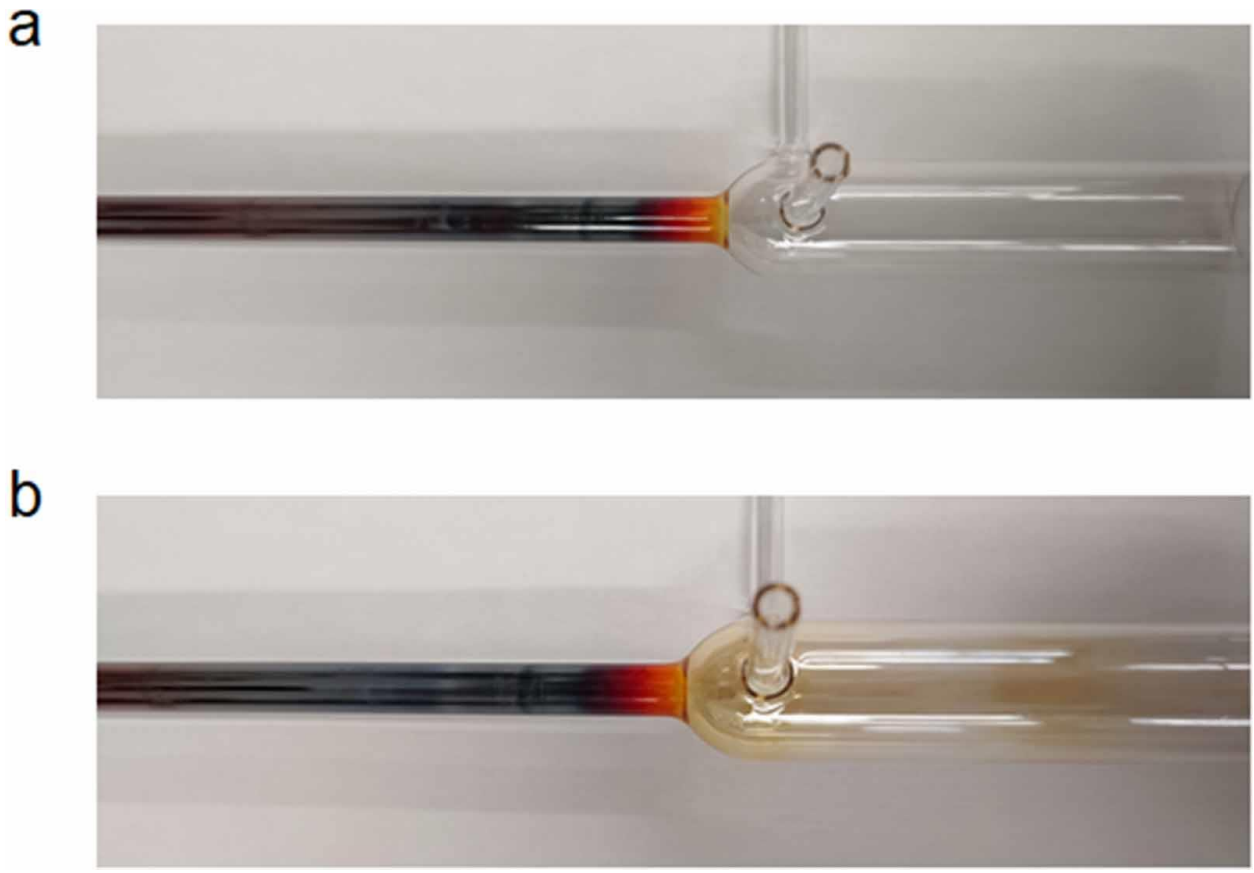

Figure 5-4. Images of the UMN2 reactor used for silicon quantum dot synthesis. The electrode pair was located 2 cm to the left of the tube expansion. (a) Photograph of a plasma reactor run with a silane flow rate (Ar/He/SiH_4 = 50/13.3/0.7 sccm) that leads to the formation and collection of ~3 nm Si quantum dots. Note that deposition of a parasitic silicon film is only observed upstream (left) of the electrodes but not downstream (right) of the electrodes. This observation is consistent with the assumption that trapped particles around the electrode position act as sink of silicon precursor, preventing silicon film deposition downstream of the electrodes. (b) Photograph of the same plasma reactor operated at lower silane flow rate (0.35 sccm) so that particle nucleation and collection is avoided. Note that film deposition now also occurs downstream of the electrodes, suggesting that the precursor sink due to trapped particles is removed, because the precursor density is too low for particle nucleation.

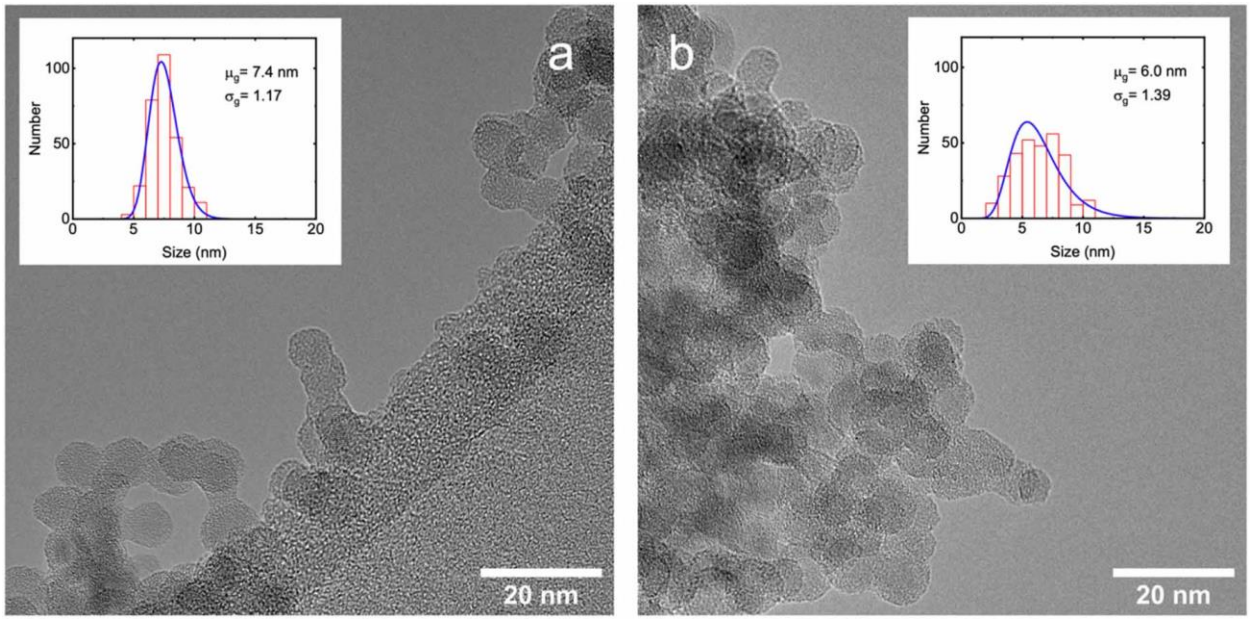

Figure 5-5. Particle trapping acting as a size filter in the nanoparticle synthesis with nonthermal plasmas. Transmission electron micrographs of silicon nanocrystals and associated size distributions (insets). (a) Particles that exit the plasma reactor in steady state and (b) particles that are representative of those collected from the trapping region after plasma turn-off.

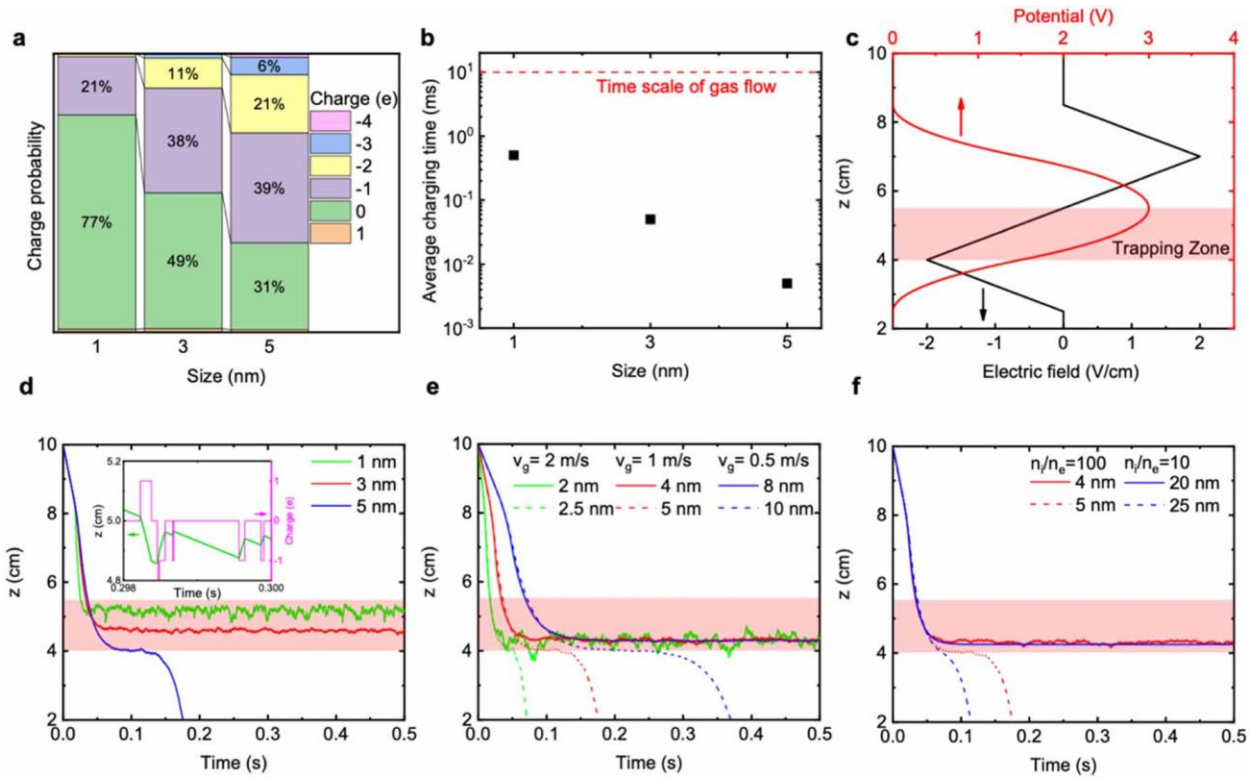

Figure 5-6. Parametric Monte Carlo model results of particle trapping. All results except (f) are for a positive ion density n_i of 5×10^{11} cm^{-3} and a free electron density n_e of 5×10^{9} cm^{-3}. (a) Fraction of time that particles are found in a certain charge state for three different particle sizes. (b) Comparison of the typical charging times with the time scale of the gas flow through the trapping zone. (c) Electrostatic potential profile and electric fields. (d) Axial position of particles at three different diameters as function of time. The insert shows the particle trajectory and its correlation with the fluctuating particle charge for a 1 nm particle. (e) Influence of the gas flow velocity on the critical size for particle trapping. (f) Influence of plasma electronegativity on the critical size for particle trapping.

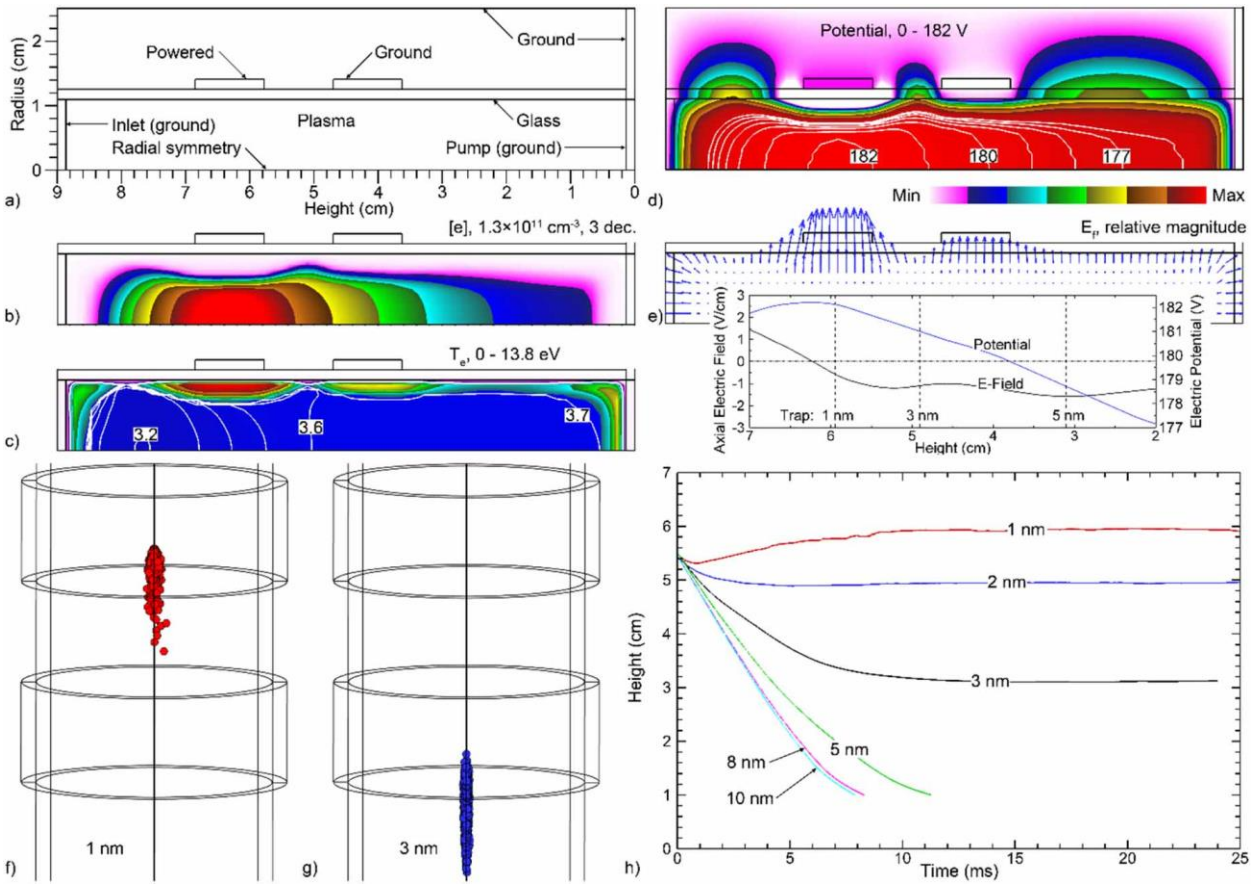

Figure 5-7. Reactor simulation and trapped particle locations. Self-consistent two-dimensional plasma hydrodynamics simulations for operating conditions of 1 Torr, gas flow rate 75 sccm, gas mixture Ar/He/SiH_4 = 99/0.9/0.1 with capacitively coupled power deposition of 10 W at a frequency of 10 MHz. Results are time averages over an RF period. (a) Model geometry, (b) electron density, (c) electron temperature, (d) plasma (electric) potential, and (e) electric field vectors with inset showing electric field and potential along the axis. Trapping locations are shown for (f) 1 nm particles and (g) 3 nm particles. (h) Average locations of particles as a function of time. The final locations are also indicated in the insert to (e).

5.9 References

[1] A. Piel, *Plasma Physics*, Springer Berlin Heidelberg (2010).

[2] A. Melzer, **962,** *Physics of Dusty Plasmas*, 962: Springer International Publishing (2019).

[3] J. Knipping, H. Wiggers, B. Rellinghaus, P. Roth, D. Konjhodzic and C. Meier, J. Nanosci. Nanotechnol. **4,** 1039 (2004).

[4] L. Mangolini, E. Thimsen and U. Kortshagen, Nano Lett. **5,** 655 (2005).

[5] T. Chen, K. V. Reich, N. J. Kramer, H. Fu, U. R. Kortshagen and B. I. Shklovskii, Nat. Mater. **15,** 299 (2016).

[6] F. Meinardi, S. Ehrenberg, L. Dhamo, F. Carulli, M. Mauri, F. Bruni, R. Simonutti, U. Kortshagen and S. Brovelli, Nat. Photonics **11,** 177 (2017).

[7] P. Xia, E. K. Raulerson, D. Coleman, C. S. Gerke, L. Mangolini, M. L. Tang and S. T. Roberts, Nat. Chem. **12,** 137 (2020).

[8] U. R. Kortshagen, R. M. Sankaran, R. N. Pereira, S. L. Girshick, J. J. Wu and E. S. Aydil, Chem. Rev. **116,** 11061 (2016).

[9] A. Alvarez Barragan, N. V. Ilawe, L. Zhong, B. M. Wong and L. Mangolini, J. Phys. Chem. C **121,** 2316 (2017).

[10] S. Exarhos, A. Alvarez-Barragan, E. Aytan, A. A. Balandin and L. Mangolini, ACS Energy Lett. **3,** 2349 (2018).

[11] N. B. Uner and E. Thimsen, J. Phys. D. Appl. Phys. **53,** (2020).

[12] T. Matsoukas, M. Russell and M. Smith, J. Vac. Sci. Technol. A Vacuum, Surfaces, Film. **14,** 624 (1996).

[13] V. A. Schweigert and I. V. Schweigert, J. Phys. D. Appl. Phys. **29,** 655 (1996).

[14] M. S. Barnes, J. H. Keller, J. C. Forster, J. A. O'Neill and D. K. Coultas, Phys. Rev. Lett.

68, 313 (1992).

[15] V. E. Fortov, A. G. Khrapak, S. A. Khrapak, V. I. Molotkov and O. F. Petrov, Physics-Uspekhi **47,** 447 (2004).

[16] V. Fortov, A. Ivlev, S. Khrapak, A. Khrapak and G. Morfill, Phys. Rep. **421,** 1 (2005).

[17] S. Khrapak and G. Morfill, Contrib. to Plasma Phys. **49,** 148 (2009).

[18] H. M. Thomas, M. Schwabe, M. Y. Pustylnik, C. A. Knapek, V. I. Molotkov, A. M. Lipaev, O. F. Petrov, V. E. Fortov and S. A. Khrapak, Plasma Phys. Control. Fusion **61,** (2019).

[19] T. J. A. Staps, M. I. van de Ketterij, B. Platier and J. Beckers, Commun. Phys. **4,** (2021).

[20] R. Gopalakrishnan and C. J. Hogan, Phys. Rev. E - Stat. Nonlinear, Soft Matter Phys. **85,** 1 (2012).

[21] T. Ono, U. R. Kortshagen and C. J. Hogan, Phys. Rev. E **102,** 1 (2020).

[22] K. S. Ashrafi, R. Yousefi, M. Chen, L. S. Matthews and T. W. Hyde, Phys. Rev. E **102,** 1 (2020).

[23] G. Praburam and J. Goree, J. Vac. Sci. Technol. A Vacuum, Surfaces, Film. **12,** 3137 (1994).

[24] G. S. Selwyn, J. E. Heidenreich and K. L. Haller, Appl. Phys. Lett. **57,** 1876 (1990).

[25] C. R. Gorla, S. Liang, G. S. Tompa, W. E. Mayo and Y. Lu, J. Vac. Sci. Technol. A Vacuum, Surfaces, Film. **15,** 860 (1997).

[26] R. M. Sankaran, D. Holunga, R. C. Flagan and K. P. Giapis, Nano Lett. **5,** 537 (2005).

[27] R. Le Picard, A. H. Markosyan, D. H. Porter, S. L. Girshick and M. J. Kushner, Plasma Chem. Plasma Process. **36,** 941 (2016).

[28] R. Gresback, Z. Holman and U. Kortshagen, Appl. Phys. Lett. **91,** (2007).

[29] A. Bapat, C. Anderson, C. R. Perrey, C. B. Carter, S. A. Campbell and U. Kortshagen, Plasma Phys. Control. Fusion **46,** (2004).

[30] S. J. Lanham, J. Polito, X. Shi, P. Elvati, A. Violi and M. J. Kushner, J. Appl. Phys. **130,** 163302 (2021).

[31] C. F. Bohren and D. R. Huffman, Physics Bulletin **35,** *Absorption and Scattering of Light by Small Particles*, 35: Wiley (1998).

[32] L. Boufendi, J. Hermann, A. Bouchoule, B. Dubreuil, E. Stoffels, W. W. Stoffels and M. L. de Giorgi, J. Appl. Phys. **76,** 148 (1994).

[33] S. K. Friedlander, *Smoke, Dust, and Haze - Fundamentals of Aerosol Dynamics (2nd Edition)*, Oxford University Press (2000).

[34] G. Sauerbrey, Zeitschrift für Phys. **155,** 206 (1959).

[35] F. S. Lai, S. K. Friedlander, J. Pich and G. M. Hidy, J. Colloid Interface Sci. **39,** 395 (1972).

[36] J. D. Landgrebe and S. E. Pratsinis, J. Colloid Interface Sci. **139,** 63 (1990).

[37] Z. Xiong, S. Lanham, E. Husmann, G. Nelson, M. A. Eslamisaray, J. Polito, Y. Liu, J. Goree, E. Thimsen, M. J. Kushner and U. R. Kortshagen, J. Phys. D. Appl. Phys. **55,** 235202 (2022).

[38] P. Agarwal and S. L. Girshick, Plasma Chem. Plasma Process. **34,** 489 (2014).

[39] J. E. Allen, B. M. Annaratone and U. de Angelis, J. Plasma Phys. **63,** 299 (2000).

[40] U. Kortshagen and U. Bhandarkar, Phys. Rev. E **60,** 887 (1999).

[41] L. Verlet, Phys. Rev. **159,** 98 (1967).

[42] P. Agarwal and S. L. Girshick, Plasma Sources Sci. Technol. **21,** 055023 (2012).

[43] M. Mamunuru, R. Le Picard, Y. Sakiyama and S. L. Girshick, Plasma Chem. Plasma

Process. **37,** 701 (2017).

[44] C. Mehringer, C. Kloner, B. Butz, B. Winter, E. Spiecker and W. Peukert, Nanoscale **7,** 5186 (2015).

[45] K. I. Hunter, J. T. Held, K. A. Mkhoyan and U. R. Kortshagen, ACS Appl. Mater. Interfaces **9,** 8263 (2017).

[46] O. Yasar-Inceoglu, L. Zhong and L. Mangolini, J. Phys. D. Appl. Phys. **48,** 314009 (2015).

Chapter 6 Scaling of Silicon Nanoparticle Growth in Low Temperature Flowing Plasmas[‡‡]

The physics of growing nanoparticles in plasmas is interconnected and complex. Traditionally, assumptions are made about the plasma conditions and chemistry because direct measurements are difficult due to deposition. This work aims to isolate operating conditions and to holistically model the plasma and particle growth, with the goal of giving insight into fundamental operation and underlying physics of plasma-based nanoparticle growth. An established and successful technique to produce NPs is using a capacitively coupled plasma (CCP) in a cylindrical geometry. Although a robust synthesis technique, optimizing or specifying NP properties using CCPs is challenging.

This work features results from a computational investigation for growth of silicon NPs in flowing inductively coupled plasmas (ICPs) using Ar/SiH_4 gas mixtures of up to a few Torr. ICPs produce more locally constrained and quiescent plasma potentials. These positive plasma potentials produce an electrostatic trap for negatively charged NPs which can significantly extend the residence time of NPs in the plasma, which in turn provides a controllable period for particle growth. The computational platforms used in this study consist of a 2-dimensional plasma hydrodynamics model, a 3-dimensional nanoparticle growth and trajectory tracking model and a molecular dynamics simulation for deriving reactive sticking coefficients of silane radicals on Si NPs. Trends for nanoparticle growth as a function of SiH_4 inlet fraction, gas residence time, energy

[‡‡]Results and portions of the text that appear in this chapter were previously published in the paper by S. J. Lanham *et al.*, "Scaling of silicon nanoparticle growth in low temperature flowing plasmas" J. Appl. Phys. **130,** 163302 (2021).

deposition per particle, pressure, and reactor diameter are discussed. The general path for particle synthesis is trapping of small NPs in the positive electrostatic potential, followed by entrainment in the gas flow upon reaching a critical particle size. Optimizing or controlling NP synthesis then depends on the spatial distribution of plasma potential, density of growth species, and the relative time that particles spend in the electrostatic trap and flowing through higher densities of growth species upon leaving the trap.

This work was primarily done at the University of Michigan. Coupled plasma and kinetic nanoparticle synthesis modeling was done by Prof. Kushner's research group. Molecular dynamics simulation results for nanoparticle sticking coefficients were done by Prof. Angela Violi's research group.

6.1 Introduction

Low temperature plasmas have been used to produce nanoparticles (NPs) under condition unavailable to traditional liquid or gas techniques [1-3], making it possible to form NPs with unique compositions [4-8]. A few experiments have been done to characterize NP growth as a function of plasma operating conditions [9-11]. The traditional mechanism for NP growth is detailed by Boufendi and Bouchoule, but predicting particle size is not well understood [12]. Particles in plasma generally charge negative, as a complex function of size and plasma conditions [13-15]. A few computational growth models have been developed, but are computationally expensive and are usually 0- or 1-dimensional [14,16-19]. Further information is detailed in Section 1.4.2.

In this paper, we report on results from a computational investigation of silicon NP synthesis in flowing LTPs with the goals of clarifying how operating conditions in a cylindrical

reactor affect plasma properties and the resulting impact this has on NP growth rates. The algorithms used here are less computationally intensive than sectional models [18] while agreeing systematically with their results. Simulations were performed of inductively coupled plasmas (ICP) sustained in Ar/SiH_4 mixtures in cylindrical reactors having diameters of up to 1.5 cm, pressures of 0.25 to 2.5 Torr and silane mole fractions of 0.1% to 50%. The computational platforms used in the study are a 2-dimensional hybrid-multi-fluid plasma model coupled with a 3-dimensional kinetic model for particle growth and tracking. Reactive sticking coefficients for silane radicals onto growing NPs were computed using molecular dynamics methods. The intent of this work is to assess how trapping of negatively charged particles in the positive plasma potential influences growth rates and particle size. The ICP system was chosen since for cylindrical reactors, the plasma potential is quiescent with locally defined maximum compared to, for example, capacitively coupled systems. We found that when negatively charged NPs become trapped near the peak in the plasma potential, the trapping time can span multiple gas residence times. The particles are de-trapped when they grow large enough that fluid drag forces begin to dominate, and the NPs flow out of the reactor. Growth continues as the NPs flow downstream through a region that is rich in growth precursors. The charging of the NPs is dynamic, negative and increasing in magnitude when trapped in the plasma, while discharging as they flow downstream.

The models used in this investigation are described in Section 6.2. Trends for nanoparticle growth with SiH_4 inlet fraction, gas residence time, energy per particle, pressure, and reactor radius are discussed in Section 6.3. Concluding remarks are in Section 6.4.

6.2 Description of the Models

6.2.1 Plasma and Kinetic Dust Models

The reactor scale plasma chemistry and hydrodynamics were modeled using the Hybrid Plasma Equipment Model (HPEM), a two-dimensional multi-fluid plasma simulator, described in detail in Ref. [20]. Briefly, the HPEM uses a modular approach to address the relevant physics using a time slicing technique. In this work, the Electromagnetics Module (EMM) was used to compute azimuthal electric fields and their absorption in the plasma produced from an antenna powered at radio frequency (RF). Secondary electron emission from surfaces is addressed in the Electron Energy Transport Module (EETM), where a Monte Carlo simulation is used to track their trajectories and generate electron impact source functions. These source functions are used in the Fluid Kinetics Poisson Module (FKPM). The FKPM computes separate fluid continuity, momentum and temperature equations for each heavy species (neutrals and ions). Continuity and temperature equations are solved for electrons assuming a drift-diffusion formulation for momentum. Rate coefficients for the electron energy equation are obtained from local solutions of Boltzmann's equation for the electron energy distribution. Poisson's equation for the electric potential is solved semi-implicitly with each time step in the FKPM for self-consistency. The full set of equations are integrated for multiple gas residence times until a pseudo-steady state is reached.

The Ar/SiH_4 reaction mechanism used in this work is a concise version from the work by Picard *et al.* [18] with data from previous works [21,22]. The species included in the simulation are listed in Table 6-I. Particle growth is addressed in the DTS which feeds back to the FKPM the local values of NP density and charge on the NPs. These values are then used in the charge balance for solution of Poisson's equation, for the attachment (or neutralization) of electrons and ions on

the NPs. In the DTS, the Havne's P-parameter [23–25] is much less than 1, meaning that the NP density is too low to significantly impact the electric potential in the reactor. For the conditions addressed here, the electronegativity parameter, α_0, the ratio of negative ions to electrons [26], is ≈10 where power deposition is large in the vicinity of the antenna. α_0, increases to >1,000 downstream as the plasma flows out of the reactor. This large electronegativity decreases the impact of a low P-parameter.

NP transport and growth were addressed using a 3-dimensional kinetic model, the DTS, embedded in the HPEM. This model is described in detail in Chapter 2.2, and has been published in previous works as the DTS [27–29] and the prior dust particle transport model [30]. The DTS obtains plasma properties from the HPEM, including electric fields, and species densities, temperatures, and momentum flux fields. The precursors to NPs are initialized randomly in the plasma and their trajectories are integrated based on the relevant forces: gravitational, electrostatic and inter-particle Coulomb forces, ion drag, viscous fluid drag, thermophoresis and Brownian motion. The specific details and implementation of these forces can be found in Chapter 2.2, so will not be discussed here for brevity.

A couple of the more important aspects of the model for this work are the stochastic charging and particle growth algorithms. An example output using the stochastic charging algorithm is shown in Fig. 6-1. The relative fluctuations around the mean particle charge decreases with increasing particle size, corroborating that fluctuations are less important for larger sized particles. The frequency of oscillations increases with increasing particle size as current to the particle increases in magnitude, with particle charge changing ~1q per ms for a 1 nm NP to charge varying 100s of q per ms for 100 nm particles.

Several new capabilities were added to the model to address growing dust particles specifically for this work. In previous versions of the DTS, the trajectories of non-growing particles were tracked. Here, the capability to track the mass and diameter of each dust pseudo-particle was added. The time rate of change of mass of NP *i* is given by,

$$\frac{dM_i}{dt} = \sum_j v_j N_j 4\pi r_i^2 S_{c,j} \Delta m_j \ , \ v_j = \sqrt{\frac{8k_B T_j}{\pi m_j}} \tag{6.1}$$

where the mass of dust particle *i* is M_i having radius r_i. The summation is over all the species j which contribute to dust particle growth, having thermal speed v_j, number density N_j, mass m_j and temperature T_j. The quantity Δm_j is the mass added to the dust particle which is not necessarily equal to the incoming radical mass. The difference would account for example, the desorption of hydrogen from a sticking reaction of SiH with the dust particle. The largest unknown for this growth model is $S_{c,j}$ – the sticking probability for a collision between the dust particle and the dust growth species. The values used in this work were estimated using another model which will be discussed in Chapter 6.2.2, and has been published in more detail recently [31].

6.2.2 Radical Sticking Probabilities

One of the most fundamental data required for modeling NP growth in a silane containing plasma is the reaction probability (or sticking coefficient) of silane radicals on the NP. These sticking coefficients were obtained using molecular dynamics simulations performed with LAMMPS [42]. $Si_{29}H_{36}$ particles were first constructed with atomic interactions modelled using a classical reactive force field [43] in combination with a dynamic charge equilibration model [44,45]. Collisions were simulated between silanes (SiH_x, x = 1-4) and the $Si_{29}H_{36}$ NP. Each $Si_{29}H_{36}$ species was prepared by generating 5 independent conformations in vacuum under

canonical conditions at the target temperature (400 K) by using a stochastic velocity rescale thermostat [46]. To simulate the collisions, one of these conformations was randomly chosen and the atomic and the atomic velocities of atoms in the NP were initialized by random selection from a Maxwell-Boltzmann distribution with the additional constraint of zero linear momentum for each NP.

The SiH_x and NP were placed 2.5 nm apart (d_o) and a fixed initial speed v_i directed along the line connecting the two centers of mass was added, resulting in an impact parameter equal to zero. Speeds were chosen so that the cumulative Maxwell speed distribution was sampled uniformly at 200 intervals. The system was simulated for a for a length of time τ to satisfy $\tau \cdot v_i = 2d_o$. A total of 25 trajectories were performed for each value of v_i. The time step for integrating trajectories was 10^{-4} fs as tests showed that longer integration times did not guarantee energy conservation during collisions.

The evolution of the system was monitored by computing the composition and the number of clusters at the end of the simulation. Two atoms were assigned to the same cluster if their distance was less than the van der Waals distance for each pair, namely 0.44, 0.32 and 0.148 nm for Si/Si, Si/H, and H/H pairs, respectively. Based on the number and composition of the clusters, the sticking probability $p(T, v_i)$ was computed at each temperature, T, and collision speed v_i. Finally, the sticking coefficient was obtained from:

$$S_c(T) = \sum_i p(T, v_i)\, w(T, v_i) \tag{6.2}$$

where the weights w are based on the Maxwell-Boltzmann distribution [47].

The resulting sticking coefficients are listed in Table 6-II. Generally, the probability of a silane radical to be captured by the larger particle decreases with an increase in temperature due

to the average higher kinetic energy that needs to be accommodated after the collision. The number of free radical sites on the impinging silane species greatly impacts the probability of sticking. There is little likelihood of chemically bonding with 0 radical sites (SiH_4, S_c=0) for the temperatures of interest while there is nearly always sticking with 3 radical sites (SiH, S_c=0.945). The sticking probability is non-linear with free radical sites. Additional sticking coefficients were approximated for Si_2H_x species (x=2,3,5,6) based on the silane radical data and fractional number of radical sites.

6.3 Dust Particle Growth in Flowing Inductively Coupled Plasmas

6.3.1 Base Case

This work focuses on the consequences of electrostatic trapping on nanoparticle growth in flowing low temperature plasma reactors, as have been used in several demonstrations of plasma synthesis of nanoparticles [4,6,7,48]. An inductively coupled plasma (ICP) reactor was chosen for this work since the plasma potential is more localized and quiescent compared to capacitively coupled plasma systems. A schematic of the ICP reactor used in this computational investigation is shown in Fig. 6-2. For the base case, the glass tube cylindrical reactor has a radius of 1 cm and a length of 8 cm, with electrically grounded boundaries for the inlet and outlet, as would occur using a metallic mesh. Power is inductively coupled into the plasma from a three-turn antenna delivering 10 W at 10 MHz in the base case with an inlet flow of Ar/SiH_4 = 98/2 at 50 sccm. The pressure is held constant at 1 Torr by adjusting the outlet flow rate. The temperature of the inlet gases and surrounding reactor surfaces are held constant 325 K. These operating conditions correspond to a gas residence time (τ) of 33 ms and an average energy per particle [defined as flow

rate (molecules-s^{-1}) multiplied by power] of 2.8 eV, which is 0.5 eV below the average energy of breaking Si-H bonds at 3.3 eV [49].

Plasma properties for the base conditions are shown in Fig. 6-2. The electron density peaks close to the powered antenna at 8×10^{10} cm^{-3} and decreases by three orders of magnitude downstream by the pump. This decrease is due to the large rate of electron dissociative attachment to silane and dissociative recombination of silane ions, both of which are sources of radicals. The electron temperature T_e is maximum at 4.3 eV adjacent to the antenna, decreasing moving away from the antenna due to both elastic and inelastic collisions for the (relatively) high pressure of 1 Torr. T_e decreases to 1.5 eV downstream. Plasma potential peaks at 24.7 V off-axis (0 cm > r >1 cm) where the ion production is maximum. The surface of the dielectric tube charges negatively, down to -7.7 V at a minimum, to balance the electron and positive current to its surface. The electronegativity of the plasma is quantified by α_0, which is the ratio of the total negative ion density to the electron density. α_0 increases from 10 at the peak of the electron density to 4,000 downstream, as electrons are rapidly consumed by attachment and dissociative recombination.

The dominant positive ion at the peak of the power deposition is Ar^+ with a density of 1×10^{12} cm^{-3}, while the densities of H^+ and SiH_3^+ are more than an order of magnitude lower. The trend reverses downstream (flow distance of 7 cm) where the dominant positive ions are H^+ and SiH_3^+ with densities of 2×10^{11} cm^{-3} and 3×10^{11} cm^{-3} respectively. This change in abundance is due to the increase in density of SiH_4 fragments and their availability to charge transfer with Ar^+ whose density decays to 3×10^{7} cm^{-3} downstream. The dominant negative charge carrier throughout the reactor is $Si_2H_5^-$, with a density of 1×10^{12} cm^{-3} upstream of the power deposition zone and 5×10^{12} cm^{-3} downstream.

Gas temperature and densities of SiH_x (x=1-4) and H atoms for the base case are shown in Fig. 6-3. As silane flows into the reactor and encounters the region of power deposition under the antenna, electron impact dissociation depletes its density, decreasing by 2 orders of magnitude from its maximum of 4.1×10^{14} cm^{-3} by the time the flow reaches the pump. Localized gas heating to 375 K occurs near the center of the reactor adjacent to the antenna which produces rarefaction. In addition to electron impact dissociation, dehydrogenation of SiH_x occurs progressively downstream from collisions with Ar excited states and culminates with SiH being the predominant radical. The maximum density of SiH_3 (2.0×10^{13} cm^{-3}) occurs on the upstream side of the plasma zone where SiH_4 is first dissociated. Dissociation of SiH_3 produces SiH_2 whose maximum density (1.1×10^{12} cm^{-3}) occurs near the center of the plasma zone. The maximum density of SiH (1.4×10^{12} cm^{-3}) occurs downstream of the plasma zone following dissociation of SiH_2. The H atom density has a maximum of 1.4×10^{14} cm^{-3} in the plasma zone, decreasing to less than 10^{13} cm^{-3} by the pump. In addition to reactions with silane species, H atoms also have the potential to etch the NPs and so moderate their size, a process not included in the model. This etching could impact the size of NPs that are trapped for long times.

To provide guidance on the particle growth potential of the distribution of Si_xH_y radicals, we define the reactive density N_r as the sum of the products of radical density and their sticking coefficients, S_c. The reactive density is shown in Fig. 6-3f. Higher densities of reactive species are found downstream, which suggests that particle growth may be important well outside the region of maximum power deposition.

Predictions from the DTS are shown in Fig. 6-4 for the base case conditions. The sizes of the particles are indicated by the diameter of the image's individual particles. The charge on the particles is indicated by the color of the images. 1,000 particles with a diameter of 1 nm were

initialized in the reactor between the turns of the antenna. Forces acting on the particles produce negligible movement of the particles on the microsecond timescale (Fig. 6-4a). The currents to small particles on these time scales result in particle charging being dominated by stochastic collisions with ions and electrons, which leads to a variation in particle charges. After 0.5 ms (Fig. 6-4b), particles have grown on average to 1.3 nm with charges ranging from 0 to -4q with an average charge of -1.6q. For these sizes of particles and amount of charge, particle movement is dominated by electrostatic forces as particles act as large negative ions which seek the maximum in the plasma potential where they are electrostatically trapped. For these conditions, the plasma potential is maximum in an annulus centered under the antenna, which results in a torus of trapped particles. The stochastic charging process results in particles that do statistically become momentarily neutral or charged positively. Those particles that are at any time neutral tend to flow downstream due to fluid drag and thermophoretic forces, the latter which accelerates particles away from the maximum in gas temperature under the antenna. Those particles that are momentarily charged positive are accelerated away from the maximum in plasma potential towards the walls. If not neutralized before arriving at the wall, the positively charged particles neutralize by depositing their charge on the wall.

By 4 ms (Fig. 6-4c), particles grow to several nm in size and become more uniform in charge with an average of -5.5q. There is still a statistical distribution of charges (-12q to 0q) though particles are almost exclusively charged negatively. Particles form a ring near the maximum in the plasma potential where the electrical forces of ion drag and electrostatic acceleration balance. After several gas residence times (τ = 33 ms, and t = 99 ms in Fig. 6-4d), particles grow to nearly 100 nm on the average. The position of the ring shifts further downstream as the fluid drag force increases significantly with particle size. This fluid drag then balances

forces at a less positive potential in the electrostatic trap in the direction of the pump. The distribution of particle sizes and charge, and Coulomb interactions between particles prevent the particles from converging in a small volume.

Further particle growth results in fluid drag forces dominating and the particles being pulled out of the electrostatic trap. The particles then flow downstream (Fig. 6-4e), where the electron temperature T_e and the electron density decrease in favor of negative ions. Particle charging then becomes dominated by collisions with positive and negative ions which, downstream, have nearly equal densities and similar mobilities. These conditions reduce the need for particle charging as the floating electrical potential trends towards zero. As a result, the average particle charge also trends towards zero. In the absence of electrical forces (the ion drag, electrostatic forces and Coulomb interactions scale with particle charge), the ring of particles disperses. Growth accelerates downstream due to the higher value of N_r. By the time of exiting the reactor, particles spend nearly 4τ in the plasma by being trapped by the plasma potential. This long residence time results in fairly large particles (>100 nm).

The NP size distribution leaving the reactor is fairly mono-disperse with less than a 1% standard deviation. We attribute this narrow size distribution to the initial nuclei that are seeded in the plasma having the same size. This result implies that broad size distributions may be attributable to a random distribution of nuclei sizes.

6.3.2 Inlet SiH_4 Fraction

Lower mole fractions of SiH_4 in the inlet flow are expected to produce a more electropositive plasma while increasing silane fractions will trend towards producing an ion-ion plasma. The consequences of inlet silane mole fraction (0.1% to 50%) on electron density, plasma potential, SiH_4 density and N_r are shown in Figs. 6-5 and 6-6. Other parameters from the base

conditions were held constant – 1 Torr, 10 W at 10 MHz, with 50 sccm total inlet flow. Values in Figs. 6-5 and 6-6 are shown as a function of axial position (measured from the inlet) on the axis of the reactor (r = 0 cm). The electron density increases with decreasing SiH_4 inlet fraction due to lower rates of power loss to non-ionizing collisions (dominantly dissociation of SiH_x) and lower rates of electron attachment to form negative ions. In all cases, the electron density decreases by at a factor of at least 10^4 due to the presence of thermally attaching Si_xH_y radicals and dissociative recombination. At lower SiH_4 fractions (< 2%), the dominant ion shifts from SiH_3^+ to Ar^+ even in the region of the maximum power deposition. Increasing the SiH_4 mole fraction leads to flatter axial profiles in the plasma potential resulting from the lower electron density and increased electronegativity, while there is an increasingly higher plasma density and potential off-axis due to more localized power deposition.

The fractional dissociation of SiH_4 increases with decreasing inlet mole fraction. Decreasing inlet SiH_4 fraction results in increased gas heating. An increase in T_e produces an increase in plasma potential which in turn produces more ion acceleration leading to charge exchange heating. The higher gas temperature leads to more rarefaction. The weighted densities of reactive species N_r, shown in Fig. 6-6b, increase with increasing inlet fraction, which should lead to faster particle growth. There is only a small difference in N_r when increasing the inlet mole fraction from 25% to 50%. By this mole fraction, the production of radicals is limited by power deposition and not by availability of silane.

The average particle diameters as a function of time for different silane mole fractions are shown in Fig. 6-6c. The particle growth rates increase with increasing SiH_4 inlet fraction due to the increase in N_r. Particle sizes are shown up to the time that the (untrapped) particles flow out of the reactor. Particles for the two lowest fractions of SiH_4 (0.1% and 0.25%) remain trapped in

the plasma over the total simulation time (500 ms, >10 τ) and do not flow out of the reactor. The final particle sizes do not directly correspond with growth rates. For example, the final particles sizes are 26.7, 62.7, 42.7, and 86.8 nm for 0.1, 0.25, 0.5 and 1.0% SiH_4 fractions. The final particle size results from the integrated growth during the particle's entire residence time in the reactor. The particle's residence time is determined by the trapping electrical potential in the plasma (larger for smaller mole fractions) and the densities of growth species (larger for larger mole fractions). Increasing particle size increases the fluid drag forces, while the electrostatic force depends on particle charge and the local electric field. Therefore, particles reach the critical size which enables fluid drag forces to overcome the trapping potential and flow out of the reactor at different sizes for different silane mole fractions. Once the NPs escape from the electrostatic trap, they continue to grow while flowing downstream through regions where N_r is large.

For example, the gas residence time is τ=33 ms in these cases based solely on flow rate and volume of the reactor. Accounting for differences in position of the maximum in plasma potential, the NPs particles should flow out of the reactor in ≈20 ms after reaching a critical size where fluid drag overcomes the electrostatic force. For the base conditions (2% SiH_4), particles should take about 100 ms to reach this size as shown in Fig. 6-4c. The time that the particles flow out of the reactor is 120 ms, as shown in Fig. 6-6c). Decreasing the inlet SiH_4 fraction increases the trapping potential while the growth rate decreases. The balance of residence vs growth rate favors the influence of growth rate, which overall results in smaller particles.

Increasing the inlet SiH_4 fraction results in a mix of smaller, similarly sized, and a few larger particles due to the decreased trapping potential but highly increased growth rates. The highest inlet fractions have a nearly flat axial plasma potential having only moderate trapping which results in particles flowing out of the plasma in approximately one residence time. This

shorter exposure time to radicals then decreases the final particle size. However, a few ms of extra time trapped in the plasma can lead to significantly larger particles. For example, the particle size increases from 126 nm to 153 nm in going from 50% to 25% inlet SiH_4 fraction, the latter having a more positive trapping potential, while the density of growth species N_r is nearly the same. With particles trapped for 5.0 ms longer for the smaller mole fraction, overall growth is proportionately larger.

Overall, the growth rates of particles in the plasma closely follow from what one might expect intuitively – increased inlet mole fraction produces larger densities of growth precursor which enables higher growth rates. However, the final particle sizes are ultimately determined by residence times of particles in the presence of the growth species, which in turn are determined by the trapping of negatively charged NPs in the plasma.

6.3.3 Gas Residence Time (τ)

Negatively charged NPs can remain in the plasma for several gas residence times due to electrostatic trapping, while the total time spent in the plasma directly impacts the size of the NPs. The impact of gas residence time (τ) was investigated by performing simulations with τ in the range of 10 ms to 500 ms. The specific input parameters are listed in Table 6-III. With constant power deposition, residence time determines the energy deposition per inlet molecule which then affects fractional dissociation and radical production. To minimize these dependencies the power deposition was adjusted (0.67 W to 33.3 W) to produce a constant energy deposition per inlet molecule/atom of 2.8 eV. Higher powers are applied to higher flow rates to maintain the constant specific energy deposition.

Plasma properties for different gas residence times are shown in Fig. 6-7 as a function of axial distance from the inlet on axis (r = 0). Electron densities increase with decreasing residence

time (higher flow rate) due to the higher applied power required to keep the energy deposition per molecule constant. The electron temperature has a consistent profile for all cases with a slight trend for increasing temperature with increasing gas residence time. With the gas mole fractions, dissociation fraction and gas temperatures nearly the same (due to the constant energy deposition/molecule), the self-sustaining electron temperature is also nearly the same. Since the plasma potential in glow discharges generally scales with electron temperature, the plasma potential has nearly the same peak value between the turns of the antenna, while the profile becomes more uniform along the reactor length with increasing τ (lower flow rate). This is indicative of transitioning from an electropositive to an electronegative plasma with increasing gas residence time.

The densities of particle growth species are shown in Fig. 6-8. Longer gas residence times τ (lower flow rates) result in diffusive transport being more dominant, producing more uniform distributions of SiH_4 and reactive dissociation products. With shorter residence times τ (higher flow rates) advective transport dominates with there being less opportunity for diffusion upstream towards the inlet. As a result, the reactive density N_r, for τ = 10 ms is negligible at the inlet with there being larger densities downstream. Conversely with τ = 500 ms, the diffusion of reactants upstream is able to compete with advection downstream, and the distribution of N_r is nearly uniform. However, when integrating along the length of the discharge, the average value of N_r is nearly constant since the energy deposition per molecule is constant.

Particle diameters as a function of time for different flow rates (growth rates being the slope of diameter vs time) are shown in Fig. 6-8c. Increasing the gas residence time increases the final particle size. The fluid drag force scales with fluid velocity which decreases with longer gas residence times (lower flow rates). The end result is that similarly sized and charged particles are

trapped at the peak of the plasma potential (similar for all flow rates) longer for lower flow rates (long τ). Particle growth rates increase for shorter residence times due to there being higher densities of reactive species at the location of the particle trap at the peak in plasma potential at ≈2.5 cm. However, with the higher flow rates, the particles stay trapped for a shorter period of time, which reduces their final size.

6.3.4 Energy Deposition Per Particle

Power deposition is one of the primary control parameters for particle growth as power directly impacts the densities of reactive species. However, the inventory of reactive species is determined by the fractional dissociation of the feedstock SiH_4, which in turn is largely determined by the energy deposition per inlet molecule (E_p). However, even when controlling for E_p, electron density and gas heating can impact particle growth rates and so the final particle size. A parameterization of energy per particle E_p was conducted while varying power from 0.5 W to 25 W, producing values of E_p of 0.14 to 7.0 eV/particle. The range of conditions are shown in Table 6-IV.

The electron density and plasma potential as a function of distance from the inlet on axis (r = 0) for different energy per particle (E_p) are shown in Fig. 6-9 for otherwise the base-case conditions. The peak electron density spans 2 orders of magnitude from the lowest power (0.5 W, $n_e \approx 2\times10^9$ cm^{-3}, E_p = 0.14 eV/particle) to the highest power (25 W, $n_e \approx 3\times10^{11}$ cm^{-3}, E_p = 7.0 eV/particle). The majority of this increase is simply due to the 50-fold increase in power deposition. Other contributions include the increasing dissociation of SiH_4 and increasing gas temperature, both of which make for less collisional conditions and higher ionization efficiency. The maximum gas temperature spans 327 to 465 K for 0.5 W to 25 W. The electron density

decreases downstream in all cases due to thermal attachment to radicals, dissociative recombination and diffusion to the walls.

Axial profiles for silane fraction are shown in Fig. 6-10a and reflect the increasing rates of dissociation and rarefaction with increasing power. With only 2.5 W (E_p = 0.70 eV/particle), the SiH_4 fraction decreases to less than 10% that at the inlet. For higher powers, the dissociation of SiH_4 is nearly complete. However, the fractional decrease is in part exaggerated by the increase in the total density due to the production of dissociation fragments. The rebound in silane mole fraction downstream can be largely attributed to H atom consumption. For low powers (0.5 W, E_p = 0.14 eV/particle and 1 W, E_p = 0.28 eV/particle), the fractional dissociation of SiH_4 is smaller and the fraction of H atoms is an order of magnitude (or more) smaller than SiH_4. For higher power, the dissociation of SiH_4 is nearly complete which leads to H fractions exceeding those of SiH_4 under the antenna. At 25 W (E_p = 7.0 eV/particle), the SiH_4 fraction is 2 orders of magnitude smaller than that of H atoms (0.004% compared to 0.8%). Once formed, H radicals are reactive and recombine on the walls, decreasing their density downstream, leaving the reactor with a mole fraction of 0.02%. The end result is an increase in the SiH_4 mole fraction to 0.01% at the pump. The densities of the weighted growth species, N_r, are shown in Fig. 6-10b for different E_p. The general trend is as expected – N_r increases with increasing power. At powers above 10 W (E_p = 2.8 eV/particle), the silane is highly dissociated and N_r begins to saturate. Even with the silane fully dissociated, N_r continues to increase as, for example, SiH_3 is converted to SiH_2 which has a higher sticking probability and so a larger contribution to N_r.

Average NP sizes as a function of time for different E_p are shown in Fig. 6-10c. As expected, the particle growth rate (slope of the size vs time) increases with increasing E_p due to the increase in reactive species densities. The time that a particle spends in the plasma increases

up to an energy deposition of E_p = 4.2 eV/particle or 15 W. (Recall that the data in Fig. 6-10c extends to when the particles leave the system if not trapped.). Lower E_p produces smaller local maxima in the plasma potential with lower electron densities. The confining electric fields are smaller and there is less particle charging. As a result, fluid drag forces overcome the electrostatic trapping forces at smaller NP size, which reduces residence time and particle size. For E_p > 4.2 eV/particle (power > 15 W), the particles grow faster due to the increase in N_r however the trapping potential is also lower, enabling fluid drag to overcome the trapping potential earlier. This shorter residence time leads to final particle sizes decreasing for higher powers. Even with faster growth rates, if the particles are trapped for less time the net growth can be less.

6.3.5 Gas Pressure

Nanoparticles are typically grown in plasmas having pressures of half to a few Torr. However even within this range of pressure, discharge characteristics can vary significantly. The consequences of gas pressure on NP growth for a pressure range of 0.25 to 2.5 Torr were investigated, with the input parameters shown in Table 6-V. The parameters were chosen to have a constant gas residence time and constant energy per particle. Axial profiles for plasma properties while varying gas pressure are shown in Fig. 6-11. The inventory of electrons (volume integral of plasma density) is fairly constant as the energy/particle is constant. The peak electron density increases with increasing pressure at the location of maximum power deposition due to the decrease in electron mean free path (0.34 cm to 0.03 cm from 0.25 to 2.5 Torr at 325 K) while the downstream electron density decreases with increasing pressure. Higher pressures increase the rate of electron energy loss, thereby confining the region of net positive ionization to the vicinity of the antenna. The on-axis electron temperature decreases with increasing pressure at the location of maximum power deposition due to lower rates of diffusion loss. Plasma potential decreases in

magnitude with increasing pressure due to this lower electron temperature and an increase in electronegativity.

Axial profiles of silane mole fraction and N_r for different pressures are shown in Fig. 6-12 as a function of distance from the inlet. The upstream SiH_4 fraction increases with increasing pressure as bulk fluid flow begins to dominate over diffusion – there is less of a spatial averaging of the depletion of SiH_4 at higher pressures. Downstream the trend is the opposite with decreasing silane mole fraction for higher pressures. With the decrease in importance of axial diffusion with increasing pressure, advection dominates the transport of silane.

The weighted growth species density N_r, as shown in Fig. 6-12b, increases with increasing pressure due, in part, to lower diffusion loses. Average particle diameters as a function of time for different pressures are shown in Fig. 6-12c. The particle growth rate increases with increasing pressure due to the increase in the densities of growth species. Particles are trapped in the plasma for longer periods with decreasing pressure due to the lower fluid drag forces and larger plasma potential. At the lowest pressures (0.5 and 0.25 Torr), the particles remained in the reactor until the end of the simulation time (500 ms). For the higher pressures typically used to grow particles, the final particle sizes range between 100 – 120 nm. These trends may indicate that pressure is not a major factor in determining particle size (keeping other parameters constant), and could instead be used to fine-tune the gas residence time and eV/particle.

6.3.6 Radius of Plasma Tube

A large portion of experimental work on plasma synthesis of nanoparticles has been performed using cylindrical (glass tube) reactors. As there has been little standardization of reactor specifications, the consequences of reactor dimensions on particle growth were investigated. The tube radius was varied while keeping the gas residence time, pressure and energy per particle

constant. Achieving these constraints requires adjusting both the input power and the inlet flow rate. The parameters varied in this study are in Table 6-VI.

The radius of the plasma tube was varied from 0.75 to 1.5 cm while keeping the reactor length 8 cm. The resulting axial profiles of plasma properties are shown in Fig. 6-13. With constant energy deposition per particle, the maximum plasma density is nearly constant with a maximum occurring off axis near the antenna from 7.2×10^{10} cm^{-3} to 1.0×10^{11} cm^{-3} for 0.75 and 1.5 cm radius respectively. The larger rate of radial diffusion with smaller radii produces a larger decrease in electron density with flow downstream. In a classical glow discharge with electron losses dominated by diffusion to the walls, electron temperature increases with decreasing radius to increase ionization to offset these losses. Since electron losses in the region of maximum power is a mix of attachment, dissociative recombination and diffusion, the electron temperature only modestly increases on axis (3.3 eV to 3.6 eV) with decreasing radius while a radius decrease from 1.5 cm to 0.75 cm increases diffusion losses by a factor of 4. Near the antenna, the electron temperature is 4.2 to 4.3 eV for all reactor radii. For nearly constant plasma density and pressure, the electromagnetic skin depth is nearly constant (≈1.9 cm) and so power deposition occurs closer to the axis with smaller tubes. This increase in local power deposition then contributes to the increase in T_e along the axis. The peak plasma potential relative to the negative wall potential is nearly constant as a function of radius of the discharge tube, having a small increase due to the increase in electron temperature. Here, the plasma potential relative to ground decreases with increasing radius due to negative charging of the glass tube.

Silane mole fraction and reactive species density N_r for different radii are shown in Fig. 6-14. With residence time, energy per particle and pressure constant, the profiles of silane density are similar. The lower silane mole fraction for smaller radius is attributable to the electromagnetic

skin depth reaching to the axis with there being more power deposition adjacent to the axis. (In a perfectly cylindrically symmetric system with purely collisional power deposition, the inductively coupled power on the axis is zero.). In spite of maintaining energy per particle constant, there is an increasing density of particle growth species with increasing radius, likely a result of more wall losses by diffusion at small radii. The increase in N_r leads to a higher rate of particle growth for larger radii, as shown in Fig. 6-14c. The electrostatic plasma potential traps NP in a ring near the peak plasma potential adjacent to the powered antenna where the plasma properties are a weak function of radii. Particles reach similar sizes before fluid drag dominates, which results in particles with a final size of ≈120 nm.

6.4 Concluding Remarks

The trapping of nanoparticles (NP) in low temperature plasmas largely results from their acquiring negative charge and being attracted to the maximum in plasma potential. In ICPs, this maximum occurs in the vicinity of the antenna. In flowing reactors, the final NP size results from the residence time of the NP and the local density of radicals which contribute to its growth. The location of electrostatic trapping of NPs will depend on other forces (e.g., particle-particle Coulomb interactions, ion-drag, thermophoresis). However, these forces in ICPs are typically not large enough to remove NPs from the trap. In flowing plasmas, the particles are generally removed from the trap by fluid drag when reaching a critical size. Results from a computational investigation were discussed to develop scaling laws for the growth of Si nanoparticles in ICPs based on their trapping and ultimately de-trapping.

The growth rates and final sizes of NPs can be controlled by tuning the gas residence time and energy deposition per particle. Small nanometer sized particles charge primarily negative and

are most sensitive (on a relative basis compared to other forces) to the electrostatic positive plasma potential. This electrostatic trapping enables small particles to remain in the reactor for times exceeding several gas residence times - growing until a critical threshold in size is reached where fluid drag becomes a dominant force to remove the particles from the trap. Once the NPs are entrained in the gas flow, they generally enter a region downstream in which the density of growth species is larger, thereby enhancing their growth rates. The final particle size is then determined by two residence times – the time the particle spends in the electrostatic trap and the time the particle spends flowing downstream through the higher density of growth species, a fraction of the gas residence time.

The inlet fraction of precursor gas, silane in this study, directly affects the growth rates of the nanoparticles due to increased availability of growth species. However, large SiH_4 fractions create electronegative plasmas in which the trapping potential for negative charged NPs can be significantly lower. This lower trapping potential reduces the residence time of NPs in the electrostatic trap, which leads to some unpredictability in final particle sizes.

When keeping energy deposition per particle constant, gas residence time can be used to control final particle size. Longer residence times (lower flow rates) result in lower growth rates due to there being lower local densities of growth species whose transport is dominated by diffusion rather than advection. However, final particle size increases with increasing gas residence time (lower flow rates) due to the NPs spending much more time in the plasma. NPs must reach a size where fluid drag can overcome the electrostatic trapping potential and then flow out of the reactor over the gas residence time while continually growing.

Energy per particle E_P directly affects the densities of reactive species and so the growth rates of nanoparticles. With increasing E_P (or power for all other parameters remaining constant),

production of growth species eventually saturates due to dissociation of the feedstock gases. Power also to some degree controls the trapping potential for NPs as increasing power decreases the electronegativity of the plasma and increases rarefaction. It was found that these competing factors leave room for optimization – for a given set of operating conditions, there may be an optimum power or E_P to produce a given size particle.

When controlling for gas residence time and E_P, nanoparticles grow faster at higher pressure due to there being higher densities of reactive growth species. However, final particle size remained similar across a range of pressures (0.75 to 2.5 Torr) due to there being increased fluid drag and lower trapping potential at higher pressure which ultimately reduces the residence time of the NPs. Gas pressure may also be a tuning parameter when the goal is to keep the NP size constant while varying other properties (e.g., core-shell particles).

The choice of LTP reactor to synthesize NPs having desired morphological or compositional properties is a multi-dimensional optimization process. Current best practice has evolved to use capacitively coupled plasmas (CCPs) [50]. The growth of NPs in these systems has been robust and able to synthesize a variety of types of NPs [5,51,52]. The plasma potential in these CCPs, at least in the tubular reactors now commonly used to synthesize NPs, is less well defined spatially, which leads to difficulty in controlling the electrostatic trapping potential that enables predictable and controlled growth of NPs. With the plasma potential more localized and predictable in ICPs, avenues open up to use the electric trap as an incubator for particle growth, which is then emptied when the NPs reach a critical size. This capability, perhaps combined with power pulsing, would provide an avenue to finely control the size of NPs in the range of 20-100 nm. This advantage diminishes for NPs of less than a few nm in size when the stochastic charging

of the particles may produce a distribution of negative, positive and neutral NPs. The positive and neutral NPs are less controllable due to their inability to be trapped.

In addition to control of the size and properties of the NPs, utilization of the feedstock gases, silane in this case, is also important in industrial applications. Ultimately the rate of production of NPs and cost (in part determined by utilization of feedstock gases) determine the practicality of industrially implementing these techniques. Since ICPs typically produce larger dissociation fractions than CCPs for otherwise identical operating conditions, the average radical has a higher sticking coefficient in ICPs compared to CCPs. These higher sticking coefficients are beneficial with respect to NP nucleation and growth. However, the higher sticking coefficients are detrimental with respect to sticking to and film growth on walls, which is loss reducing feedstock utilization. In this regard, control of wall conditions (e.g., temperature) may be important in reducing film growth and increasing utilization. Here, CCPs may have an advantage over ICPs in that the average ion energy striking surfaces is higher in CCPs than ICPs. These higher ion energies produce higher rates of sputtering of films on the walls, at least those in the active plasma zone, returning SiH_x radicals to the gas phase which can participate in particle growth. An optimized process that takes advantage of the controlled trapping afforded by ICPs while limiting film growth and increasing utilization might use an ICP operating in a mixed E-mode and H-mode [42]. The mixed E-mode/H-mode operation will produce more energetic ions onto surfaces to sputter film while not significantly perturbing the cycle averaged plasma potential.

Table 6-I. Species Used in the Plasma Chemistry Model.

Argon and electrons

Ar, $Ar(1s_5)$, $Ar(1s_4)$, $Ar(1s_3)$, $Ar(1s_2)$, Ar(4p), Ar(4d), Ar^+, e

Hydrogen species

H_2, H_2^*, H, H^*, H^+

Silane species

SiH_4, SiH_3, SiH_2, SiH, Si_2H_6, Si_2H_5, Si_2H_3, Si_2H_2, SiH_3^+, SiH_3, SiH_2^-

Table 6-II. Species sticking coefficients (S_c) onto NPs used in this work derived using molecular dynamics simulation. The technique consists of launching molecules onto a representative $Si_{29}H_{36}$ molecule and counting the fraction of chemisorbed impacts. Note that the coefficients for Si_2H_x species were estimated based on the number of dangling bonds with reference to SiH_x values.

Species	S_c	T_{gas}
SiH_4	0.	400
SiH_3	0.125	400
SiH_2	0.66	400
SiH	0.945	400
Si_2H_6	0.	
Si_2H_5	0.1	
Si_2H_3	0.3	
Si_2H_2	0.66	

Table 6-III. Species Operating conditions for the parameter sweep varying input gas flow rate to control gas residence time (τ). Input silane fraction remained at 2%.

Pressure (Torr)	Flow rate (sccm)	Power (W)	τ (ms)	Energy per particle (eV)
1	167.8	33.4	10	2.8
1	66.7	13.3	25	2.8
1	50.0	10	33	2.8
1	41.7	8.3	40	2.8
1	33.4	6.7	50	2.8
1	22.2	4.4	75	2.8
1	16.7	3.3	100	2.8
1	11.1	2.2	150	2.8
1	8.3	1.7	200	2.8
1	6.7	1.3	250	2.8
1	3.3	0.67	500	2.8

Table 6-IV. Operating conditions for the parameter sweep varying energy per particle. The input fraction of SiH_4 remains at 2%.

Pressure (Torr)	Flow rate (sccm)	Power (W)	τ (ms)	Energy per particle (eV)
1	50	0.5	33	0.14
1	50	1.0	33	0.28
1	50	2.5	33	0.70
1	50	5.0	33	1.4
1	50	10	33	2.8
1	50	15	33	4.2
1	50	20	33	5.6
1	50	25	33	7.0

Table 6-V. Operating conditions for the parameter sweep varying gas pressure, keeping gas residence time and energy per particle constant.

Pressure (Torr)	Flow rate (sccm)	Power (W)	τ (ms)	Energy per particle (eV)
0.25	12.5	2.5	33	2.8
0.5	25	5	33	2.8
0.75	37.5	7.5	33	2.8
1.0	50	10	33	2.8
1.25	62.5	12.5	33	2.8
1.5	75	15	33	2.8
1.75	87.5	17.5	33	2.8
2.0	100	20	33	2.8
2.5	125	25	33	2.8

Table 6-VI. Operating conditions for the parameter sweep varying radius of the discharge tube while keeping gas residence time, energy per particle and inlet silane mole fraction constant 2%.

Radius (cm)	Length (cm)	Pressure (Torr)	Flow rate (sccm)	Power (W)	τ (ms)	Energy per particle (eV)
0.75	8	1.0	28.1	5.6	33	2.8
1.0	8	1.0	50	10.0	33	2.8
1.25	8	1.0	78.1	15.6	33	2.8
1.5	8	1.0	112.5	22.5	33	2.8

6.5 Figures

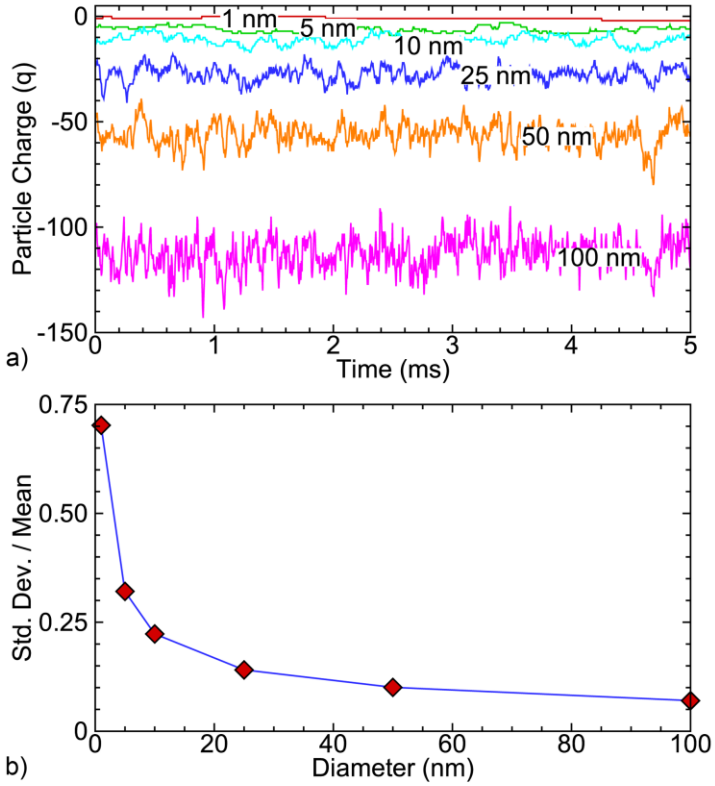

Figure 6-1. Particle charging characteristics. a) Particle charge (in units of elementary charge) as a function of particle size (1 – 100 nm) for particles immersed in the base case reactor (1 Torr, 10 W, 50 sccm, Ar/SiH_4 = 98/2). The particles were initialized in the same position in the reactor with no movement to isolate the charging algorithm. b) Standard deviation of the charge fluctuations scaled by the mean particle charge for particle sizes of 1 – 100 nm. The magnitude of the relative charge fluctuations decrease with increasing particle size.

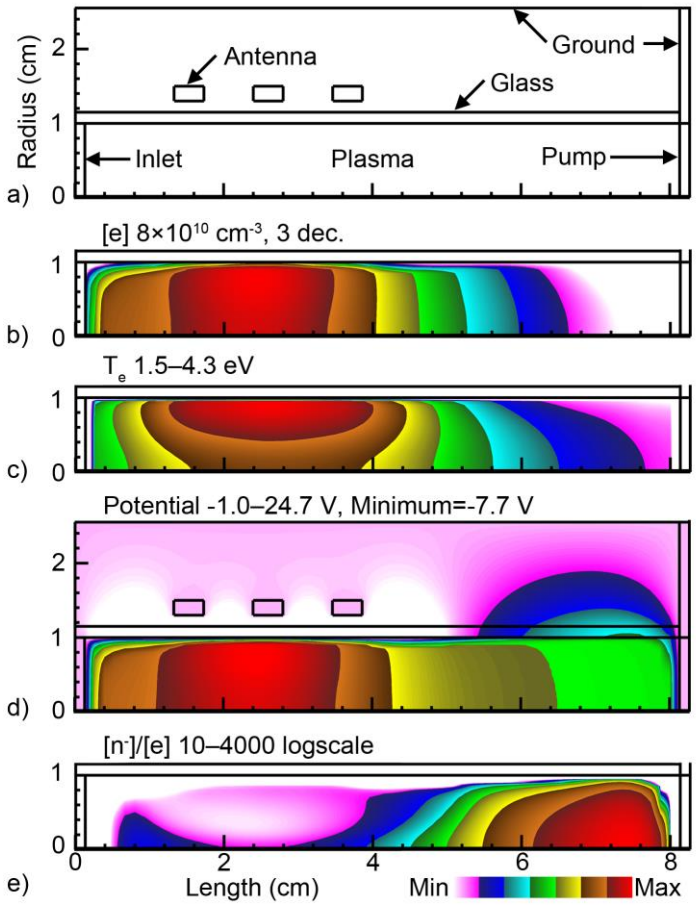

Figure 6-2. Reactor and plasma properties for the base case conditions (1 Torr, 10 W, 50 sccm, Ar/SiH_4 = 98/2). a) Schematic of the reactor, b) electron density, c) electron temperature, d) electric potential and e) electronegativity parameter α = [N-]/[e]. The maximum value is shown in each frame. 2 dec or 3 dec indicates the number of decades plotted on a log-scale.

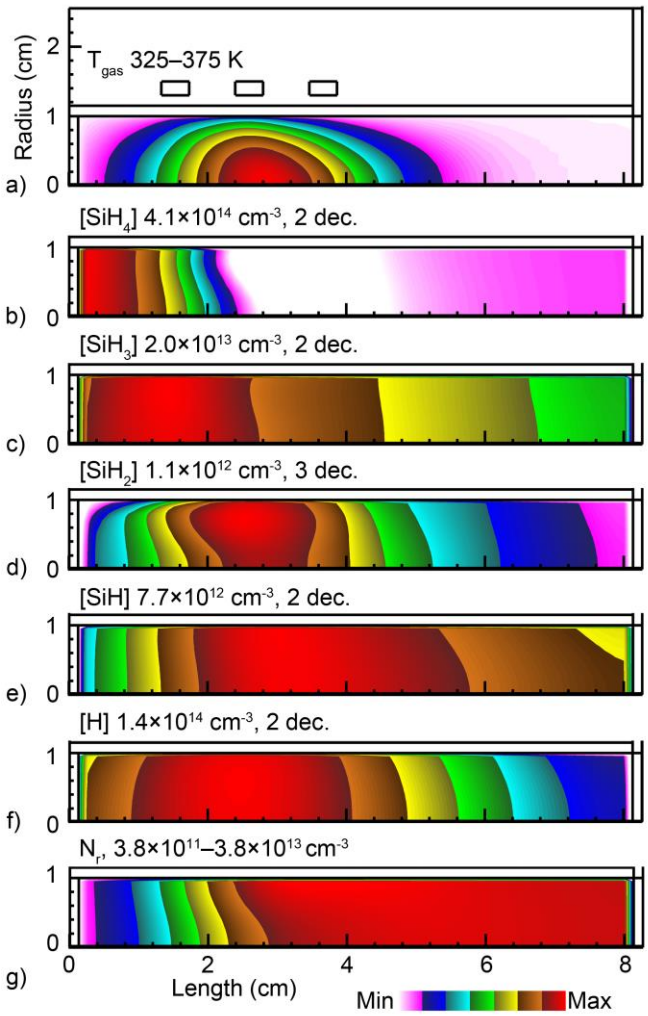

Figure 6-3. Plasma properties for the base case conditions (1 Torr, 10 W, 50 sccm, Ar/SiH_4 = 98/2). a) Gas temperature (Tgas), b) SiH_4 density, c) SiH_3 density, d) SiH_2 density, e) SiH density, f) H density and g) N_r (sum of radical density times sticking coefficient to the NP). The maximum value is shown in each frame. 2 dec or 3 dec indicates the number of decades plotted on a log-scale.

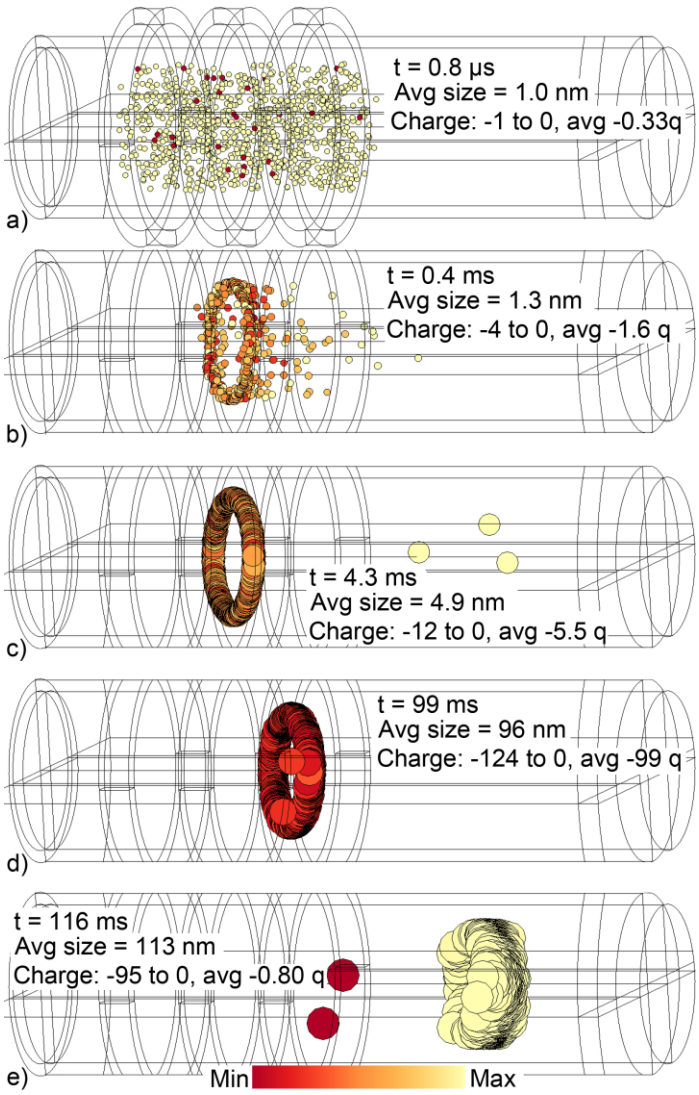

Figure 6-4. Particle locations for the base case conditions (1 Torr, 10 W, 50 sccm, Ar/SiH_4 = 98/2) at different times a) 0.8 μs, b) 0.4 ms, c) 4.3 ms, d) 99 ms and e) 116 ms. The sizes of the NPs are indicated by the size of the individual images. The charge on the NPs are color coded, with the range of charge noted in each frame.

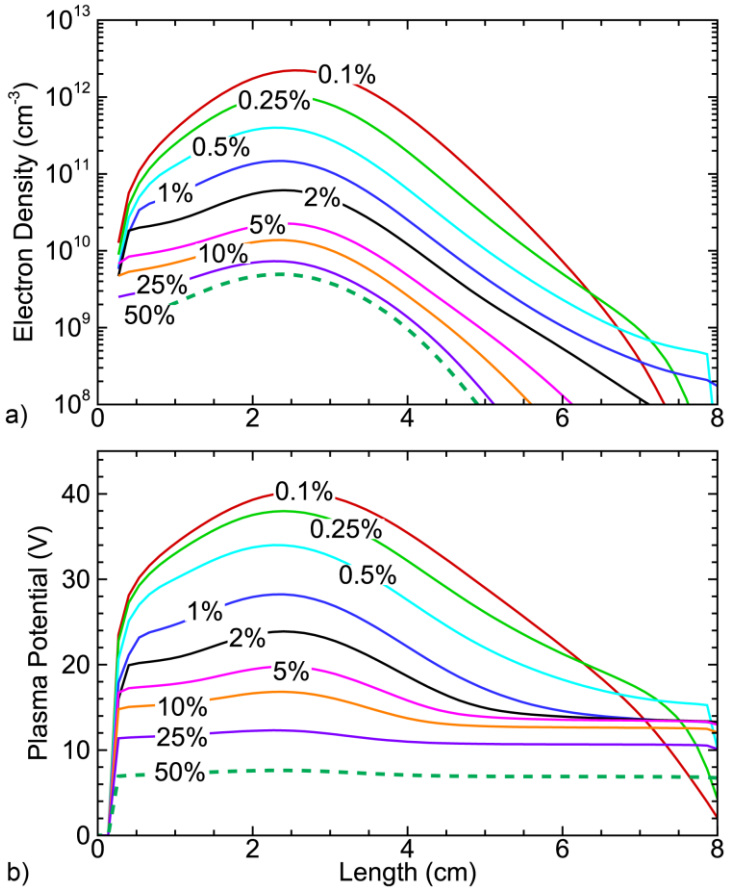

Figure 6-5. Plasma properties along the axis while varying SiH_4 inlet fraction from 0.1% to 50%. a) Electron density and b) plasma potential. Curves are labeled with the SiH_4 mole fraction.

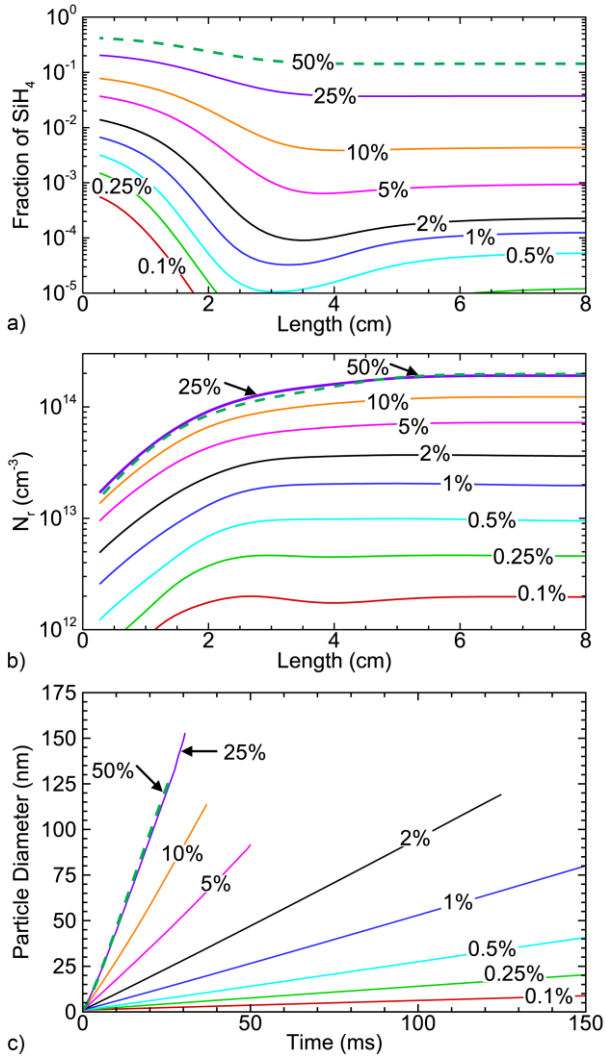

Figure 6-6. Plasma and particle properties along the axis while varying SiH_4 inlet fraction from 0.1% to 50%. a) SiH_4 mole fraction, b) density of scaled growth species, N_r and c) average particle sizes as a function of time. Curves are labeled with the SiH_4 mole fraction.

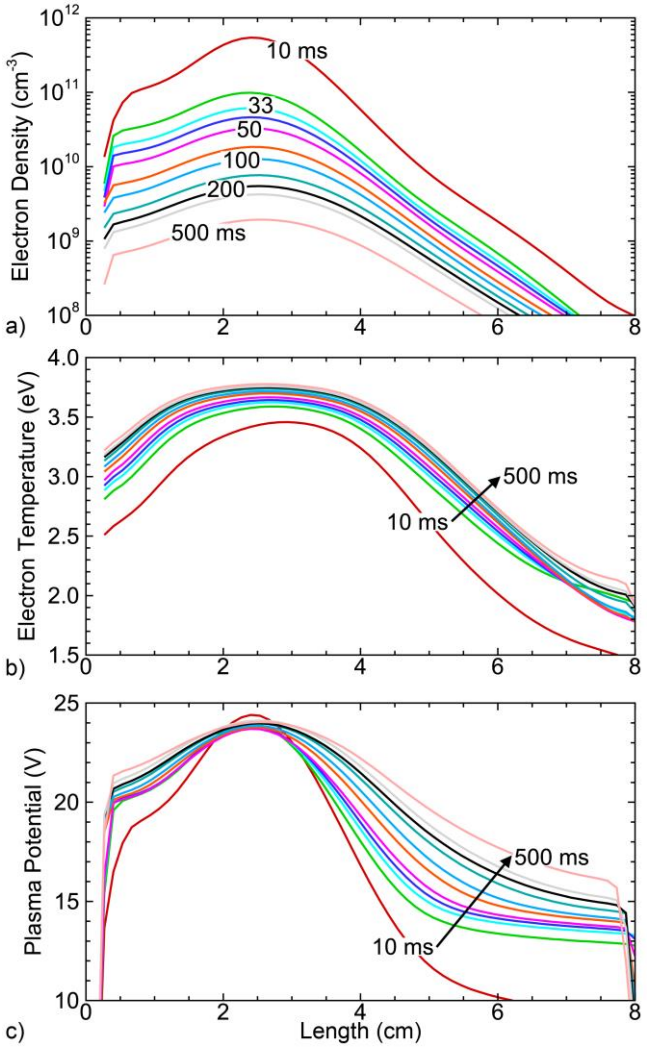

Figure 6-7. Plasma properties along the axis while varying gas residence time from 10 ms to 500 ms. a) Electron density, b) electron temperature and c) plasma potential. Curves are labeled with the gas residence time.

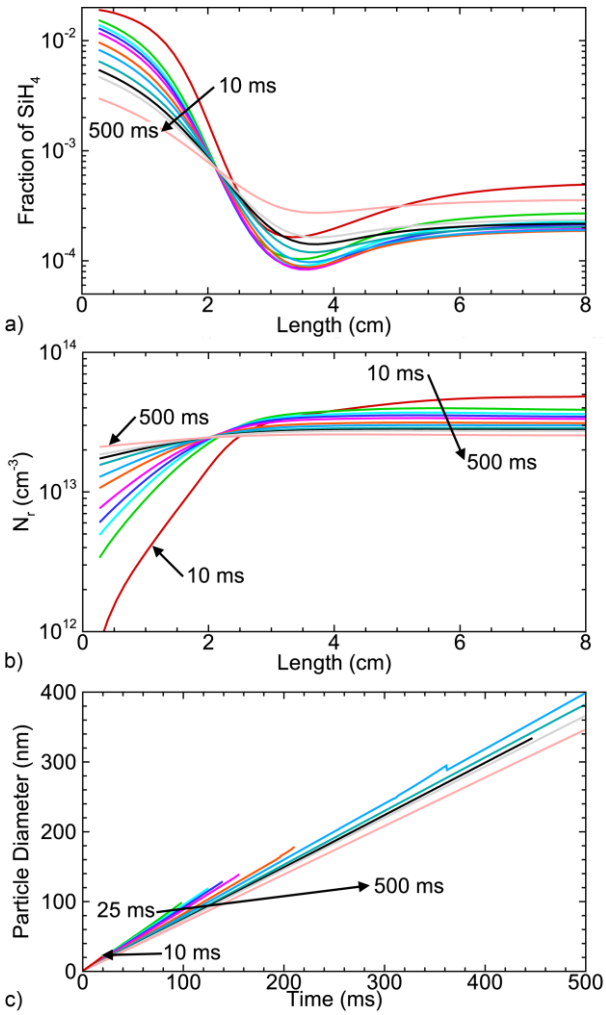

Figure 6-8. Plasma and particle properties along the axis while varying gas residence time from 10 ms to 500 ms. a) SiH_4 mole fraction, b) density of scaled growth species, N_r and c) average particle sizes as a function of time. Curves are labeled with the gas residence time.

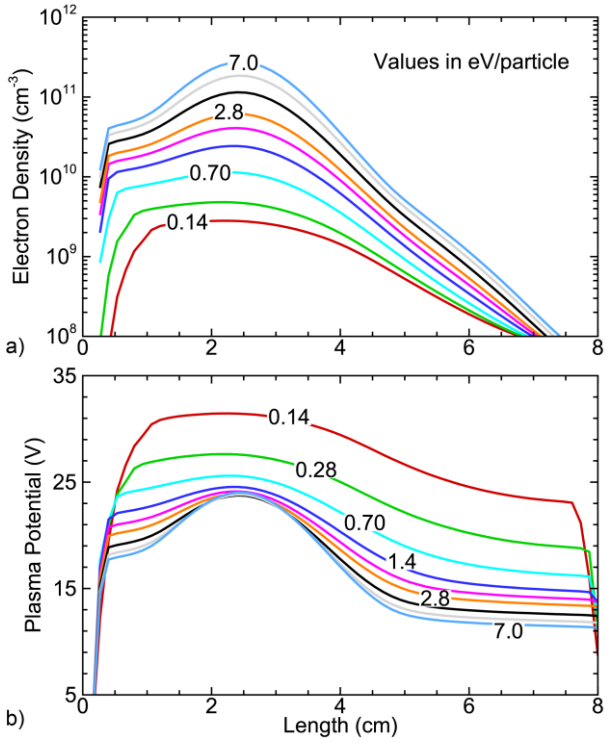

Figure 6-9. Plasma properties along the axis while varying energy/particle EP from 0.14 to 7.0. a) Electron density and b) plasma potential. Curves are labeled with the value of EP.

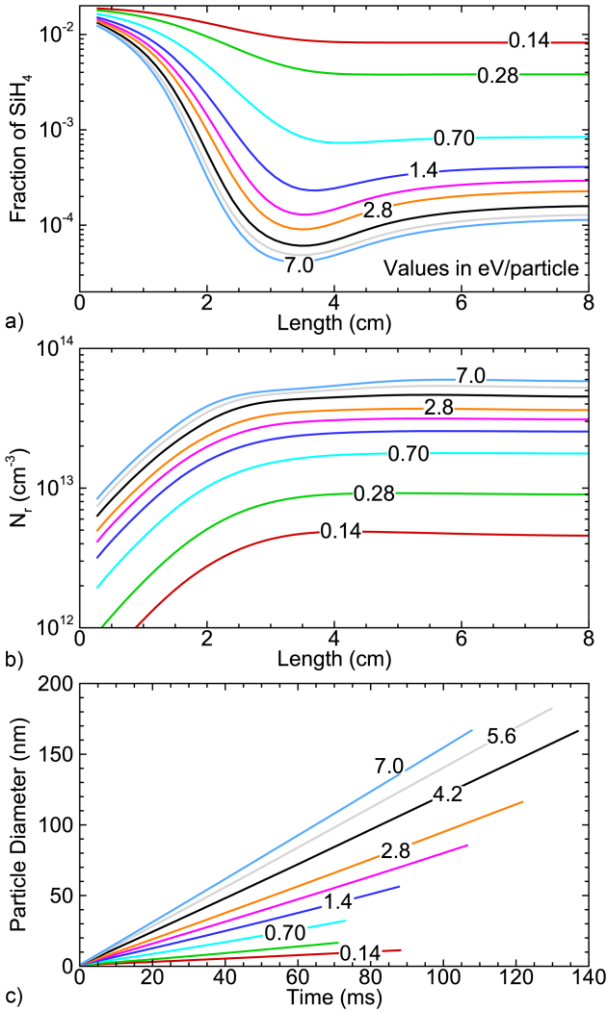

Figure 6-10. Plasma and particle properties along the axis while varying energy/particle EP from 0.14 to 7.0 eV/particle. a) SiH_4 mole fraction, b) density of scaled growth species, N_r and c) average particle sizes as a function of time. Curves are labeled with values of EP.

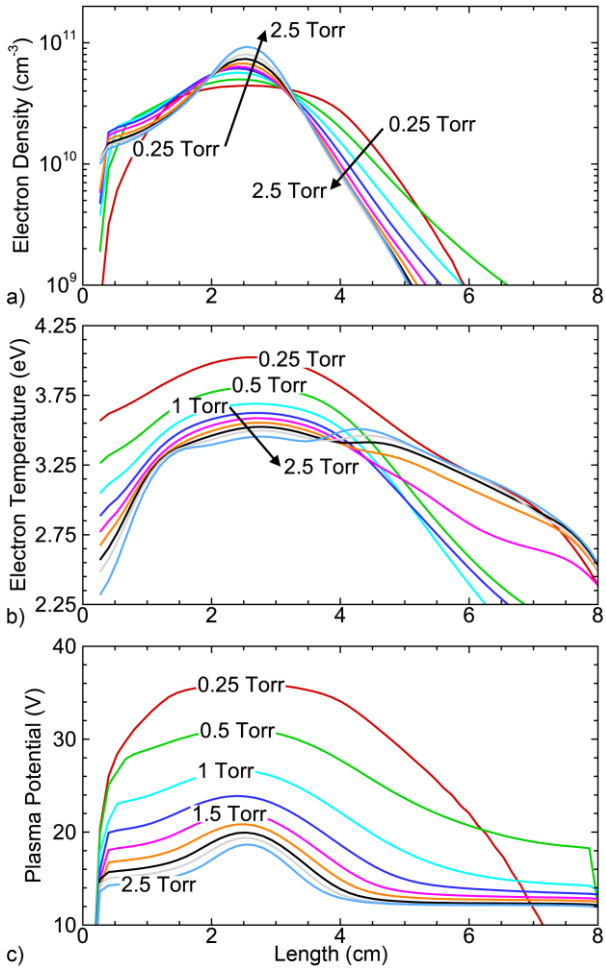

Figure 6-11. Plasma properties along the axis while varying gas pressure for 0.25 to 2.5 Torr. a) Electron density, b) electron temperature and c) plasma potential. Curves are labeled with the gas pressure.

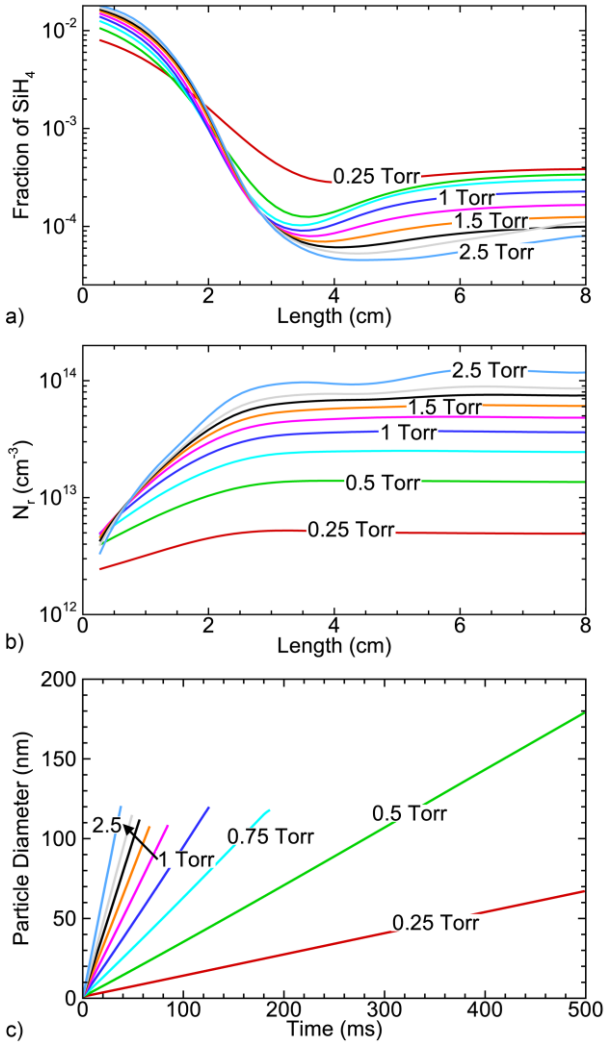

Figure 6-12. Plasma and particle properties along the axis while varying gas pressure from 0.25 to 2.5 Torr. a) SiH_4 mole fraction, b) density of scaled growth species, N_r and c) average particle sizes as a function of time. Curves are labeled with the gas residence time.

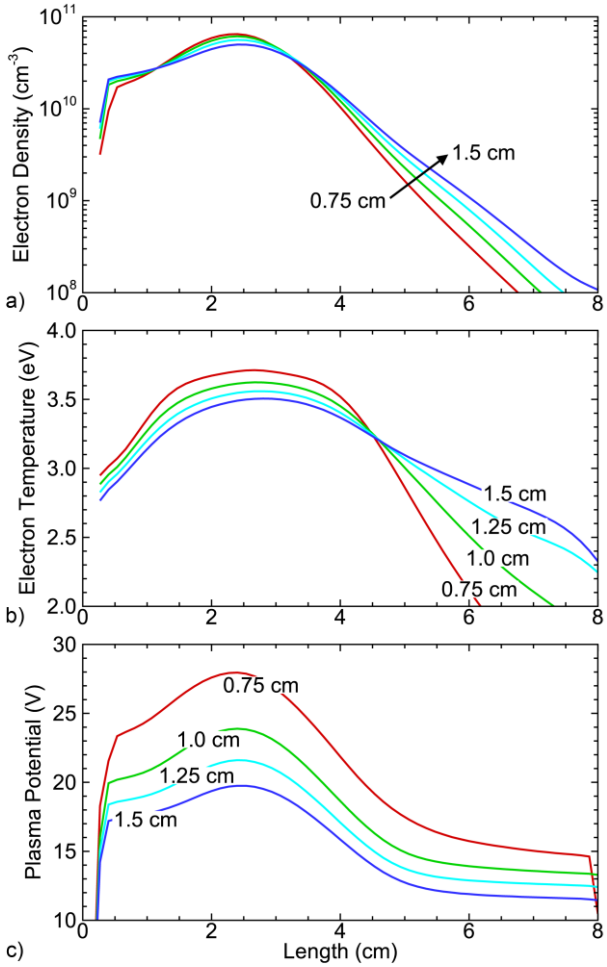

Figure 6-13. Plasma properties along the axis while varying radius of the discharge tube from 0.75 to 1.5 cm. a) Electron density, b) electron temperature and c) plasma potential. Curves are labeled with the tube radius.

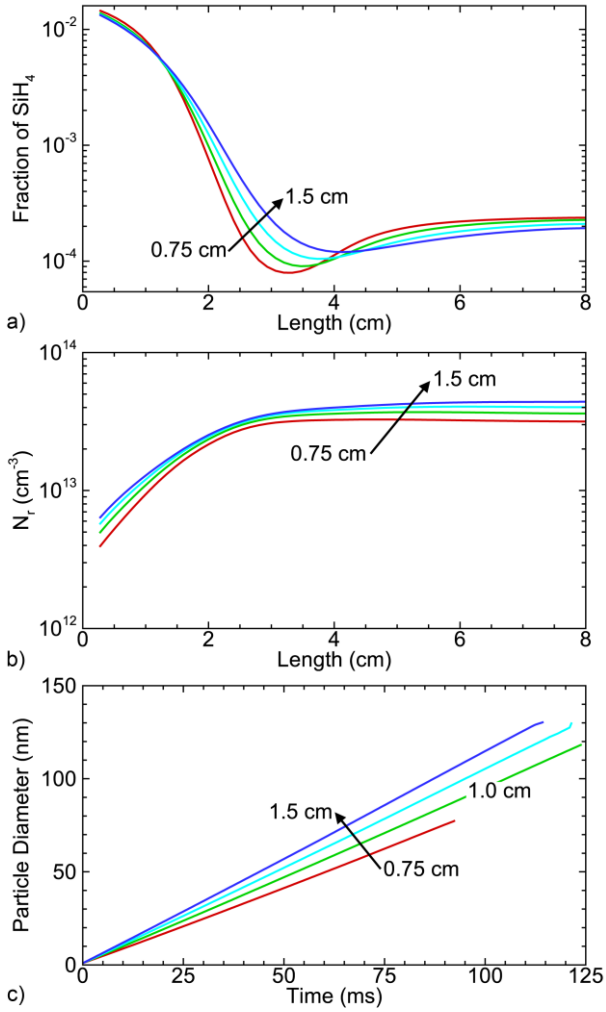

Figure 6-14. Plasma and particle properties along the axis while varying radius of the discharge tube from 0.75 to 1.5 cm. a) SiH_4 mole fraction, b) density of scaled growth species, N_r and c) average particle sizes as a function of time. Curves are labeled with the tube radius.

6.6 References

[1] U. Kortshagen, J. Phys. D. Appl. Phys. **42,** (2009).

[2] A. Bapat, C. Anderson, C. R. Perrey, C. B. Carter, S. A. Campbell and U. Kortshagen, Plasma Phys. Control. Fusion **46,** (2004).

[3] U. Kortshagen, Plasma Chem. Plasma Process. **36,** 73 (2016).

[4] L. Mangolini, E. Thimsen and U. Kortshagen, Nano Lett. **5,** 655 (2005).

[5] A. Alvarez Barragan, N. V. Ilawe, L. Zhong, B. M. Wong and L. Mangolini, J. Phys. Chem. C **121,** 2316 (2017).

[6] E. Thimsen, U. R. Kortshagen and E. S. Aydil, J. Phys. D. Appl. Phys. **48,** (2015).

[7] B. L. Greenberg, S. Ganguly, J. T. Held, N. J. Kramer, K. A. Mkhoyan, E. S. Aydil and U. R. Kortshagen, Nano Lett. **15,** 8162 (2015).

[8] A. Ho, R. Mandal, R. R. Lunt and R. J. Anthony, ACS Appl. Nano Mater. **4,** 5624 (2021).

[9] C. R. Gorla, S. Liang, G. S. Tompa, W. E. Mayo and Y. Lu, J. Vac. Sci. Technol. A Vacuum, Surfaces, Film. **15,** 860 (1997).

[10] U. R. Kortshagen, R. M. Sankaran, R. N. Pereira, S. L. Girshick, J. J. Wu and E. S. Aydil, Chemical Reviews **116,** 11061 (2016).

[11] A. Izadi and R. J. Anthony, Plasma Process. Polym. **16,** 1 (2019).

[12] L. Boufendi and A. Bouchoule, Plasma Sources Sci. Technol. **3,** 262 (1994).

[13] V. A. Schweigert and I. V. Schweigert, J. Phys. D. Appl. Phys. **29,** 655 (1996).

[14] P. Agarwal and S. L. Girshick, Plasma Sources Sci. Technol. **21,** (2012).

[15] C. Cui and J. Goree, IEEE Trans. Plasma Sci. **22,** 151 (1994).

[16] P. Agarwal and S. L. Girshick, Plasma Chem. Plasma Process. **34,** 489 (2014).

[17] U. Kortshagen and U. Bhandarkar, Phys. Rev. E - Stat. Physics, Plasmas, Fluids, Relat.

Interdiscip. Top. **60,** 887 (1999).

[18] R. Le Picard, A. H. Markosyan, D. H. Porter, S. L. Girshick and M. J. Kushner, Plasma Chem. Plasma Process. **36,** 941 (2016).

[19] X. Chen and C. J. Hogan, Chem. Eng. J. **411,** 128383 (2021).

[20] M. J. Kushner, J. Phys. D. Appl. Phys. **42,** 194013 (2009).

[21] M. J. Kushner, J. Appl. Phys. **71,** 4173 (1992).

[22] J. Perrin, O. Leroy and M. C. Bordage, Contrib. to Plasma Phys. **36,** 3 (1996).

[23] C. K. Goertz, Rev. Geophys. **27,** 271 (1989).

[24] O. Havnes, T. K. Aanesen and F. Melandsø, J. Geophys. Res. **95,** 6581 (1990).

[25] J. Goree, Plasma Sources Sci. Technol. **3,** 400 (1994).

[26] R. N. Franklin, Plasma Sources Sci. Technol. **11,** (2002).

[27] S. J. Lanham, J. Polito, X. Shi, P. Elvati, A. Violi and M. J. Kushner, J. Appl. Phys. **130,** 163302 (2021).

[28] H. H. Hwang, E. R. Keiter and M. J. Kushner, J. Vac. Sci. Technol. A Vacuum, Surfaces, Film. **16,** 2454 (1998).

[29] V. Vyas, G. A. Hebner and M. J. Kushner, J. Appl. Phys. **92,** 6451 (2002).

[30] S. J. Choi, P. L. G. Ventzek, R. J. Hoekstra and M. J. Kushner, Plasma Sources Sci. Technol. **3,** 418 (1994).

[31] X. Shi, P. Elvati and A. Violi, J. Phys. D. Appl. Phys. **54,** 365203 (2021).

[32] S. Plimpton, Journal of Computational Physics **117,** 1 (1995).

[33] J. C. Fogarty, H. M. Aktulga, A. Y. Grama, A. C. T. Van Duin and S. A. Pandit, J. Chem. Phys. **132,** (2010).

[34] N. Aiichiro, Comput. Phys. Commun. **104,** 59 (1997).

[35] A. K. Rappé and W. A. Goddard, J. Phys. Chem. **95,** 3358 (1991).

[36] G. Bussi, D. Donadio and M. Parrinello, J. Chem. Phys. **126,** (2007).

[37] K. I. Hunter, J. T. Held, K. A. Mkhoyan and U. R. Kortshagen, ACS Appl. Mater. Interfaces **9,** 8263 (2017).

[38] In Encyclopedia of Inorganic Chemistry (American Cancer Society, 2006).

[39] X. Chen, T. Seto, U. R. Kortshagen and C. J. Hogan, Powder Technol. **373,** 164 (2020).

[40] S. Exarhos, A. Alvarez-Barragan, E. Aytan, A. A. Balandin and L. Mangolini, ACS Energy Lett. **3,** 2349 (2018).

[41] A. Woodard, K. Shojaei, G. Nava and L. Mangolini, Plasma Chem. Plasma Process. **38,** 683 (2018).

[42] C. Qu, S. J. Lanham, S. C. Shannon, S. K. Nam and M. J. Kushner, J. Appl. Phys. **127,** 133302 (2020).

Chapter 7 Using Pulsed Power to Control Growth of Silicon Nanoparticles in Low Temperature Flowing Plasmas

Low temperature plasmas have seen increasing use for synthesizing high quality, mono-disperse nanoparticles (NPs). Recent work has highlighted that an important process in NP growth in plasmas is particle trapping – small, negatively charged nanoparticles become trapped by the positive electrostatic potential in the plasma, even if only momentarily charged. In this paper, results are discussed from a computational investigation into how pulsing the power applied to an inductively coupled plasma (ICP) reactor may be used for controlling the size of NPs synthesized in the plasma. The model system is an ICP at 1 Torr to grow silicon NPs from an Ar/SiH_4 gas mixture. This system was simulated using a 2-dimensional plasma hydrodynamics model coupled to a 3-dimensional kinetic NP growth and trajectory tracking model. The effects of pulse frequency and pulse duty cycle will be discussed. We identify separate regimes of pulsing while growing NPs where particles become trapped for one pulsed cycle, a few cycles, and many cycles – each having noticeable effects on particle size distributions. For the same average power, pulsing can have a stronger trapping potential for particles when compared to continuous wave power, potentially increasing particle mono-dispersity. Pulsing may also offer a larger degree of control over particle size for the same average power.

7.1 Introduction

Plasma based synthesis of nanometer sized particles is an active area of research, showing desirable improvements over existing methods of synthesizing nanoparticles (NPs) [1–3].

However, plasma based methods require considerable tuning of the plasma source and operating conditions to produce NPs with the desired properties (e.g., size distribution, particle crystallinity, composition) [3–5]. These plasma sources are highly coupled systems, with small changes in operating conditions having outcomes on NP properties that are difficult to predict a priori. NPs having increased complexity (e.g. core-shell nanoparticles, where composition varies spatially) are highly sought after for their tunable optical properties, and require a greater degree of control of plasma properties to produce [6–10]. Current plasma-based NP manufacturing techniques will likely be challenged to keep up with the desired designs of NPs for optical and energy applications. Additional control techniques and understanding are needed of plasma-synthesis techniques to meet these demands. The plasmas of interest are flowing systems having pressures of a few Torr, typically a rare gas with a small fraction of the feedstock gases (e.g., SiH_4 for synthesizing Si NPs). Power is coupled to the plasma using inductive and capacitive excitation.

Pulsing the power applied to the plasma is a technique used in the plasma material processing community to control ion energies and fluxes to surfaces, particularly for microelectronics fabrication [11–16]. Using a combination of source (plasma producing) and bias (voltage to accelerate ions) pulsing [17,18] can improve processing capabilities over continuous wave power, enabling new techniques such as atomic layer etching [19]. The concept of controlling ion energies with pulsing is straight forward – positive ions are accelerated across the sheath in contact with a surface and strike the surface with an energy proportional to the sheath potential (for a collisionless sheath) and so control is relegated to control of the sheath potential. In practice, there are many complicating factors, such as collisions in the sheath, ion transit time compared to applied frequency, changes in dc bias voltage, variation in surface flux, and changes to plasma chemistry. In spite of these complications, pulsing the power is a relatively simple way

to control the potential and charged species densities in the plasma, and an extension of this concept could be applied to plasmas for NP synthesis to control their properties.

Pulsed power has been computationally investigated as a method for controlled growth of films from Si nanoparticles [20] and investigated experimentally [21]. Power modulation (sometimes coupled with modulated inflow of feedstock) has also been investigated for particle growth [22,23] and has shown improvements in Si/SiO_x composite NPs for lithium-ion batteries [24].

Particles in low temperature plasmas generally charge negative as a consequence of higher electron temperature and mobility compared to ions. As a consequence of their negative charging, they are often confined in the plasma by the positive plasma potential and outwardly directed electric fields in the bounding sheaths to the plasma. There have been many studies leveraging negative particle charging to study fundamental physics, such as Yukawa interactions [25], phase transitions, and more recently dynamic charging in the afterglow of plasmas [26–31]. However, the charge of particles in the plasma varies greatly with size. In studies of transport processes and thermodynamics, micron sized particles are typically used which acquire thousands of charges, and those charge states tend to be fairly stable. Smaller nanometer sized particles may be a mix of negative, neutral and in some cases positive particles, with an individual NP changing its charge state [32,33]. In spite of NP dynamically changing their charge, electrostatic trapping of nanometer sized particles can occur even if particles are only temporarily charged negative, a condition that may enable particle growth and monodispersity [34].

In this paper, we report on results from a computational investigation of using pulsed power for nanoparticle synthesis in flowing LTPs. Simulations were performed of a cylindrical inductively coupled plasma (ICP) reactor sustained in a rare gas with a dilute silane precursor for

various pulsed duty cycles and frequencies with other parameters held constant (2 cm reactor diameter, 50 sccm of 98/2 Ar/SiH_4, 1 Torr, 10 W average power). The computational platforms used in the study are a 2-dimensional hybrid-multi-fluid plasma model coupled with a 3-dimensional kinetic model for particle growth and trajectory tracking. The intent of this work is to assess how trapping of negatively charged and transiently charged particles in the positive plasma potential influences growth rates and particle size under various pulsed conditions compared to continuous wave power. (The trapping potential itself varies over the pulsed cycle.) We found that pulsing may offer increased control over particle sizes. In particular, pulsing may be a method to increase particle monodispersity compared to continuous wave power under certain conditions. This narrowing of the size distribution is primarily due to increased trapping potential and negative particle charging when using pulsing with the same average power as cw plasmas. Particle sizes can also be tuned with the pulsing frequency and duty cycle by several factors over continuous power conditions.

The models used in this investigation are described in Section 7.2. The effects of pulsing, considering duty cycle and pulse frequency, on nanoparticle growth and trapping are discussed in Section 7.3. Concluding remarks are in Section 7.4.

7.2 Description of the Models

The plasma chemistry, growth, and transport of nanoparticles in LTPs involves complex multi-scale processes, which we address by using two separate but coupled models. The Hybrid Plasma Equipment Model (HPEM), a 2-dimensional plasma multi-fluid hydrodynamics model (discussed in Section 7.2.1), was used to model the reactor scale plasma and obtain parameters needed to model the nanoparticle growth. The Dust Transport Simulator (DTS) is a 3-dimensional

kinetic model that was used to compute trajectories and growth of nanoparticles in the plasma, and will be discussed in Section 7.2.2. Information is coupled between the two models to generate a self-consistent solution.

7.2.1 Reactor Scale Plasma Model

The reactor scale plasma chemistry and hydrodynamics were modeled using the Hybrid Plasma Equipment Model (HPEM), a two-dimensional multi-fluid plasma simulator, described in detail in Ref. [35]. Briefly, the HPEM separates relevant physics into different modules, and information between modules is shared using a time-slicing technique. In this work, the Electromagnetics Module (EMM) was used to solve for azimuthal electric fields produced by an antenna powered at radio frequency (RF) and their absorption by the plasma. The EMM uses a frequency domain solution. Secondary electron emission from surfaces is addressed in the Electron Energy Transport Module (EETM), where a Monte Carlo technique is used to generate electron impact source functions. The Fluid Kinetics Poisson Module (FKPM) is the main time-stepping module, and was used to compute separate fluid continuity, momentum and temperature equations for each heavy species (neutrals and ions). Continuity and temperature equations are solved for electrons assuming a drift-diffusion formulation for momentum. Poisson's equation for the electric potential is solved semi-implicitly with each time step in the FKPM for self-consistency.

Rate coefficients for electron impact processes and electron transport coefficients are obtained from the electron energy distribution (EED) produced using a two-term spherical harmonic solution to Boltzmann's equation, assuming spatial averaged composition. EEDs are produced over a range of E/N (electric field/gas number density) producing a table that is interpolated as a function of electron temperature.

The Ar/SiH_4 reaction mechanism used in this work is an updated version of that used most recently in Lanham *et al.* [36], with data from previous works [37–39]. The mechanism has been expanded to include ArH^+ and H_3^+, which have previously been found to be the dominant ions for silane plasmas under certain conditions [40]. The species included in the simulation are listed in Table 7-I.

Particle growth is addressed in the DTS which feeds back local values of NP density and charge to the FKPM. These values are then used in the charge balance for solution of Poisson's equation, for the attachment (or neutralization) of electrons and ions on the NPs.

7.2.2 DTS and Nanoparticle Growth Model

NP transport and growth were addressed using a 3-dimensional kinetic model, the DTS, embedded in the HPEM. The implementation used in this work has been described previously [36], and so the physics and mechanics of the model will only be described briefly. The DTS obtains plasma properties from the HPEM, including electric fields, and species densities, temperatures, and momentum flux fields. The precursors to NPs are initialized in the plasma and the particle mass, charge, and positions are integrated in time. Forces on particles are computed, divided by the mass to obtain acceleration, with trajectories being integrated using a second order technique. Particle charge is integrated from currents derived using Orbital Motion Limited (OML) trajectories [41,42], considering individual contributions from electrons, positive ions, and negative ions. Small NPs (i.e. < 10 nm), can have significant stochastic charging [43], so the integrated currents (discrete charge per time step) were treated as rare events with a Poisson distribution to emulate this effect and to maintain charge as integer values.

The relevant forces acting on the particles include gravitational, electrostatic and inter-particle Coulomb forces, ion drag, viscous fluid drag, thermophoresis and Brownian motion. The

gravitational force acting on nm size particles is small compared to the other forces, but was included for self-consistency. The electrostatic force is computed by the charged particles interacting with the local electric field. For negative charged particles, as is typical for the types of dusty plasmas considered in this work, the force points towards the peak plasma potential and negative particles become trapped, while positive particles are accelerated out of the plasma. To account for the electrostatic forces between NPs, particles interact directly with each other through a shielded Coulombic force given by a spherically symmetric solution to the Debye Hückel equation [44]. Direct computation of all coulomb interactions between particles has poor scaling of order N^2, so only particle interactions within a few linearized Debye length are calculated. This assumption has been found to be accurate in previous works due to the exponential decay in screening with distance [45].

The ion-drag force results from ions having a directed velocity approaching, for example, a negatively charged NP, and undergoing a parabolic (positive ion) or hyperbolic (negative ion) orbit about the NP. The change in momentum of the ion due to this orbital motion is imparted to the NP. Since the momenta of positive ions are typically directed towards the boundaries of the plasma, the ion-drag force usually accelerates negative NPs towards the boundaries of the plasma. The ion-dust momentum transfer cross section is approximated using a semi-analytic expression from the work of Kilgore *et al.* [46] and coupled with the work of Khrapak *et al.* [47], which agree well with simulation and modeling results [46,48].

The forces due to viscous fluid drag are derived for hard sphere particles from classical thermodynamics [49–51]. The driving force for viscous fluid drag is to minimize the difference between the dust particle velocity and the bulk advective fluid velocity. The thermophoretic force can be an important force for particle motion, driven by temperature gradients, where particles

move towards colder gas temperatures or surfaces. An effective force of Brownian motion due to random collisions with the background gas is also included. This force is more important for smaller particles, ~1 nm where the momentum transfer from individual atoms and molecules can be significant, while decreasing in significance with increasing particle size.

Growth of particles in the plasma is assumed to be dominated by the thermal flux of radicals to the particle surface. The time rate of change of mass of NP *i* is:

$$\frac{dM_i}{dt} = \sum_j v_j N_j 4\pi r_i^2 S_{c,j} \Delta m_j \ , \ v_j = \sqrt{\frac{8k_B T_j}{\pi m_j}} \tag{7.1}$$

where the mass of dust particle *i* is M_i having radius r_i. The summation is over all particle growth species j, having thermal speed v_j, number density N_j, mass m_j and temperature T_j. The quantity Δm_j is the mass added to the dust particle. The probability of specific species j sticking to the dust particle after a collision is $S_{c,j}$ and the values used in this work are shown in Table 7-II [36,52]. Particles are initialized in the plasma above a critical size of the regime where surface growth dominates, in this work assumed to be 1 nm. The mass and diameter of each dust pseudo-particle are individually tracked to allow for there to be spatial dependence in the particle growth processes. Particle agglomeration is modeled by particles combining if they touching, however this is rare as dust particles are typically charged negative.

The conditions and timescales to grow nanoparticles in low temperature plasmas are numerically difficult to resolve. A time slicing technique was employed to address different timescales. First, the plasma is fully simulated under continuous wave power for several gas residence times with numerical acceleration to achieve steady-state species densities and temperature. Second, power to the plasma is pulsed over several cycles to reach a periodic steady-state in the potential and charged species densities. The time averaged power during the pulsing

is the same as that for cw power portion of the simulation. The gas residence times for growing NPs is typically on the order of ms and resolving multiple pulses at those frequencies would be impractical. Shorter pulses (50 μs) were modeled in the plasma, which has the added benefit of having a negligible effect on the long-term chemistry as the plasma achieves a steady state during the power-on period. Third, after a periodic steady-state for the plasma in pulsing is reached, particles are initialized in the DTS and time-slicing is used to scale the 50 μs plasma pulse to longer times for the particles. The particles are tracked until they flow out of the reactor by passing through a plane approximately 1 cm above the pump port where statistics are collected.

7.3 Pulsed Power for NP Growth

7.3.1 Pulsed versus CW Power Comparison

This work focuses on the methods that pulsed power may be used to control the growth of nanoparticles in flowing low temperature plasma reactors. The rationale for this work is that NPs can be electrostatically trapped in flowing LTPs [6,8,9,53], and power modulation affects the trapping process. The charge on NPs varies as the plasma properties vary, as do the electrostatic trapping forces. A cylindrical inductively coupled plasma (ICP) reactor was chosen for this computational investigation, a typical geometry growing NPs. A schematic of the model geometry is shown in Fig. 7-1, and is based on reactors used in experiments for NP synthesis [54,55]. The glass tube cylindrical reactor has a radius of 1 cm and a length of 8 cm, with electrically grounded boundaries for the inlet and outlet, as would occur using a metallic mesh. Power is inductively coupled into the plasma from a three-turn antenna delivering 10 W at 10 MHz with an inlet flow of Ar/SiH_4 = 98/2 at 50 sccm. The pressure is held constant at 1 Torr by adjusting the outlet flow rate, giving an average gas residence time of 33 ms. The temperature of the inlet gases and

surrounding reactor surfaces are held constant at 325 K.

Plasma properties and chemistry for the base conditions are also shown in Fig. 7-1. Under steady-state operation, the electric potential in the plasma peaks at 26.7 V between the coils of the antenna at the location of maximum ion production (Fig. 7-1b). The surface of the dielectric tube charges negatively near the coils to -2.2 V at a minimum to balance the electron and positive ion fluxes to its surface. The on-axis (r=0 cm) electron density and temperature profiles are shown in Fig. 7-1d. The electron density peaks close to the powered antenna ($1 > r > 0$ cm) at 8.6×10^{10} cm^{-3} and decreases by nearly three orders of magnitude downstream by the pump. This decrease is due to the large rate of electron dissociative attachment to silane and dissociative recombination of silane ions, both of which are sources of radicals to grow NPs. The electron temperature T_e has a maximum at 4.2 eV adjacent to the antenna (Fig. 7-1c), decreasing to 1.7 eV moving away from the antenna due to both elastic and inelastic collisions for the (relatively) high pressure of 1 Torr.

The dominant positive ion varies spatially, with SiH_3^+ being the dominant ion near the inlet (density of 4×10^{11} cm^{-3}) where the SiH_4 density is high and SiH_3^+ can be readily produced by electron impact ionization. Close to the wall of the reactor adjacent to the antenna, Ar^+ and Ar_2^+ achieve their maximum densities of 5×10^{11} cm^{-3} and 3×10^{11} cm^{-3}, respectively, and decrease downstream due to charge exchange reactions. Downstream, ArH^+ and H_3^+ become the dominant positive ions with densities 2×10^{12} cm^{-3} and 3×10^{12} cm^{-3} respectively, as the density of hydrogen increases from the dissociation of silane. The dominant negative charge carrier throughout the reactor is $Si_2H_5^-$, with a density ranging from 2×10^{12} cm^{-3} upstream where power deposition is high to 5×10^{12} cm^{-3} downstream where a nearly fully ion-ion plasma is formed. SiH_3^- contributes to the negative charge in the powered zone between the antenna, with a density of 2×10^{11} cm^{-3}, greater than the peak electron density.

The on-axis densities of nanoparticle precursors and growth species are shown in Fig. 7-1e for the length of the reactor. Silane flows into the reactor and dissociates by electron impact reactions primarily in the high power deposition region between the antenna, decreasing by 2 orders of magnitude from its peak density of 3.8×10^{14} cm^{-3} upstream. Localized gas heating up to 433 K occurs near the center of the reactor resulting in gas rarefaction. SiH_2 and SiH_3 are produced from electron impact dissociation of SiH_4, additionally producing atomic H. SiH_2 rapidly inserts into fully hydrogenated silanes and is one of the fundamental growth species in the mechanism of nanoparticle formation [39]. These reactions create Si_2H_6 from SiH_4, consuming SiH_2 in the process and leaving the density heavily localized (maximum of 1×10^{12} cm^{-3}) where its production is at a maximum. Dehydrogenation of $Si_{1\text{-}2}H_x$ species occurs progressively downstream from collisions with Ar excited states. Hydrogen abstraction from Si_2H_6 forms Si_2H_5 which becomes the main silicon radical downstream with a density 2×10^{14} cm^{-3}. In addition to reactions with silane species, H atoms can etch NPs and impact the size of trapped particles, a process not included in the model.

Pulsed periodic steady-state values for the spatially averaged density and electron density weighted temperature are shown in Fig. 7-2a for 50 μs plasma pulse with the power profile shown in Fig. 7-2b. The average power deposition is 10 W with a duty cycle of 50% spent at peak power, with a few μs of rise and fall time. When the power first turns on, T_e spikes to an average over 5 eV and is higher in between the antenna to rapidly ionize the plasma by electron impact reactions [56]. The electric potential in the plasma spikes to 57 V, higher than the 26.7 V for continuous wave power, due to the low electron density and high temperature at the onset of a pulse. When the power turns off, T_e decreases quickly due to the high collisionality at 1 Torr. With the electric potential being proportional to T_e there is a commensurate decrease in plasma potential as well.

Thermal electron attachment to radicals, dissociative recombination and diffusion to the walls produces the decrease in electron density. Since the pulse frequency is relatively high at 20 kHz, the electron density does not have time to fully dissipate and may have some influence on the results of the particle simulation. Since the DTS model uses time-slicing, the time NPs experience is greater than in the plasma portion of the simulation. The plasma pulsing may be more akin to a high-low power pulse than strictly on-off.

The dynamics of nanoparticle growth captured in the DTS are shown in Figures 7-3 and 7-4, comparing growth under continuous wave power (Fig. 7-3) and under pulsed operation (Fig. 7-4) for the same average power of 10 W. The images are for a series of time snapshots following initiation of the particles. The sizes of the particles are indicated by the diameter of the symbol. The symbols are color coded with charge on the particle. The pulse period is 5 ms with a duty cycle of 50%. In both cases, particles are initialized between the first two turns of the antenna. Analyzing the sequential steps of particle growth and transport are more clear when following the evolution of this burst of particles. Continuous particle generation is discussed below.

For continuous wave power, within a few ms most of the particles charged to an average of -1.4 q for an average particle diameter of 3.3 nm. Due to a no-slip boundary condition on the fluid dynamics, the gas velocity profile in the reactor is parabolic shaped, with highest velocity on-axis, decreasing towards the walls. This velocity profile results in particles forming a ring shape in the plasma – negative particles are trapped by the positive plasma potential, but particles on-axis are accelerated downstream on the center of the reactor (t=8 ms). The plasma potential is also 0.4 V more positive in a torus centered under the coils, thereby providing a deeper trap for negative particles.

Thermophoresis can be a dominant force for trajectories of particles in plasmas, driven by

macroscopic temperature gradients. In this case, it was assumed that the temperature of the glass tube was 325 K, so the thermophoretic force will always point from the plasma (with gas temperature >325 K) to the walls. In actuality, significant heating of the glass occurs, and the direction of the thermophoretic force may change and increase particle trapping rather than decrease it.

Particles continue growing to an average radius of 14.4 nm, and charging negatively -10.1q on average by 16 ms. At t=26.5 ms, the majority of particles are still trapped by the plasma potential and are on average 23.6 nm in radius with a charge of -15.1q. The axial location at which the particles are trapped slowly moves downstream up until this time due the increasing fluid drag forces afforded by the larger particles. By t=37.0 ms, the average particle radius increases to an average of 32.5 nm and the force due to fluid drag begins to dominate over electrostatic trapping. At this time, the trap is emptied and particles begin to flow downstream. Due to the steep gradients in charged species densities and temperatures, moving downstream shifts the dominant negative current to the particles from hot light electrons to cold heavy ions. The particles then begin to neutralize, leaving fluid drag as the dominant force. Particles acquire the speed of the local gas flow, leaving the reactor at 49 ms with an average radius of 41.7 nm.

NP growth and transport dynamics using pulsed power are shown in Fig. 7-4. Particles were initialized in the plasma at the onset of a pulse. The maximum electric potential in the plasma is plotted as a function of time in Fig. 7-5a, with the cw values shown for reference. The average location of NPs in the axial direction is shown in Fig. 7-5b and in the radial direction in Fig 7-5c. Average charge on the NPs as a function of time is shown in Fig. 7-5d, and diameter is shown in Fig. 7-5e. At t=2.81 ms, the power for the first pulse is still on and the particles have grown to a radius of 3.2 nm with an average charge of -4.4q. The particles are more negatively charged

compared to particles grown under cw conditions at a similar time and size. The number of charges on the particle is largely determined by the magnitude of the electrical floating potential which is proportional to electron temperature. The average higher T_e during the power-on portion of the pulse then produces a larger (negative) floating potential and larger (more negative) charge on the NP. The electrostatic trapping force on the particles during the power-on portion of pulsing is greater due to the more negative charge on the NP and more positive plasma potential compared to continuous wave power. The end result is that the trapping location is a more finely defined torus compared to cw power with a larger average radius (Fig. 7-5c).

As the power decreases, particles quickly discharge to an average charge near 0 (t = 4.91 ms, Fig. 7-4 and Fig. 7-5d). When the NP are small (a few nm), there is the possibility that charging might statistically be positive [32,33]. In these simulations, we observe few (if any) positively charged NPs. In the absence of a trapping force particles move downstream in response to fluid drag, and spread radially inwards and outwards with the average radius decreasing. When the power turns back on at t=5 ms, the electron temperature increases and the positive electric potential is re-established. Particles re-charge negatively and are accelerated upstream against the bulk fluid flow towards the electrostatic trapping zone. Particles drift outwards from the axis and inwards from the walls, towards a more positive electric potential in the plasma, again forming a ring (t = 11.9 ms). The particles are now larger (radius = 11.1 nm) with a larger more negative charge (-17.1q).

This process of particles charging negative when the power is turned on and becoming trapped upstream in the plasma, followed by discharging and flowing downstream when the power is turned off repeats for approximately 7 cycles. With each cycle, the NPs grow larger, are susceptible to fluid drag forces and so are trapped lower in the reactor. If the plasma properties at

the trapping location for each pulse were the same, you would expect the (negative) charge to increase each cycle as the NPs are larger. This trend occurs up to the 6th cycle for which the most negative NPs are produced (-36q). On the 7th cycle, the trapping location is on the fringe of the power-deposition zone where the electron temperature is beginning to decrease. In spite of the particle being larger than on the 6th cycle, the charge on the 7th cycle is less negative (-32q). At t=37.3 ms on the 8th cycle when the power is on, particles are on average 33 nm but charge only to -4.9q due to fluid drag transporting the particles downstream where the both the electron temperature and density are low. Beyond the 8th cycle, the particles are far enough downstream that they do not significantly charge when the power turns on, coupled with the particles being larger and more susceptible to fluid drag. At this point, pulsing has a small effect on the transport of particles as they are entrained in the flow and leave the reactor.

Statistics were collected on NPs as they flow out of the reactor. The distributions of NP diameters for CW and pulsed power are shown in Fig. 7-6. These distributions result from collecting 10,000 particles into diameter bin widths of 0.5 nm. For continuous wave conditions, nanoparticles that were trapped in the plasma prior to being entrained in the gas and flowing out of the reactor have a near-normal distribution about a mean of a diameter of 39 nm with a standard deviation of about 2 nm. However, not all particles were trapped (or were momentarily trapped), leading to a second peak in the probability distribution at around 12 nm. These particles flow out of the plasma a short time after being seeded, a consequence of stochastic charging – particles are allowed to accrue positive charge, which will have the opposite effect of trapping since the axial electrostatic force will point downstream. These particles may also be statistically closer to the axis where the gas flow speed is higher, producing a larger fluid drag force. Particles that transport a few cm downstream from the peak in the plasma potential will likely not "recover" to become

trapped for these plasma conditions. Downstream of the peak in the plasma potential, the plasma is highly electronegative (small electron density) with a low electron temperature, that will not re-charge particles enough to become trapped.

The NP size distribution leaving the reactor when using pulsed power is shown in Fig. 7-6b. This distribution is also for a bin width of 0.5 nm with N≈10,000 particles collected. The collected particles have a more narrow size distribution, 5 nm wide peaking at 41 nm, than for the continuous plasma. The irregular shape comes from there being striations in particle density at the end of a pulse – as the particles leave the electrostatic trapping zone, particles closer to this zone may become negatively charged when the power turns on again and become partially trapped. These results suggest that using pulsed instead of continuous wave power may be a method to modify or tune the NP size distribution, in this case increasing monodispersity in particle sizes.

The ability to tune the NP size distribution with pulsed power, discussed in more detail below, is clearly a function of the pulse power format. For example, consider comparing NP grown using cw and pulsed processes using the same average power. During the power-on period, the instantaneous power is higher than during cw operation. As a result, the electrostatic trapping potential may be greater due both to higher (positive) peak potential in the plasma and more negative charge on the NPs (Fig. 7-5d). The production of growth species (e.g., silane radicals) differs little between cw and pulsing since their densities depend largely on average power. With the densities of growth species being nearly the same, the average growth rates of NPs using pulsed and CW at the same power are essentially the same (Fig. 7-5e). However, the time spent in the plasma is a function of pulsing, which then translates to a different distribution of NP sizes. Using pulsed power may widen the parameter space of viable conditions to grow nanoparticles by increasing the trapping potential.

7.3.2 Effects of Pulse Period / Pulse Repetition Frequency

The pulse period (or inverse of pulse repetition frequency) is the time required for a full power pulse to repeat. To isolate the effects of the pulse period on nanoparticle growth, time slicing of the same 50 μs power pulse shown in Fig. 7-2 was used to approximate varying pulse length on NP growth without greatly changing charged species densities or neutral chemistry. This method provided effective pulse periods ranging from 2 ms to 80 ms (10 W average power, 50% duty cycle).

Results from the DTS are shown in Fig. 7-7 for PDF (probability distribution function for particle diameter) and average diameter. The PDF for a 5 ms pulse was compared to continuous wave operation with the same average power, and similar size NPs were produced – the PDFs were spread around 40 nm. Shorter pulses (higher repetition rates) produced PDFs having a mean radius increasing for shorter pulses – 4 ms (250 Hz), 3 ms (333 Hz) and 2 ms (500 Hz) pulses produces mean sizes of 43 nm, 47 nm, and 49 nm, respectively. Shorter pulses result in there being shorter power-off periods allowing less time for particles to flow downstream from the trapping zone in the plasma. The trapping potential remains higher (more positive) than under continuous wave power, and manifests as monodisperse distributions. Pulsing may be a method to increase particle sizes over similar conditions with CW power, producing mean sizes that are larger than under continuous wave operation while increasing particle monodispersity.

Increasing pulse length reduced particle diameter. The 6 ms pulse period (167 Hz) produced the most monodisperse PDF centered around 37 nm – smaller particles than for CW and the base case 5 ms (200 Hz) pulse. This result implies that there is an optimal pulse period (PRF) if monodisperse distributions is the goal. Longer pulse periods of 8 ms (125 Hz) and 10 ms (100 Hz) produced bi-modal PDFs – a consequence of particles becoming striated when the power turns,

with some particles becoming trapped for another pulse while others continue to flow out of the reactor. Since particles are seeded at the onset of a pulse, it is highly likely that they are trapped for half of the pulse period (50% duty cycle × pulse period). For the 10 ms pulse, the smaller peak in the PDF at 20 nm results from particles that were only trapped only for the initial 5 ms when the power was first turned on. The peak in the PDF at 28 nm comes from particles which were again caught in the trap on the second pulse, and spent (at a minimum) 5 ms more in the plasma zone. The PDF for the 8 ms pulse case shows a similar trend, however, particles are trapped for 2 or 3 pulses rather than just one, due to the shorter pulse period. As a result, the bimodal peaks in the PDF are closer together than for the PDF resulting from the 10 ms pulse.

For these conditions, the 10 ms pulse trapped particles for 1 or 2 pulses. Operating with longer pulse periods (lower PRF) one would expect particles to remain trapped for only a single pulse. As expected, increasing the pulse period increases the average particle size as shown in Fig. 7-7b. For longer pulse periods, particles remain in the trapped zone until the power turns off, providing direct control over how long particles spend growing by surface radical deposition. These longer pulses produce monodisperse PDFs with mean diameters ranging from 28 nm to 58 nm. The particle diameters can be larger than under CW operation for the same average power because the trapping potential when the power is on is akin to operating at double the power. However, the monodisperse distributions arise, in part, from seeding the particles only at the beginning of the pulse. If particles were continuously formed one might expect broader distributions skewed to have smaller particle size.

The ability to tune particle PDFs using the pulse period is summarized in Fig. 7-7c, where the average particle diameters for as a function of pulse period are plotted. Error bars indicate standard deviation, with large error bars indicating the presence of either dual-peaked distributions

(such as with 8 and 10 ms pulse periods), increasing natural spread in the distribution, or outliers. Under CW operation, the average particle diameter for trapped particles is 39 nm. Using pulse power provides a method to customization the mean size by nearly 50% in both directions (larger and smaller)

The pulse periods that provide flexibility in particle diameter will heavily depend on the gas residence time. The important factors to consider are the size of the trapping region in the plasma, the gas velocity or residence time, and the pulse period. For longer gas residence times, particles will move downstream from the trapped zone slower and longer pulses may be beneficial. If particles move too far downstream from the high plasma density region when the power is turned off, they will likely not charge negative (or recharge to their prior state) when the power turns on again. As a result, the electrostatic force during the pulse will not dominate over the fluid drag force, and the particles will not be retrapped. Using these guidelines, it should be possible to estimate pulsing times for specific systems that could give beneficial results.

7.3.3 Effects of Pulse Duty Cycle

The pulse duty cycle is defined as the ratio of time spent with the power on compared to the total pulse period. To achieve the same average power, the peak power must scale inversely with the duty. The end result is that shorter duty cycles have higher power applied in a short time, leading to larger spikes in electron density and electric potential in the plasma, as shown in Fig. 7-8. The same procedure was followed as discussed in Sec. II – 50 μs plasma pulses (with duty cycles ranging from 0.1 to 0.8) were simulated in the HPEM until a pulsed periodic steady state was reached. At that time, the DTS was executed for several pulses with time-slicing to model particles growing with 5 ms pulses.

PDFs from the results of the DTS are plotted in Fig. 7-8c for duty cycles of 0.1 to 0.8 for

5 ms pulse periods (200 Hz). Narrow PDFs were produced for duty cycles greater than 0.5, resulting in average diameters that are greater than those produced by continuous wave operation. The average particle diameters for these distributions are all within a few nm of each other. Having the power be on for additional fractions of a ms can make the difference between particles being trapped for an extra pulse or not. Other factors such as changes in the peak electron density and potential play less of an important role on the overall size distributions of particles for a set pulse period provided that the average power is constant. The benefits of pulsing even at a duty cycle of 0.8 (80% of the time spent at peak power with the rest of the time ramping the power) show benefits over operating with continuous wave power – increased uniform distributions with slightly larger particle size.

PDFs for lower duty cycles are also plotted in Fig. 7-8c. With a duty cycle of 0.4, the average particle diameter decreases to 29 nm with a larger spread. Lower duty cycles (0.1, 0.2, and 0.3) have the power on only long enough to trap the particles for a single pulse (or two, as seen by the second peak in the PDF at 17 nm for duty cycle of 0.3). The average particle diameters for various duty cycles of 0.1 to 1.0 (cw) are shown in Fig. 7-8d. For a given pulse period (in this case 5 ms), choice of duty cycle results in the particles being trapped for many pulses (dc = 0.5-0.8) or for only one pulse (dc = 0.1-0.3). There may only be a small range of duty cycles (for a given pulse period) where particles are trapped for an intermediate number of pulses. These trends indicate that the pulse period (or pulse repetition frequency) may be the most effective first order control mechanism for PDF, while the pulse duty cycle may be better for fine tuning particle properties after. The physics at play are the same – particles can be trapped in the plasma when the power is on, and changing the duty cycle changes the ratio of time particles spend trapped compared to be dominantly affected by fluid drag. For longer duty cycles, where particles are

trapped for multiple pulses, the small changes in electron density and electric potential in the plasma have only a small effect on the particles produced in the plasma.

7.3.4 Continuous Particle Seeding

One aspect of the results discussed above is that particles were initialized at the beginning of the simulation and tracked over time. The motivation was to less ambiguously track the particle dynamics from birth to collection. Since pulsing is periodic, the specific time during a pulse when particles are initialized may have an impact, particularly for longer pulses with pulse periods near the gas residence time. It was also assumed that particles spawn in a set location between the first and second antenna turns. Both assumptions were tested by allowing for continuous particle seeding, with initialization locations scaled to the spatial density of SiH_2 – one of the major mechanistic growth species for NPs, shown in Fig. 7-9a. SiH_2 readily inserts into fully hydrogenated Si_xH_y, so is consumed quickly after being formed by electron impact dissociation of SiH_4. These processes produce a density of SiH_2 localized within the antenna, with a maximum of 1.3×10^{12} cm^{-3}, decreasing by two orders of magnitude near both the inlet and pump. Based on this distribution, assuming particles are seeded between within the antenna is reasonable.

For continuous wave operation, 10,000 particles were initialized in the plasma using the spatial discussion of SiH_2. Particles were continuously replaced into this spatial distribution when particles were lost by flowing out of the system. This process continued until the spatial distribution (Fig. 7-9b) and size distribution (Fig. 7-9c) reached steady-state values. Achieving the steady state resulted in collecting >300,000 particles.

In the steady-state, a natural spatial afterglow forms in the plasma, with particles downstream being almost all neutral charged due to currents to particles being dominated by both positive and negative ions, rather than electrons. Within the small cm size trapping zone between

the antenna, there is a clear gradient in particle sizes with smaller particles being trapped closer to the peak plasma potential (upstream near the inlet) and larger, more negative charged particles further downstream near the pump, as shown in Fig. 7-9b. This is a natural consequence of the fluid drag force scaling more with particle size than the electrostatic trapping force. For continuous wave power, the distribution of particle sizes is very similar when comparing continuous vs static particle seeding (Fig. 7-9c and Fig 7-6a). The distribution features two peaks – one centered around 38 nm where particles are trapped in the plasma and another near 10 nm where particles do not get trapped. Since particles are initialized to the SiH_2 density (rather than constrained to between the antenna), more small particles are created overall and the peak of small particles is larger than under CW conditions.

For the 5 ms, 50% duty cycle pulsed case, 50,000 particles were initialized in the plasma and reseeded when lost. More particles were used so fewer pulses were required to obtain similar statistics in the distributions, and >700,000 particles were collected flowing out of the reactor. The particles (charge and size) in the reactor are shown in Fig. 7-10. The PDF shown for these conditions is in Fig. 7-9d and should be compared to the PDF produced by static seeding shown in Fig. 7-6b. With continuous seed, there is a peak in the PDF of small particles centered around 10 nm. These are particles that were not trapped by the plasma. Some of the population in this small-diameter peak in the PDF can be attributed to particles being initialized far outside of the trapping region where the electron density is low, and will not charge negative enough to be trapped when the power turns on. The peak in the PDF corresponding to trapped particles has shifted to an average of 37 nm compared to 41 nm for static seeding. This shift is likely a consequence of particles no longer being seeded when the power first turns, a condition which results in particles not being trapped for the entire duration of the power prior to particles flowing

downstream when power is turned off. This results in the PDF having a broader extent, with particles on average likely being trapped for one fewer pulse. The ratio of trapped particles with large size to untrapped, small particles is larger with pulsed operation, a possible benefit for using pulsed power over continuous wave.

The dynamics captured in the DTS for the 5 ms, 50% duty cycle pulsed case with continuous particle seeding are shown in Fig. 7-10. Particle positions are plotted with the color indicating particle size (Figs. 7-10a and 7-10b) or charge (Fig. 7-10c). When the power is on, particles form a ring in the trapping zone ordered from 1.9 nm to 20 nm. Particles are negatively charged, ranging from ≈-1q up to -25q for larger particles. When the power turns off, particles move out radially and discharge, with an average charge of ≈0 q. Pulsing appears to cause radial compressions in the particle positions as they move downstream, spaced coinciding to the power pulses.

7.4 Concluding Remarks

In inductively coupled plasmas, power is deposited in the vicinity of the antenna, producing high temperature electrons and creating a maximum in the electric potential. Negatively charged nanoparticles (NPs) will experience an electrostatic force towards this volume and can become trapped. Recent works have shown this type of particle trapping in the plasma may be an important mechanism of NP growth, where particles can continue to grow via surface deposition of radical species. Once a critical particle size is reached, the force due to fluid drag overcomes the electrostatic trapping force, particles flow out of the high plasma density trapping zone, and eventually flow out of the reactor. Results from a computational investigation into how pulsing the plasma can manipulate this trapping zone, and the effects on the dynamics of nanoparticle

growth were discussed.

When controlling for power, pulsing can (temporarily) create higher density plasmas with higher average electron temperatures which can charge NPs in the trapping region more negative than under continuous wave operation. This temporary, but strong trapping may have benefits when compared to operating with continuous wave power, for instance, being able to create more monodisperse particle size distributions. This work qualitatively shows that pulsing the power can lead to tunable particle size distributions by effectively controlling the length of time particles remain (and can grow) in the plasma. Ultimately, the factors that come into play are the size of the trapping zone, the local gas velocity or residence time, and the duty cycle (the fractional time during the pulse period that power is on). If particles are allowed to flow downstream outside of the powered trapping zone, they will be unable to charge negative and become trapped again. This is not necessarily a bad thing – power can be turned off after a certain time to produce NPs with a tunable smaller size.

With source pulsing alone, particles were able to move nearly a cm while still being trapped from pulse to pulse. This gives credence to the idea of having additional control schemes to move particles around the reactor based on the concept of electrostatic trapping. Decoupling the plasma source power and charged species densities from the trapping potential may be possible using separate powered electrodes, and could lead to advances in complex nanoparticle production using low temperature flowing plasmas.

Table 7-I. Species used in the plasma chemistry mechanism in the Hybrid Plasma Equipment Model.

Argon and electrons

Ar, Ar($1s_5$), Ar($1s_4$), Ar($1s_3$), Ar($1s_2$), Ar(4p), Ar(4d), Ar_2^*, Ar^+, Ar_2^+, e

Hydrogen species

H_2, H_2^*, H, H^*, H^{**}, H^+, H_2^+, H_3^+, ArH^+

Silane species

SiH_4, SiH_3, SiH_2, SiH, Si_2H_6, Si_2H_5, Si_2H_3, Si_2H_2, SiH_3^+, SiH_3^-, SiH_2^-, $Si_2H_5^-$

Table 7-II. Sticking coefficients (S_c) for species impacting Si NPs, used to model NP growth.

Species	S_c	T_{gas}
SiH_4	0.	400
SiH_3	0.125	400
SiH_2	0.66	400
SiH	0.945	400
Si_2H_6	0.	
Si_2H_5	0.1	
Si_2H_3	0.3	
Si_2H_2	0.66	

7.5 Figures

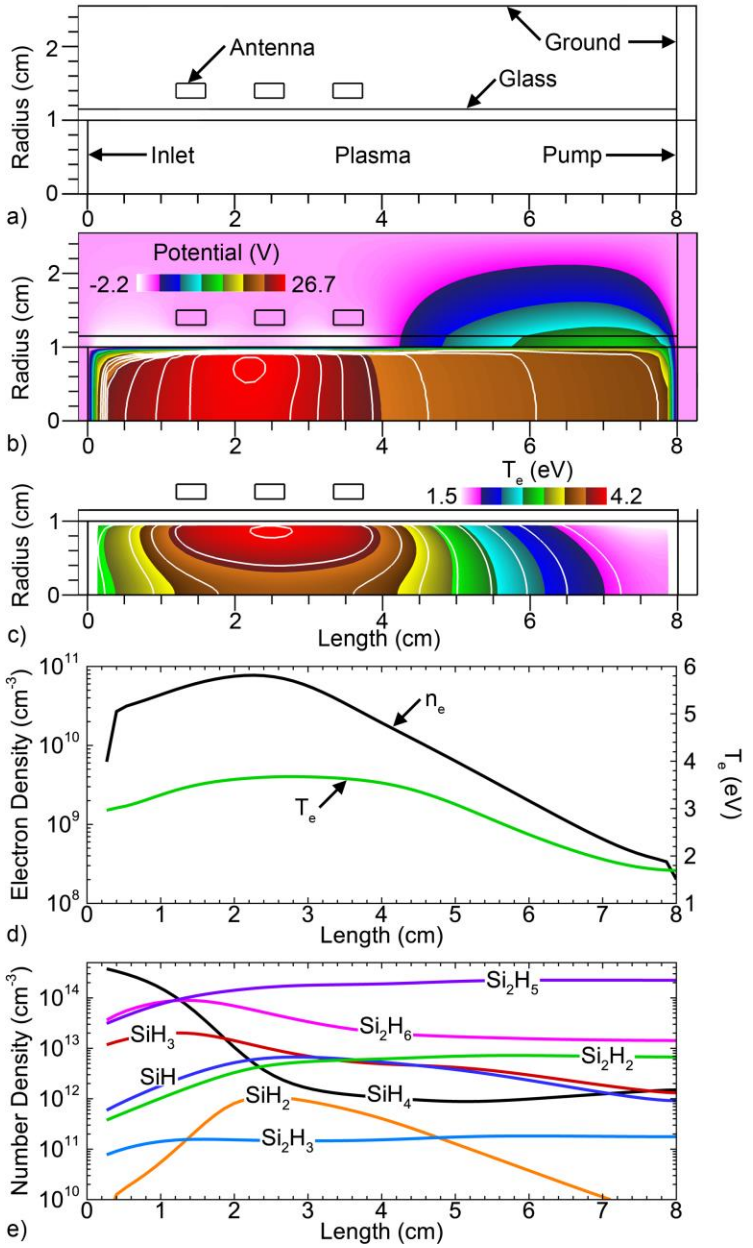

Figure 7-1. Reactor and plasma properties for continuous wave power (1 Torr, 10 W average power, 50 sccm, $Ar/SiH_4 = 98/2$). a) Schematics of the glass tube reactor, b) Potential in the plasma under CW conditions, c) Average electron density and electron temperature for CW conditions, d) Steady-state Si nanoparticle growth precursor densities along the reactor length (R=0).

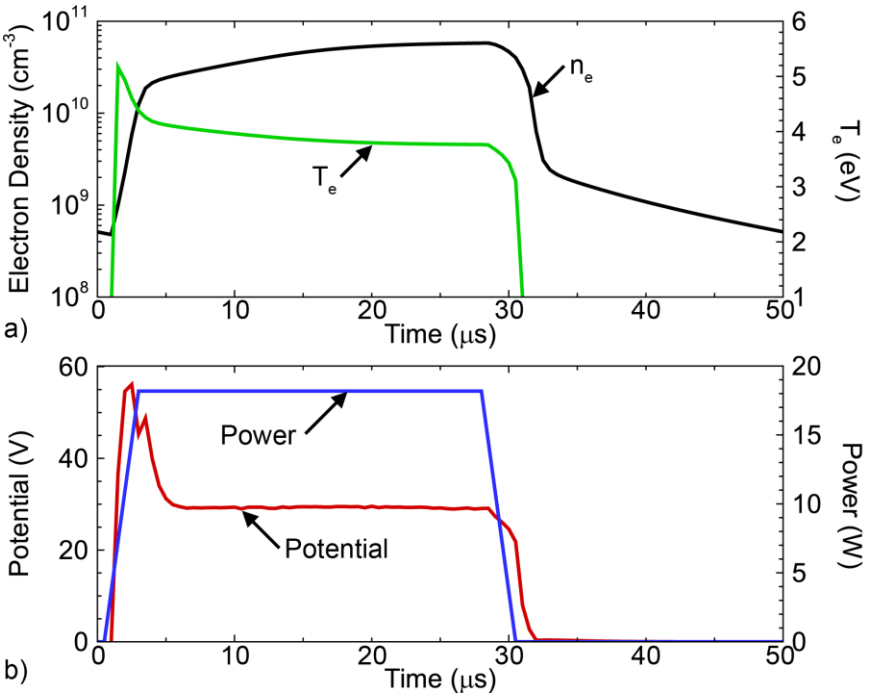

Figure 7-2. Pulsed periodic properties for a 50 μs pulse with a 50% duty cycle (1 Torr, 10 W average power, 50 sccm, Ar/SiH_4 = 98/2). a) Pulsed periodic electron density and temperature, and b) the power profile and maximum electric potential in the plasma.

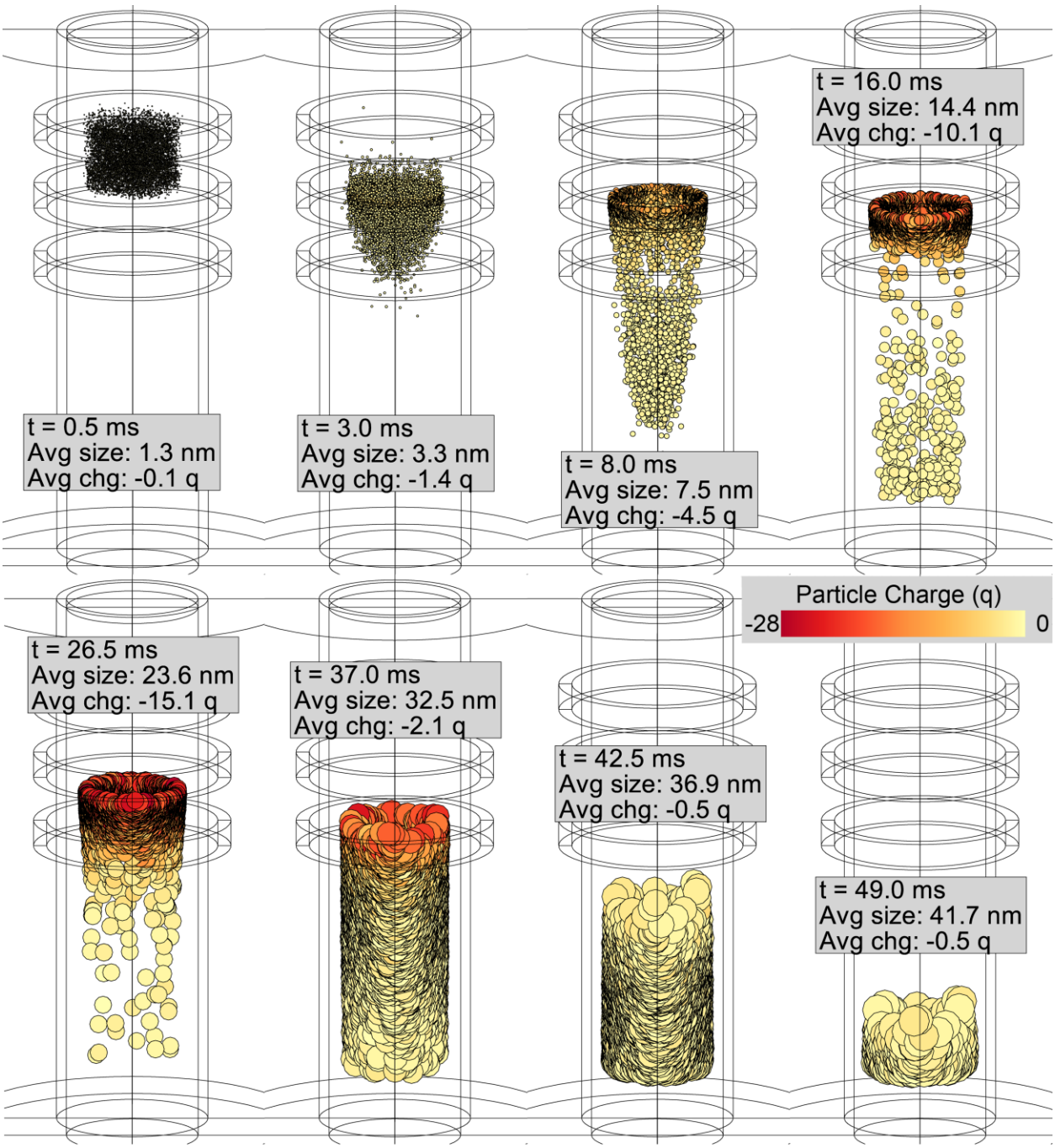

Figure 7-3. Nanoparticle positions and properties over time for continuous wave power (10 W). Particle sizes correspond to the nanoparticle diameter at the time indicated, and particle charge is depicted by the color.

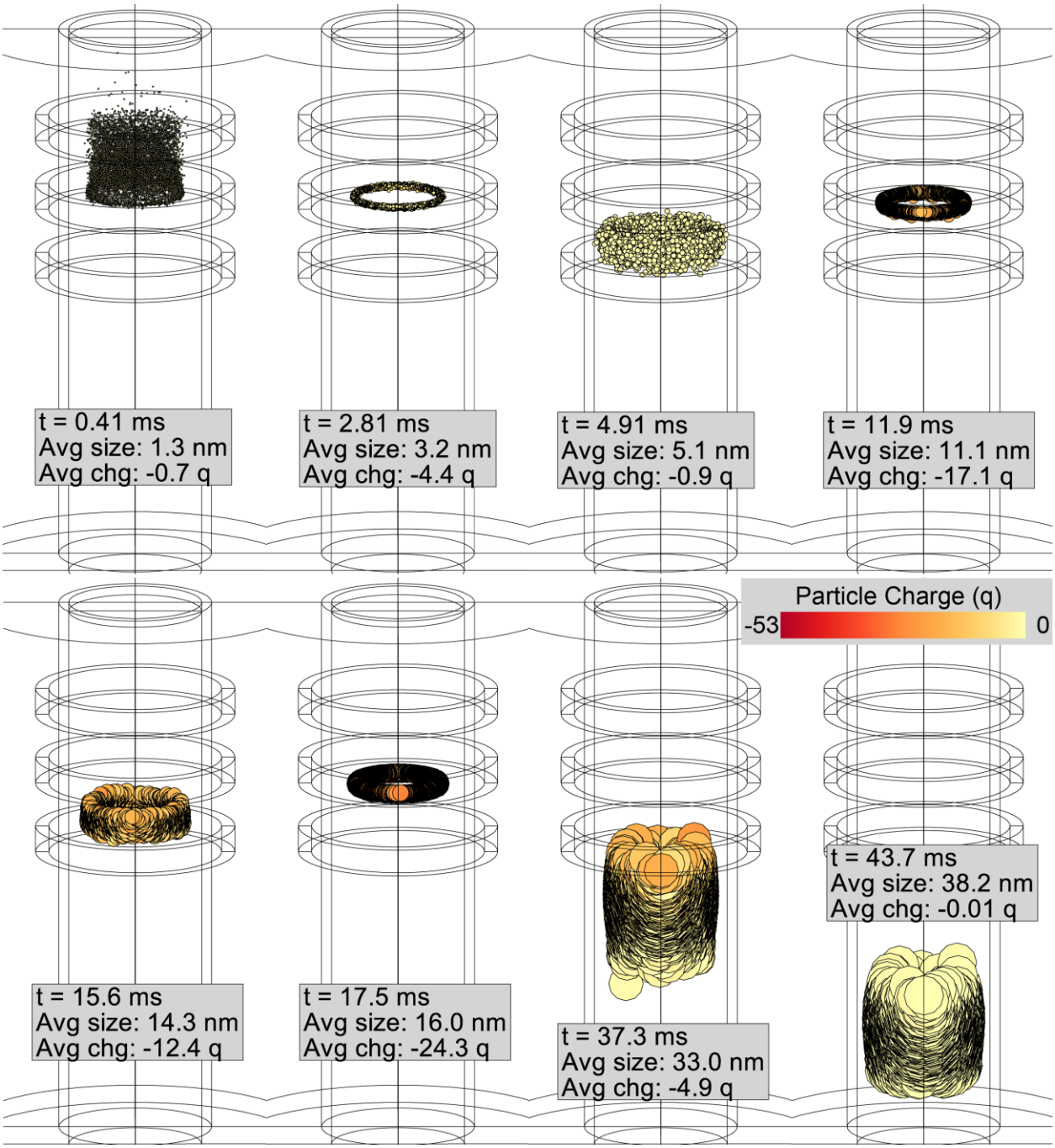

Figure 7-4. Nanoparticle positions and properties over time under pulsed conditions (10 W average power, 50% duty cycle, 5 ms pulse approximated by time slicing). Particle sizes correspond to the nanoparticle diameter at the time indicated, and particle charge is depicted by the color. Using pulsed power leads to more negative particle charge during the power on and increased trapping compared to continuous wave power.

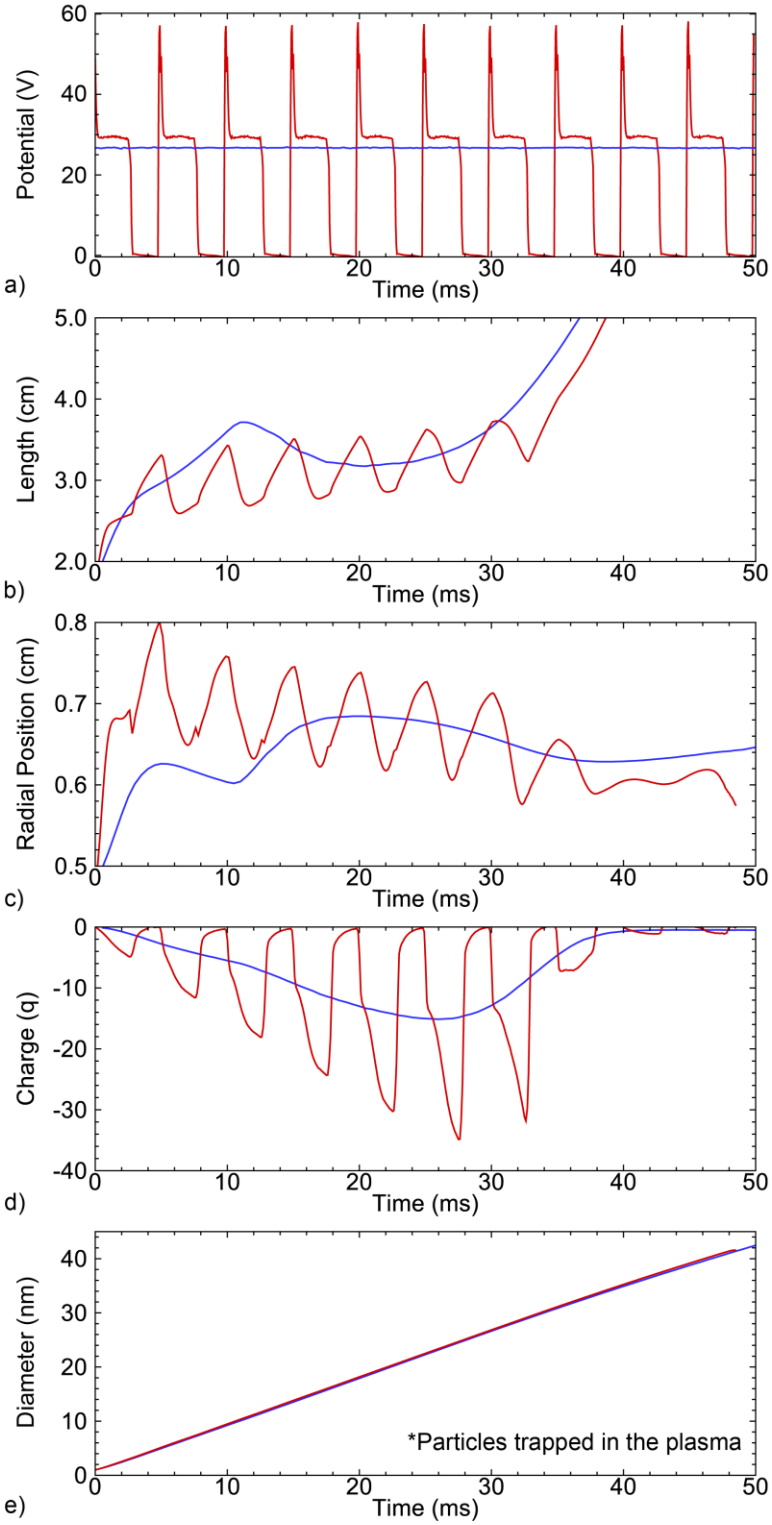

Figure 7-5. Time resolved properties of the plasma and nanoparticles for pulsed (red) and CW (blue) for the simulations depicted in Fig. 7-2. a) Maximum potential in the plasma over time, b) average axial position of the NPs in the plasma, c) average radial position of the NPs in the plasma, d) average charge on the NPs, and e) the average particle diameter of particles in the plasma over time, indicating similar growth rates for pulsed and CW power.

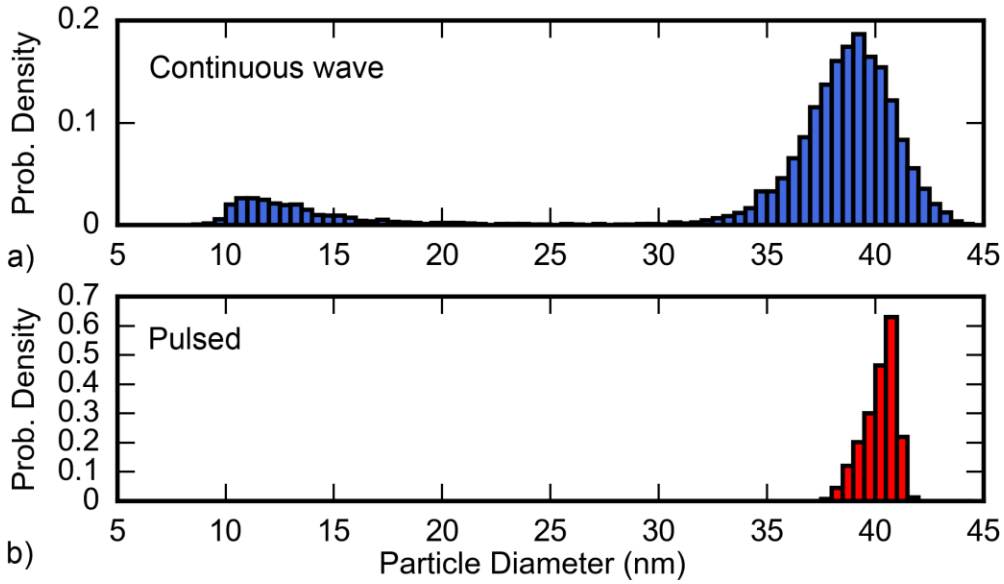

Figure 7-6. Size distributions of the NPs collected leaving the reactor for a) continuous wave power and b) for the pulsed conditions (5 ms pulse, 10 W average power, 50% duty cycle) of the simulations depicted in Fig. 7-3 and Fig. 7-4, respectively. The histogram of the raw data (N≈10,000 particles, bin width of 0.5 nm) was scaled to a probability density for comparison.

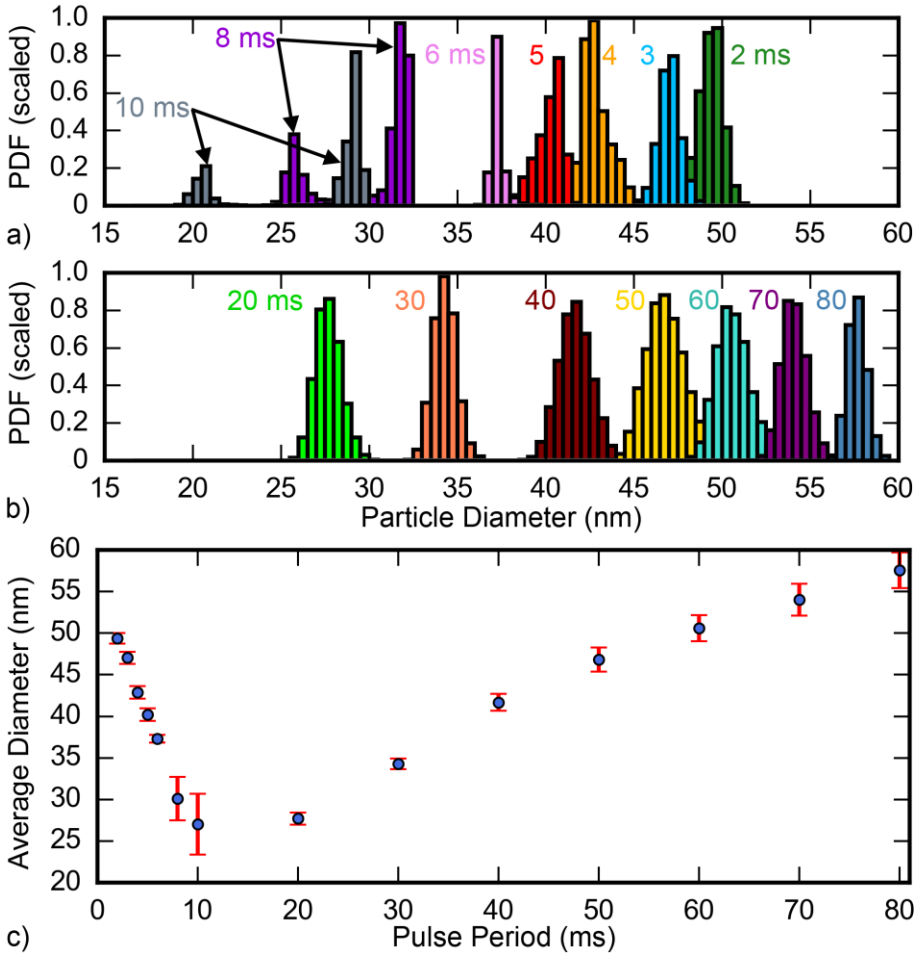

Figure 7-7. Size distributions of the NPs collected leaving the reactor for different pulse periods ranging from a) 2 ms to 10 ms, where the distributions shift to smaller sizes with increasing pulse period, and b) 20 ms to 80 ms, where the size distributions shift to larger sizes with increasing pulsed period. The average values are plotted in c) with standard deviation bars, indicating a large degree of customization available with pulsing. The probability density functions of particle size (N≈10,000 particles, bin width of 0.5 nm) were scaled for convenience.

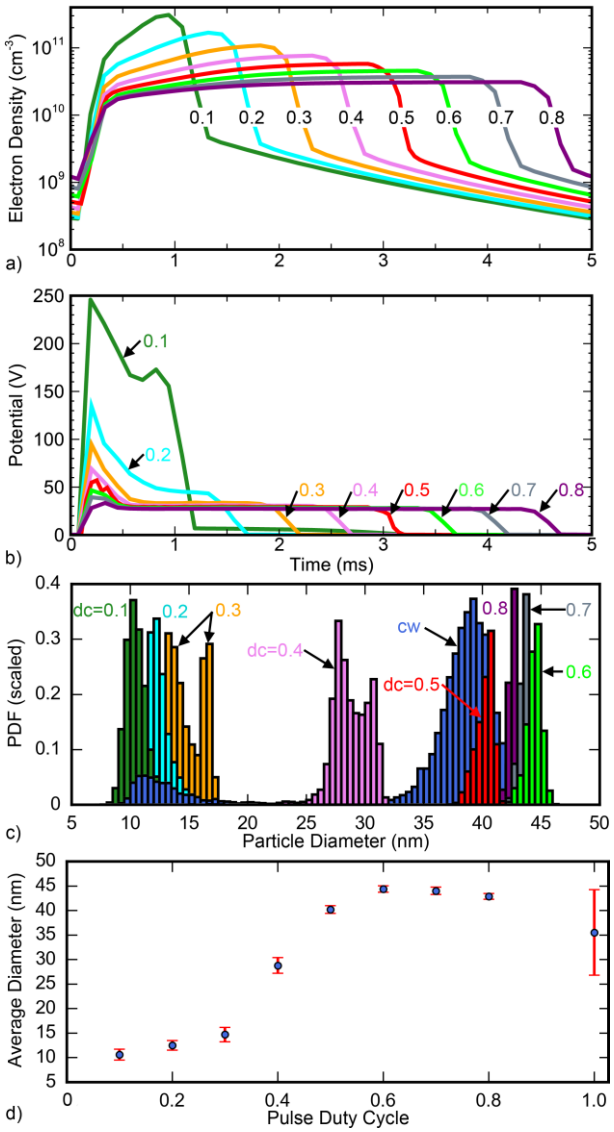

Figure 7-8. Plasma properties and NP diameters for various pulse duty cycles while holding the pulse period and power constant at 5 ms and 10 W, respectively. a) Electron density, showing increased peak density with decreasing duty cycle, b) increasing peak in the plasma potential with decreasing duty cycle, c) size distributions (scaled) of the NPs collected leaving the reactor, and d) average particle diameter with standard deviation bars. Note that 50 ms pulses were modeled in the plasma simulation, and the time scales in a) and b) are in the NP frame of reference.

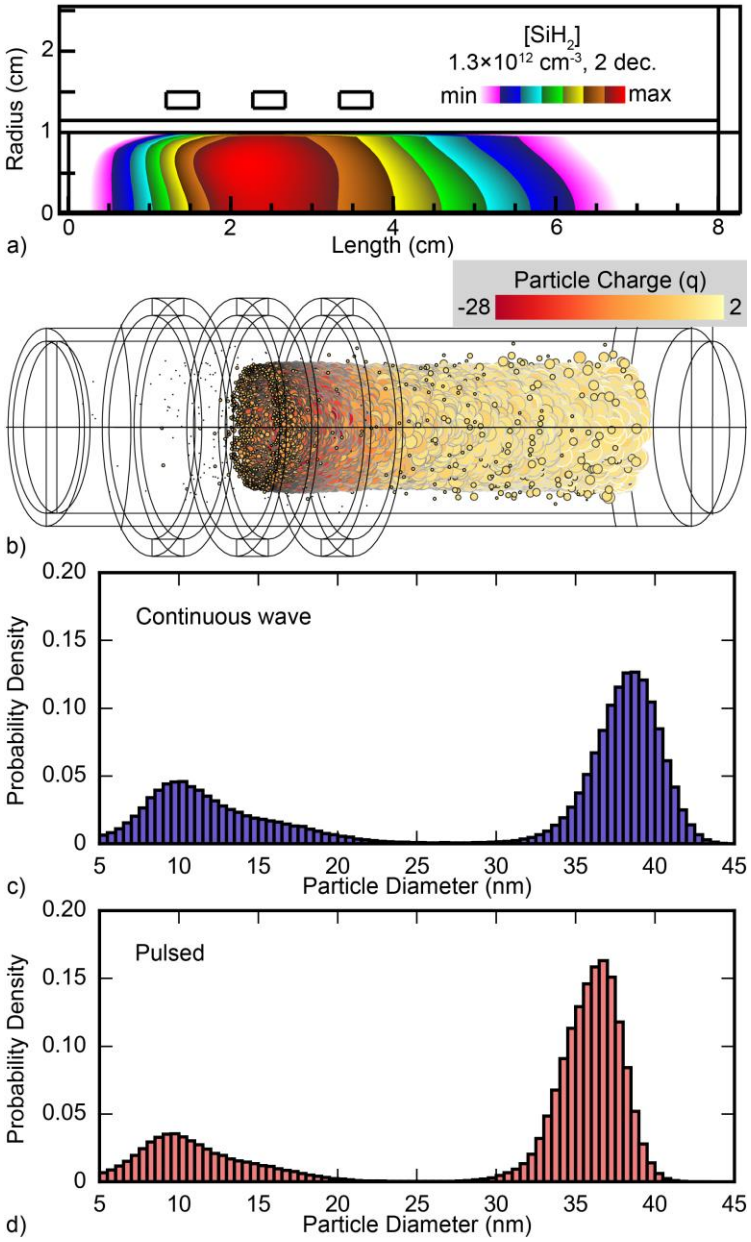

Figure 7-9. Results when considering continuous particle seeding. a) The spatial SiH_2 density, used to determine seeding location probabilities in the DTS, b) the 3-dimensional steady-state output of the DTS with nanoparticles of relative size and charge indicated by color and c) Size distributions of the NPs collected leaving the reactor for continuous wave power and for the pulsed conditions (5 ms pulse, 10 W average power, 50% duty cycle).

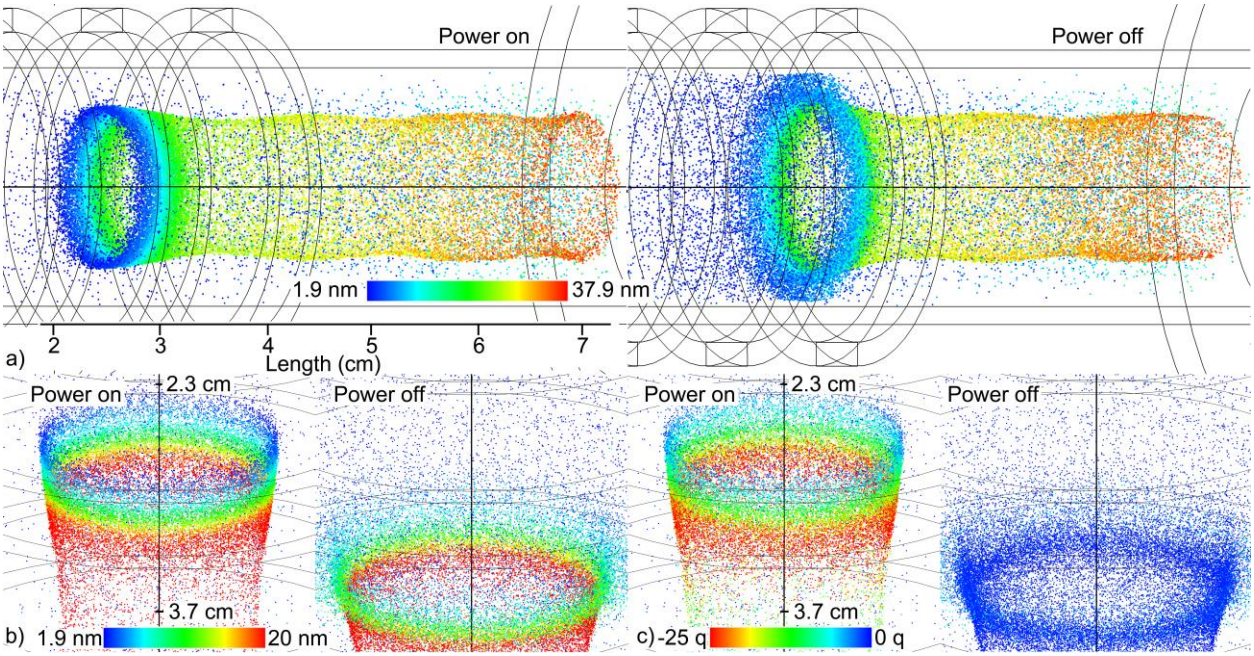

Figure 7-10. Output of the DTS at two times (power on – right before it turns off; power off – right before the power turns back on) for pulsed conditions with continuous particle seeding (5 ms pulse, 10 W average power, 50% duty cycle). a) Particle size indicated by color from 1.9 nm to 37.9 nm, b) particle size indicated by color, rescaled to 1.9 nm to 20 nm, and c) particle charge indicated by color.

7.6 References

[1] U. Kortshagen, J. Phys. D. Appl. Phys. **42,** (2009).

[2] A. Bapat, C. Anderson, C. R. Perrey, C. B. Carter, S. A. Campbell and U. Kortshagen, Plasma Phys. Control. Fusion **46,** (2004).

[3] U. R. Kortshagen, R. M. Sankaran, R. N. Pereira, S. L. Girshick, J. J. Wu and E. S. Aydil, Chem. Rev. **116,** 11061 (2016).

[4] C. R. Gorla, S. Liang, G. S. Tompa, W. E. Mayo and Y. Lu, J. Vac. Sci. Technol. A Vacuum, Surfaces, Film. **15,** 860 (1997).

[5] A. Izadi and R. J. Anthony, Plasma Process. Polym. **16,** 1 (2019).

[6] L. Mangolini, E. Thimsen and U. Kortshagen, Nano Lett. **5,** 655 (2005).

[7] A. Alvarez Barragan, N. V. Ilawe, L. Zhong, B. M. Wong and L. Mangolini, J. Phys. Chem. C **121,** 2316 (2017).

[8] E. Thimsen, U. R. Kortshagen and E. S. Aydil, J. Phys. D. Appl. Phys. **48,** (2015).

[9] B. L. Greenberg, S. Ganguly, J. T. Held, N. J. Kramer, K. A. Mkhoyan, E. S. Aydil and U. R. Kortshagen, Nano Lett. **15,** 8162 (2015).

[10] A. Ho, R. Mandal, R. R. Lunt and R. J. Anthony, ACS Appl. Nano Mater. **4,** 5624 (2021).

[11] B. Ramamurthi and D. J. Economou, J. Vac. Sci. Technol. A Vacuum, Surfaces, Film. **20,** 467 (2002).

[12] D. J. Economou, J. Phys. D. Appl. Phys. **47,** 303001 (2014).

[13] L. Xu, D. J. Economou, V. M. Donnelly and P. Ruchhoeft, Appl. Phys. Lett. **87,** 041502 (2005).

[14] S. Samukawa, Appl. Phys. Lett. **64,** 3398 (1994).

[15] H. Shin, W. Zhu, L. Xu, V. M. Donnelly and D. J. Economou, Plasma Sources Sci. Technol.

20, 055001 (2011).

[16] S. Banna, A. Agarwal, G. Cunge, M. Darnon, E. Pargon and O. Joubert, J. Vac. Sci. Technol. A Vacuum, Surfaces, Film. **30,** 040801 (2012).

[17] S. Banna, A. Agarwal, K. Tokashiki, H. Cho, S. Rauf, V. Todorow, K. Ramaswamy, K. Collins, P. Stout, J. Y. Lee, J. Yoon, K. Shin, S. J. Choi, H. S. Cho, H. J. Kim, C. Lee and D. Lymberopoulos, IEEE Trans. Plasma Sci. **37,** 1730 (2009).

[18] A. Agarwal, P. J. Stout, S. Banna, S. Rauf, K. Tokashiki, J.-Y. Lee and K. Collins, J. Appl. Phys. **106,** 103305 (2009).

[19] P. Brichon, E. Despiau-Pujo, O. Mourey and O. Joubert, J. Appl. Phys. **118,** 053303 (2015).

[20] C. Larriba-Andaluz and S. L. Girshick, Plasma Chem. Plasma Process. **37,** 43 (2017).

[21] W. Chen, J.-L. Maurice, J.-C. Vanel and P. Roca i Cabarrocas, J. Phys. D. Appl. Phys. **51,** 235203 (2018).

[22] N. Kodama, Y. Tanaka, K. Kita, Y. Uesugi, T. Ishijima, S. Watanabe and K. Nakamura, J. Phys. D. Appl. Phys. **47,** 195304 (2014).

[23] K. Akashi, Y. Tanaka, Y. Nakano, R. Furukawa, T. Ishijima, S. Sueyasu, S. Watanabe and K. Nakamura, Plasma Chem. Plasma Process. **41,** 1121 (2021).

[24] M. Kambara, S. Hamazaki, N. Kodama and Y. Tanaka, J. Phys. D. Appl. Phys. **52,** 325502 (2019).

[25] T. E. Sheridan and J. C. Gallagher, Phys. Plasmas **23,** 110703 (2016).

[26] I. V. Schweigert and A. L. Alexandrov, J. Phys. D. Appl. Phys. **45,** 325201 (2012).

[27] L. Wörner, A. V. Ivlev, L. Couëdel, P. Huber, M. Schwabe, T. Hagl, M. Mikikian, L. Boufendi, A. Skvortsov, A. M. Lipaev, V. I. Molotkov, O. F. Petrov, V. E. Fortov, H. M. Thomas and G. E. Morfill, Phys. Plasmas **20,** 123702 (2013).

[28] I. B. Denysenko, N. A. Azarenkov, K. Ostrikov and M. Y. Yu, Phys. Plasmas **25,** 013703 (2018).

[29] B. van Minderhout, T. Peijnenburg, P. Blom, J. M. Vogels, G. M. W. Kroesen and J. Beckers, J. Phys. D. Appl. Phys. **52,** 32LT03 (2019).

[30] B. van Minderhout, J. C. A. van Huijstee, B. Platier, T. Peijnenburg, P. Blom, G. M. W. Kroesen and J. Beckers, Plasma Sources Sci. Technol. **29,** 065005 (2020).

[31] N. Chaubey, J. Goree, S. J. Lanham and M. J. Kushner, Phys. Plasmas **28,** 103702 (2021).

[32] M. Mamunuru, R. Le Picard, Y. Sakiyama and S. L. Girshick, Plasma Chem. Plasma Process. **37,** 701 (2017).

[33] S. L. Girshick, J. Vac. Sci. Technol. A **38,** 011001 (2020).

[34] Z. Xiong, S. Lanham, E. Husmann, G. Nelson, M. A. Eslamisaray, J. Polito, Y. Liu, J. Goree, E. Thimsen, M. J. Kushner and U. R. Kortshagen, J. Phys. D. Appl. Phys. **55,** 235202 (2022).

[35] M. J. Kushner, J. Phys. D. Appl. Phys. **42,** 194013 (2009).

[36] S. J. Lanham, J. Polito, X. Shi, P. Elvati, A. Violi and M. J. Kushner, J. Appl. Phys. **130,** 163302 (2021).

[37] M. J. Kushner, J. Appl. Phys. **71,** 4173 (1992).

[38] J. Perrin, O. Leroy and M. C. Bordage, Contrib. to Plasma Phys. **36,** 3 (1996).

[39] R. Le Picard, A. H. Markosyan, D. H. Porter, S. L. Girshick and M. J. Kushner, Plasma Chem. Plasma Process. **36,** 941 (2016).

[40] M. Jiménez-Redondo, M. Cueto, J. L. Doménech, I. Tanarro and V. J. Herrero, RSC Adv. **4,** 62030 (2014).

[41] J. E. Allen, Phys. Scr. **45,** 497 (1992).

[42] J. E. Allen, B. M. Annaratone and U. de Angelis, J. Plasma Phys. **63,** 299 (2000).

[43] Chunshi Cui and J. Goree, IEEE Trans. Plasma Sci. **22,** 151 (1994).

[44] J. E. Daugherty, R. K. Porteous and D. B. Graves, J. Appl. Phys. **73,** 1617 (1993).

[45] V. Vyas, G. A. Hebner and M. J. Kushner, J. Appl. Phys. **92,** 6451 (2002).

[46] M. D. Kilgore, J. E. Daugherty, R. K. Porteous and D. B. Graves, J. Appl. Phys. **73,** 7195 (1993).

[47] S. A. Khrapak, A. V. Ivlev, G. E. Morfill and H. M. Thomas, Phys. Rev. E - Stat. Physics, Plasmas, Fluids, Relat. Interdiscip. Top. **66,** 4 (2002).

[48] S. J. Choi and M. J. Kushner, IEEE Trans. Plasma Sci. **22,** 138 (1994).

[49] L. Talbot, R. K. Cheng, R. W. Schefer and D. R. Willis, J. Fluid Mech. **101,** 737 (1980).

[50] G. K. Batchelor and C. Shen, J. Colloid Interface Sci. **107,** 21 (1985).

[51] D. J. Rader and A. S. Geller, Plasma Sources Sci. Technol. **3,** 426 (1994).

[52] X. Shi, P. Elvati and A. Violi, J. Phys. D. Appl. Phys. **54,** 365203 (2021).

[53] K. I. Hunter, J. T. Held, K. A. Mkhoyan and U. R. Kortshagen, ACS Appl. Mater. Interfaces **9,** 8263 (2017).

[54] A. Bapat, C. R. Perrey, S. A. Campbell, C. Barry Carter and U. Kortshagen, J. Appl. Phys. **94,** 1969 (2003).

[55] C. A. Beaudette, H. P. Andaraarachchi, C.-C. Wu and U. R. Kortshagen, Nanotechnology **32,** 395601 (2021).

[56] G. A. Hebner and C. B. Fleddermann, in IEEE Conference Record - Abstracts. 1997 IEEE International Conference on Plasma Science **82,** 141 (IEEE, 1997).

Chapter 8 Conclusions and Future Work

Low temperature plasmas have been widely used for material processing, particularly in the semiconductor industry owing to the capability to control flux of ions and other chemically reactive species to surfaces in unique ways. Pulsing the power to generate the plasma has shown benefits, offering additional customizability and enabling further means of control. The utility of low temperature plasmas has become more appreciated by other fields of study, in particular plasma-based nanoparticle synthesis which is one of the main points of focus in this dissertation. The results shown in this work used the 2-dimensional Hybrid Plasma Equipment Model to computationally model low temperature plasmas on the reactor scale. The Dust Transport Simulator was used to kinetically model particle growth in the plasma. Summaries of each chapter are presented in Sec. 8.1. The main contributions of this work are summarized in Sec. 8.2. Details about future work are addressed in Sec. 8.3.

8.1 Summary

Chapter 1 details fundamental physics that govern low temperature plasmas relevant to this work. The benefits of using low temperature plasmas for material processing were outlined, specifically focusing on uses in the semiconductor industry and newer ventures into nanoparticle synthesis. Inductive and capacitive plasma sources were introduced, and the benefits of pulsed power in these systems were discussed. The field of dusty plasmas and the subset of nanoparticle

containing plasmas were reviewed. Current plasma-based nanoparticle growth theory and computational models, along with shortcomings in current understanding, were presented.

In Chapter 2, the computational models used for this thesis were discussed. Plasma simulation was done using the Hybrid Plasma Equipment Model (HPEM), a 2-dimensional multi-fluid simulator for low temperature plasmas. The HPEM was updated to better interface with the Dust Transport Simulator (DTS), a 3-dimensional kinetic particle model to track trajectories, charge, and growth of nanoparticles in the plasma. Significant modifications of the DTS were needed to capture particle growth. The updated code enables numerical exploration into the mechanism of nanoparticle growth in low temperature plasmas, something that is difficult to measure via experiments.

Chapter 3 details collaborative research into pulsed inductively coupled plasmas. The 2-dimensional plasma model (HPEM) was benchmarked against 3-dimensional plasma measurements for pulsed Ar plasmas and were found to be in good agreement. This modeling was extended to pulsed electronegative plasmas (Ar/Cl_2) where the E- to H-mode transition of power deposition naturally occurs from pulse to pulse. Modeling of these types of plasmas was found to heavily depend on the power matching network connected to the antenna.

In Chapter 4, the effects of a chirped bias electrode in an inductively coupled plasma processing chamber were discussed. Sweeping the frequency of the voltage applied to the bias lead to ions hitting a wafer for processing at energies that differ from using the component frequencies independently. This difference was a consequence of the dynamic charging and discharging of the self-generated dc bias which balances the current. Plasma systems should be treated holistically when modeling, a major benefit of using a full system simulator. The idea of frequency tuning as a tool for matching power was also briefly discussed.

In Chapter 5, the idea of particle trapping in plasma nanoparticle synthesis reactors was introduced. Experimental results from three separate plasma reactors, and two separate computational models for nanoparticle trajectories (one being the Dust Transport Simulator) were used to give credence to this theory. This work may constitute a shift in perspective of the plasma-based nanoparticle synthesis community – previous works assumed nanometer sized particles were not confined in the plasma and simply were entrained by the local gas flow. Engineering of systems to trap particles in specific locations may be possible to create custom-designed nanoparticles.

In Chapter 6, the scaling of Si nanoparticle growth rates in Ar/SiH_4 plasmas was explored using the coupled HPEM/DTS. Small, sub-nm sized particles were initialized in the plasma and particle trajectories, charge, and growth were tracked. The mechanism for particle growth under a wide range of conditions showed that particles were trapped in the plasma over multiple gas residence times. During this time, particles grew via flux of radical growth species until a critical particle size was reached – where the force due to fluid drag overcame the electrostatic trapping force, and particles naturally flowed out of the reactor. Particle growth rates while varying operating conditions (power, flow rate, pressure, reactor diameter) were discussed.

Finally, Chapter 7 details how pulsed power may be beneficial for plasma-based nanoparticle synthesis. The HPEM/DTS combined computational model was used to model nanoparticle synthesis using Ar/SiH_4 plasmas. For the same average power, more narrow particle size distributions may be achieved using pulsing. This is due to increased particle trapping when the power is on – both the increased T_e and n_e lead to more negative charged particles. The effects of varying the pulse repetition frequency and duty cycle on particle sizes were characterized.

8.2 Contributions

The work from this thesis intellectually contributes to the low temperature plasma field in a few distinct ways, listed below.

1. Pulsing the power in low temperature plasmas, in many cases, necessitates resolving the E- to H- transition between modes of power deposition in inductively coupled plasmas (ICPs).

Significant effort has gone into researching the hysteresis of E-H mode transitions in ICPs, mostly studied on time scales for the systems to be in steady-state. Pulsing the power blurs the lines between distinct modes, particularly for conditions where the plasma density significantly decays in the afterglow. When power is initially turned on at the beginning of a pulse, power may only be able to be deposited capacitively due to a large electromagnetic skin depth. Even after peak plasma density is reached, capacitive power may still significantly contribute to the total power. The specifics of the matching network used to supply this power can have a significant effect on plasma reignition each pulse as well. These ideas have inspired further investigations into alternative methods to reignite the plasma such as external photon sources, or simply not fully turning off the power (low to high power pulsing) to still obtain some of the benefits of pulsing.

2. The mechanism for nanoparticle growth in low temperature plasmas likely depends on electrostatic particle trapping in the plasma.

Prior to work contained in this thesis, the predominant belief in the plasma-based nanoparticle synthesis community was that particles were mostly neutral or singly negative charged. Modeling work using the coupled HPEM/DTS consistently showed particles charging more negative and becoming electrostatically trapped. This seemed to be the natural result when including as much of the physics as was reasonably possible – no tuning parameters are included

in the model. Evidence of particle trapping was later found by collaborators through experiments and with separate computational models. This has been seen as quite an exciting development for the field – possibly leading to breakthroughs for controlling nanoparticle growth.

3. Pulsing the power in plasmas for nanoparticle synthesis is an additional method to control particle growth.

Further modeling work using the coupled HPEM/DTS showed that pulsing the power may give additional benefits for nanoparticle synthesis in low temperature plasmas. Under certain conditions, pulsing increased nanoparticle monodispersity (a very desirable quality). Varying the pulse duty cycle and pulse repetition frequency could be a method to control the average nanoparticle size. Simple source pulsing alone shows the potential for electrostatic manipulation of particle positions in the plasma, an idea left to expand on as future work.

4. The long-term impact of this research shows the potential for breakthroughs in plasma-based nanoparticle synthesis.

The above intellectual contributions holistically depict a very promising future for plasma-based nanoparticle synthesis. The updated DTS can be used by future researchers to model specific systems and bring improvements to nanoparticle manufacturing. Nanoparticles are already used in a wide variety of fields such as the medical, chemical, energy, and electronics industries. Specific applications are outside the scope of this dissertation, but higher quality nanoparticles may be envisioned by some to revolutionize any of these fields. With the improved mechanistic understanding developed from this research, it may soon be possible to synthesize particles with properties that may now seem impossible.

8.3 Future Work

Modeling pulsing the power in inductively coupled plasma reactors is numerically challenging since the system is constantly in a transient state. The work presented in this thesis was only possible due to the modular nature of the Hybrid Plasma Equipment Model – i.e. decoupling the electromagnetic solution for the inductive power in the electromagnetics module (EMM) by solving in the frequency domain. When the power initially turns on, the plasma conductivity can significantly change on sub-rf cycle timescales which can lead to numerical instabilities. Note this is not simply a numerical problem, but one that can present experimental challenges as well [1]. Further resolving the E- to H- transition may require moving to a time-domain solution rather than the frequency domain. However, this makes the results more dependent on the specifics of the matching network in the simulation rather than a general solution (e.g. I(t) and/or V(t) supplied to the antenna rather than a specified power). More accuracy may also be obtained by moving to a fully kinetic simulation (rather than fluid based), in particular to resolve the electrostatic waves seen propagating into the bulk of the plasma.

There are several improvements that could be made to better capture the physics of low temperature plasmas for nanoparticle synthesis over what is shown in this work. Experiments typically operate in conditions where the synthesis gas is assumed to be totally consumed in the plasma – either through wall deposition or forming nanoparticles. The particle densities capable of being ran in the Dust Transport Simulator are much smaller than this, and have negligible impact on the reactive species densities in the plasma. Increasing the number of particles used in the simulation easily becomes cache limited when operating on CPUs. Moving the DTS to GPU computation seems like a logical step, particularly for particle-particle interactions, but the full calculation needed per particle is far from a simple implementation. Using pseudoparticles (where

particles inside of the DTS count as thousands of particles, for example) may be another solution, but the method for resolving particle-particle interactions would need to be addressed (particles clouds interacting with other particles via shielded interactions is likely poorly characterized as a direct pair-wise interaction). The best course of action is unclear, and likely a combination of some of the proposed solutions will be necessary.

Another improvement that is left as future work is composition tracking of the particles – enabling modeling of more complex particle growth such as for core-shell nanoparticle. Preliminary work was done to track the composition of particles as a function of radius in the DTS, however, the algorithm fails to capture atomic monolayer limits. Future improvements would be to switch to a surface coverage model to track composition. An added benefit of this approach is that it also provides valuable information that may be needed to capture particle temperature in the model, since surface reactions become a main contributor to particle temperature under many conditions [2]. The ability to predict crystal structure (dependent on particle temperature) with various operating conditions would be very valuable.

8.4 References

[1] G. A. Hebner and C. B. Fleddermann, J. Appl. Phys. **82,** 2814 (1997).

[2] N. J. Kramer, R. J. Anthony, M. Mamunuru, E. S. Aydil and U. R. Kortshagen, J. Phys. D. Appl. Phys. **47,** 075202 (2014).